Macromolecular Dynamics and Structure in Crowded and Confined Environments

by

A Dissertation submitted to the School of Graduate Studies in partial fulfillment of the requirements for the degree of

Doctor of Philosophy

Department of Physics and Physical Oceanography

Memorial University of Newfoundland

June 10, 2018

St. John's   Newfoundland

Abstract

Macromolecular crowding and confinement, the effects caused by high concentrations of macromolecules in solution and/or in small compartments, are believed to influence diffusion processes, intermolecular interactions, protein folding, and intracellular transport in living cells. Understanding mechanisms of transport in biological systems (such as living cells) is complex and challenging. We construct cell mimetic environments in which the artificial macromolecules (e.g. polyethylene glycol, Ficoll70) are compartmentalized not in cells but in concentrated environments and agarose gel networks. In this work we have established a system to generate stable and monodisperse droplets of hierarchical confinement. The goal of this study is to measure translational diffusion in crowded and confined geometries of varying concentrations of different macromolecules on diffusion. We have combined the use of pulsed-field-gradient nuclear magnetic resonance (PFG NMR) with small-angle neutron scattering (SANS) in order to obtain new insights in simple model systems of macromolecular crowding. The NMR and SANS techniques complement each other. Using PFG NMR technique, we have monitored the dynamics of synthetic macromolecules with multiple chemical components in complex environments. SANS, on the other hand, yields structure (size) of macromolecules. Our experimental findings in cell mimetic environments provide an important step towards gaining further insights into the effects of macromolecular crowding on diffusion and conformation.

Acknowledgements

I would like to thank to my supervisor, Dr. Anand Yethiraj, for his trust in my capabilities and his support in every aspects of this work. My acknowledgements go to all the people who helped me in any aspects of this work, namely: Ms. Somayeh Khajehpour Tadavani, Dr. Celine Schneider, Mr. David Davidson, Dr. Lilin He and Dr. William Hamilton.

I would also like to acknowledge my supervisory committee: Dr. Kristin M. Poduska and Dr. James Munroe for their appreciative comments during the supervisory committee meetings.

I would like to express my thanks to Dr. Valerie Booth and Ms. Donna Jackman for providing bacterial cell lysate. In addition, I would like to acknowledge Dr. Arun Yethiraj for his collaboration and constructive contribution.

Thanks to Mr. Brian Power and Mr. Stephen Milway for helping me with microfluidic design.

Table of Contents

List of Tables

List of Figures

List of Abbreviations

NMR	Neuclear magnetic resonance
PFG	Pulsed field gradient
PFG NMR	Pulsed-field-gradient neuclear magnetic resonance
PFG-SE	Pulsed-field-gradient spin echo
PFG-STE	Pulsed-field-gradient stimulated echo
FID	Free-induction decay
TMS	Tetramethylsilane
RF	Radio frequency
SANS	Small angle neutron scattering
NSE	Neutron spin echo
PEG	Polyethylene glycol
PVP	polyvinylpyrrolidone
SDS	Sodium dodecyl sulfate
PEO	Polyethylene oxide
IDP	Intrinsically disordered proteins
RBC	Red blood cell
HeLa	Henrietta Lacks
FRET	Förster resonance energy transfer

FCS	Fluorescence correlation spectroscopy
FITC	Fluorescein isothiocyanate
EGFP	Enhanced Green Fluorescent Protein
MC	Monte Carlo
MD	Molecular dynamics
E. coli	Escherichia coli
DNA	Deoxyribonucleic acid
RNA	Ribonucleic acid
BSA	Bovine serum albumin
CI2	Chymotrypsin inhibitor 2
NaCl	Sodium chloride
PDI	Polydispersity index
AO	Asakura-Oosawa
DLVO	Derjaguin-Landau-Verwey-Overbeek
CMC	Critical micellar concentration
MSD	Mean-square displacement

Chapter 1

Introduction

Biological systems (such as living cells) are packed with macromolecules such as proteins, nucleic acids, actin filaments, cytoskeletons, and organelles that occupy a significant part (between 7% and 40%) of the total volume. Such a condition in living cells has been termed as "macromolecular crowding" rather than "concentrated" because multiple kinds of macromolecules are present, each at a low concentration but collectively at a high concentration.

Entropy is important, because a macromolecule is expected to exclude other molecules from its neighborhood. When one increases the packing fraction of macromolecules in solution, the number of ways that one can place added molecules is progressively restricted to the part of space from which they are `not excluded`. The consequence of this phenomenon is to decrease the self-diffusion coefficient as well as alter the conformational dynamics of proteins. This macromolecular crowding has been viewed primarily as a non-specific excluded volume effect.

However, most proteins are charged and have hydrophobic and polar chemical groups, so "chemical" interactions (charge, hydrophobicity, hydrogen bonding) are likely also important in macromolecular crowding. Hence the macromolecules of in-

1

terest interact with each other `via` specific and non-specific interactions which are extremely varied.

Another thing that `makes life difficult` is that often there are many competing interactions, all of comparable strength. Moreover, biological environments are not homogeneous. Biological systems have hierarchical structure and organization. Understanding mechanisms of transport in such a complex system is challenging.

In this thesis, we consider toy models of crowding and confinement. Although toy models, by definition, do not capture all the details and complexities of real systems, they provide insights and understanding for the underlying physical phenomena. Since toy models are simple, it is possible to describe them analytically, or using computer simulations. One can then compare theoretical predictions with experiments. We studied the effects of crowding and confinement on relatively simple systems with increasing levels of complexity in order to capture, in a recursive manner, the details and complexities of real biological systems. Our model system has two components: (1) polymer (polyethylene glycol) that mimics protein, and (2) a nanoparticle (Ficoll70) that mimics the macromolecular crowder.

The focus of this dissertation is to combine the use of pulsed-field-gradient nuclear magnetic resonance (PFG NMR) with small-angle neutron scattering (SANS) in order to obtain new insights in simple model systems of macromolecular crowding. The NMR and SANS techniques complement each other. The magnetic resonance spin echo yields direct dynamical information on the millisecond-to-second timescale `via` pulsed-field-gradient NMR (PFG-NMR) diffusion measurements. This can be done for many species in the same system simultaneously using their different ^{1}H chemical shifts.

PFG-NMR can typically be used in dilute suspensions to obtain hydrodynamic radii from the measured diffusion coefficients using the Stokes-Einstein relation. The

Stokes-Einstein relation is strictly valid at infinite dilution, and at finite concentrations there are hydrodynamic corrections. However, in the presence of crowding, the size (and shape) of the macromolecule can also be changed. SANS, on the other hand, yields the size of macromolecules as well as the presence of structure on larger length-scales. Tandem SANS/NMR experiments can be carried out on very similar (although not identical, because deuteration is not required for ^{1}H NMR) sample preparations because the contrast in both cases comes from the nuclear spin. Hence, we independently measure true hydrodynamic size *via* small-angle scattering measurements to construct a complete picture of the macromolecular dynamics.

Understanding the physics of macromolecular crowding and confinement in a living system involves some background concepts. Chapter 2 reviews cell organization to identify a few general features that may apply to the model bio-mimetic environment. It includes an overview of polymer theories as well as building blocks of self-assembly in polymers. We begin with general definitions for polymers and present the physical parameters which are used to characterize the average size of each of these building blocks. In this chapter we briefly outline colloidal interaction forces and the theory relating to dynamics in colloidal suspensions. We also present relevant studies of polymer dynamics in crowded solutions as well as structural properties of polymer–nanoparticle mixtures. We conclude this chapter with a brief review of macromolecular confinement and relevant studies on the diffusion in gel media.

We used PFG-NMR and SANS measurements, coupled with rheology, to investigate the dynamics and structral evolution of polymer in the presence crowders at varying concentrations. Chapter 3 describes the experimental techniques. We discuss the two main relaxation processes and the mechanism behind the relaxation processes in NMR. We outline the main pulse sequences (pulsed-field-gradient spin echo (PFG-SE) and pulsed-field-gradient stimulated echo (PFG-STE)) which are used to measure

the molecular self-diffusion coefficient. We then present the fundamentals of scattering. Discussed next are analysis methods based on Debye theory and the Guinier approximation, which are used to obtain the radius of gyration of the polymer chain. Finally, we discuss basic concepts in rheology including flow curves, as well as the theory of rheology.

Chapter 4 - 7 are the experimental results. In Chapter 4, we elucidate the nature of a model system of macromolecular crowding composed of nonionic polymer polyethylene glycol (PEG) and uncharged polysaccharide (Ficoll70) in aqueous solution. We present the diffusion and structure measurements of the PEG-Ficoll70 system in an aqueous solution over a wide range of PEG concentration and Ficoll70 packing fraction. This work is published [1].

In Chapter 5, we explore the dynamics and the structure of a macromolecular system composed of a nonionic polymer polyethylene glycol (PEG) and charged polysaccharide (charged Ficoll70) in aqueous solution. We present complementary measurements of PFG NMR, SANS, and rheology to explore the mobility, microviscosity, and bulk viscosity of this system. This work is published [2].

In Chapter 6, we present our diffusion and rheology measurements for the uncharged and charged Ficoll70 system. We investigate evidence for the presence of an equilibrium phase composed of monomers and clusters in solutions. In all the work done, we obtain weight-averaged diffusion coeffcients which must then be coupled with a reasonable model (for example monomer and cluster states). We used experimental data and a simple model to quantify the variation of the monomer and cluster fraction over the entire range of Ficoll70 packing fraction. This work is published [3].

Water-in-oil emulsions, due to their high stability and high efficiency of encapsulation of water phases, are good cell–like compartments. In Chapter 7, we examine the formation of micro-scale confinement in the form of monodisperse and stable

water-in-oil emulsion using a flow focusing microfluidic geometry and subsequent characterisation using microscopy as well as NMR. We also present the generation of agarose microbeads for the spatial localization of synthetic macromolecules in a more compartmentalized environment. This chapter reports diffusion measurements of synthetic macromolecules in both micro-scale and nano-scale confinement. This work is published [4].

Finally, in Chapter 8, we conclude with a summary of the achievements and possible future avenues of research made possible by the work contained in this thesis.

Bibliography

[1] S. Palit, L. He, W. A. Hamilton, A. Yethiraj, and A. Yethiraj, "Combining diffusion NMR and SANS enables precise measurements of polymer chain compression in a crowded environment," Physical Review Letters, vol. 118, p. 097801, 2017.

[2] S. Palit, L. He, W. A. Hamilton, A. Yethiraj, and A. Yethiraj, "The effect of crowder charge in a model polymer–colloid system for macromolecular crowding: Polymer structure and dynamics," The Journal of Chemical Physics, vol. 147, no. 11, p. 114902, 2017.

[3] S. Palit and A. Yethiraj, "Dynamics and cluster formation in charged and uncharged Ficoll70 solutions," The Journal of Chemical Physics, vol. 147, no. 7, p. 074901, 2017.

[4] S. Palit, S. K. Tadavani, and A. Yethiraj, "Realization of a stable, monodisperse water-in-oil droplet system with micro-scale and nano-scale confinement for tandem microscopy and diffusion NMR studies," Soft Matter, vol. 14, pp. 448–459, 2018.

Chapter 2

Background and Theory

The cellular interior represents an exquisitely complex and crowded environment. It imposes unique physiochemical constraints on its components governing their properties over multiple length-scales and time-scales. In addition, every cell type harbors a specific biological form in composition [1] which adds another level of complexity. The sum of these factors gives rise to the unique behaviors of the systems under investigation. This chapter starts with a brief overview of the biological cell.

2.1   Cell and Cellular Organization

The cell is the basic working unit of an organism; in the case of prokaryotes and single-celled eukaryotes, it is the entirety of the organism. In general, the cell is organized around its cytosol– a gel-like substance in which organelles, proteins, and other cytoplasmic structures are suspended. Figure 2.1 shows a realistic representation of the cytosol. This figure clearly shows that due to its high content of macromolecules, there is actually not much free space in the cytosol. The cytosol is therefore crowded. This crowdedness is not due to the large amounts of a single protein species, but due

to the high total protein content. The cellular compartments such as the mitochondria and nucleus are also filled with similarly crowded cytosols [2]. The nucleus is a particularly interesting example because its cytosol can be further subdivided into nucleolar and chromosome domains [3]. While crowding occurs inside the organelles as well as the cytosol, the following discussion focuses on the cytosol for the sake of simplicity.
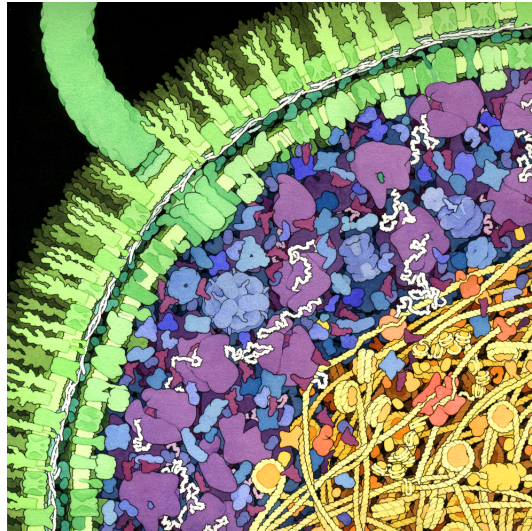
Figure 2.1: A cross-sectional sketch of the cytoplasm of E. coli. Illustration by David S. Goodsell, the Scripps Research Institute. The cytoplasmic region is shown in blue and purple. The nucleotide region, which contains DNA wrapped around histones, is shown in yellow [4].

The number and type of molecules in the cytosol depend on the cell type and probably also on the cell cycle stage [5, 6]. The total concentration of protein in a cell is estimated to be around 50-400 mg/ml, corresponding to 5-40% of its total volume [1, 7]. Zimmermann and Trach estimated the protein content of E. coli to be around 10 to 40% in units of weight/volume [8]. Similarly, Lanni et al. obtained a value of 200-300 mg/ml for 3T3 fibroblasts [9]. Since most of the space in the cytosol is already occupied by other macromolecules, it is tempting to ask how proteins fold and function in such surroundings. This is particularly important because most of

our current information on protein folding was obtained from in vitro experiments in dilute solutions. In fact, experimentalists often strive to use the most dilute solution possible in order to avoid non-idealities and to focus on the pure protein properties. However, given the composition of the cytosol, non-idealities are to be expected. This raises another question: to what extent do inferences drawn from in vitro experiments accurately represent the in vivo situation? Various non-idealities could arise in the cytosol, such as excluded volume effects and non-specific interactions. In addition, the cytosol may be much more viscous than the very dilute solutions used for in vitro studies.

Even this more realistic picture of the cytosol neglects an important layer of complexity: the spatial and temporal organization of the cytosol [10]. The cytosol is not homogenous–its composition varies both spatially and temporally. Differences in its local composition can cause density fluctuations and changes in the local concentrations of specific proteins. These differences can create what are effectively (micro-) compartments based on local density fluctuations rather than an enclosing membrane [11].

Macromolecules, together with flexible polymer chains (such as proteins), are confined at high concentrations within the cellular membrane. This milieu might be considered as a complex colloidal systems of polymer-nanoparticle mixtures in which molecules or poly-molecular particles with a dimension between 1 nm and 1 μm are dispersed in a continuous phase of a different composition. Therefore, we introduce the macromolecular crowding within the context of a tractable experimental model system, idealizing crowding agents as hard spheres and polymers as soft, effective spheres with variable size.

In following sections we reviewed relevant properties of polymer and colloids, focusing on polymer conformations, and second, identify colloidal interactions that apply

to the crowded environment within living cell.

2.2   Polymers

Polymers are ubiquitous in today's world. Plastic food wraps, different kinds of adhesives and rubbers are some of many examples of polymeric materials, without which one can not imagine modern life. Hermann Staudinger, in the 1920s, identified a polymer as a long chain of repeated units. In the early 1950s, Giulio Natta and Karl Ziegler discovered a process for synthesizing many plastics such as polyethylene and polypropylene. Since then many striking findings have been discovered and new polymeric materials have been synthesized. For example, polymer nanocomposites, which are composed of nanosized particles dispersed in a polymer matrix, are currently used in a wide range of applications, from the automobile industry to high-tech electronics and solar cells. Modern medicine also relies heavily on polymeric materials such as contact lenses; artificial joints are also examples of polymeric materials. Hydrogels and polymer-based carriers play an important role in drug-delivery, since a drug is usually suspended in a polymer matrix in order to safely reach its target. In addition to man-made polymers, polymers also occur in nature. Examples of naturally occurring polymers are silk, wool, DNA, cellulose, and proteins.

The systems we are discussing in this work are macromolecular systems such as polymers, polysaccharides, and gels. Synthetic polymers that are commonly used by researchers as a means to simulate crowding are polyethylene glycol (PEG), Ficoll, and dextran (the latter two being branched polysaccharides). Naturally occuring polymers often used for this purpose are proteins such as bovine serum albumin (BSA), lysozyme, hemoglobin etc. Synthetic polymers in this context are long, high molecular weight molecules made up of a chain of smaller, simpler identical molecules. In con-

trast a biological poly-amino acid chain (a protein) is composed of any of 20 different monomers.

2.2.1 Polymer Structure and Dynamics

Polymer molecules are characterized using various physical parameters. Some physical parameters are the degree of polymerisation, the number averaged molecular weight, the weight average molecular weight, and the polydispersity [12]. The degree of polymerisation is the number of structural repeat units or monomers in a polymer chain. Unlike atoms, or small molecules, polymer synthesis never yields molecules with identical degree of polymerization. The number-averaged molecular mass $\overline{M}_n = \sum_{i=1}^{n} N_i M_i / \sum_{i=1}^{n} N_i$ and the weight-averaged molecular mass $\overline{M}_w = \sum_{i=1}^{n} N_i M_i^2 / \sum_{i=1}^{n} N_i M_i$ are used to characterize a polymer solution or a polymer melt that consists of the same type of molecules but with different chain lengths, where N_i is the number of polymer chains (molecules) of molecular weight M_i. A useful measure of the polydispersity is the polydispersity index $PDI = \overline{M}_w / \overline{M}_n$.

The Ideal Chain

Consider a polymer chain composed of $n \gg 1$ monomers connected by bonds. Such a chain is called ideal if any pair of monomers i and j separated by a sufficient number of bonds along the chain ($|i - j| \gg 1$) do not interact with each other at any distances. An ideal polymer, as any other polymer, has many potential conformations. The conformations that a polymer can create depend on its flexibility. There are several models of an ideal polymer chain where the control of its flexibility is based on assumptions restricting the range of allowed bond and torsion angles. The most common examples of these models are the freely jointed chain model, the freely rotating chain model, and the worm-like chain model. To demonstrate the difference

between ideal and real chains, it is sufficient to take the simplest model which is a freely jointed chain model. According to this model all bond angles are equally likely and independent of each other [13]. All bonds are of equal length $l = |r_i|$, where r_i is a bond vector between monomers i and $i-1$. The simplest quantity to characterize the size of the ideal chain is the end-to-end vector. It is determined as the sum of all bond vectors,

$$R = \sum_{i=1}^{n} r_i \tag{2.1}$$

However, the end-to-end vector averaged over all possible states of the polymer is zero, i.e., $\langle R \rangle = 0$, because the configurations with end-to-end vector R and $-R$ are equally probable. For this reason the mean-square end-to-end distance is used instead:

$$\langle R^2 \rangle = \langle R.R \rangle = \sum_{i=1}^{n} \sum_{j=1}^{n} \langle r_i . r_j \rangle \tag{2.2}$$

Here $\langle . \rangle$ denotes the ensemble average. By definition, the scalar product of bond vectors can be written as $r_i . r_j = l^2 \cos \Theta_{ij}$, where Θ_{ij} is a bond angle between bond vectors r_i and r_j. Since directions of bonds of an ideal polymer are not correlated, the angle Θ_{ij} can vary in the range from 0 to 2π with equal probability for $i \neq j$ [12]. Therefore the scalar product of bond vectors averaged over all monomer positions is $\langle r_i . r_j \rangle = l^2 \langle \cos \Theta_{ij} \rangle = 0$ if $i \neq j$ and the only contributions to the mean-square end-to-end distance give the scalar products of equal bond vectors. Thus, the mean square end-to-end distance is written as

$$\langle R^2 \rangle = \sum_{i=1}^{n} \langle r_i . r_i \rangle = n \, l^2. \tag{2.3}$$

The mean-square end-to-end distance allows us to estimate the size of the polymer as $\langle R^2 \rangle^{1/2} = n^{1/2} l$. Obviously, $\langle R^2 \rangle^{1/2}$ is significantly less than the polymer contour

length $L = nl$. This means that polymers very rarely form stick-like configurations, but they are rather entangled to a coil due to polymer flexibility. The flexibility is an essential property of polymers. The mechanism of the flexibility, however, can differ depending on polymer type and its chemical details. In order to construct a universal model independent of the flexibility mechanism one needs to introduce a quantitative parameter, which is a measure of the polymer flexibility. The Kuhn length is such a parameter which is associated with the size of an actual polymer and defines a length scale beyond which correlations between polymer segments do not play a role [14]. Indeed, in a typical polymer there are correlations between neighboring bonds and only distant bonds are uncorrelated, implying that $\langle \cos \Theta_{ij} \rangle = 0$ holds only when $|i - j| = \infty$ and the sum over all bond vectors converges to a finite value denoted by $C_i' = \sum_{j=1}^{n} \langle \cos \Theta_{ij} \rangle$. Then, the mean-square end-to-end distance given by Eq. 2.3 converts to

$$\langle R^2 \rangle = l^2 \sum_{i=0}^{n} C_i' = nl^2 \, C_n, \tag{2.4}$$

where $C_n = \sum_{i=1}^{n} C_i'/n$ is the Flory characteristic ratio defined as the average of the values C_i' over all polymer bonds. Due to the absence of correlations between the distant bonds, C_n converges to a finite value C_∞ for a infinitely long polymers $(n \rightarrow \infty)$. Thus, the approximation of the mean-square end-to-end distance for a long polymer can be expressed in the following form

$$\langle R^2 \rangle \simeq nl^2 \, C_\infty. \tag{2.5}$$

The mean-square end-to-end vector remains proportional to the number of bonds along the polymer and the square of the bond length, however, now the correlations of neighboring bonds are also taken into account. This allows us to introduce the concept of a polymer Kuhn segment by treating a polymer as a sequence of N freely joined

segments of Kuhn length a. The Kuhn length a is determined by the dual requirement $L = Na$, where L is the contour length of the actual polymer, and $\langle R^2 \rangle = Na^2 = C_\infty n l^2$ [13]. Each of the Kuhn segments contains a number of polymer bonds, beyond which the bond correlations are neglected. This model is a universal model describing all ideal polymers independent of the local chemical polymer structure.

So, for N number of monomers of size a, an ideal polymer chain is expressed as [15]

$$\langle R^2 \rangle = Na^2, \tag{2.6}$$

with a being the length of a Kuhn segment and N the number of Kuhn monomers.

As an example, let us consider a linear chain, non-ionic polymer, polyethylene glycol (PEG) 20000, which is one of the components in our study of macromolecular crowding and confinement. The molecular weight of each PEG unit is 44 g/mol. The chemical structure of PEG is shown in Figure 2.3. The two C-O bonds in the PEG monomer (each 0.145 nm) and the C-C bond (0.15 nm) add up to a monomer length 0.44 nm. The number of monomers, n, in a PEG 20000 chain is $20000/44 \approx 450$, and the contour length, $L = 450 \times 0.44 \approx 200$ nm. The Kuhn length (a) is known to be 0.76 nm [16, 17]. It follows that there are $N = 200/0.76 \approx 263$ Kuhn segments.

Another quantity that can characterize the size of a polymer is the radius of gyration. The square of the radius of gyration, R_g^2, is the mean squared distance between monomers and the polymer's center of mass and given by [12]

$$R_g^2 = \frac{1}{N} \sum_{i=0}^{N-1} (R_i - R_{cm})^2, \tag{2.7}$$

where the vector R_i is the position vector of the i-th monomer and R_{cm} is the position

vector of the polymer's center of mass,

$$R_{cm} = \frac{\sum\limits_{i=0}^{N-1} m_i\, R_i}{\sum\limits_{i=0}^{N-1} m_i} = \frac{\sum\limits_{i=0}^{N-1} R_i}{N}. \tag{2.8}$$

This assumes that all monomers have the same mass which is a reasonable assumption for most polymers. In comparison with the end-to-end distance, which can be easily calculated for linear polymers, the radius of gyration allows one to estimate the size of polymers of any architecture, such as branched or ring polymers, where the end-to-end distance is not well defined. For a Gaussian chain, the mean-square radius of gyration can be expressed as $\langle R_g^2 \rangle = Na^2/6$. An estimate of the R_g for PEG 20000 is $\sqrt{263} \times 0.76/\sqrt{6} \approx 5.03$ nm. For PEG 20000 in water at room temperature, the experimental value of R_g, obtained by SANS, is about 5.00 ± 0.04 nm.

The configurations of an ideal chain composed of N monomers can be described by a random walk of monomers since all interactions of distant monomers are neglected and there are no correlations between bond directions. The probability distribution function in this case is given by [14]

$$\begin{aligned} P(R, N) &= \frac{1}{\sqrt{2\pi \langle R^2 \rangle}} \exp\left(-\frac{R^2}{2\langle R^2 \rangle} \right) \\ &= \left(\frac{1}{2\pi Na^2} \right)^{1/2} \exp\left(-\frac{R^2}{2Na^2} \right). \end{aligned} \tag{2.9}$$

Here we assume that each step of the random walk is of length a and independent of previous steps.

The Self-Avoiding Polymer

Polymer conformations change dramatically if we include the effect of monomer monomer interactions which were neglected in the previous section. To show this, we consider a polymer consisting of N monomers of size a, but this time each of the monomers has an excluded volume V_{ex}. Such polymers are called self-avoiding polymers. Due to the excluded volume, monomers of a self-avoiding polymer effectively repel each other on small length scales, leading to an increase of polymer size compared to an ideal polymer, and as a consequence a reduction in the entropy of the polymer. In order to find the size of a self-avoiding polymer one needs to determine a balance between the effective repulsion energy of monomers which swells the polymer and the entropy loss due to such deformation from the ideal state. One of the most successful theories estimating this balance is the Flory theory which is a mean field theory. Following Flory's idea, let us assume that the self-avoiding polymer is swollen to the size R which is larger than the size of an ideal polymer chain $R_{id} = aN^{1/2}$. Then the volume occupied by the polymer scales like R^3, where for brevity we have denoted $\langle R^2 \rangle^{1/2}$ by R. Within this volume we assume that monomers are uniformly distributed and the correlations between them are ignored. The probability of a monomer to be found within the excluded volume of another monomer is a product of the excluded volume V_{ex} and the monomer number density $N/V \sim N/R^3$. Also, the size of the self-avoiding polymer R_{SA} in the equilibrium state [13, 15] is

$$R_{SA} \approx V_{ex}^{1/5} a^{2/5} N^{3/5} \tag{2.10}$$

Thus, the size of the self-avoiding polymer still scales with number of monomers, but with a different power law than the ideal polymer. The ratio of the sizes of a self-avoiding and an ideal polymer composed of an equal number of monomers,

$R_{SA}/R_{ID} \approx (V_{ex}N^{1/2}/a^3)^{1/5}$, shows that the size of a self-avoiding polymer is indeed significantly larger than that of an ideal chain.

Dynamics of Polymer Chains

Understanding the dynamics of polymer chains is key to predicting properties of polymer solutions such as diffusion coefficients, viscosity, sedimentation coefficient, and various rheological properties. The first successful model of polymer dynamics was developed by Rouse [18]. In this model, a polymer chain is modeled as a string of beads connected by springs. The only interaction taken into account within the Rouse model is that between consecutive beads *via* the springs, and the hydrodynamic interaction between beads is ignored.

The Rouse model leads to the prediction that a chain diffusion coefficient scales as $D \sim N^{-1}$, where N is the number of beads in the chain. In dilute solution, however, the hydrodynamic interaction between the chain monomers is important and cannot be ignored. The Zimm model, an extension of the Rouse approach, takes into account hydrodynamic interactions [19]. The Zimm model predicts the dependencies of the chain diffusion coefficient and the chain relaxation time on the chain size, given by $D \sim R^{-1}$. Using the scaling dependence of R on N in a good solvent, $R \sim N^\nu$, where $\nu = 0.588$ is the Flory's exponent, the Zimm model predicts that $D \sim N^{-\nu}$.

2.2.2   The Dilute, Semi-dilute and Cross-over Regimes

Polymer solutions are traditionally divided into three regimes depending on the polymer concentration: dilute, semi-dilute and concentrated. In the following sections some scaling laws of the three regimes of polymer solutions are described.

In a dilute polymer solution, each polymeric molecule is isolated from the others and adopts a globular structure. The dependence of R_g, the radius of gyration of the

polymer on N, the number of monomers per polymer molecule, arises from the notion that a polymer molecule is a statistical object composed of N units. According to the 'freely jointed chain' model or the 'Gaussian' model, the monomer units are assumed to be randomly distributed throughout the molecule volume [14]. Accordingly, the size of the polymer is proportional to the square root of N. $R_g \sim N^{1/2}$ does not take into account that there are many forbidden conformations to the polymer due to the excluded volume effects between distant monomers on the same chain. Taking those conformations into account results in polymer swell (the self-avoiding walk), and R_g is expected to be larger than predicted from $R_g \sim N^{1/2}$. Indeed, light scattering experiments with dilute polymer solutions and theory show that R_g scales like $R_g \sim N^\nu$ [20]. It was shown that the value of $\nu = 0.588$ is universal and does not depend on the chemical nature of the monomers.

In the semidilute regime, polymer molecules cannot be considered as distinct globules, since they are too dense. Rather, the solution can be regarded as a network with a certain average mesh size. When polymer chains interpenetrate, it is meaningless to describe them using parameters derived from N, since the physical location of each monomer is such that it could possibly belong to several polymer molecules.

There is a fundamental difference between the dilute regime and the semi-dilute one. The overlap concentration (c^*) is the concentration at which polymer coils begin to overlap, c^* is expected to be comparable with the local concentration inside a single coil by:

$$c^* \cong \frac{N}{R_g^3} \tag{2.11}$$

When the polymer concentration $c_p \sim c^*$ the coils are in contact but not yet penetrating, thus the mesh size should be comparable with the size of one coil, R_g. For $c_p > c^*$, the network structure must depend on the concentration and not on the degree of polymerization N (the chains must be much longer than the mesh size).

Thus, the mesh size decreases rapidly with concentration.

In highly concentrated solutions, polymer chains increasingly overlap each other, and the swelling of any chain is counteracted by the presence of other chains, leading to a screening effect of the excluded volume interactions between monomers belonging to the same chain. One may regard this situation similarly to the dilute regime with the exception that R_g is now much smaller and depends on polymer concentration rather than on the length of the chain (N or molecular weight). It was suggested to define R_g in a concentrated solution (R_g^{conc}) as a modification of R_g in dilute solution (R_{g0}) [15].

$$R_g^{conc} = R_{g0}\, f\left(\frac{c_p}{c^*}\right) \tag{2.12}$$

Imposing $R_g \sim N^{1/2}$, the following relation between R_g^{conc} and polymer concentration is obtained:

$$R_g^{conc} \sim c_p^{-1/8}. \tag{2.13}$$

This suggests that polymer chains shrink slightly as the concentration increases.

The Semiempirical Equation of State

In a two-component system, the variation of osmotic pressure with volume fraction of solute over the complete range of concentrations is the equation of state of the system. The semiempirical equation of state for PEG, connecting its osmotic pressure with its solution concentration and its transition between the unentangled (dilute) and entangled (semidilute) regimes, is well known. In the semidilute range of concentrations, where scaling laws may apply, des Cloizeaux has proposed a scaling form of the equation of state [21], where the osmotic pressure is expressed as combination of power laws of the reduced concentration c_p/c^*. Cohen et al. [22] have assessed the accuracy of the des Cloizeaux scaling expression for the equation of state in the case

of aqueous solutions of PEG, and found good agreement at concentrations that are in the semi-dilute range, provided that the prefactor α of the scaling law was adjusted. Initially, they claimed that a single value of α was adequate to obtain this agreement for all PEG solutions, and therefore that they had obtained a single parameter equation of state [22]. At lower concentrations where the polymer solution was dilute rather than semidilute, they found pressures that were higher than the scaling law, due to the fact that the macromolecules have more degrees of freedom when they do not overlap. Then they made the statement that at all concentrations the osmotic pressure of a polymer solution could be approximated by the sum of the van't Hoff ideal pressure of the macromolecules and the scaling pressure calculated at the actual concentration through the des Cloizeaux expression with the adequate prefactor [23].
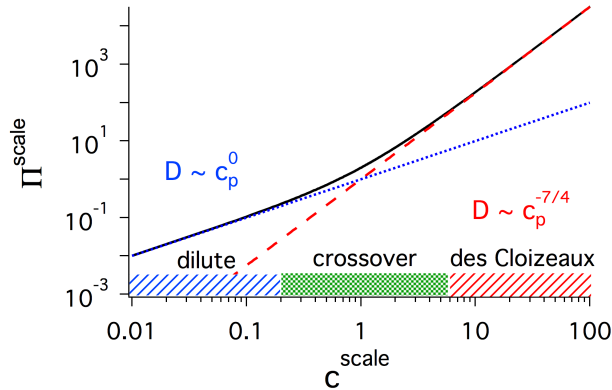
Figure 2.2: The phenomenological scaling form (solid black line), Equation 2.14, of Cohen et al. is an excellent description for pure PEG in water (no crowder). Here a crossover concentration $c^{\#} = \alpha^{-4/5} c^{\star} = \alpha^{-4/5} N^{-4/5} / \bar{V}$. For $c^{\text{scale}} \equiv c_p/c^{\#} \leqslant 0.1$, the system is in the dilute limit (dotted blue line), while for $c^{\text{scale}} \equiv c_p/c^{\#} \geqslant 6$, it is in the semi-dilute limit (dashed red line): the crossover regime (green hashed region) is in between $(0.1 < c^{\text{scale}} < 6)$.

In brief, the derived equation is a linear combination of a low-concentration van't Hoff term [24] and a higher-concentration des Cloizeaux term [21]. A single parameter α locates the crossover from dilute van't Hoff to semidilute des Cloizeaux behavior. In terms of the normalized osmotic pressure $\tilde{\Pi} = \Pi/(RT/M_m \bar{V})$, the scaling form

19

is [23]

$$\Pi^{\text{scale}} = \tilde{\Pi} N^{9/5} \alpha^{4/5} = \left(\frac{c_p}{c^\#}\right) + \left(\frac{c_p}{c^\#}\right)^{9/4}. \tag{2.14}$$

Here the concentration is scaled with respect to a crossover concentration $c^\# = \alpha^{-4/5} c^\star = \alpha^{-4/5} N^{-4/5}/\bar{V}$.

For PEG ($M_w = 18000$ Da), $\alpha = 0.49 \pm 0.01$, the partial specific volume $\bar{V} = 0.825$ ml/g and the scaled concentration $c^\# = \alpha^{-4/5} N^{-4/5}/\bar{V} \sim 0.02$ g/ml, which is related by a constant factor of 1.77 to the overlap concentration $c^\star = 0.01$ g/ml. Thus it can be seen that the expected dilute limit (dotted blue line in Figure 2.2) occurs for $c^{\text{scale}} < 0.1$ (actual polymer concentrations $c_p < 0.002$ g/ml) and the semi-dilute regime (dashed red line in Figure 2.2) for $c^{\text{scale}} > 6$ ($c_p > 0.1$ g/ml). Hence the crossover regime occurs for $0.1 < c_p/c^\# < 6$, where the osmotic pressure deviates from $(c_p/c^\#)^1$ and $(c_p/c^\#)^{9/4}$.

2.3 Colloids

The focus of this thesis is to examine a simplified experimental polymer-colloid model systems that could provide insight into macromolecular crowding in cellular environments. Many biological macromolecules (proteins, for example) are polymers. A macromolecule that is commonly used to mimic a crowded environment is the compact polysachharide nanoparticle, Ficoll70. We thus begin by briefly reviewing colloidal interactions.

2.3.1 The Excluded Volume Interaction

The term "macromolecular crowding" is applied to biological systems because the total concentration of macromolecules inside cells is so high that a significant proportion

of the volume ($\sim 30\%$) is physically occupied and unavailable to other molecules [1, 25–28]. Therefore, one of the most important ingredients in crowding is the excluded volume effect, which is entirely a non-specific physical effect originating from steric exclusion [29].

When does this excluded volume effect matter? Colloids often have a hard, impenetrable core, and the distances between particles are comparable to the size of the particles, the entropy loss due to excluded volume will be significant. The excluded volume interaction in a monodisperse system of hard colloidal spheres manifests itself as an infinite mutual repulsion whenever two sphere centers are at a distance of one particle diameter, i.e. they cannot get any closer. For non-spherical particles, this will be a shape dependant repulsion that is a function of the mutual orientation of the molecules. Macromolecules such as globular proteins are approximately spherical, so we consider spheres as the starting point for our discussion.

The excluded volume interaction in monodisperse hard spheres leads to entropically driven colloidal phase transitions from fluid to solid phases [30]. At low packing fraction, the fluid phase is stable because it has higher entropy. But above $\phi = 0.545$, the ordered solid phase is actually entropically favored [31]. This phase persists from $\phi = 0.545$ to 0.74, the maximal packing of monodisperse spheres. But at $\phi = 0.58$, the crystallization of the colloids can be (under some circumstances e.g. particle polydispersity) arrested [32] by the appearance of a metastable state known as a glass which is characterized by a large increase in the viscosity of the system [33].

2.3.2 The Depletion Interaction

Excluded volume in its simplest form is an entropic repulsion. But entropy can also give rise to attractions *via* the depletion interaction. The theory of depletion interaction, developed by Asakura and Oosawa [34], considers a system that contains

proteins (modeled as large impenetrable spheres of radius R) and non-interacting polymers (modeled as impenetrable small spheres of radius of gyration R_g) in a solvent. When two proteins are closer to each other than the diameter of the polymer, $2R_g$, their exclusion zones overlap. Overlap of excluded (or depletion) volumes increases the volume accessible to the polymer. The physical outcome of this situation is simple: when two spheres are closer than $2R_g$, the polymer coils are squeezed out so that they no longer balance the osmotic pressure exerted by the polymers on the outside of the spheres. As a result, the spheres attract each other when their surfaces are closer than a characteristic size, depending on the polymers in the system. The representation of a polymer molecule by an equivalent hard sphere is physically unrealistic because, even if the chain-like polymer is contained in a spherical envelope, this sphere is penetrable. The Asakura-Oosawa (AO) theory is valid only in the limit of low polymer concentrations, below the semidilute regime (where the representation of polymers as spheres is justified), as well as when $R > R_g$ (the so called "colloid limit").

2.3.3   The Electrostatic Interaction

It is not always realistic to treat macromolecules as hard spheres. In fact the biological cell is a thick "Coulomb soup" where electrostatic interactions affect the structures and dynamics of the constituent macromolecules [35]. The electrostatic interaction between a charged surface and free charges in solution plays an important role in colloidal systems. Because of the ions on the surface, a cluster of opposite charged ions in solution (called "counterions") gather around it and form a diffuse layer [36]. The surface ions and the cloud of counterions form the electrical double layer. The thickness of the double layer is κ^{-1}, known as the Debye-Hückel screening length. The Debye-Hückel screening length can be controlled experimentally by controlling

solvent parameters [37]:

$$\frac{1}{\kappa} = \frac{1}{e}\sqrt{\frac{\epsilon K_B T}{2 c N_a}} \qquad (2.15)$$

where e is the electronic charge, $\epsilon = K\epsilon_0$ is the permittivity constant composed of the vacuum dielectric permittivity ϵ_0 and the dielectric constant of the medium K, c is the molar concentration of a monovalent salt, N_a is the Avogadro number, T is the temperature and K_B is the Boltzmann constant. The Debye-Hückel screening length, κ^{-1}, is a key parameter that measures the contribution of valency, concentration and dielectric constant to the screening of interactions between charges in solutions. In this work, the solutions of charged Ficoll70 were all prepared with added salt in order to keep the conductivity at 1 mS/cm, resulting in a Debye-Hückel screening length $\kappa^{-1} = 3.2 \pm 0.5$ nm.

If two charged macromolecules of radius R approach each other, there is a repulsive force that pushes them apart. In this case, the effect of the diffuse layer plays a dominant role. According to Derjaguin-Landau-Verwey-Overbeek (DLVO) theory, the repulsive interaction potential (known as DLVO potential) in SI units is [38]

$$U_R(r) = 2\pi\epsilon R\psi_0^2 \ln[1 + \exp\{-\kappa(r - 2R)\}], \qquad (2.16)$$

where $\psi_0 = \dfrac{\sigma}{\epsilon\kappa}$, the particle surface potential and σ is the surface charge per unit area. From Equation 2.16, for $r > 2R$, when the Debye-Hückel screening length κ^{-1} is short, i.e. when $\kappa(r - 2R)$ is large, the repulsive potential goes to zero.

23

2.4 Diffusion

In 1828, Robert Brown investigated the random motion of pollen grains in water [39].
Particles in fluids undergo near continual random displacements due to collisions and
subsequent momentum transfer with the surrounding solvent molecules– a situation
termed "Brownian motion". For a large number of particles initially located near to
the same region in space, such Brownian motion has the consequence that the particles
will tend to disperse over time, this situation being known as diffusion.

In 1855, Adolf Fick wrote [40] the first phenomenological law for diffusion, his
model was adapted from the heat conduction equation by Fourier. In Fick's first law,
the diffusive properties of salts dispersing in water is in terms of the dependence of
flux (J) on concentration (Φ) and a diffusion coefficient (D_0) such that [41].

$$J = -D_0 \frac{\delta \Phi}{\delta r} \tag{2.17}$$

The time-dependence of solute concentration, the rate of change of concentra-
tion per unit time, also known as Fick's second law, depends on both the diffusion
coefficient and the second derivative of concentration such that:

$$\frac{\delta \Phi}{\delta t} = -D_0 \frac{\delta^2 \Phi}{\delta r^2} \tag{2.18}$$

Fick's laws are unable to relate macroscopic diffusion to the movement of single
particles.

Throughout the period from 1905 to 1908, three scientists, Einstein, Smoluchowski
and Langevin, all using different approaches, were able to provide a theoretical link
between the phenomenological diffusion coefficient utilized by Fick and the system
properties governing the individual particle displacements, Δr, occurring over time

period, Δt.

Einstein (and Sutherland, independently [42]) [43] realized that instead of trying to relate the movements of diffusing particles to their velocity it was imperative to relate their movement to distance traveled. Considering the stochastic nature of the diffusion process, Einstein reasoned that the average distance traveled by a particle undergoing Brownian motion was zero. However, the mean squared displacement (MSD) provides an alternative physical quantity for determining the total distance traveled in n dimensions during a time period (Δt) such that:

$$\left\langle |\Delta r(t)|^2 \right\rangle = 2n\, D_0\, \Delta t \tag{2.19}$$

Einstein concluded that the rate of diffusion was determined by the interplay between thermal energy that caused the movement of a particle and the corresponding friction between the particle and its surroundings environment. The Einstein relation, published in 1905, links D_0, the translational diffusion coefficient (in dimensions of $m^2\ s^{-1}$), and μ, the mobility of particles:

$$D_0 = \mu\, K_B\, T, \tag{2.20}$$

where K_B is the Boltzmann constant and T is the absolute temperature. The mobility μ is the ratio of the particle velocity to the applied force, $\mu = v/F$. In the limit of low Reynolds number (meaning laminar, smooth, and continuous flow of small particles in a fluid), the mobility μ is simply the inverse of the drag coefficient (i.e., friction experienced by the particle). For spherical particles of hydrodynamic radius R_H, Stokes law, which deals with the frictional force exerted on spherical objects in a

viscous fluid, gives a drag coefficient, (which is an inverse mobility)

$$\mu^{-1} = 6\,\pi\,\eta\,R_H,\tag{2.21}$$

where η is the bulk viscosity of the medium. Combining above equations yields the Stokes-Einstein relation,

$$D_0 = \frac{K_B\,T}{6\,\pi\,\eta\,R_H}\tag{2.22}$$

This useful relation is routinely used to estimate diffusion coefficients of globular proteins in aqueous solution. Small molecules (such as sugars and nucleotides) of approximately 0.5 nm diameter, diffuse quickly with a diffusion coefficient of order 10^{-10} m^2 s^{-1}; molecules of the size of the protein (3-5 nm) diffuse more slowly ($3 - 10\times10^{-12}$ m^2 s^{-1}); whereas larger vesicles (500-1000 nm) diffuse as slowly as 1×10^{-13} m^2 s^{-1}, taking hours to travel across a cell of 15 μm in diameter [44].

Typically, pulsed-field-gradient (PFG) NMR can be used in dilute suspensions to obtain hydrodynamic radii from the measured diffusion coefficients using the Stokes-Einstein relation. However, in the presence of crowding, the size (and shape) of the macromolecule can also be changed. In addition, crowding makes the mobility a function of the packing fraction. Since we only have access to the effective mobility in dynamics measurements, we need independent measures of true hydrodynamic size *via* small angle scattering measurements to construct a complete picture of the macromolecular dynamics.

In this work we use PFG-NMR with small-angle neutron scattering (SANS) in order to obtain new insights in simple model systems of macromolecular crowding.

2.4.1 Microviscosity and Bulk viscosity

The Stokes-Einstein equation (Equation 2.22) has accurately described the motion of diffusing molecules under many conditions, but its accuracy has been questioned in complex solutions. In 1951 Mooney suggested that the Stokes-Einstein equation was only valid at infinite dilution (i.e. where the diffusing species only interacts with solvent) [45]. He suggested that the bulk viscosity of a solution was not always the same as the viscosity sensed by diffusing molecule. This means that crowded solutions would exhibit different viscosities depending on the nature of the crowding agent and diffusing species. He defined viscosity as a function of the size of a crowding agent, its concentration, and a substance specific constant. Since then, multiple studies have come out supporting this idea of microviscosities that differ from bulk viscosity [46–48].

The viscosity sensed by the probe is called the microviscosity and the viscosity that is sensed by a device such as a rheometer (or a viscometer) is referred to as the bulk viscosity. A comparison between microviscosity and bulk viscosity has shown deviations from the Stokes-Einstein equation in dextran solutions [49]. When a probe demonstrates only one mode of translational diffusion, as in the case of simple diffusion, its diffusion coefficient can be directly related to the bulk viscosity by the Stokes-Einstein equation. The authors of that study suggest that the deviations could be due to a major component of microviscosity existing in the dextran solutions, which is smaller than the bulk viscosity in magnitude. Other studies have reported diffusion coefficients of proteins that suggest a difference between microviscosity and bulk viscosity [48, 50, 51]. On the basis of these previous studies, we can identify microviscosity with the frictional force experienced by a macromolecule diffusing in a crowded solution due to interactions with its environment at the micrometer length scale. The

friction experienced by the macromolecule does not necessarily correspond to the bulk viscosity because the former is a measure of the probe's local friction, whereas the latter would measure the friction experienced by an infinitely large probe. The microviscosity is a function of both the crowding density and relative size of each co-solute in a mixture. These two factors would contribute to the measured microviscosity, which would be reflected in the altered translational mobility [49].

The differences between these two viscosities could result in another phenomenon known as sub-diffusion or anomalous diffusion [52], which could significantly slow down reactions in the cell. Solute diffusion that cannot be described by Stokes-Einstein relation for Brownian motion (Equation 2.22) is defined as anomalous diffusion, which is discussed in the next section.

2.4.2 Anomalous Diffusion

The mean-square displacement (MSD) of a particle diffusing in three dimensions is given by

$$\left\langle |\Delta r(t)|^2 \right\rangle = 6\,D_0\,\Delta t \tag{2.23}$$

Fick's law is an established phenomenological law for describing diffusion in isotropic fluids. However, there is no reason to assume that it can be applied to a more complex system such as a crowded environment [53]. Diffusion in complex media such as dense polymer solutions and the cytoplasm may be hindered by interactions with obstacles, transient binding or crowding [54]. Hence, in complex media, the MSD would be expected to obey a power law:

$$\left\langle |\Delta r(t)|^2 \right\rangle = 6\,\Gamma\,t^\alpha. \tag{2.24}$$

Γ is a constant that does not depend on time and is known as the transport factor

and has dimensions of length-squared per fractional time [55]. If the exponent (α) is less than 1, then diffusion is said to be subdiffusive. From the above relation we can define an apparent diffusion coefficient $D(t)$ that would depend on the timescale or, equivalently, the lengthscale of the measurements:

$$D(t) = \Gamma\, t^{\alpha-1} \qquad (2.25)$$

The non-linear time dependence of the MSD can arise from hard interactions between diffusing particles (volume exclusion) [46] or soft interactions (non-specific binding) [56]. Volume exclusion has been attributed to causing anomalous diffusion and to affecting how viscosity is perceived by different molecules. The anomalous diffusion argument is that the crowding agents in crowded solutions physically obstruct the movement of diffusing molecules causing their MSD to have a non-linear relation with time. Volume exclusion is also thought to possibly change rates of diffusion as a function of crowding agent characteristics (such as size and shape) and concentration while still exhibiting Brownian motion [46]. Regardless of the mechanism, one often expects the dynamics to be diffusive at long-enough times: anomalous dynamics is thus often examined by comparing the differences between short and long time dynamics [57].

2.5   A Model of Macromolecular Crowding

The effects of crowding can be mimicked `in vitro` by the addition of a high volume fraction crowding agent. However, using such artificial crowding agents can be complicated, as these crowding molecules can sometimes interact in other ways with the process being examined, such as by binding weakly to one of the components. Hence an ideal crowder should: 1) be highly soluble, 2) have a defined shape, 3) form no

attractive interactions with the polymer/protein of interest, and 4) not interfere with the spectroscopic techniques used in the study. It should be noted, however, that non-idealities might need to be considered as one develops increasingly more realistic model systems of crowding.

Crowding with another protein may seem to be the most straightforward option since that would most closely represent the situation encountered in the cell. However, protein crowders are usually not soluble in sufficiently high concentrations and form numerous charge-charge interactions as most proteins have many charged residues distributed over their surface. It is therefore necessary to either screen these charges with either high salt concentrations or to just use low protein concentrations. Another important concern is that spectroscopic techniques used to probe target protein will be subject to interference from the protein crowder. Since the protein crowder is present at a much higher concentration, it may dominate the signal and complicate the analysis. That being said, crowder macromolecules composed of protein and RNA, would be important eventually in a realistic model system for crowding. For practical reasons, we take a simpler starting point.
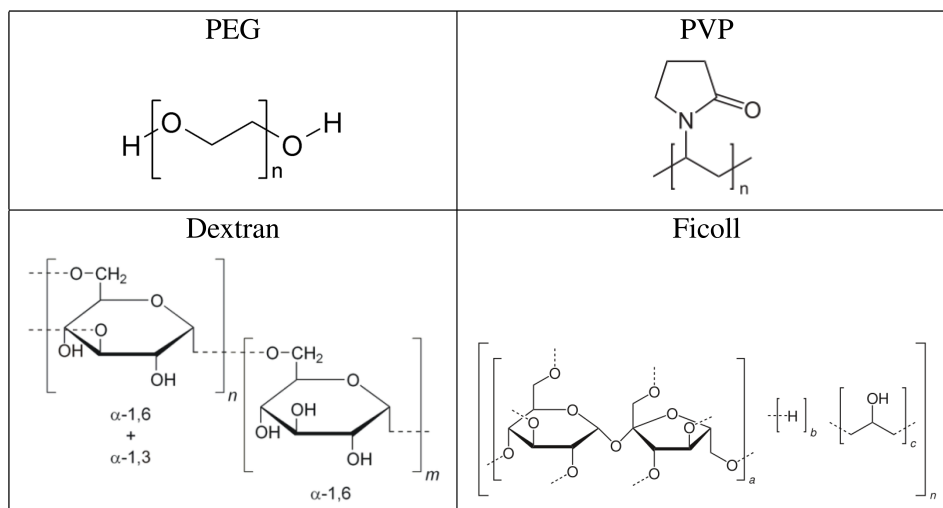
Figure 2.3: Chemical structure of polymers typically used as crowders.

An alternative option is to use synthetic polymers, to induce the effects of macromolecular crowding. Polymers that have been used for this purpose include polyethylene glycol (PEG), dextrans, Ficoll, and polyvinylpyrrolidone (PVP). These crowding agents offer an advantage that they can be prepared in different sizes. PEG is a polymer of ethylene glycol, PVP of N-vinylpyrrolidone, dextran of glucose, and Ficoll of sucrose (Figure 2.3). They are highly soluble (up to 400 mg/mL or more in water) and bear no charge at neutral pH. When studying excluded volume effects, it is desirable to avoid attractive interactions between the crowding agent and the polymer/protein of interest. There is evidence that both PEG and PVP forms attractive interactions with proteins in addition to inducing volume exclusion [58–61]. Another important property of the crowding agents is their molecular shape. PEG and PVP are likely to be very flexible polymers [62]. In contrast, Ficoll has a more compact spherical shape. This is because Ficoll is highly branched copolymer of sucrose and epichlorohydrin, which gives it a relatively compact and often sphere-like structure [63–66]. However, dynamic light scattering (DLS) studies have shown that Ficoll 70kDa adopts a structure that is intermediate between a sphere and a random coil [67]. In another study, Ficoll was modelled as a spherocylinder with a radius of 1.4 nm [68]. Dextran is a polymer of D-glucose with a lower degree of branching than Ficoll that adopts a more elongated, flexible shape [66, 69].

2.6   Overview of Previous Crowding Studies

Different experimental techniques as well as computer simulations have been used to study the conformations and dynamics of macromolecules in crowded media have led to a plethora of results in the cell interior and in related model systems. In this section we provide a mini compilation of the reports addressing the structure and transport

in macromolecular crowding.

2.6.1 Structure

An important parameter in studies of conformational structure of biopolymers in a crowded environment is $\lambda = R_g/R_c$, where R_g is the polymer radius of gyration and R_c is the hydrodynamic radius of the crowder, with the regime $\lambda > 1$ ($\lambda < 1$) being referred to as the protein (colloid) limit [70].

Single-molecule Förster resonance energy transfer (FRET) spectroscopy was used to quantify structure of proteins, using PEG as a crowder. For four proteins (and a range of crowder sizes) the radius of gyration was obtained as a function of the volume fraction of the crowder; counterintuitively, chain compression was observed to be stronger with larger crowders [71].

The conformation of polymers is often studied experimentally by small-angle neutron scattering (SANS). SANS has recently been performed to monitor the effect of macromolecular crowding on the size of a protein complex ($R_g = 23$Å) with a high volume fraction ($\Phi_c = 0.4$) of a low-molecular-mass polyethylene glycol (PEG, $R_g = 6$Å) as the crowding agent (the ratio $\lambda = R_g/R_c = 3.8$) . The radius of gyration, R_g, of a protein complex was observed to be reduced by only 3% due to the osmotic pressure exerted by PEG molecules [72].

Intrinsically disordered proteins (IDP) are biopolymers which, due to their conformational flexibility, should be influenced by crowded cellular environments. Using SANS, it was found that the hydrodynamic size of IDP ($R_g = 33$Å) as a function of the concentration of a small globular protein ($R_g = 15$Å) exhibited a 13% decrease for modest crowder packing fractions increases from $\Phi_c = 0$ to ~ 0.07 [73]; for this system $\lambda \sim 2$. On the other hand, another SANS-based study of similar λ revealed that the radius of gyration of the IDP ($R_g = 30$Å) was insensitive to the presence of globular

protein ($R_g = 20$Å) crowders, and showed only a 6% reduction for $\Phi_c \sim 0.2$ [74].

For proteins, the impacts of macromolecules on structure and folding have been well-studied, but parallel studies involving RNA are much more limited. The influence of macromolecular crowders on RNA function and folding has been evaluated for a variety of macromolecular crowding agents. These studies of macromolecular crowding revealed that crowding agents, such as high molecular weight PEGs, dextrans, and Ficolls, in 10 mM salt solution induce 7-fold compaction of RNA structure [75] and comparable results were found using biological macromolecular crowders [76]. In addition, theoretical predictions concerning RNA compaction in the presence of macromolecular crowders have a good agreement with the experimental findings [77, 78].

Le Coeur et al. used SANS to measure the influence of a crowding agent (Ficoll 70) on the radius of gyration of deuterated PEG polymer in water [79, 80]. Focusing initially on aqueous solutions of polymers and crowding agents of comparable radii of gyration ($\lambda = 1$), Le Coeur et al. measured the PEG radius of gyration for varying concentrations of Ficoll 70. By extrapolating to zero polymer concentration, they were able to extract the radius of gyration of a single PEG coil [79]. With increasing mass fraction of the crowding agent, Le Coeur et al. observed a significant compression of the PEG coils. Moreover, the fractional compression increased with the molecular weight of the PEG [80].

Computer simulations have become important tools in crowding studies. Denton and coworkers have performed Monte Carlo simulation studies to explore the response of coil size to crowding in a binary mixtures of ideal polymer coils and hard-sphere nanoparticles [81]. The polymers in their study have a radius of gyration equal to the nanoparticle radius ($\lambda = 1$). These authors observed that polymer coils, modelled as effective penetrable ellipsoids, both contracted and (in the protein limit) became more spherical when crowded by impenetrable, spherical nanoparticles. For crowder volume

fractions (Φ_c) ranging up to 20% the simulation indicate a significant compression of polymer, the distribution shifting to smaller polymer size with increasing nanoparticle crowding. For $\Phi_c = 0.1$ and 0.2, the fractional reductions in polymer radius of gyration are, respectively, 0.915 and 0.826 [82].

Linear polymers and big inert molecules have been used to mimic the intrinsically-disordered proteins (IDPs) and crowders, respectively. A detailed investigation on the size of a linear polymer chain in a concentrated solution of colloidal spherical crowders was presented by Kang et. al., based on computer simulations of a crowding induced structural change of polymers [83]. By using the crowder concentration and the size ratio λ between the polymer and the crowder as control parameters, they have proposed a general picture for the collapse of biopolymers under steric crowding. The result indicated that the size of the polymer coil reduces monotonically with Φ_F [83]. It was shown that smaller crowders, which exert a higher osmotic pressure onto the polymer, compact it to a larger extent as compared to the bigger ones. Thus, for long biopolymers as DNA (large λ), even weak crowding can lead to a coil-to-globule transition. This behavior is, however, not possible for much shorter molecules as IDPs ($\sim O(100)$ residues) even in the limit of close packing.

While there are thus still questions with regard to macromolecular structure in the presence of crowders, a key opportunity in studying polymer conformations in the presence of macromolecular crowding is to extract structure and dynamics for the same system [84]. In this work we build a model crowded systems with increasing levels of complexity in order to capture both structural and dynamical aspects of macromolecular crowding. We have added increasing level of interaction by changing macromolecule/crowder size ratio and investigate the effects of crowding agents, both charged and uncharged at different packing fractions. By tuning interacting forces, can we predict and control how crowding agent perturb polymer conformations and

induce coils to swell or shrink? Our findings provide new insights into the underlying factors of macromolecular crowding and show how these effects can be connected to simulations and theoretical models.

2.6.2 Dynamics

The reduction of the mobility of a macromolecule in crowded media can be measured by measuring the self-diffusion coefficient as a function of the concentration. There are two general approaches for experimental determination of the diffusion coefficient: methods that measure the time dependent behaviour of a large number of particles over relatively large regions of space and methods that involve observing the properties of individual particles over a small region of space. Experimental techniques belonging to the former category include pulsed-field-gradient nuclear magnetic resonance (PFG NMR) [85], optical microscopy-based observation of light absorbing or light-emitting solutes [86, 87], neutron scattering [88, 89] and single- and multi-wavelength dynamic light scattering experiments [90, 91]. Experimental methods belonging to the later category, i.e. methods capable of observing intracellular single molecule diffusive motion at the microsecond and 100-nm level of precision (approximately) are largely due to technological advances in optical microscopy.

Riveros-Moreno and Wittenberg have measured the concentration dependence of the self-diffusion coefficient in myoglobin and hemoglobin solutions [92], by measuring macroscopic diffusion across a gradient, up to volume fractions of 20% and 26%, respectively. They found a plateau at low protein concentration followed by an exponential decrease of diffusivity down to more than one order of magnitude at higher protein concentration.

Neutron scattering is a non-invasive technique to access macroscopic dynamics at high protein concentrations. The dynamics of hemoglobin was studied inside red blood

cells (RBCs) by neutron spin-echo spectroscopy [93]. For contrast reasons, the first study was performed using red blood cells, which have been dialysed against D_2O, at the physiological temperature of 37ºC from $0.02\text{Å}^{-1} \leqslant Q \leqslant 0.13\text{Å}^{-1}$. The diffusion of hemoglobin at high concentration can be understood on the basis of theoretical concepts developed for colloidal suspensions. The main difference is that the effective hydrodynamic volume fraction of the protein must include the hydration shell because of the higher surface over volume ratio of the proteins. The protein-protein friction in the RBCs is mainly controlled by hydrodynamic interactions.

Using high-resolution neutron backscattering spectroscopy and neutron spin echo (NSE), Roosen-Runge et al. [57, 94] probed the self-diffusion of bovine serum albumin (BSA) proteins in crowded aqueous solutions, where the same protein served as crowding agent. The protein motion was inferred from the incoherent dynamic structure factor of the hydrogen atoms. Increasing the protein content up to a volume fraction of 30%, a 10-fold reduction of the translational short-time diffusion coefficient over its value in dilute solutions was observed. Moreover, it has been found that the short time self-diffusion of the investigated model proteins as a function of the protein volume fraction can be understood in terms of models from colloid physics. It is noted that for an accurate comparison with theory, the calibration of the effective hydrodynamic volume fraction occupied by the proteins in the solution including their hydration shell is crucial, and a considerable effort has been made toward the accuracy of the determination of this volume fraction [57]. This determination of the volume fraction is accurate for globular proteins such as BSA.

Häußler studied diffusive dynamics of interacting protein spheres (apoferritin) by neutron spin echo [95, 96]. Apoferritin consists of a spherical shell built of 24 protein units and carries net negative charge at pH 5. The electrostatic interaction was modified by adding various amounts of NaCl to the solutions with different protein

volume fractions from 5% to 20%. The study demonstrates that the proteins show classical diffusion only at relatively low concentration and high ionic strength. Hence the diffusion coefficient approaches the free-particle value of apoferritin and coincides with the diameter of the apoferritin shell (12.2 nm). The dynamic picture at higher concentration solutions reflects the influence of both direct electrostatic and indirect interactions. At low salt concentration and higher volume fraction a strongly peaked structure factor is observed, which is explained in terms of heterogeneity by formation of crystallites in solution.

NSE has been used extensively by Porcar, Liu, and coworkers [88, 89] to study the reversible cluster formation in solutions of globular proteins such as lysozyme where the interaction contains both a short-range attraction and long-range repulsion. The short-range attractions drive association into clusters, but the association to a cluster surface is eventually limited by the overall charge of a cluster, leading to greater long-range repulsion between clusters (or between a cluster and a protein in solution). These study indicate that dynamic clusters with a finite lifetime and in equilibrium with the monomers can be formed at very high concentration. At low volume fraction, the lysozyme solution is mainly constituted by monomers. However, more and more clusters are formed upon increasing concentration. These clusters are termed "dynamic clusters" to indicate that the monomers are rapidly exchanging between monomeric and cluster state. The properties of the protein solution are determined by the properties of the dynamic clusters in the short-time limit probed by NSE. However, the authors conclude that the macroscopic properties in the long time limit are determined by monomeric proteins.

NMR spectroscopy is a powerful technique to study structure and dynamics of macromolecules in solution. The non-invasive character of NMR and the transparency of biological materials to the radio frequency fields used have led to a spectacular devel-

opment of NMR methods for the spectroscopic study of living organisms. Pielak and co-workers used NMR spectroscopy to quantify both the rotational and translational diffusion of the protein chymotrypsin inhibitor 2 (CI2) in a variety of crowded solutions as function of crowder concentration [56]. The crowding agents comprised glycerol, synthetic polymers (PVP, Ficoll), globular proteins (BSA, ovalbumin, lysozyme), and E. coli cell lysates. The bulk viscosity of the solution increases with crowder concentration. The Stokes-Einstein relation suggests a reduced diffusivity ($D \propto 1/\eta$) which describes the measured CI2 diffusion coefficients in glycerol solution and also translational diffusion in ovalbumin, BSA, and cell lysate. In solutions of synthetic polymers, transport is affected less than expected from the increase of viscosity, and the translational motion of CI2 is impeded more than its rotational motion. Surprisingly, the opposite effect was found in protein-crowded solutions and in the cell lysate: rotational diffusion coefficients were suppressed stronger than translational diffusion and stronger than the Stokes–Einstein relation would imply. The findings were attributed to weak non-specific, non-covalent chemical interactions between proteins, while synthetic polymers tend to form a loose mesh work.

Barhoum and Yethiraj used PFG NMR to detect the onset of macromolecular crowding [97]. In their work, diffusion measurements were carried out on a model system composed of anionic surfactant sodium dodecyl sulfate (SDS) and nonionic polymer polyethylene oxide (PEO) in aqueous solution. The variation of the observed SDS diffusion coefficient with concentration shows a plateau at low SDS concentration that is followed by a rapid decrease at concentrations above the critical micellar concentration (CMC). Hence, in the SDS concentration regime below the CMC, the SDS is in the monomeric state while in the SDS concentration regime above the CMC, the SDS is partitioned between monomeric and micellar states. The PFG NMR signal attenuation associated with the SDS peak exhibits monoexponential behaviour over

the whole range of SDS concentration suggests that the exchange between SDS micelles and free solution must be very rapid on the NMR time scale: micelles are thus the original dynamic clusters. They introduced a self-consistent model to obtain the variation of the free monomer concentration and the free micellar concentration over the entire range of SDS concentration.

Virk et al. examined the dynamics of four amino acids up to their solubility limit in water using PFG-NMR experiments and coupled this with molecular dynamics (MD) simulations *via* models that incorporate obstruction (excluded volume effects) and complex formation [98]. The experimental amino acid diffusion coefficients showed the presence of aggregation and obstruction at all amino acid concentrations. The MD simulations are quite sensitive to the force field used; nevertheless Virk et al. find strong evidence for the importance of obstruction effects, but also find that complex formation is likely to be relevant because all experimental diffusion coefficients are lower than those predicted by obstruction-only models. Also, crowding effects on water has been observed by comparing the change in the water diffusion coefficient with amino acid concentration. There was strong evidence that the diffusive path of water molecules in these systems was obstructed by the presence of amino acids.

Owing to technological advances in the 1990s, the fluorescence correlation spectroscopy (FCS) technique has quickly become an established tool for dynamic studies. In a pioneering work, Schwille et al. [99] established the application of FCS to the cytoplasm by studying the diffusion of tetramethyl-rhodamine dye in various mammalian and plant cells. They found anomalous diffusion in the different cell types with $\alpha \approx 0.6$ but the same data may equally well be rationalised by fitting a mixture of two normally diffusing components, the faster one being 5-fold slower than in aqueous solution. The slow component showed diffusion coefficients up to 40 times smaller than the fast one and comprised 35-60% of the molecules and was attributed

to membrane-bound dye.

Weiss et al. [100] introduced differently sized FITC labelled dextrans in HeLa cells and characterised their motion with FCS. The obtained values for α varied between 0.71 and 0.84 non-monotonically depending on the size of the dextran, which covered hydrodynamic radii in buffer solution between 1.8 and 14.4 nm. The dwell times, on the other hand, increased systematically from 0.4 to 16 ms. Complementing their study by $\mathtt{in\,vitro}$ experiments with unlabelled dextran as crowding agent, the authors found a systematic decrease of diffusion coefficient with the concentration of dextran, which suggests to quantify the degree of crowdedness in terms of the anomalous diffusion exponent (α).

The dependence of the diffusion coefficient on the concentration of crowding agent was monitored by FCS by Banks and Fradin [101], who used globular proteins streptavidin and EGFP as tracers in dextran solution. The resulting diffusion exponent α (which is 1 for normal diffusion) decrease rapidly for increasing concentrations of dextran obstacles and approach 0.74 ± 0.02 for high concentrations, the dynamics is strongly sub-diffusive. Further, the motion of the small fluorescein molecules as well as of the dextran crowders itself shows simple diffusion even at high dextran concentration. If a globular protein is used as crowding agent, streptavidin motion is only slightly anomalous with $\alpha \approx 0.91$ at high concentrations.

Verkman et al. [52, 102] characterised the transport of differently sized tracers in Ficoll-crowded solution using FCS with an illumination region of 0.5 μm in diameter. The tracers covered about two decades in size: from rhodamine green to albumin, dextrans, and DNA fragments to fluorescent polystyrene beads with up to 100 nm in diameter. Although the FCS correlations displayed simple diffusion in all cases, tracer transport slows down drastically upon systematically crowding the solution. The obtained diffusion coefficients are suppressed by two to three orders of magnitude

as Ficoll concentration increases up to 60 wt% and follow an exponential decrease with respect to Ficoll concentration. All tracers showed qualitatively the same behaviour, independently of their size. Using the smaller glycerol as crowding agent, the reduction of diffusion is smaller, but still exponential. For the large tracers, the slow diffusion to a large extent can be explained by the change of the bulk viscosity of the crowded fluid. This correlation is less pronounced for the small rhodamine green molecule, which appears to sense the microviscosity of its local environment.

Dauty and Verkman [103] investigated the size-dependent transport of DNA in the cytoplasm of living HeLa cells with DNA molecules sized between 20 to 4500 base pairs and labelled with a single fluorophore. The motion of DNA was followed by FCS. The fitting of correlation functions for sizes above 250 bp required a two-component model with a short diffusion time of 5-20 ms independent of DNA size. DNA diffusion was found to be significantly reduced in comparison to the free diffusion in saline by factors of up to 40, with a pronounced dependence on molecular weight above 500 bp. The authors have corroborated their findings by **in vitro** experiments using crowded solutions, cytosol extracts, and reconstituted actin networks. Only for the actin networks, the suppression of the DNA diffusion coefficient over its free value was sensitive to the molecular weight, recreating the behaviour in intact HeLa cells. In all other environments, simple diffusion was observed with the diffusion coefficient reduced by factors not exceeding 5. The authors concluded that mobile obstacles cannot explain the strongly reduced mobility of DNA in living cells and that the actin cytoskeleton presents a major restriction to cytoplasmic transport. Further, the sensitivity of diffusion to the molecular weight may be explained by entanglement effects with the actin mesh and reptation dynamics of the elongated DNA molecules.

All these studies highlight several key issues and unresolved questions: How do crowding agents, such as globular proteins and nanoparticles, act to modify dynamics

of macromolecules in the cell nucleus? How do intramolecular interactions, for example, repulsion between segments within a polymer in a good solvent, affect dynamics of macromolecules in crowded environments? How do non-steric interactions (e.g., long-ranged electrostatic interactions) between crowding agents and between crowders and macromolecules, modify crowding mechanisms? More generally, what is the interplay between excluded-volume and other nonspecific interactions? For example, by varying ionic strength or other solution conditions, can mobility of macromolecules be steered? How do crowding agents influence protein-protein clustering?

While it is easy to show that (idealized) crowding effects can in principle have significant effects on macromolecular behavior, there are at least three major issues that, need to be kept in mind. First, there is the question of whether truly inert crowding agents exist that can be used in experiments to provide excluded-volume effects only, or whether it is inevitable that all crowding agents will also cause additional effects that must be considered. Second, there is the perhaps related question of whether theoreticians can develop predictive models that can quantitatively describe the effects of the crowding agents used experimentally. Third, and arguably the most important issue, there is the question of whether an environment dominated by idealized macromolecular crowding agents such as Ficoll or Dextran is even a good mimic of a true intracellular environment such as the cytoplasm of E. coli.

Two types of volume exclusion–hard particle exclusion and confinement–are observed inside biological cells. Globular proteins can be represented by hard particles, whereas cytoskeleton networks can provide confining spaces. In this thesis, cytoskeleton networks in a cell is mimicked *via* a gel network inside droplets that are produced using microfluidic devices. The next section presents investigations of Brownian motion of macromolecules through a multi-scale confining geometry.

2.7 Macromolecular Confinement

In the cell, there exists a crowded environment of organelles, macromolecules, chromatin, membranes, and cytoskeletal filaments. The cell is not, however, simply a soup of its constituent parts, rather there exists an ordered structure referred to as compartmentalisation. Biological membranes hold biomolecules inside micron sized compartments. This is also termed as macromolecular confinement. Maintenance of compartmentalisation within the cell has fundamental implications for cellular function. In the cytoplasm, compartmentalisation is commonly achieved by confining macromolecules in lipid membranes thereby creating organelles such as mitochondria, lysosomes, Golgi apparatus, etc [1].

In the late 1990s scientists successfully compartmentalized genes in small aqueous droplets of water in oil emulsion for directed evolution of proteins and RNAs [104] giving rise to the technique known as $in\,vitro$ compartmentalization (IVC) [105]. This appeared as a simple example of artificial cell production, where gene expression function was occurring within a close compartment resembling the cell. This work not only broadened the applicative field of artificial cell systems but also showed the compatibility of expression systems with polydisperse and later on with monodisperse emulsions achieved using droplet-based microfluidics. Due to the micron dimensions of microdroplets produced through droplet-based systems, it has become clear that this technology will be useful in experimental biology [106], cell mimic, and directed evolution. A major investigation of this thesis focused on the development of microdroplets that are further structured internally using agarose gel networks where dynamics of macromolecules can be carried out.

The primary backbone of agarose gel consists of 1,3-linked β-D-galactopyranose and 1,4-linked 3,6-anhydro-α-L-galactopyranose [107]. Research results have revealed

that agarose gels have typical characteristics that resemble the living tissues in composition, rheological nature, and water content and therefore have been widely used as artificial tissues to study small molecules or macromolecules transportation process, which could be expected to closely simulate $in\,vivo$ molecular transport in living tissues [108, 109].

2.7.1 Nanoscale Confinement: Macromolecular Diffusion in Gels

Consider the sugar agarose. It is used as a model macroporous network which consists of repeating units of β-D galactose and 3,6-anhydro-a-L galactose linked together by ether bonds. A macroporous structure comprised of α-helices held together by physical crosslinks is believed to form upon cooling a hot aqueous agarose solution [110]. The gel first forms intermediate α-helices, then larger aggregate fibers of polysaccharide to yield a fairly rigid structure [111]. In chemically cross-linked gels, the fibers are typically formed by a single chain that has both flexibility and mobility. When charged, the repulsion between the single chains can cause the gel to swell substantially. This is not observed in agarose gels. Because the charged agarose gels do not swell, the spaces inside the gel remain constant over a wide range of ionic strength. So one particular advantage of using a rigid gel such as agarose is the elimination of variations in the volume fraction occupied by the fibers.

2.7.2 Theory for Diffusion through Gels

To date, predictions for the diffusivity of macromolecules through gels have been relatively unsuccessful [112, 113]. The reasons for the difficulty in developing a theory lie in the complexity of the hydrodynamic interactions between a mobile macromolecule and

its surrounding environment. There has been substantial effort placed in predicting the diffusivity of spheres in straight cylindrical pores [114], but because the hydrodynamic interactions are very sensitive to alterations in the microstructure it seems unlikely that extensions of this particular model to fibrous structures will give accurate predictions. However, these theories yield insight into the nature and complexity of hydrodynamic interactions. Due to the difficulty in predicting the hydrodynamic interactions, arguments have been made which attempt to erroneously minimize their importance. The most well known and widely used model which does not include hydrodynamic interactions was developed by Ogston and is based upon the stochastic jump probability of a sphere [115].

Ogston Diffusion Model

Ogston et al. used the random fiber matrix model that was developed for the partition coefficient theory to predict the reduction in diffusivity of a sphere through a gel network [115]. Their expression for the hindered diffusivity was based upon a stochastic jump through the spaces of a randomly oriented fiber network without considering hydrodynamic interactions. Assuming that any jump that would result in a collision with a fiber would not occur, Ogston formulated the probability of completing a jump. By assuming that the frequency of jumps inside the gel phase was the same as in the bulk solution, Ogston et al., used the jump probability to formulate an expression for the hindered diffusivity.

$$\frac{D_g}{D_0} = \exp\left(-\frac{(R_H + R_f)}{R_f}\,\Phi^{0.5}\right), \tag{2.26}$$

where D_g is the intramembrane diffusivity, D_0 is the free solution diffusion coefficient, Φ is the volume fraction of fibers, R_H is the radius of the spherical solute, and R_f is the radius of the gel fiber. This model does not include hydrodynamic interactions, which

have been found to be instrumental in describing the resistance to the solute mobility in cylindrical pores. As a matter of fact, Ogston's stochastic jump model for the hindered diffusivity has had only limited success in describing existing experimental data and tends to overestimate the diffusion coefficient.

2.7.3 Overview of Diffusion Through Gels

Diffusion in a gel is complex. A solute diffusing in an inhomogeneous medium can experience steric, chemical, and electrostatic interactions. Steric interactions describe the physical interaction of solute particles with the structure of the medium they are diffusing in. For example, an agarose gel is an irregular 3D matrix of fibers filled with water. A solute can diffuse freely in the water, but in agarose it will be impeded by the fibers. This has the effect of decreasing the diffusion coefficient of solutes in such a fibrous medium.

Several physical parameters affect the diffusion of solute particles in a gel medium. In solution, the diffusion coefficient is inversely proportional to the hydrodynamic radius of the particle and the viscosity of the solvent. In a fibrous medium, a greater dependence is placed on the hydrodynamic radius of the solute. The relationship between the hydrodynamic radius of a solute and the pore size (the amount of space between the fibers) of a fibrous medium plays a large role in how the solute is able to diffuse in such a medium.

The Ogston model has been used to obtain quantitative information about the nature of the gel such as pore radius and gel fiber radius. For a 6% concentration of agarose gel, the average distance between fibers is around 11 nm which is large enough to accommodate many proteins [116]. Another study of 2% agarose gel estimated the pore radius (which is distinct from R_f, the radius of the gel fiber) in the range of 85-103 nm [117]. As the hydrodynamic radius of the probe molecule in increased,

and approaches the pore radius, the diffusion coefficient decreases further until no penetration is observed [117].

Rates of diffusion are also strongly affected by the gel matrix. That is, the diffusivity of the macromolecules through gel matrices is restricted when compared to the diffusion in bulk solution. There are two components in this reduction: frictional resistance and tortuosity. In the diffusion of macromolecules in well defined pores, the frictional resistance (hydrodynamic effects) have been found to be instrumental in predicting the reduction in mobility [114]. In gels, the surfaces are less well defined than in a pore and it is difficult to know precisely where the gel fibers are for any given diffusing macromolecule. In addition, hydrodynamic effects are long range and predictions or calculations for the diffusivity require the use of a many proximate fibers [118, 119]. The second reason for the reduction in the diffusivity is tortuosity. Because the trajectory of a macromolecule through the gel matrix is not straight there is an increase in path length that will contribute to the reduction in the apparent diffusivity.

As the agarose content increases, the inter-fiber spacing decreases and the polymer chain mobility decreases effectively. As a result there is a decrease in the observed diffusion coefficient [120]. The diffusion coefficient of a variety of proteins has been measured in crosslinked agarose matrices with concentration ranging from 2% to 6% agarose [112]. Again, the diffusion coefficient decreased as the agarose content increased for all proteins studied.

Diffusion coefficients of macromolecules in neutral agarose gels and agarose-dextran composite gels decrease with the increasing radius of the solute [121]. The concentration of agarose and dextran was also varied in these experiments. As expected, as the agarose content increased, the diffusivity decreased as a result of increasing diffusional hindrance. The effective medium model gave an adequate prediction of

decreased diffusion with respect to the addition of dextran.

From a fundamental point of view, precise measurements for model systems are needed to reveal the underlying transport principles. It is known that the presence of obstacles slows down the transport and that this is more pronounced for larger molecules. However, the basic underlying mechanisms and their effects are not yet completely understood. In particular, the motion of particles through a gel matrix represents an intricate problem as the gel matrix can respond to the particle motion. A nontrivial dependence of the diffusion behavior on both the host and the guest, i.e. the gel and the diffusing particles, is expected. The behavior of the host is mainly characterized by a typical pore size. However, topological constraints resulting from the nontrivial and dynamically changing connectivity of the pores also have an impact on the diffusion of the guest molecules. The diffusion coefficient is also influenced by the structural properties of the guest molecules such as hydrodynamic radius, shape, molecular weight or charge distribution. The significance of sieving, entanglements, chemical interactions, partitioning, oscillation of pores etc. is still controversially discussed. In addition, the average size of the pores is also under debate.

Bibliography

[1] A. B. Fulton, "How crowded is the cytoplasm?," Cell, vol. 30, no. 2, pp. 345–347, 1982.

[2] A. Partikian, B. Ölveczky, R. Swaminathan, Y. Li, and A. Verkman, "Rapid diffusion of green fluorescent protein in the mitochondrial matrix," The Journal of Cell Biology, vol. 140, no. 4, pp. 821–829, 1998.

[3] T. Cremer, M. Cremer, S. Dietzel, S. Müller, I. Solovei, and S. Fakan, "Chromosome territories–a functional nuclear landscape," Current Opinion in Cell

Biology, vol. 18, no. 3, pp. 307–316, 2006.

[4] D. S. Goodsell, The machinery of life. Springer Science & Business Media, 2009.

[5] K. Luby-Phelps, "Cytoarchitecture and physical properties of cytoplasm: volume, viscosity, diffusion, intracellular surface area," International Review of Cytology, vol. 192, pp. 189–221, 1999.

[6] B. G. Fuller, "Self-organization of intracellular gradients during mitosis," Cell Division, vol. 5, no. 1, p. 5, 2010.

[7] R. J. Ellis and A. P. Minton, "Cell biology: join the crowd," Nature, vol. 425, no. 6953, pp. 27–28, 2003.

[8] S. B. Zimmerman and S. O. Trach, "Estimation of macromolecule concentrations and excluded volume effects for the cytoplasm of escherichia coli," Journal of Molecular Biology, vol. 222, no. 3, pp. 599 – 620, 1991.

[9] F. Lanni, A. S. Waggoner, and D. L. Taylor, "Structural organization of interphase 3t3 fibroblasts studied by total internal reflection fluorescence microscopy.," The Journal of Cell Biology, vol. 100, no. 4, pp. 1091–1102, 1985.

[10] K. Luby-Phelps, "The physical chemistry of cytoplasm and its influence on cell function: an update," Molecular Biology of the Cell, vol. 24, no. 17, pp. 2593–2596, 2013.

[11] J. Holthuis and C. Ungermann, "Cellular microcompartments constitute general suborganellar functional units in cells," Biological Chemistry, vol. 394, no. 2, pp. 151–161, 2013.

[12] M. Rubinstein and R. H. Colby, Polymer physics, vol. 23. Oxford University Press New York, 2003.

[13] M. Doi, <u>Introduction to polymer physics</u>. Oxford University Press, 1996.

[14] M. Muthukumar, "Polymer translocation through a hole," <u>The Journal of Chemical Physics</u>, vol. 111, no. 22, pp. 10371–10374, 1999.

[15] P.-G. De Gennes, <u>Scaling concepts in polymer physics</u>. Cornell University Press, 1979.

[16] F. Kienberger, V. P. Pastushenko, G. Kada, H. J. Gruber, C. Riener, H. Schindler, and P. Hinterdorfer, "Static and dynamical properties of single poly (ethylene glycol) molecules investigated by force spectroscopy," <u>Single Molecules</u>, vol. 1, no. 2, pp. 123–128, 2000.

[17] H. Lee, R. M. Venable, A. D. MacKerell Jr, and R. W. Pastor, "Molecular dynamics studies of polyethylene oxide and polyethylene glycol: hydrodynamic radius and shape anisotropy," <u>Biophysical Journal</u>, vol. 95, no. 4, pp. 1590–1599, 2008.

[18] P. E. Rouse Jr, "A theory of the linear viscoelastic properties of dilute solutions of coiling polymers," <u>The Journal of Chemical Physics</u>, vol. 21, no. 7, pp. 1272–1280, 1953.

[19] B. H. Zimm, "Dynamics of polymer molecules in dilute solution: viscoelasticity, flow birefringence and dielectric loss," <u>The Journal of Chemical Physics</u>, vol. 24, no. 2, pp. 269–278, 1956.

[20] M. Doi and S. F. Edwards, <u>The theory of polymer dynamics</u>, vol. 73. Oxford University Press, 1988.

[21] J. des Cloizeaux, "The Lagrangian theory of polymer solutions at intermediate concentrations," <u>Journal de Physique</u>, vol. 36, no. 4, pp. 281–291, 1975.

50

[22] P. L. Hansen, J. A. Cohen, R. Podgornik, and V. A. Parsegian, "Osmotic properties of poly (ethylene glycols): quantitative features of brush and bulk scaling laws," Biophysical Journal, vol. 84, no. 1, pp. 350–355, 2003.

[23] J. A. Cohen, R. Podgornik, P. L. Hansen, and V. A. Parsegian, "A phenomenological one-parameter equation of state for osmotic pressures of peg and other neutral flexible polymers in good solvents," The Journal of Physical Chemistry B, vol. 113, no. 12, p. 3709, 2009.

[24] J. H. van't Hoff, "The role of osmotic pressure in the analogy between solutions and gases," Journal of Membrane Science, vol. 100, no. 1, pp. 39–44, 1995.

[25] R. J. Ellis, "Macromolecular crowding: Obvious but underappreciated," Trends in Biochemical Sciences, vol. 26, no. 10, pp. 597–604, 2001.

[26] A. P. Minton, "Excluded volume as a determinant of macromolecular structure and reactivity," Biopolymers, vol. 20, no. 10, pp. 2093–2120, 1981.

[27] S. B. Zimmerman and A. P. Minton, "Macromolecular crowding: biochemical, biophysical, and physiological consequences," Annual Review of Biophysics and Biomolecular Structure, vol. 22, no. 1, pp. 27–65, 1993.

[28] A. P. Minton, "Influence of excluded volume upon macromolecular structure and associations in 'crowded' media," Current Opinion in Biotechnology, vol. 8, no. 1, pp. 65–69, 1997.

[29] A. P. Minton, "The influence of macromolecular crowding and macromolecular confinement on biochemical reactions in physiological media," Journal of Biological Chemistry, vol. 276, p. 10577, 2001.

[30] B. Alder and T. Wainwright, "Phase transition for a hard sphere system," The Journal of Chemical Physics, vol. 27, no. 5, pp. 1208–1209, 1957.

[31] F. Sciortino and P. Tartaglia, "Glassy colloidal systems," Advances in Physics, vol. 54, no. 6-7, pp. 471–524, 2005.

[32] W. Van Megen and P. Pusey, "Dynamic light-scattering study of the glass transition in a colloidal suspension," Physical Review A, vol. 43, no. 10, p. 5429, 1991.

[33] Z. Cheng, J. Zhu, P. M. Chaikin, S.-E. Phan, and W. B. Russel, "Nature of the divergence in low shear viscosity of colloidal hard-sphere dispersions," Physical Review E, vol. 65, no. 4, p. 041405, 2002.

[34] S. Asakura and F. Oosawa, "On interaction between two bodies immersed in a solution of macromolecules.," Journal of Chemical Physics, vol. 22, p. 1255, 1954.

[35] M. Muthukumar, Polymer translocation. CRC Press, 2016.

[36] W. B. Russell, W. Schowalter, and D. Saville, Colloidal dispersions. Cambridge University Press, 1991.

[37] R. J. Hunter, Zeta potential in colloid science: principles and applications, vol. 2. Academic Press, 2013.

[38] E. J. W. Verwey, J. T. G. Overbeek, and J. T. G. Overbeek, Theory of the stability of lyophobic colloids. Courier Corporation, 1999.

[39] A. N. Borodin and P. Salminen, Handbook of Brownian motion-facts and formulae. Birkhäuser, 2012.

[40] J. Philibert, "One and a half century of diffusion: Fick, Einstein, before and beyond," Diffusion Fundamentals, vol. 4, no. 6, pp. 1–19, 2006.

[41] A. Fick, "On liquid diffusion," Journal of Membrane Science, vol. 100, no. 1, pp. 33–38, 1995.

[42] W. Sutherland, "A dynamical theory of diffusion for non-electrolytes and the molecular mass of albumin," The London, Edinburgh, and Dublin Philosophical Magazine and Journal of Science, vol. 9, no. 54, pp. 781–785, 1905.

[43] A. Einstein, Investigations on the Theory of the Brownian Movement. Courier Corporation, 1956.

[44] L. Mirny, "Biophysics: Cell commuters avoid delays," Nature Physics, vol. 4, no. 2, pp. 93–95, 2008.

[45] M. Mooney, "The viscosity of a concentrated suspension of spherical particles," Journal of Colloid Science, vol. 6, no. 2, pp. 162–170, 1951.

[46] P. D. Ross and A. P. Minton, "Hard quasispherical model for the viscosity of hemoglobin solutions," Biochemical and Biophysical Research Communications, vol. 76, no. 4, pp. 971–976, 1977.

[47] Y. Wang, L. A. Benton, V. Singh, and G. J. Pielak, "Disordered Protein Diffusion under Crowded Conditions," The Journal of Physical Chemistry Letters, vol. 3, no. 18, pp. 2703–2706, 2012.

[48] D. Lavalette, C. Tétreau, M. Tourbez, and Y. Blouquit, "Microscopic viscosity and rotational diffusion of proteins in a macromolecular environment," Biophysical Journal, vol. 76, no. 5, pp. 2744–2751, 1999.

[49] A. B. Goins, H. Sanabria, and M. N. Waxham, "Macromolecular Crowding and Size Effects on Probe Microviscosity," Biophysical Journal, vol. 95, no. 11, pp. 5362–5373, 2008.

[50] G. Chirico, M. Placidi, and S. Cannistraro, "Fractional Stokes-Einstein relationship in biological colloids: Role of mixed stick- slip boundary conditions," The Journal of Physical Chemistry B, vol. 103, no. 10, pp. 1746–1751, 1999.

[51] N. A. Busch, T. Kim, and V. A. Bloomfield, "Tracer diffusion of proteins in DNA solutions. 2. green fluorescent protein in crowded DNA solutions," Macromolecules, vol. 33, no. 16, pp. 5932–5937, 2000.

[52] A. James, J. A. Dix, and A. S. Verkman, "Crowding effects on diffusion in solutions and cells," Annual Review Biophysics, vol. 37, p. 247, 2008.

[53] R. Gorenflo, F. Mainardi, D. Moretti, G. Pagnini, and P. Paradisi, "Discrete random walk models for space–time fractional diffusion," Chemical Physics, vol. 284, no. 1, pp. 521–541, 2002.

[54] J. Wu and K. M. Berland, "Propagators and time-dependent diffusion coefficients for anomalous diffusion," Biophysical Journal, vol. 95, no. 4, pp. 2049–2052, 2008.

[55] F. Oosawa and S. Asakura, "Surface tension of high-polymer solutions," The Journal of Chemical Physics, vol. 22, no. 7, pp. 1255–1255, 1954.

[56] Y. Wang, C. Li, and G. J. Pielak, "Effects of proteins on protein diffusion," Journal of the American Chemical Society, vol. 132, no. 27, pp. 9392–9397, 2010.

[57] F. Roosen-Runge, M. Hennig, F. Zhang, R. M. Jacobs, M. Sztucki, H. Schober, T. Seydel, and F. Schreiber, "Protein self-diffusion in crowded solutions," Proceedings of the National Academy of Sciences, vol. 108, no. 29, pp. 11815–11820, 2011.

[58] J. Bloustine, T. Virmani, G. Thurston, and S. Fraden, "Light scattering and phase behavior of lysozyme-poly (ethylene glycol) mixtures," Physical Review Letters, vol. 96, no. 8, p. 087803, 2006.

[59] G. Tubio, B. Nerli, and G. Picó, "Relationship between the protein surface hydrophobicity and its partitioning behaviour in aqueous two-phase systems of polyethyleneglycol–dextran," Journal of Chromatography B, vol. 799, no. 2, pp. 293–301, 2004.

[60] D. J. Winzor and P. R. Wills, "Molecular crowding effects of linear polymers in protein solutions," Biophysical Chemistry, vol. 119, no. 2, pp. 186–195, 2006.

[61] A. C. Miklos, M. Sarkar, Y. Wang, and G. J. Pielak, "Protein crowding tunes protein stability," Journal of the American Chemical Society, vol. 133, no. 18, pp. 7116–7120, 2011.

[62] J. Armstrong, R. Wenby, H. Meiselman, and T. Fisher, "The hydrodynamic radii of macromolecules and their effect on red blood cell aggregation," Biophysical Journal, vol. 87, no. 6, pp. 4259–4270, 2004.

[63] L. Stagg, S.-Q. Zhang, M. S. Cheung, and P. Wittung-Stafshede, "Molecular crowding enhances native structure and stability of α/β protein flavodoxin," Proceedings of the National Academy of Sciences, vol. 104, no. 48, pp. 18976–18981, 2007.

[64] D. Homouz, L. Stagg, P. Wittung-Stafshede, and M. S. Cheung, "Macromolecular crowding modulates folding mechanism of α/β protein apoflavodoxin," Biophysical Journal, vol. 96, no. 2, pp. 671–680, 2009.

[65] D. Homouz, H. Sanabria, M. N. Waxham, and M. S. Cheung, "Modulation of calmodulin plasticity by the effect of macromolecular crowding," Journal of Molecular Biology, vol. 391, no. 5, pp. 933–943, 2009.

[66] M. Bohrer, G. D. Patterson, and P. Carroll, "Hindered diffusion of dextran and ficoll in microporous membranes," Macromolecules, vol. 17, no. 6, pp. 1170–1173, 1984.

[67] D. Venturoli and B. Rippe, "Ficoll and dextran vs. globular proteins as probes for testing glomerular permselectivity: effects of molecular size, shape, charge, and deformability," American Journal of Physiology - Renal Physiology, vol. 288, no. 4, pp. F605–F613, 2005.

[68] A. A. Fodeke and A. P. Minton, "Quantitative characterization of polymer-polymer, protein- protein, and polymer- protein interaction via tracer sedimentation equilibrium," The Journal of Physical Chemistry B, vol. 114, no. 33, pp. 10876–10880, 2010.

[69] M. G. Davidson and W. M. Deen, "Hindered diffusion of water-soluble macromolecules in membranes," Macromolecules, vol. 21, no. 12, pp. 3474–3481, 1988.

[70] K. J. Mutch, J. S. van Duijneveldt, and J. Eastoe, "Colloid–polymer mixtures in the protein limit," Soft Matter, vol. 3, no. 2, pp. 155–167, 2007.

[71] A. Soranno, I. Koenig, M. B. Borgia, H. Hofmann, F. Zosel, D. Nettels, and B. Schuler, "Single-molecule spectroscopy reveals polymer effects of disordered

proteins in crowded environments," Proceedings of the National Academy of Science, vol. 111, p. 4874, 2014.

[72] A. Rajapaksha, C. B. Stanley, and B. A. Todd, "Effects of macromolecular crowding on the structure of a protein complex: A small-angle scattering study of superoxide dismutase," Biophysical Journal, vol. 108, p. 967, 2015.

[73] D. Johansen, C. M. Jeffries, B. Hammouda, J. Trewhella, and D. P. Goldenberg, "Effects of macromolecular crowding on an intrinsically disordered protein characterized by small-angle neutron scattering with contrast matching," Biophysical Journal, vol. 100, p. 1120, 2011.

[74] D. P. Goldenberg and B. Argyle, "Minimal effects of macromolecular crowding on an intrinsically disordered protein: a small-angle neutron scattering study," Biophysical Journal, vol. 106, no. 4, pp. 905–914, 2014.

[75] S. Nakano, H. T. Karimata, Y. Kitagawa, and N. Sugimoto, "Facilitation of RNA enzyme activity in the molecular crowding media of cosolutes," Journal of the American Chemical Society, vol. 131, no. 46, pp. 16881–16888, 2009.

[76] M. Nashimoto, "Correct folding of a ribozyme induced by nonspecific macromolecules," The FEBS Journal, vol. 267, no. 9, pp. 2738–2745, 2000.

[77] N. A. Denesyuk and D. Thirumalai, "Crowding promotes the switch from hairpin to pseudoknot conformation in human telomerase rna," Journal of the American Chemical Society, vol. 133, no. 31, pp. 11858–11861, 2011.

[78] A. Kudlay, M. S. Cheung, and D. Thirumalai, "Influence of the shape of crowding particles on the structural transitions in a polymer," The Journal of Physical Chemistry B, vol. 116, no. 29, pp. 8513–8522, 2012.

[79] C. Le Coeur, B. Demé, and S. Longeville, "Compression of random coils due to macromolecular crowding," Physical Review E, vol. 79, no. 3, p. 031910, 2009.

[80] C. Le Coeur, J. Teixeira, P. Busch, and S. Longeville, "Compression of random coils due to macromolecular crowding: Scaling effects," Physical Review E, vol. 81, no. 6, p. 061914, 2010.

[81] A. R. Denton, "Crowding in polymer–nanoparticle mixtures," International Review of Cell and Molecular Biology, vol. 307, p. 27, 2014.

[82] B. Lu and A. R. Denton, "Crowding of polymer coils and demixing in nanoparticle–polymer mixtures," Journal of Physics: Condensed Matter, vol. 23, no. 28, p. 285102, 2011.

[83] H. Kang, P. A. Pincus, C. Hyeon, and D. Thirumalai, "Effects of macromolecular crowding on the collapse of biopolymers," Physical Review Letters, vol. 114, no. 6, p. 068303, 2015.

[84] S. Barhoum, S. Palit, and A. Yethiraj, "Diffusion NMR studies of macromolecular complex formation, crowding and confinement in soft materials," Progress in Nuclear Magnetic Resonance Spectroscopy, vol. 94-95, pp. 1–10, 2016.

[85] E. O. Stejskal and J. E. Tanner, "Spin diffusion measurements: spin echoes in the presence of a time-dependent field gradient," The Journal of Chemical Physics, vol. 42, no. 1, pp. 288–292, 1965.

[86] L. Guo, J. Y. Har, J. Sankaran, Y. Hong, B. Kannan, and T. Wohland, "Molecular diffusion measurement in lipid bilayers over wide concentration ranges: a comparative study," ChemPhysChem, vol. 9, no. 5, pp. 721–728, 2008.

[87] N. Lorén, M. Nydén, and A.-M. Hermansson, "Determination of local diffusion properties in heterogeneous biomaterials," Advances in Colloid and Interface Science, vol. 150, no. 1, pp. 5–15, 2009.

[88] L. Porcar, P. Falus, W.-R. Chen, A. Faraone, E. Fratini, K. Hong, P. Baglioni, and Y. Liu, "Formation of the dynamic clusters in concentrated lysozyme protein solutions," The Journal of Physical Chemistry Letters, vol. 1, no. 1, pp. 126–129, 2009.

[89] Y. Liu, L. Porcar, J. Chen, W.-R. Chen, P. Falus, A. Faraone, E. Fratini, K. Hong, and P. Baglioni, "Lysozyme protein solution with an intermediate range order structure," The Journal of Physical Chemistry B, vol. 115, no. 22, pp. 7238–7247, 2010.

[90] B. J. Berne and R. Pecora, Dynamic light scattering: with applications to chemistry, biology, and physics. Courier Corporation, 2000.

[91] A. Papagiannopoulos, The structure and dynamics of polyelectrolyte combs. PhD thesis, University of Leeds, 2005.

[92] V. Riveros-Moreno and J. B. Wittenberg, "The self-diffusion coefficients of myoglobin and hemoglobin in concentrated solutions," Journal of Biological Chemistry, vol. 247, no. 3, pp. 895–901, 1972.

[93] W. Doster and S. Longeville, "Microscopic diffusion and hydrodynamic interactions of hemoglobin in red blood cells," Biophysical Journal, vol. 93, no. 4, pp. 1360–1368, 2007.

[94] F. Roosen-Runge, M. Hennig, T. Seydel, F. Zhang, M. W. Skoda, S. Zorn, R. M. Jacobs, M. Maccarini, P. Fouquet, and F. Schreiber, "Protein diffusion in

crowded electrolyte solutions," Biochimica et Biophysica Acta (BBA)-Proteins and Proteomics, vol. 1804, no. 1, pp. 68–75, 2010.

[95] W. Häussler, "Neutron spin echo studies on ferritin: free-particle diffusion and interacting solutions," European Biophysics Journal, vol. 37, no. 5, pp. 563–571, 2008.

[96] W. Häußler, "Structure and dynamics in apoferritin solutions with paracrystalline order," Chemical Physics, vol. 292, no. 2, pp. 425–434, 2003.

[97] S. Barhoum and A. Yethiraj, "An NMR study of macromolecular aggregation in a model polymer-surfactant solution," The Journal of Chemical Physics, vol. 132, no. 2, p. 024909, 2010.

[98] A. S. Virk, T. Stait-Gardner, S. A. Willis, A. M. Torres, and W. S. Price, "Macromolecular crowding studies of amino acids using NMR diffusion measurements and molecular dynamics simulations," Frontiers in Physics, vol. 3, p. 1, 2015.

[99] P. Schwille, U. Haupts, S. Maiti, and W. W. Webb, "Molecular dynamics in living cells observed by fluorescence correlation spectroscopy with one-and two-photon excitation," Biophysical Journal, vol. 77, no. 4, pp. 2251–2265, 1999.

[100] M. Weiss, M. Elsner, F. Kartberg, and T. Nilsson, "Anomalous subdiffusion is a measure for cytoplasmic crowding in living cells," Biophysical Journal, vol. 87, no. 5, pp. 3518–3524, 2004.

[101] D. S. Banks and C. Fradin, "Anomalous diffusion of proteins due to molecular crowding," Biophysical Journal, vol. 89, no. 5, pp. 2960–2971, 2005.

[102] E. Dauty and A. Verkman, "Molecular crowding reduces to a similar extent the diffusion of small solutes and macromolecules: measurement by fluorescence correlation spectroscopy," Journal of Molecular Recognition, vol. 17, no. 5, pp. 441–447, 2004.

[103] E. Dauty and A. Verkman, "Actin cytoskeleton as the principal determinant of size-dependent DNA mobility in cytoplasm a new barrier for non-viral gene delivery," Journal of Biological Chemistry, vol. 280, no. 9, pp. 7823–7828, 2005.

[104] D. S. Tawfik and A. D. Griffiths, "Man-made cell-like compartments for molecular evolution," Nature Biotechnology, vol. 16, no. 7, p. 652, 1998.

[105] B. T. Kelly, J.-C. Baret, V. Taly, and A. D. Griffiths, "Miniaturizing chemistry and biology in microdroplets," Chemical Communications, no. 18, pp. 1773–1788, 2007.

[106] Y. Schaerli and F. Hollfelder, "The potential of microfluidic water-in-oil droplets in experimental biology," Molecular Biosystems, vol. 5, no. 12, pp. 1392–1404, 2009.

[107] N. Fatin-Rouge, A. Milon, J. Buffle, R. R. Goulet, and A. Tessier, "Diffusion and partitioning of solutes in agarose hydrogels: the relative influence of electrostatic and specific interactions," The Journal of Physical Chemistry B, vol. 107, no. 44, pp. 12126–12137, 2003.

[108] M. D. Mitchell, H. L. Kundel, L. Axel, and P. M. Joseph, "Agarose as a tissue equivalent phantom material for NMR imaging," Magnetic Resonance Imaging, vol. 4, no. 3, pp. 263–266, 1986.

[109] A. Balgude, X. Yu, A. Szymanski, and R. Bellamkonda, "Agarose gel stiffness determines rate of drg neurite extension in 3d cultures," <u>Biomaterials</u>, vol. 22, no. 10, pp. 1077–1084, 2001.

[110] E. M. Johnson and W. M. Deen, "Hydraulic permeability of agarose gels," <u>AIChE Journal</u>, vol. 42, no. 5, pp. 1220–1224, 1996.

[111] J. Porath, L. Torgny, J.-C. Janson, <u>et al.</u>, "Agar derivatives for chromatography, electrophoresis and gel-bound enzymes: III. rigid agarose gels cross-linked with divinyl sulphone (dvs)," <u>Journal of Chromatography A</u>, vol. 103, no. 1, pp. 49–62, 1975.

[112] M. Moussaoui, M. Benlyas, and P. Wahl, "Diffusion of proteins in sepharose c1-b gels," <u>Journal of Chromatography A</u>, vol. 591, no. 1-2, pp. 115–120, 1992.

[113] E. M. Johnson, D. A. Berk, R. K. Jain, and W. M. Deen, "Hindered diffusion in agarose gels: test of effective medium model," <u>Biophysical Journal</u>, vol. 70, no. 2, pp. 1017–1023, 1996.

[114] W. Deen, "Hindered transport of large molecules in liquid-filled pores," <u>AIChE Journal</u>, vol. 33, no. 9, pp. 1409–1425, 1987.

[115] B. Preston and J. Wells, "On the transport of compact particles through solutions of chain-polymers," in <u>Proceedings of the Royal Society of London A</u>, vol. 333, pp. 297–316, The Royal Society, 1973.

[116] A. Ogston, "The spaces in a uniform random suspension of fibres," <u>Transactions of the Faraday Society</u>, vol. 54, pp. 1754–1757, 1958.

[117] A. Pluen, P. A. Netti, R. K. Jain, and D. A. Berk, "Diffusion of macromolecules in agarose gels: comparison of linear and globular configurations," Biophysical Journal, vol. 77, no. 1, pp. 542–552, 1999.

[118] R. Phillips, W. Deen, and J. Brady, "Hindered transport of spherical macromolecules in fibrous membranes and gels," AIChE Journal, vol. 35, no. 11, pp. 1761–1769, 1989.

[119] R. J. Phillips, W. M. Deen, and J. F. Brady, "Hindered transport in fibrous membranes and gels: effect of solute size and fiber configuration," Journal of Colloid and Interface Science, vol. 139, no. 2, pp. 363–373, 1990.

[120] N. Hirota, Y. Kumaki, T. Narita, J. P. Gong, and Y. Osada, "Effect of charge on protein diffusion in hydrogels," The Journal of Physical Chemistry B, vol. 104, no. 42, pp. 9898–9903, 2000.

[121] K. B. Kosto and W. M. Deen, "Diffusivities of macromolecules in composite hydrogels," AIChE journal, vol. 50, no. 11, pp. 2648–2658, 2004.

Chapter 3

Experimental Techniques

In this work, we have combined the use of pulsed-field-gradient nuclear magnetic resonance (PFG NMR) with small-angle neutron scattering (SANS) in order to obtain new insights in simple model systems of macromolecular crowding. The NMR and SANS techniques complement each other. The magnetic resonance spin echo yields direct dynamical information on the millisecond-to-second timescale *via* pulsed-field-gradient NMR (PFG NMR) diffusion measurements. Typically, PFG NMR can be used in dilute suspensions to obtain hydrodynamic radii from the measured diffusion coefficients using the Stokes-Einstein relation. The Stokes-Einstein relation is strictly valid at infinite dilution, and at finite concentrations there are hydrodynamic corrections. However, in the presence of crowding, the size (and shape) of the macromolecule can also be changed. In addition, crowding makes the mobility a function of the packing fraction.

SANS, on the other hand, yields structure (size) of macromolecules. Since we only have access to the effective mobility in dynamics measurements, we performed independent measures of radius of gyration *via* small-angle scattering measurements to construct a complete picture of the macromolecular dynamics. We also have used

rheology in order to construct a quantitative picture between the microscopic and macroscopic environment.

3.1 NMR Spectroscopy

Nuclear magnetic resonance is a quantum mechanical phenomenon which is based on the magnetic properties of the nucleus. It occurs when the nuclei of certain atoms are immersed in a static magnetic field and exposed to a second oscillating magnetic field [1]. Nuclei with a non-zero spin quantum number have a magnetic moment. In other words the nucleus behaves like a tiny bar magnet. This magnetic moment can be thought semi-classically of as arising from the spinning of a charged particle.

3.1.1 Basic Theory of NMR

In classical physics, when a magnetic dipole is placed inside a magnetic field $(\vec{B}_o)$, its potential energy is given by

$$U = -\vec{\mu} . \vec{B}_o, \tag{3.1}$$

where $\vec{\mu}$ denotes a classical magnetic dipole moment. Likewise, when a nuclear spin is placed inside a magnetic field, its nuclear spin Hamiltonian depends on both its own nuclear magnetic dipole moment and the external magnetic field it experiences. The nuclear dipole moment of a given nucleus is given by

$$\vec{\mu} = \gamma \, \vec{I}, \tag{3.2}$$

where γ is the gyromagnetic ratio which is an intrinsic property of any nucleus ($\gamma_{1_H} = 26.752 \times 10^7$ s^{-1} T^{-1} and $\gamma_{2_H} = 4.107 \times 10^7$ s^{-1} T^{-1}), and $\hat{I}$ is a dimensionless spin angular momentum operator. Nuclei that have non-zero angular momentum also

have a non-zero nuclear magnetic moment. The z component of the magnetic moment is given by

$$\vec{\mu}_z = \gamma \, \vec{I}_z. \tag{3.3}$$

For a nuclear spin in a magnetic field of strength B_o applied along the z-axis, the Hamiltonian is [2]

$$\hat{H} = -\gamma \, B_o \, \hat{I}_z. \tag{3.4}$$

Here $\hat{I}_z$ is an operator which represents the z component of the nuclear spin angular momentum is specified by

$$\hat{I}_z = m \, \hbar, \tag{3.5}$$

where m is the magnetic quantum number and is restricted to values of m = (- I, - I+1,..., I), with a total of 2I +1 possible degenerate sublevels. Nuclei that have non-zero angular momentum also have a non-zero nuclear magnetic moment. In the field of NMR spectroscopy, the atomic nuclei are classified into non-detectable nuclei with an even number of protons and even number of neutrons (i.e. I=0 such as ^{12}C and ^{16}O) and detectable nuclei with either odd number of protons and odd number of neutrons or odd mass number (i.e. I is an integer and half integer, respectively) such as ^{2}H and ^{1}H, ^{15}N, and ^{13}C, respectively [1, 2].

In biological applications of NMR spectroscopy, nuclei with spin 1/2 are most important (i.e. ^{1}H, ^{15}N, ^{13}C). ^{1}H NMR is also most widely used for diffusion measurements *via* pulsed-field-gradient NMR [3], which is the primary experimental tool to be used in this work. The following discussion will therefore be restricted to spin 1/2 nuclei. In a spin 1/2 system $\hat{I}_z$ has just two eigenfunctions, characterized by m $= + \frac{1}{2}$ and m $= - \frac{1}{2}$. The two corresponding eigenstates $|\alpha >$ (i.e. 1/2 state) and

$|\beta>$ (i.e. -1/2 state) obey the eigenvalue equations:

$$\hat{I}_z \, |\alpha> = +\frac{1}{2} \hbar \, |\alpha>$$
$$\hat{I}_z \, |\beta> = -\frac{1}{2} \hbar \, |\beta>$$

(3.6)

$|\alpha>$ thus has eigenvalue $+\frac{1}{2}\hbar$, and $|\beta>$ has eigenvalue $-\frac{1}{2}\hbar$. These are also the eigenfunctions of the Hamiltonian in Equation 3.4. Therefore the effect of the Hamiltonian operator on $|\alpha>$ yields

$$\hat{H} \, |\alpha> = -\gamma \, B_o \, \hat{I}_z |\alpha>$$
$$= -\gamma \, B_o \, \frac{1}{2} \hbar \, |\alpha>$$
$$= -\frac{1}{2} \hbar \, \gamma \, B_o \, |\alpha> .$$

(3.7)

$\omega_o = -\gamma \, B_o$ is called the Larmor frequency and corresponds to an energy $E = -\frac{1}{2} \hbar \, \omega_0$. Although ω_o takes on negative values when $\gamma > 0$, the absolute value of this frequency is typically referred as the Larmor frequency. Our NMR experiments have been carried out using a NMR spectrometer that operates with a magnetic field $B_0 = 14$ T. With $\gamma_{1_H} = 26.752 \times 10^7$ s^{-1} T^{-1}, the Larmor frequency (ω_0) of ^{1}H nucleus is $2\pi (6 \times 10^8)$ rad s^{-1} (commonly referred to as 600 MHz). The frequency of the radio waves is in the range ≈ 0.3 MHz to ≈ 300 GHz; thus NMR is possible with electromagnetic fields oscillating at radio frequency. Using the same approach, it is easy to show that $|\beta>$ is also an eigenfunction, with eigenvalue $+\frac{1}{2} \hbar \, \omega_0$.

An equilibrium exists between the $|\alpha>$ and $|\beta>$ states, with the relative populations given by the Boltzmann distribution [1]

$$\frac{n_{\alpha,eq}}{n_{\beta,eq}} = \exp\left(\frac{\Delta E}{K_B T}\right),$$

(3.8)

where $n_{\alpha,eq}$ and $n_{\beta,eq}$ are the equilibrium populations in the spin up state (α) and spin down state (β) respectively, T is the temperature, and ΔE is the energy difference between the two nuclear spin states. For 600 MHz, the difference in population is 0.0001, which indicates a very small magnetization. Applying an external magnetic field results in non-degenerate energy levels, with two energies of $\pm\frac{1}{2}\hbar\gamma B_o$, where the state $|\alpha>$ has the lowest energy. The difference in the energy levels between the $|\alpha>$ and $|\beta>$ states, and therefore the energy required for a transition to occur between these two states, is $\pm\hbar\gamma B_o$. In general, at equilibrium the net magnetization of the sample is along the direction of B_o. When the magnetization is flipped away from the z-axis then the sample magnetization will experience a torque from the magnetic field B_o which drives the magnetization vector to possess a precessional motion about the direction of the magnetic field with a Larmor frequency: $\omega_0 = -\gamma B_o$. For magnetic field strengths commonly applied in NMR experiments, ω_0 is in the radio frequency range [2]. Within a given molecule, nuclei of the same isotope experience minute differences in magnetic field strength, due to variations in electron density and the magnetic fields of adjacent nuclei. This fact gives a molecule a spectrum of precessional frequencies for a given applied magnetic field.

3.1.2   The Pulse and Acquire Experiment

In this section the simplest of all NMR experiments will be described; this experiment is known as pulse and acquire. This experiment consists of a single excitation pulse followed immediately by detection of the resulting free-induction decay (FID). The frequency spectrum is then usually obtained by a Fourier transformation of the FID.

It has been previously shown that the $|\beta>$ state has a small excess population over the $|\alpha>$ state. As a result, in the equilibrium state, there is a small net magnetization orientated along the z-axis. In this state there is no net precession of the
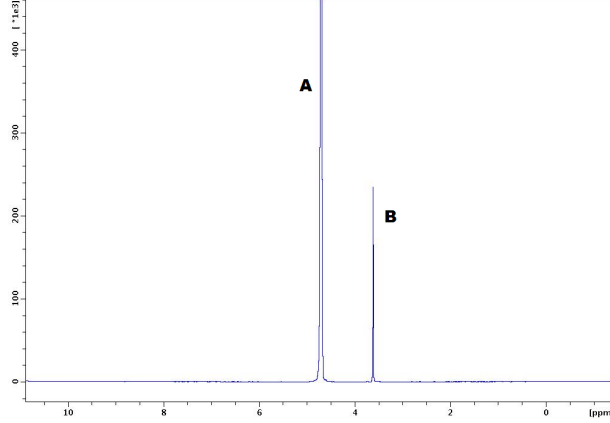
Figure 3.1: 1D ^{1}H-NMR spectrum for PEG/H_2O sample at a sample temperature 298 K. Peak A is the water peak, while the peak region marked "B" is the principal PEG peak.

magnetization and therefore no observable signal. It is necessary to perturb this equilibrium state of the magnetization. This can be accomplished by the application of a radio-frequency electromagnetic pulse, $\vec{B}_1(t)$. Assuming that the oscillating magnetic field (i.e. implicitly the oscillating RF pulse) $\vec{B}_1(t)$ is along the x-axis:

$$\vec{B}_1(t) = \hat{i}B_1 \cos \omega t, \tag{3.9}$$

where B_1 has a maximum radio frequency amplitude and ω is the frequency of the radio frequency pulse. Equation 3.9 implies that the magnetic field vector is oscillating between $\hat{i}B_1$ and $-\hat{i}B_1$ and passing through zero. Simply, we can assume that $\vec{B}_1(t)$ is a linear combination of two counter-rotating magnetic fields components (i.e. clockwise and counterclockwise rotating magnetic fields). One of the components is rotating in the same way as the nuclear spin does while the another component is rotating in the opposite direction of the spin precession:

$$\vec{B}_1(t) = \vec{B}^1_{res}(t) + \vec{B}^1_{non\text{-}res}(t) = \frac{\vec{B}_1}{2}\left[\hat{i}\cos(\omega t) + \hat{j}\sin(\omega t)\right] + \frac{\vec{B}_1}{2}\left[\hat{i}\cos(\omega t) - \hat{j}\sin(\omega t)\right]$$

$$(3.10)$$

We only consider the resonant field component $\vec{B}^1_{res}(t)$ because it rotates in the same sense as nuclear spin precession. In a reference frame rotating with the Larmor frequency, the resonant component is nearly static, while the non-resonant is oscillating rapidly about zero; this oscillation frequency increases with B_o. In the presence of a strong external static magnetic field B_o, the resonant component $\vec{B}^1_{res}(t)$ thus has the dominant direct effect on the orientation of the nuclear spin. It causes the net magnetization no longer to be orientated along the z-axis and therefore no longer at equilibrium. The angle, Θ, of rotation on resonance is given by

$$\Theta = -\gamma\, B_1\, \tau, \qquad (3.11)$$

where τ is the duration of the RF pulse. The net magnetization, when not oriented along the z-axis, will precess at the Larmor frequency about the external magnetic field (i.e. the z-axis). The precession of a magnetic moment about a static magnetic field will induce a current in a coil placed close to it. Detection of the NMR signal is achieved by measuring the current induced in this coil. Measuring this current as a function of time yields a free induction decay (FID). For a single isolated nucleus, the FID will resemble a damped sinusoidal decay with a frequency equal to the Larmor frequency of the nucleus. The decay is damped because the equilibrium state is re-established by relaxation, to be discussed in detail in the next section. The FID is recorded in the time domain, but for spectroscopy, frequency domain spectra are most convenient. In order to inter-convert time domain and frequency domain, the method of Fourier transformation is used [3].

Since the value of a nuclear Larmor frequency ω_o depends on the value of the operating magnetic field strength B_0 of the NMR spectrometer, then for different NMR spectrometers which operate at different field strengths, the same nuclei at the same chemical environment have different values of Larmor frequency and so different peak positions on the frequency scale. In order to compare the peak positions in the 1D spectra between NMR spectrometers which operate at different fields, a chemical shift scale is defined as a magnetic field independent scale. On this scale, the peak position is reported by measuring the peak's frequency ν_i relative to a reference peak frequency ν_{ref} of a known compound. Tetramethylsilane (TMS), with chemical formula $(CH_3)_4Si$, is the most common standard reference compound for ^1H NMR. TMS is typically chosen as a reference in organic solvents because it is chemically inert and has a single peak NMR spectrum. Thus, the peak position in the chemical shift scale is defined by the following equation [1]

$$\delta(\text{ppm}) = \frac{\nu_i - \nu_{ref}}{\nu_{spectrometer}} \times 10^6,\tag{3.12}$$

where $\nu_{spectrometer}$ is the NMR spectrometer frequency and the position of the standard reference compound is defined to be at 0 ppm on the chemical shift scale. In Figure 3.1, a Fourier transformed 1D spectrum of a PEG/water suspension is shown.

A 90° RF pulse rotates the net magnetization into the xy plane. In a reference frame rotating at the precession frequency, the magnetization is static, i.e., is "in phase", assuming a perfectly uniform field, and no relaxation. Over time, the magnetization loses phase coherence due to local magnetic field inhomogeneity and spin-spin relaxation.

3.1.3 Chemical Shift

There is a magnetic interaction between an external magnetic field and the nuclear spins. The external magnetic field causes an induced magnetic field in the electron cloud. So the nuclear spins feel a local magnetic field which is the combination of the external as well as the induced magnetic field. But the electrons have different chemical environments at different sites. There is thus a local variation of the magnetic field [2]. As shown in Figure 3.1, due to the difference in chemical environment, protons located in the PEG polymer chain experience slightly different magnetic fields than the protons of water. This is known as chemical shift. In section 3.3, we will discuss pulsed-field-gradient NMR (PFG-NMR), where diffusivity of many species in the same system can be measured simultaneously using their different ^{1}H chemical shifts.

3.2 Relaxation in NMR

Generally, the term "relaxation" is used for the re-establishment of thermal equilibrium of a perturbed system (a system that obeys the Boltzmann distribution function). In the presence of a magnetic field, if a sample is undisturbed for a long time, it reaches a state of thermal equilibrium. But a radio frequency pulse perturbs the system to a non-equilibrium state. Relaxation is the process of regaining the equilibrium of a spin system through interactions with the environment. Relaxation processes in NMR are roughly divided into two types: longitudinal and transverse.

3.2.1 Longitudinal (spin-lattice) Relaxation

Longitudinal relaxation is the process during which the longitudinal component of the sample magnetization re-establishes its maximum value along the direction of the applied magnetic field [1]. A nuclear spin inside the sample experiences both an external uniform magnetic field B_0 and internal oscillating local fields B_{loc}. One of the origins of these local fields is the magnetic fields associated with magnetic dipole moments of nearby nuclear spins inside the sample. Because of resonance, local fields that happen to be oscillating at close to the Larmor frequency have a disproportionately large effect in rotating a magnetic moment to new directions just like an applied resonance pulse. In addition, the direction and the magnitude of these local fields at nuclear sites change continuously due to the thermal motion of molecules. According to the Boltzmann distribution, the population of nuclear spins in the lower energy state is higher than that in the higher energy state. The local fields will either rotate a given spin towards or away from the z-axis. However, the Boltzmann distribution ensures that the rotation towards the z-axis are more frequent than the rotation away from the z-axis. Thus, the magnetization is driven to equilibrium by thermal motions.

The above termed mechanism is often refer as a "non-secular" contribution [1] (i.e. arising from local fields oscillating at frequencies close to the Larmor frequency) to transverse relaxation; when the longitudinal magnetization relaxes back to equilibrium, so does the transverse magnetization.

3.2.2 Transverse (spin-spin) Relaxation

In equilibrium, there is a net longitudinal (z) magnetization, which is practically undetectable in comparison with the diamagnetic response of the sample to the B_0 field.

NMR therefore typically involves $(90^{\circ})_x$ or $(90^{\circ})_y$ pulses which rotate the nuclear spins into the transverse (xy) plane. In the presence of uniform external magnetic field B_0, these spins precess in synchronization with the Larmor frequency and thus the macroscopic transverse magnetization also undergoes precessional motion [1, 2]. Transverse relaxation is the process during which the transverse components of the sample magnetization decay to zero [1]. In the presence of nearby nuclear spins, a nuclear spin will precess about the direction of the uniform magnetic field with a frequency which is proportional to the sum of both B_0 and the net z-component of the local field $B_{z,loc}$ [1]

$$\omega = -\gamma(B_0 + B_{z,loc}), \tag{3.13}$$

where $B_0 >> B_{z,loc}$, but the amplitude of the local field and the z-component of the local field vary at different nuclear spin locations in the sample. The nuclear spins will thus precess at slightly different values of Larmor frequency. This causes a loss in synchronization or phase coherence, and results in an irreversible decay in the macroscopic transverse magnetization. This mechanism is often called the "secular" contribution to transverse relaxation: it arises from the z-component of local fields varying from one spin to spin.

In NMR, the peak width is directly proportional to the transverse relaxation rate. Therefore, losing synchronization due to the secular contribution causes a peak broadening that is called homogeneous broadening. However, another broadening in a NMR peak might be caused due to the existence of an inhomogeneous magnetic field. This peak broadening is called inhomogeneous broadening [1]. Inhomogeneous broadening arises from variation of macroscopic magnetic fields due to sample imperfection or susceptibility inhomogeneities (or because of B_0 field non-uniformity, which is minimized by "shimming", which is NMR terminology to describe the careful tweaking of the B_0 field using auxiliary field adjustment coils known as shim coils).
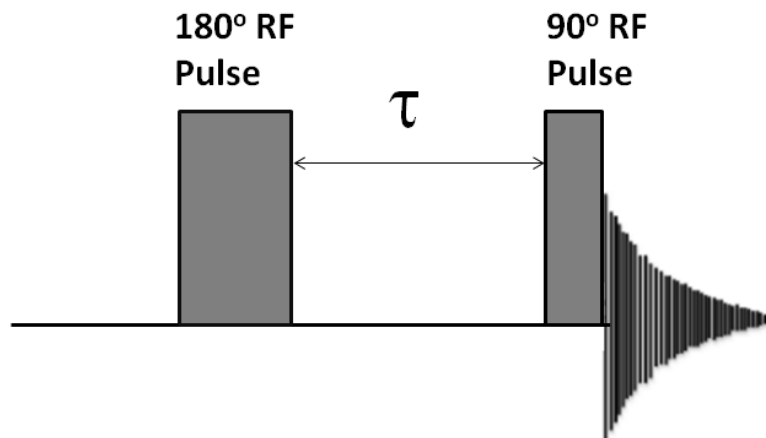
Figure 3.2: Inversion recovery pulse sequence. The function of the 180° pulse is to flip the initial longitudinal magnetization (M_o) opposite to the direction of the main magnetic field (B_o). During the τ interval, these inverted magnetization undergo T_1 relaxation as they variably seek to re-establish magnetization along the $+z$-direction.

Two techniques have been used to measure longitudinal relaxation time T_1 and transverse relaxation time T_2 of different species in the solution.

3.2.3 The Inversion Recovery Technique

This technique is used to measure the longitudinal relaxation time T_1 associated with different chemical groups inside a sample. As shown in Figure 3.2, the pulse sequence includes two successive pulses, 180° and 90° pulses respectively with a delay time τ between these two pulses [2].

The first 180° pulse inverts the magnetization of the sample, which is at equilibrium, from the z-axis to the $-z$-axis. As soon as the 180° pulse is turned off, the magnetization vector starts to relax back to its previous orientation along z-axis (equilibrium) during the delay time. During this period no signal can be detected by the NMR device because there is no available magnetization component in the xy-plane. Then, the sample is exposed to 90° pulse which is responsible for creating a transverse magnetization in the xy-plane which can be detected by the receiver coil

and recorded as a peak with specific intensity and polarity.

The pulse sequence is repeated at different values of delay time τ in order to be able to record different positive and negative peaks with different intensities such that the intensity of each peak is proportional to the magnitude of the sample longitudinal magnetization at any time τ after 180º pulse $M_z(\tau)$ [2]

$$M_z(\tau) = M_o \left(1 - 2 \exp \left(\frac{-\tau}{T_1} \right) \right), \tag{3.14}$$

where M_o is the magnitude of sample magnetization at equilibrium and T_1 is the longitudinal relaxation time. Based on Equation 3.14, turning on the 90º pulse right away after turning off 180º (i.e. $\tau = 0$) then a maximum peak intensity with magnetization amplitude $-M_o$ and with negative polarity is detected by the NMR receiver coil. On the other hand, turning on the 90º pulse at large value of τ (i.e. $\tau = \infty$) after turning off the 180º pulse then a maximum peak intensity with magnetization amplitude M_o and positive polarity is detected.

According to Equation 3.14, the longitudinal relaxation time T_1 is defined as the value of delay time at which the longitudinal sample magnetization recovers to ≈ 0.26 of its equilibrium magnetization value M_o.

The longitudinal relaxation time T_1 for PEG and Ficoll70 at all volume fractions in water were measured 770 ± 12 ms and 783 ± 14 ms respectively. Hence, the time between successive repetitions of the experiment (for signal averaging), d_1, was chosen to be large compared to the T_1 relaxation time ($d_1 \geqslant 5T_1$).

3.2.4 The Spin Echo Technique

This technique is used to measure the transverse relaxation time T_2 of different kind of nuclei magnetization inside a sample [2]. The pulse sequence, shown in Figure 3.3,
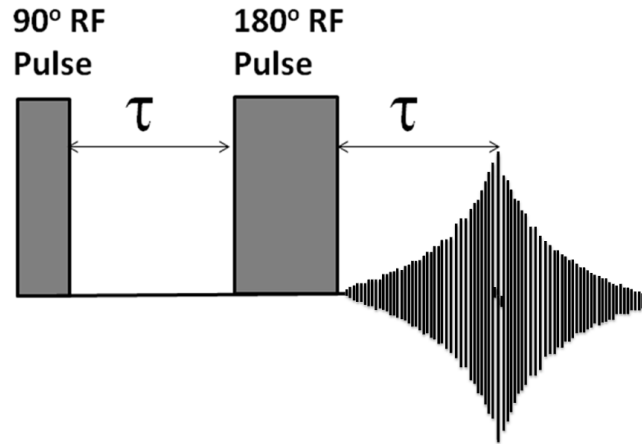
Figure 3.3: Spin echo pulse sequence. The NMR signal observed following an initial excitation 90° pulse decays with time due to both spin relaxation and any inhomogeneous effects which cause different spins in the sample to precess at different rates. The first of these, relaxation, leads to an irreversible loss of magnetization. However, the inhomogeneous dephasing can be removed by applying a 180° inversion pulse that inverts the magnetization vectors.

includes two successive pulses, 90° and 180° pulse respectively with a delay time τ between these two pulses and same period of delay time between 180° and the signal acquisition.

The first 90° pulse inverts the sample magnetization at equilibrium and creates a transverse magnetization along the -y-axis. After turning off the 90° pulse and during the first delay time τ between 90° and 180° pulses the nuclear spins start spreading out and possessing slightly different values of precession frequencies according to Equation 3.13 such that some nuclear spins precess with frequency slightly higher than Larmor frequency while some others precess with frequency slightly lower than Larmor frequency.

The next 180° pulse inverts the orientation of individual nuclear spins to the opposite side in the xy plane and it reverses the precession of nuclear spins in order to cancel the effect of nonhomogeneity in the applied uniform magnetic field which can cause dephasing in the transverse component of the sample magnetization. The

signal intensity is recorded from the top of the echo, i.e. a time τ after the 180° pulse.

The pulse sequence is repeated at different values of delay time τ in order to detect different peaks intensities such that the intensity of each peak is proportional to the magnitude of sample transverse magnetization $M_y(\tau)$ [2]:

$$M_y(\tau) = M_y(0) \exp\left(\frac{-\tau}{T_2}\right) \tag{3.15}$$

where $M_y(0)$ is the magnitude of the transverse magnetization right away after turning off the 90° pulse.

According to Equation 3.15, the transverse relaxation time T_2 is defined as the value of delay time at which the transverse component of sample magnetization decays to ≈ 0.37 (the e-folding timescale, $1/e$) of its maximum value $M_y(0)$.

The transverse relaxation time T_2 for PEG was 254 ± 3 ms while for Ficoll70, T_2 was measured 13 ± 1 ms.

3.3   NMR and Translational Motion

In the description of a one-dimensional single-pulse experiment, both B_0 and therefore ω_0 are homogeneous throughout the system. If in addition to B_0, there is a spatially dependent magnetic field gradient g, the Larmor frequency becomes spatially dependent and [4]

$$\omega = \gamma B_0 + \gamma g z. \tag{3.16}$$

The phase shift in the time interval t is given by

$$\phi(t) = \gamma B_0 t + \gamma \int_0^t g(t')z(t')\,dt' \tag{3.17}$$
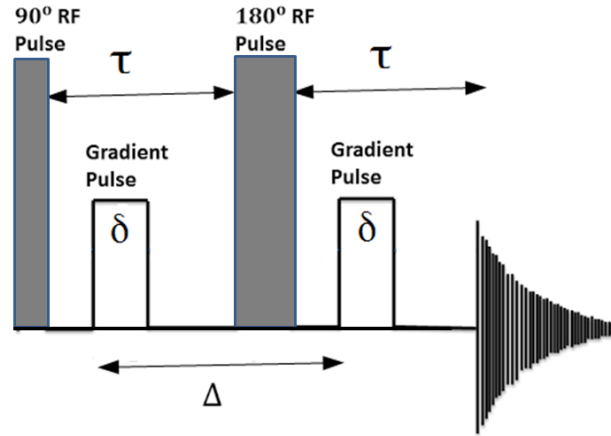
Figure 3.4: The pulsed-field-gradient spin echo pulse sequence. A 90° pulse followed by a delay of τ, then a 180° pulse followed by a second delay of length τ. The gradient pulses are of amplitude g and duration δ, and applied first after the 90° RF pulse and second after the 180° pulse.

In the most common diffusion experiments, this gradient is "pulsed" for a time duration δ. The dephasing due to the gradient pulse is a function of the gyromagnetic ratio of the nucleus and gradient strength. So a magnetic field gradient can be used to label the position of the spins.

3.3.1   The PGSE Experiment

The most common experiment to measure diffusion coefficients using NMR is the pulsed-gradient spin-echo experiment [5]. The basic premise of this technique, and all NMR techniques that measure diffusion, is the application of a magnetic field gradient which labels a specific position in the sample with a specific precessional frequency. Figure 3.4 shows a diagram of the PGSE pulse sequence. The RF portion of the pulse sequence is, as the name suggests, a simple spin-echo pulse sequence, a 90° pulse followed by a delay of τ, then a 180° pulse followed by a second delay of length τ. At this point the magnetization of the sample will refocus resulting

in an "echo". In the PGSE experiment, a magnetic field gradient pulse is applied after both RF pulses. The gradient pulses are of duration δ, and Δ is the time from the start of the first gradient pulse to the start of the second gradient pulse. The first gradient pulse causes a certain amount of phase development relative to ω_0, the precessional frequency due to the static applied field. The 180° RF pulse then inverts the sign of this phase development. If no diffusion takes place during the course of the experiment, the second gradient pulse will remove all the phase development that resulted from the first gradient pulse and the net magnetization will completely refocus, momentarily, at 2τ. This refocussing is the spin echo. However, if diffusion takes place, an incomplete refocusing of the net magnetization at 2τ will result. This means the observed signal will be attenuated [5]. Both random and directed translational motion can be measured *via* a pulsed-gradient spin echo [6].

In what follows, we make the above description more precise. The pulse sequence of a spin echo pulse sequence with gradients (thus called the pulsed-gradient spin echo or PGSE experiment) is shown in Figure 3.4. A 90_x^o radio frequency pulse is applied which rotates the magnetization from the z axis to the xy plane. During the first τ period at time t_1 a gradient pulse of duration δ and magnitude g is applied. At the end of the first τ period, the phase shift is a function of z,

$$\phi(\tau) = \gamma B_0 \tau + \gamma g \int_{t_1}^{t_1+\delta} z(t) \, dt \, . \tag{3.18}$$

Here g has a constant amplitude over the time duration δ, i.e., it is a rectangular gradient pulse. At the end of the first τ period, a 180_y^o RF pulse is applied which reverses the sign of the precession. At time $t_1 + \Delta$, a second gradient pulse of equal magnitude and duration is applied. If the spins have moved, the degree of dephasing is proportional to the displacement in the direction of the gradient in the duration Δ.

Now the total phase shift is given by [5]

$$\phi(2\tau) = \left[\gamma B_0\tau + \gamma g \int_{t_1}^{t_1+\delta} z(t)\, dt\right] - \left[\gamma B_0\tau + \gamma g \int_{t_1+\Delta}^{t_1+\Delta+\delta} z(t')\, dt'\right]$$

$$= \gamma g \left[\int_{t_1}^{t_1+\delta} z(t)\, dt - \int_{t_1+\Delta}^{t_1+\Delta+\delta} z(t')\, dt'\right] \tag{3.19}$$

The echo signal attenuation $S(\Delta, \delta, g)$ at $t = 2\tau$ can be written as

$$S(\Delta, \delta, g) = S_0 \int_{-\infty}^{\infty} P(\phi, 2\tau)\exp(i\phi)d\phi = S_0 \langle \exp(i\phi) \rangle \tag{3.20}$$

where S_0 is the signal in the absence of a field gradient. $P(\phi, 2\tau)$ is the phase distribution function. The above expression must be ensemble averaged in order to yield the signal in the expression. Since for randomly varying quantities (as in diffusion), the ensemble-averaged phase distribution function becomes a Gaussian function, and the signal can be written as

$$S(g) = S_0 \langle \exp(i\Delta\phi) \rangle = S_0 \exp \frac{-\langle (\Delta\phi)^2 \rangle}{2}, \tag{3.21}$$

where $\langle \rangle$ refers to an ensemble average.

In the short gradient pulse limit (the SGP approximation), i.e. assuming $\delta \ll \Delta$, this equation can be written (for a rectangular gradient pulse) as

$$S(g) = S_0 \exp(-\gamma^2 g^2 \delta^2 D(\Delta - \delta/3)), \tag{3.22}$$

where D is the self diffusion coefficient. Therefore in a pulsed-field-gradient experiment, one can vary a generalized gradient strength parameter k, where $k = \gamma^2 g^2 \delta^2 (\Delta - \delta/3)$. While g is the parameter that is ramped (up or down) during a single experiment to vary k, Δ can also be varied. Observation of the signal atten-
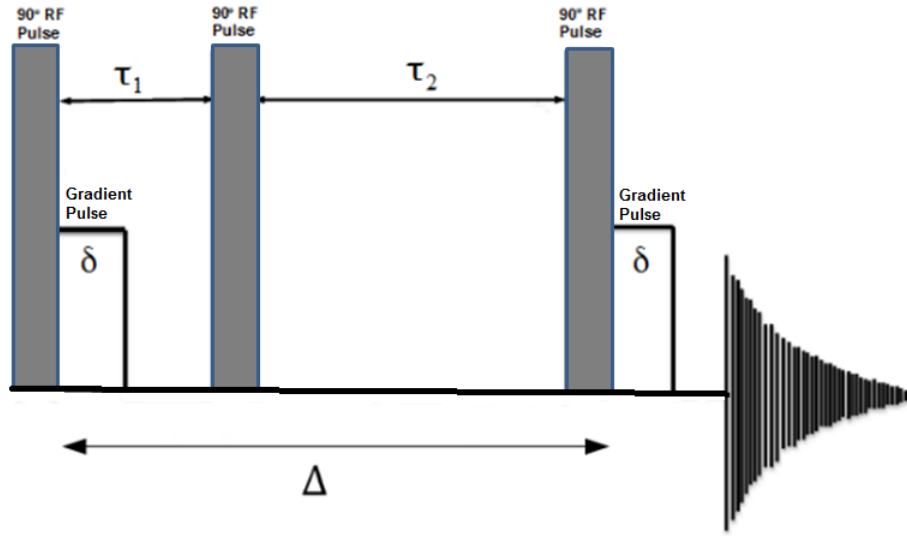
Figure 3.5: The pulsed-field-gradient stimulated echo pulse sequence. Transverse relaxation occurs during the time τ_1, longitudinal relaxation during the time τ_2, and Δ is the diffusion time. The gradient pulses are of amplitude g and duration δ, and applied after the first and third 90° RF pulse.

uation with increasing k yields the self-diffusion coefficient [4].

For the systems in which we are interested, the transverse relaxation time is short (10 - 300 ms) which causes a severe restriction on diffusion time Δ . This is because there is a second term in the attenuation equation due to transverse relaxation

$$S(g) = S_0 \exp\left(-\gamma^2 g^2 \delta^2 D(\Delta - \delta/3)\right) \exp\left(\frac{-\Delta}{T_2}\right). \tag{3.23}$$

So we use a stimulated echo pulse sequence (Figure 3.5), discussed next.

3.3.2   Pulsed Field Gradient Stimulated Echo

In the stimulated echo pulse sequence (Figure 3.5), the 180° pulse is replaced by two 90° pulses separated by a time interval τ_2 much longer than the first time interval
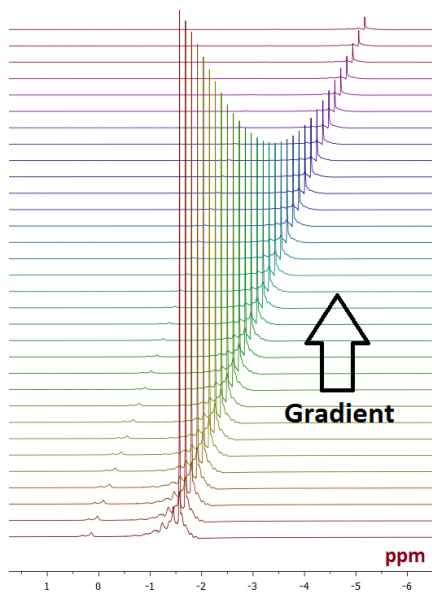
Figure 3.6: Stimulated echo signal attenuation of Ficoll70 in a solution for increasing gradient value.

τ_1 [6]. After the second 90º pulse a "homospoil" gradient (a gradient pulse that rapidly reduces the magnetization zero by dephasing the spins) is applied to kill the remnants of transverse magnetization.

The diffusion time in this experiment is determined by the largest time which is τ_2 and echo signal attenuation due to spin relaxation is determined by T_1. So the stimulated echo pulse sequence is well suited to measure slow diffusion. In all samples we study, T_1 is much longer than T_2.

3.3.3 PFG NMR Measurements

PFG NMR offers simultaneous measurement of different species either by chemical shift or relaxation time. A molecule having different chemical species has different relaxation times and individual chemical shifts. A liquid sample containing different molecular species will thus have chemical shifts for each chemical group of each

molecule. We can easily trace the particle motion just by observing the echo attenuation of these peaks in a pulsed-field-gradient spin echo experiment. By this process, the diffusion coefficient for different chemical species can be measured simultaneously in the same experiment. In a single sentence, the advantage of a PFG NMR study would be to obtain spectrally resolved diffusion coefficients.

3.3.4   Calibration of Diffusion Coefficients

It is necessary to consider the calibration of the gradient strength, since this is a pre-requisite to the determination of accurate diffusion coefficients and can itself be problematic. A number of different options are available to calibration [4]. The simplest and probably the best technique is by indirect calibration using a standard sample of known diffusion coefficient. For example, diffusion coefficient of HDO in pure D_2O or H_2O/D_2O mixtures are ideal. In this work a standard calibration sample (pure D_2O) was run prior to every set of experiments to ensure consistency between datasets. In all cases we used the diffusion coefficient of trace HDO in pure D_2O (1.902×10^{-9} m^2/s at 25ºC) [7] as our calibration standard.

3.3.5   Analysis of Diffusion Experiments

A stimulated echo pulse sequence was used to measure the diffusion coefficient. The parameters included Δ from 50 ms to 500 ms, $\delta = 2$ ms and gradient values in the various experiments reported in Chapters 5, 6, 7, and 8 were varied according to the purpose of each experiment.

In PEG/Ficoll70 solution, one can obtain diffusion coefficients for the PEG and Ficoll70 simultaneously by using their relaxation time. The signal attenuation of each peak yielded the diffusion coefficient according to the equation (from Equation 3.21)
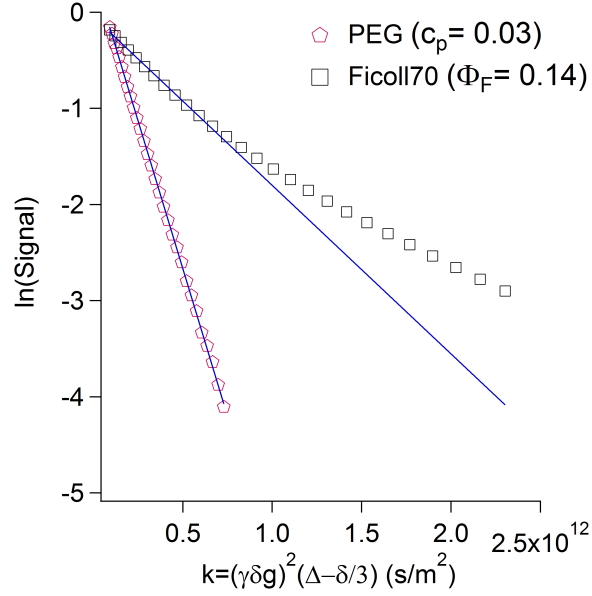
Figure 3.7: The attenuation of the signal $S(g)/S(0)$ on a log scale versus $k = (\gamma\delta g)^2(\Delta - \delta/3)$ for PEG and Ficoll70 in solution. The PEG signal exhibits mono-exponential decay as a function of the gradient parameter, k; the Ficoll signal does not.

$$S(g) = S_0 \exp\left(-\gamma^2 g^2 \delta^2 D(\Delta - \delta/3)\right) = S_0 \exp(-D\,k) \qquad (3.24)$$

where k is a gradient strength parameter where $k = \gamma^2 g^2 \delta^2(\Delta - \delta/3)$. Shown in Figure 3.6 is the signal attenuation for the water and Ficoll70 for gradient strengths (in G/cm) from 40 G/cm to 100 G/cm in 32 steps where the gradient is so large that the water signal has been completely eliminated. A signal attenuation curve for such an experiment is shown in Figure 3.7 indicates that NMR signal attenuation for Ficoll70 (packing fraction, $\phi_F = 0.14$) can not be fitted with a mono-exponential function.

In the situation where the molecular exchange between monomer and cluster is very slow (or more generally if there are multiple sizes in the chemical species that

85

remain stable over the NMR experiment), one expects the total signal to be given by

$$
\begin{aligned}
S_{total} &= S_{monomer} + S_{cluster} \\
&= S_{0,monomer} \exp(-D_{monomer}k) + S_{0,cluster} \exp(-D_{cluster}k) \quad (3.25)
\end{aligned}
$$

which is bi-exponential in nature.

A generalization to multi-exponential behaviour may be made for macromolecules existing in more than two species: $S_{total} = \sum_i S_{0,i} \exp(-D_i k)$. For two species, Equation 6.3 may be written in the form $S_{total}/S_{max} = f \exp(-D_1 k) + (1-f) \exp(-D_2 k)$, where $f = S_{0,1}/(S_{0,1} + S_{0,2})$.
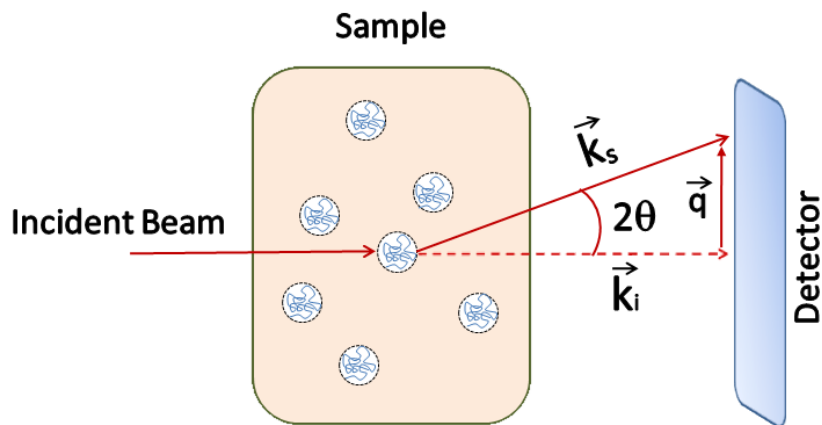
Figure 3.8: Schematics of the geometry of SANS experiments.

3.4 Small Angle Neutron Scattering

Small Angle Neutron Scattering (SANS) is a very well established method for the study of polymer and colloidal samples [8, 9], because it can detect inhomogeneities from around the atomic scale (1 nm) to close to the micron scale (600 nm), and partial deuteration can be used in order to enhance the contrast between scatterers, and between the scatterers and the solvent.

SANS exploits the dual wave/particle nature of the neutrons. Since they have zero charge, neutrons are scattered by nuclei in samples or by the magnetic moments associated with unpaired electron spins (dipoles) in magnetic samples. Neutrons are mainly produced in two ways: continuously by a nuclear fission reactor or in pulses by spallation from a metal target bombarded by protons in a particle accelerator. Immediately after been produced the neutrons are moderated usually using liquid hydrogen in order to slow them down (make them lose kinetic energy). These neutrons are the ones used for SANS and they are called "cold neutrons" [10]. Neutrons are scattered with the same intensity in all directions, because the wavelength of neutrons
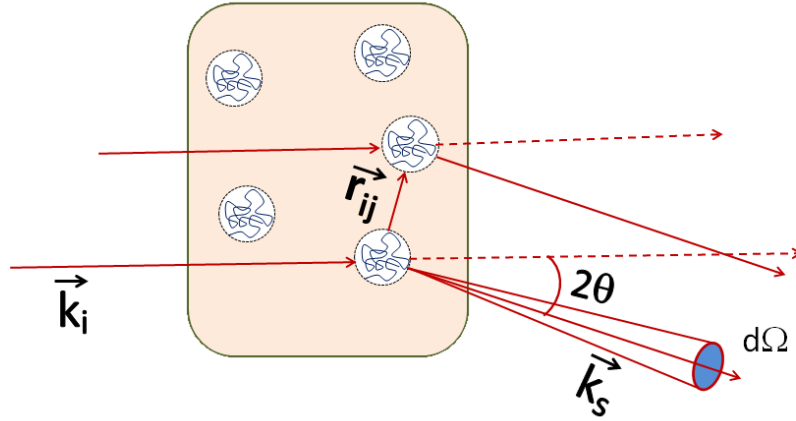
Figure 3.9: Schematic drawing of a basic scattering geometry. The incident plane wave (k_i) is scattered from two scattering center. A scattered wave (k_s) propagates into the direction of Θ. Due to the path difference of the scattered waves interference takes place. The scattering intensity is detected in a certain distance on the detector plane within an area defined by the solid angle Ω.

is orders of magnitude larger than the nucleus that scatters it. The main consequence of this is that in neutron scattering nuclei can be consider as "point scatterers".

3.4.1 Scattering Length and Cross Section

In SANS, a two dimensional detector is used. In a fixed-wavelength instrument once the wavelength (λ) has been selected (the typical operating wavelength of a SANS instrument is 6 Å [10]), the scattering length ($|\vec{q}|$) can be changed by varying the sample-detector distance [11]. As shown in Figure 3.8, for each sample-detector distance, several values of the radial distance (corresponding to different $|\vec{q}|$ values) at which neutrons are scattered can be measured. In this geometry and at small angles, the following expression for $|\vec{q}|$ can be derived:

$$|\vec{q}| = \frac{4\pi}{\lambda} \sin \Theta \qquad (3.26)$$

88

In this study, experiments were carried out at the General Purpose (GP-SANS) CG-2 instrument at Oak Ridge National Laboratory. Two sample to detector distances were used (1.7 m and 18.5 m) for a range of scattering vectors from 0.004 Å^{-1} to 0.5 Å^{-1}.

The scattering of the incident wave takes place at individual scattering centres. The detected scattering intensity results from the interference of the scattered waves propagating from the different scattering centres and having a phase difference Ψ. The phase difference (Ψ) between incident and scattered waves is

$$\Psi = \vec{q} \cdot (\vec{r}_i - \vec{r}_j) = \vec{q} \cdot \vec{r}_{ij}. \tag{3.27}$$

The individual scatterers are linked by the vector $\vec{r}_{ij}$. The scattering vector $\vec{q}$ is defined by the following relation and describes the momentum transfer during the scattering process:

$$|\vec{q}| = |\vec{k_s} - \vec{k_i}| \tag{3.28}$$

Here, $\vec{k}_i$ ($|\vec{k}_i| = 2\pi/\lambda$) is the incident wave vector with the wavelength λ and $\vec{k}_s$ is the one of the scattered waves. For an elastic small-angle scattering experiment, only the magnitude of the scattering vector is considered, which is related to a length in the reciprocal space. In the following discussion it will be assigned the unit nm^{-1}.

In neutron scattering, the sample and solvent should have different scattering length densities ($\rho(r)$) in order to have contrast (making it possible to distinguish one from the other), in the same way as in light scattering they should have different refractive indices or in small angle X-ray scattering they should have different electron densities. The scattering length densities can be calculated using the expression,

$$\rho(r) = \frac{\sum_{i=1}^{n} b_i}{V}. \tag{3.29}$$

89

Herein, b_i is the scattering length of the different species embodied in the sample and V is the molar volume, accessible *via* measurements of the macroscopic density of the sample [12]. The total amplitude of the three-dimensional Fourier transform of $\rho(r)$ of the scattering ensemble is [12]

$$
\begin{aligned}
A(q) &= \sum_{i=1}^{n} b_i \exp(i\,\vec{q}.\,\vec{r}_{ij}) \\
&= \int_V \rho(\vec{r}) \exp(i\,\vec{q}.\,\vec{r}_{ij})\,d^3r.
\end{aligned}
\tag{3.30}
$$

This relation takes into account that the integration is done over the total scattering volume V. In neutron scattering, the differential scattering cross–section $\left(\frac{d\Sigma}{d\Omega}(q)\right)$ is the dependent variable measured. It has dimensions of $(\text{length})^{-1}$, usually cm^{-1}). This quantity is usually termed the "intensity" and is represented by the symbol I(q), but this term can be misleading since in SANS what is measured is the number of neutrons at a given wavelength, scattered through a particular angle that arrive to a small area of the detector in a unit time (flux). This flux can be expressed as

$$
\begin{aligned}
I(q) &= \frac{d\Sigma}{d\Omega} = \left\langle A(q)\,A^*(q) \right\rangle \\
&= \int_V \int_V \rho(\vec{r}_i)\,\rho(\vec{r}_j) \exp(i\,\vec{q}.\,(\vec{r}_i - \vec{r}_j))\,d^3r_i\,d^3r_j.
\end{aligned}
\tag{3.31}
$$

The differential scattering cross section contains information about the size, shape, and interactions between scattering centers of the sample [13]. The experimental access to differential scattering cross section is provided by the number of events on the position sensitive detector with respect to the incident number of neutrons.

3.4.2   Scattering of Particles in Solution

Until this point, only single objects non-affected by their surrounding matrix have been discussed. Now we consider particles with a homogeneous scattering length density b_s are dispersed in a continuous medium with a scattering length density b_m. Hence, Equation 3.31 can be written as [13]:

$$I(q) = (N/V)(\Delta b)^2 P(q) \qquad (3.32)$$

In this expression N is the number density of scattering centers, V is the volume of one scattering center, $\Delta b = b_m - b_s$ is the scattering length contrast. Here $P(q)$ is the particle form factor describing its corresponding spatial geometry [12].

The simplest case is limited to single scatterer within a matrix or for high dilution. This approximation assumes that there is no correlation between the positions of the particles and thus there is no phase relation between the scattered waves [13]. Increasing the number density causes a spatial correlation and the scattered waves interfere. The correlation of the dispersed particles is provided by the structure factor $S(q)$, which also enters the observed scattering intensity,

$$I(q) = N/V(\Delta b)^2 P(q) S(q) \qquad (3.33)$$

The spatial correlation between the individual particles is described by the structure factor $S(q)$. The observed scattering intensity is thus proportional to product of the form factor and the structure factor. Any information about the form factor should go here. The corresponding transformation of $S(q)$ leads to the pair correlation function $g(r)$. For dilute systems the structure factor is unity.

3.4.3 Debye Scattering Theory

The Debye theory is used when the scatterers have dimensions comparable with λ [13], which is the case in the work in Chapter 5 and 6 (i.e. polyethyleneglycol). This has as a consequence that different parts of the same particle can behave as scattering centers. Because the distances between these centers have the same magnitude as the wavelength, there will be interference by the waves scattered by different parts of the same molecule. The form factor ($P(q)$) in this case depends on the nature and shape of the scattering particle (i.e. Gaussian chain, rod, sphere). For a Gaussian coil, for example, the expression of $P(q)$ is:

$$P(q) = \frac{2}{x^2}\left(\exp(-x) - 1 + x\right) \tag{3.34}$$

where $x = q^2 R_g^2$ and R_g is the radius of gyration of the scattering object.

In this work, SANS data are presented as plots of the intensity of the scattered neutron beam, $I(q)$ as a function of scattering vector $q = (4\pi \sin \Theta / \lambda)$, where Θ is one half of the scattering angle and λ is the neutron wavelength. The intensity can be written as $I(q) = I_0 P(q)$, where $P(q)$ is the form factor which provides information on the size and shape of the scatterers. Hence the radius of gyration of the scattering object, R_g, can be extracted from fitting the plot of $I(q)$ vs q to the Debye model.

3.4.4 Guinier Approximation

The analysis of the scattering intensities at small scattering angles (the low q limit) is useful in obtaining model independent information on the investigated structure [11]. It reveals the radius of gyration R_g, which is a measure for the density distribution around the centre of mass. It can also be used for the determination of the particle volume V_p. The Guinier equation yields

$$I(q) = I_0 \, P(q) = I_0 \, \exp\left(\frac{-q^2 \, R_g{}^2}{3}\right). \tag{3.35}$$

The approximation is restricted to the following assumptions [13]:

1. The relation is only valid for small scattering angles to fulfil $q \, R_g \ll 1$.

2. An isotropic system without inter-particle interactions is considered. Thus, the structure factor becomes unity.

3. The particles are randomly oriented and isotropically distributed.

The radius of gyration of the scattering object, R_g, can be extracted from the slope of a plot of $\ln(I/I_0)$ vs q^2. This is is commonly known as the Guinier plot.

3.4.5 Contrast Variation

One of the important features in neutron scattering is the difference in scattering length between hydrogen (-3.741×10^{-15} m) and deuterium (6.671×10^{-15} m) [14]. This difference is the basis of SANS measurements since molecules composed of light atoms (such as hydrocarbons) have a very good contrast when dissolved in deuterium oxide (D_2O). D_2O is the solvent preferred for such measurements due to its low incoherent scattering. When the scattering length contrast is equal to zero ($\Delta b = 0$), it is said that the solute is "contrast matched" (it has the same scattering density as the solvent) [13]. This can be achieved by replacing the hydrogen by deuterium in the molecule, or by changing the mixture of hydrogen/deuterium (water/heavy water) in the solvent, or both. The possibility of contrast matching the solute makes SANS measurements very suitable for work with mixtures of components (such as polymers, surfactant mixtures, surfactants and polyelectrolyte mixtures, among others) because
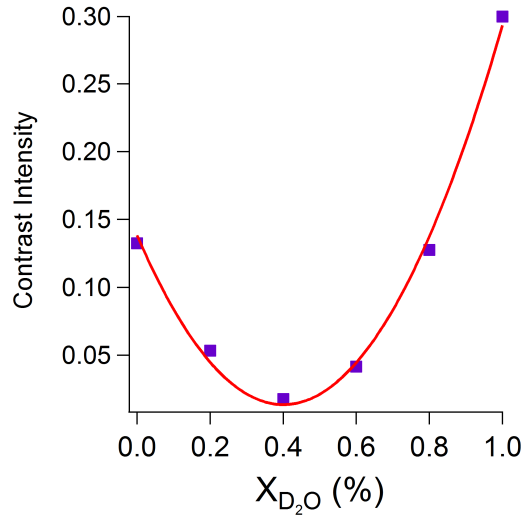
Figure 3.10: Contrast variation Ficoll70 samples in solutions containing various H_2O/D_2O ratios. The concentration at which Ficoll70 contributed minimally to the scattering signal was determined to be 60% H_2O and 40% D_2O.

it allows detecting separately the scattering from each component, permitting to see separately the conformation that each component adopts in the mixture.

In this work, the H_2O/D_2O composition points of minimum scattering intensity for Ficoll70 were determined using contrast variation Ficoll70 sample in solutions containing various H_2O/D_2O ratios. The ratio at which the scattering length densities of Ficoll70 and H_2O/D_2O were matched and therefore Ficoll70 did not contribute to the scattering signal was determined as 60% H_2O and 40% D_2O. This is shown in Figure 3.10 where intensity is plotted against H_2O/D_2O ratios. The ratio at which the scattering length densities of Ficoll70 and H_2O/D_2O were matched and therefore Ficoll70 did not contribute to the scattering signal was determined as $(60 \pm 1)\%$ H_2O and $(40 \pm 1)\%$ D_2O. Therefore only the PEG contribution appears as a q dependent intensity in the spectra regardless of Ficoll70 packing fractions.
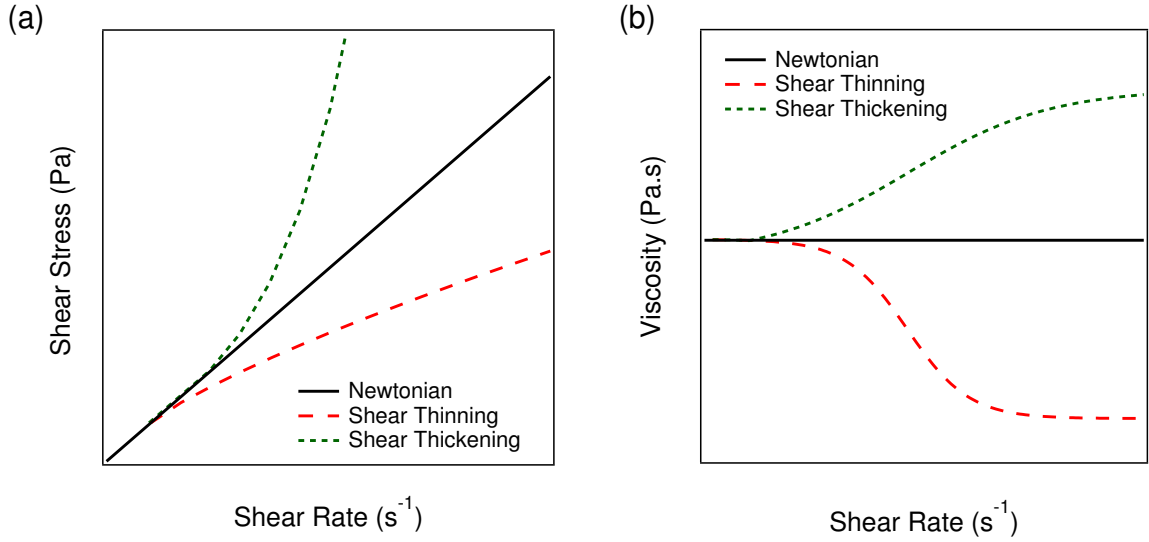
Figure 3.11: Examples of flow curves for different fluids. (a) shear stress and (b) viscosity as a function of shear rate.

3.5 Rheology

Conventionally, the flow or "rheological" properties of liquids such as water or oils are characterized by their viscosity, η, which can be thought of as the resistance of a liquid to flow or internal friction [15]. Applying a shear stress (σ) on a simple liquid will produce a time-dependent strain, γ, which is equivalent to a constant value of strain rate, $\dot{\gamma} = \frac{d\gamma}{dt}$, in Newtonian liquids. Thus,

$$\sigma = \eta\,\dot{\gamma}. \tag{3.36}$$

Therefore, in Newtonian liquids, the shear stress σ is linearly proportional to the strain rate $\dot{\gamma}$, and a plot of shear stress against shear rate yields a straight line passing through the origin, the slope of the line being the viscosity, η. However, for many suspensions there is no such linear relation between the rate of shear and the shearing stress, and the rheological behaviour is said to be non-Newtonian. Figure 3.11 shows

different types of basic flow behavior that can occur. For non-Newtonian suspension, the system exhibits shear thickening, shear thinning, or both in the same system. Shown in Figure 3.11 (a) and (b), shear thinning materials are those where the viscosity of the material decreases with increased shear rate. This phenomenon can be naturally occurring, or it can be engineered to occur. Polymer solutions are known to thin in the presence of shear, with the decrease in viscosity attributed to alignment of the polymers occurring at high shear rates. Examples of fluids that are produced so that they exhibit shear thinning include toothpaste and paints. In both cases, there are times when the user would require the fluid to be less viscous, i.e. during brushing or painting, but also times when the material is required to be viscous to reduce the likeliness of spillage or dripping. Shear thickening on the other hand is where the viscosity of the material increases with shear rate (short, green dashes in Figure 3.11 (a) and (b)). Classic examples of this property are custard or corn starch, which can become almost solid in appearance under force at short time scales. The rheological properties of a macroscopic volume of material can be measured using a viscometer or rheometer, of which there are several different forms or geometries. However, all apply a controlled stress or strain upon the material, and the response of the sample is then measured. As rheological phenomena can be observed over several decades of time, rheometers rely on accurate feedback loops in order to control the rate of flow and also accurately measure the viscosity of the fluid.

In this work, experiments were performed on an Anton Paar Physica MCR 301 rheometer, where the cone-plate measuring system was used to extract the flow curves. The cone-plate geometry has a diameter of 50 mm and cone angle of 0.5°. The flow curves experiments were carried out with shear rate varying from 0.001 to 100 s^{-1}. For all samples reported in this work, viscosity remains constant as the shear rate is varied (Figure 3.12). Thus, the Newtonian behaviour of Ficoll70 suspensions is
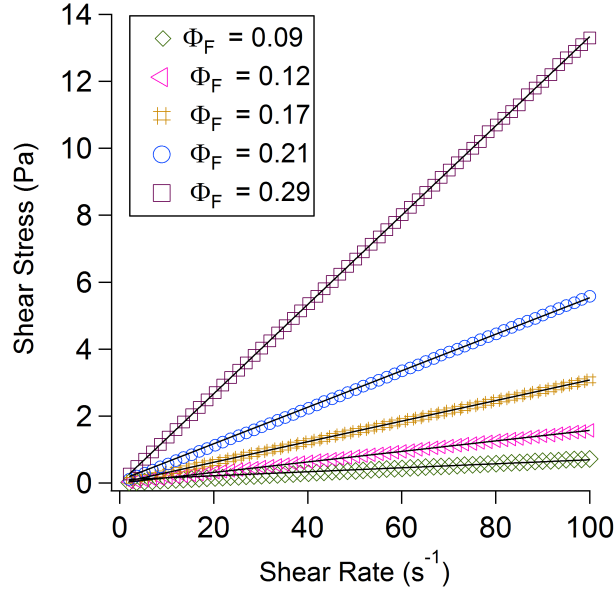
Figure 3.12: Flow curves for Ficoll70 for different packing fractios.

consistent with simple colloidal behaviour at least insofar as the σ - $\dot{\gamma}$ relationship being linear.

3.5.1 Viscosity of a Colloidal Suspension

The viscosity of a colloidal suspension η_s is greater than the viscosity of the liquid medium η_L and the ratio (η_s/η_L) is referred to as the relative viscosity η_r. For a very dilute suspension of non-interacting spheres in a Newtonian liquid, the viscosity is described by the Einstein equation

$$\eta_r = \eta_s/\eta_L = 1 + 2.5\,\phi \tag{3.37}$$

where ϕ is the packing fraction of dispersed spheres. The higher viscosity is caused by the dissipation of energy as liquid flows around the particles. A more general equation

97

for the viscosity of a suspension of non-spherical particles is

$$\eta_r(\phi) = \eta_s/\eta_L = 1 + K_H\,\phi \tag{3.38}$$

where K_H is the apparent hydrodynamic shape factor of the particles, and $K_H = 2.5$. As the concentration of the dispersed phase increases, the viscosity of a suspension is increased due to the interaction between the dispersed particles, and does not obey the Einstein equation. The rheological behavior of concentrated suspensions is much more difficult to work out. Since the publication of Einstein's basic analysis of the viscosity of a dilute suspension of rigid spheres, many investigations have attempted to predict the rheology of hard-sphere colloidal dispersions. Much of the effort has focused on extending theoretical models for dilute dispersions to concentrated dispersions of hard spheres [16–18]. Commensurate with these theoretical developments, experimentalists have worked toward developing real colloidal dispersions that approximate hard spheres [19–21]. Computational techniques that include many body hydrodynamic interactions have also been developed to enable direct numerical calculation of hard-sphere colloidal behavior [22]. As the volume fraction of particles increases, the interaction between particles during flow causes the viscosity to increase greatly. Rheological data for suspensions of uniform spherical colloidal particles are often approximated by the Krieger-Dougherty equation [19].

$$\eta_r = \eta_s/\eta_L = (1 - \phi/\phi_m)^{-[\eta]\phi_m} \tag{3.39}$$

where ϕ_m is the maximum packing fraction, and $[\eta]$ is the intrinsic viscosity, which is equal to 2.5 for dilute dispersions as defined by the Einstein relation. In suspensions of particles of anisometric shape both ϕ_m and $[\eta]$ depend on particle orientation. Brownian motion somewhat randomizes colloidal particles and increases the effective

hydrodynamic shape factor. Woods and Krieger obtained values of $\phi_m = 0.67 - 0.68$ and $[\eta] = 2.7$ for aqueous suspensions of dispersed monodisperse latex sphere smaller than 1 μm [23].

Recently, a model has been proposed that introduces an "appropriate form" of the excluded volume effects and gives a better quantitative description of the viscosity of solid and liquid suspensions of spherical particles at arbitrary packing fractions [24]. This model incorporates an effective packing fraction ϕ_{eff} as a scaling variable that leads to an universal representation of all experimental results on a master curve. For finite-sized particles, this relation leads to Einstein's expression (Equation 3.38) with the excluded volume factor $\phi/(1 - c\phi)$ instead of ϕ. Hence the the viscosity of a suspension takes the following form:

$$\eta_r(\phi) = \left(1 - \frac{\phi}{1 - c\phi}\right)^{-2.5}.$$ (3.40)

where the constant c depends on the critical concentration at which the suspension loses its fluidity.

There are other models based on hydrodynamic interactions between the suspended particles. For example, Batchelor and Green gave an exact description of the viscosity of a semi-dilute suspension of hard spheres in the limit of vanishing shear rate [16]. This theory was extended to higher particle concentrations by Russel and Gast who took the mean thermodynamic force in a concentrated dispersion into account, and treated the hydrodynamic interactions at the pair level. Wagner and Russel calculated the viscosity as a function of volume fraction taking the hydrodynamic interaction between an arbitrary number of spheres into account [17].

Even though many models have been established, there is still a discrepancy between the data and the prediction, apparently in part due to the incomplete treatment

of the hydrodynamics, and in part due to the effect of inter-particle interactions and particle softness on the rheological properties.

Bibliography

[1] J. Keeler, Understanding NMR spectroscopy. John Wiley & Sons, 2011.

[2] M. H. Levitt, Spin dynamics: basics of nuclear magnetic resonance. John Wiley & Sons, 2001.

[3] P. T. Callaghan, Principles of nuclear magnetic resonance microscopy. Oxford University Press on Demand, 1993.

[4] P. T. Callaghan, Translational dynamics and magnetic resonance: principles of pulsed gradient spin echo NMR. Oxford University Press, 2011.

[5] W. S. Price, "Pulsed-field gradient nuclear magnetic resonance as a tool for studying translational diffusion: Part 1. basic theory," Concepts in Magnetic Resonance Part A, vol. 9, no. 5, pp. 299–336, 1997.

[6] W. S. Price, "Pulsed-field gradient nuclear magnetic resonance as a tool for studying translational diffusion: Part ii. experimental aspects," Concepts in Magnetic Resonance Part A, vol. 10, no. 4, pp. 197–237, 1998.

[7] M. Holz and H. Weingartner, "Calibration in accurate spin-echo self-diffusion measurements using 1h and less-common nuclei," Journal of Magnetic Resonance (1969), vol. 92, no. 1, pp. 115–125, 1991.

[8] R.-J. Roe, Methods of X-ray and neutron scattering in polymer science, vol. 739. Oxford University Press on Demand, 2000.

[9] D. I. Svergun and M. H. Koch, "Small-angle scattering studies of biological macro-molecules in solution," Reports on Progress in Physics, vol. 66, no. 10, p. 1735, 2003.

[10] B. Hammouda, "A tutorial on small-angle neutron scattering from polymers," Gaithersburg: National Institute of Standards and Technology, 1995.

[11] W. Brown and K. Mortensen, Scattering in polymeric and colloidal systems. CRC Press, 2000.

[12] L. Feigin, D. I. Svergun, et al., Structure analysis by small-angle X-ray and neutron scattering. Springer, 1987.

[13] J. S. Higgins and H. Benoît, Polymers and neutron scattering. Clarendon Press Oxford, 1994.

[14] M. Ballauff, "Analysis of polymer colloids by small-angle x-ray and neutron scattering: Contrast variation," Advanced Engineering Materials, vol. 13, no. 8, pp. 793–802, 2011.

[15] P. E. Rouse Jr, "A theory of the linear viscoelastic properties of dilute solutions of coiling polymers," The Journal of Chemical Physics, vol. 21, no. 7, pp. 1272–1280, 1953.

[16] G. Batchelor and J. Green, "The determination of the bulk stress in a suspension of spherical particles to order c2," Journal of Fluid Mechanics, vol. 56, no. 3, pp. 401–427, 1972.

[17] W. Russel and A. Gast, "Nonequilibrium statistical mechanics of concentrated colloidal dispersions: Hard spheres in weak flows," The Journal of Chemical Physics, vol. 84, no. 3, pp. 1815–1826, 1986.

[18] J. F. Brady and J. F. Morris, "Microstructure of strongly sheared suspensions and its impact on rheology and diffusion," Journal of Fluid Mechanics, vol. 348, pp. 103–139, 1997.

[19] I. M. Krieger and T. J. Dougherty, "A mechanism for non-newtonian flow in suspensions of rigid spheres," Transactions of the Society of Rheology, vol. 3, no. 1, pp. 137–152, 1959.

[20] J. Van der Werff and C. De Kruif, "Hard-sphere colloidal dispersions: The scaling of rheological properties with particle size, volume fraction, and shear rate," Journal of Rheology, vol. 33, no. 3, pp. 421–454, 1989.

[21] P. Segre and P. N. Pusey, "Dynamics and scaling in hard-sphere colloidal suspensions," Physica A: Statistical Mechanics and its Applications, vol. 235, no. 1-2, pp. 9–18, 1997.

[22] D. R. Foss and J. F. Brady, "Structure, diffusion and rheology of brownian suspensions by stokesian dynamics simulation," Journal of Fluid Mechanics, vol. 407, pp. 167–200, 2000.

[23] M. E. Woods and I. M. Krieger, "Rheological studies on dispersions of uniform colloidal spheres I. aqueous dispersions in steady shear flow," Journal of Colloid and Interface Science, vol. 34, no. 1, pp. 91–99, 1970.

[24] C. I. Mendoza and I. Santamaria-Holek, "The rheology of hard sphere suspensions at arbitrary volume fractions: An improved differential viscosity model," The Journal of Chemical Physics, vol. 130, no. 4, p. 044904, 2009.

Chapter 4 Synopsis

The work in this chapter measures polymer radius of gyration and self-diffusivity in the presence of macromolecular crowding in a polymer-colloid system, studied in tandem by pulsed-gradient-NMR and SANS, published in Physical Review Letters, vol. 118, p. 097801, 2017. SP carried out all NMR experiments. Neutron scattering experiments at Oak Ridge National Lab were carried out by SP and AY with the assistance of instrument scientists Lilin He and William A. Hamilton. SP and AY co-wrote the paper with input from all other authors.

Chapter 4

Combining Diffusion NMR and SANS Enables Precise Measurements of Polymer Chain Compression in a Crowded Environment

4.1 Abstract

The effect of particles on the behavior of polymers in solution is important in a number of important phenomena such as the effect of "crowding" proteins in cells, colloid-polymer mixtures, and nano-particle "fillers" in polymer solutions and melts. In this work, we study the effect of spherical inert nano-particles (which we refer to as "crowders") on the diffusion coefficient and radius of gyration of polymers in solution using pulsed-field-gradient NMR and small-angle neutron scattering, respectively. The diffusion coefficients exhibit a plateau below a characteristic polymer concentration, which we identify as the overlap threshold concentration $c^\star$. Above

$c^\star$, in a crossover region between the dilute and semi-dilute regimes, the (long-time) self-diffusion coefficients are found, universally, to decrease exponentially with polymer concentration at `all crowder packing fractions`, consistent with a structural basis for the long-time dynamics. The radius of gyration obtained from SANS in the crossover regime, changes linearly with increase in polymer concentration, and must be extrapolated to $c^\star$ (obtained from NMR) in order to obtain the radius of gyration of an individual polymer chain. When the polymer radius of gyration and crowder size are comparable the polymer size is very weakly affected by the presence of crowders, consistent with recent computer simulations. There is significant chain compression, however, when the crowder size is much smaller than the polymer radius gyration.

4.2 Introduction

The cell is a dense mixture of a number of different components including flexible (e.g. nucleic acids) and globular (e.g. proteins) macromolecules. There has been considerable recent interest on these "crowding" effects, i.e., the effect of inert macromolecules on the conformational properties of flexible molecules, and on the reaction between enzymes and substrates [1, 2]. Similar physics is expected in seemingly different problems such as colloid-polymer mixtures, where the addition of polymers can either stabilize or de-stabilize a colloidal dispersion [3–5], or nano-particle polymer composites [6] where the properties of the composite are sensitive to the nature of particle-polymer interactions. In this paper we are concerned with the effect of inert spherical particles which, following the biophysics community we refer to as "crowders", on the conformational properties and dynamics of polymers in solution.

Entropy, *via* the excluded volume effect, is an important ingredient in macromolecular crowding [1, 2]; although non-specific chemical interactions can also play

a role [7, 8]. From a colloid- and polymer-science perspective, a quantitative under-standing of the entropic contributions to crowding is a necessary pre-condition to an understanding of the broader crowding problem. Even in the absence of other inter-actions, the osmotic pressure of the crowder (radius R_c) can alter the size of a flexible macromolecule (radius of gyration R_g). Entropy can give rise to attractions due to depletion forces in both the "colloid limit" ($\lambda = R_g/R_c \ll 1$) [9] and the "protein limit" ($\lambda \gg 1$) [10]. In a simple model system, i.e., a colloid-polymer mixture con-sisting of a flexible polymer (i.e. macromolecule) and compact crowder [11, 12], one thus qualitatively expects a compression of polymer chains for large λ. On the other hand, a recent study suggests [13] that changing crowder size has a weak effect. It is safe to say that we still do not have a `quantitative` understanding of the differences between various simulations and experiments on the degree of compression.

We emphasize the distinction between the focus of this Letter, which is on the effect of spherical particles on the properties of the polymers, and on the focus of work in colloid-polymer mixtures [3–5] and polymer nano-composites [6], which is on the effect of polymers on the interaction between the particles. While polymers can induce either a net attraction or repulsion between particles (depending on the inter-actions and polymer concentration), the effect of particles on polymers is generally compressive when the particles are mobile, although the situation is more complicated if the positions of the particles is quenched [14, 15].

Computer simulations of crowding employing a variety of simulation methodologies [11, 12, 16–20] indicate that crowding decreases the radius of gyration for the unfolded state, but quantitatively the results are mixed even for simple systems: for example, a polymer-nanoparticle simulation with $\lambda \sim 1$ found that the polymer chains collapsed into a compact globular form with an overall decrease of R_g by 20% for $\Phi_c = 0.35$ [11], while another simulation found more modest chain compression of about 5% [12].

106

Intrinsically disordered proteins (IDP) are flexible biopolymers that should be influenced by crowding. Two small-angle neutron scattering (SANS) experiments found that IDP exhibited a varying degree of compression for similar λ: in one study a 13% size decrease resulted at a moderate crowder packing fraction $\Phi_c = 0.07$ [21] while in another only a 6% reduction of R_g was seen for $\Phi_c \sim 0.20$ [22]. Single-molecule FRET spectroscopy was used to quantify IDP size, using a linear polymer, polyethylene glycol (PEG), as a crowder. Here, IDP chain compression was observed to be stronger with larger crowders (i.e. with λ closer to 1) [23]; in other words, IDP in a polymer solution, i.e., in an extended polymeric crowder, does the opposite of a compact crowder.

In order to make quantitative the comparisons between simulation and experiment, a useful model system employs PEG as polymeric macromolecule and a polysucrose (Ficoll70) as nanoparticle spherical crowder [24]. For $\lambda \sim 1$ and $\Phi_c = 0.25$, the PEG was reported to undergo significant chain compression to 50% of its size in free solution, significantly more than simulations have found [11, 12]. In these SANS
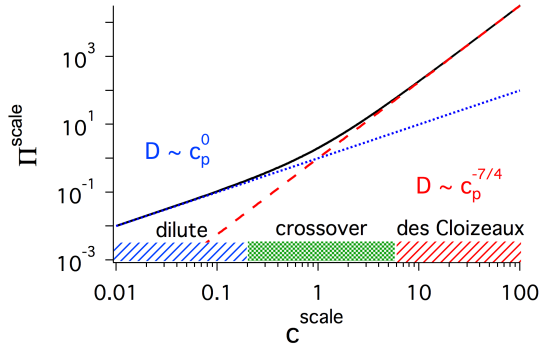
Figure 4.1: The osmotic pressure of pure PEG in water (no crowder) is well described by a phenomenological scaling form (solid black line, from Cohen et al. [25]). The solution is dilute when $c^{scale} \equiv c_p/c^{\#} \leqslant 0.2$, and in the semi-dilute entangled regime when $c^{scale} \geqslant 6$ (dashed red line): the crossover regime (green hashed region) is in between $(0.2 < c^{scale} < 6)$. The expected scaling of the self-diffusion coefficient in the dilute (blue hashed) and semi-dilute (red hashed) regimes [26] is $D \sim c_p^0$ and $D \sim c_p^{-7/4}$.

experiments [24], isolated chain behaviour was extracted from experiments at finite concentrations (0.004 g/cm^3 < c_p < 0.03 g/cm^3) by linear extrapolation to $c_p = 0$. Figure 4.1 demonstrates why such an experimental extrapolation is problematic. The osmotic pressure of neutral flexible polymer in solution may be written down as a phenomenological sum of scalings as a function of a scaled polymer concentration $c^{\#}$ [25]. The scaled osmotic pressure (details in Supplemental Material) obeys a universal behaviour as a function of the scaled concentration. In terms of scaled concentrations, the SANS experiments [24] were carried out in the range $0.2 < c^{\text{scale}} < 2$ in Figure 4.1, and are thus completely in the (green hashed) cross-over regime. It is thus wise to carry out experimental measurements to low enough concentrations in order to determine the overlap concentration $c^{\star}$ below which the polymer is dilute.

The strength of the current work is that we combine SANS measurements of polymer size with self-diffusion measurements via pulsed-field-gradient (PFG) NMR. The latter can be carried out to much lower polymer concentrations c_p than the SANS measurements, enabling clear estimates of $c^{\star}$ at different crowder packing fractions. We then use this to obtain reliable estimates of $R_g(0, \Phi_F)$ that we compare with simulations.

4.3   Polymer Self-Diffusion

PFG NMR diffusion measurements were carried out for aqueous PEG-Ficoll70 solutions in water prepared for PEG concentrations between 0.0003 and 0.03 g/cm^3 and Ficoll70 volume fractions Φ_F between 0 and 0.30. The details of the PFG NMR method were reviewed recently [27] and are summarized in the Supplemental Material. The dashed blue line in Figure 4.2(a) shows the diffusion coefficient of the last sample in a solution series that did not phase separate.
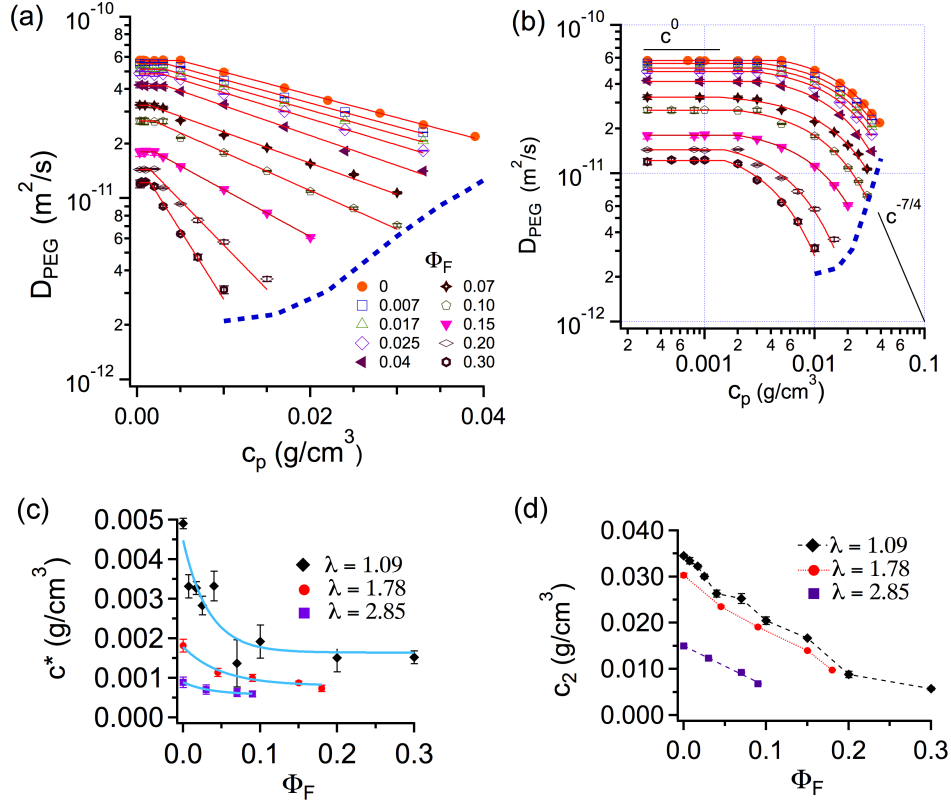
Figure 4.2: Self-diffusion: (a) Diffusion coefficient of PEG ($M_w = 20,000$) polymer in water as a function of polymer concentration c_p, in the absence of the crowder, Ficoll70, as well as for several Ficoll70 volume fractions Φ_F ($\lambda = R_g/R_c = 1.09$). A good fit to exponential behaviour is possible, `in all cases`, above a characteristic PEG concentration. $c^\star$, with an extrapolated value $D^\star$. Below this PEG concentration, a plateau is observed at $D(0, \Phi_F)$. (b) A log-log plot of D_{PEG} vs. c_p shows the plateau, and also that a power law cannot fit the data in the crossover regime. (c) Dependence of characteristic PEG concentration $c^\star$ as a function of Φ_F for 3 polymer molecular weights ($M_w = 20,000$, $M_w = 42,800$, and $M_w = 132,000$), corresponding to λ=1.09, 1.78 and 2.85. The solid blue curves may be treated as a guide to the eye. (d) From the phenomenological exponential decay in (a), a second characteristic concentration c_2 is obtained (for each Φ_F).

The PEG diffusion coefficient $D(c_p, \Phi_F)$, shown in Figure 4.2(a) with a logarithmic scale on the ordinate, is constant for low c_p. For all Φ_F, the self-diffusion coefficient decreases sharply above a (Φ_F dependent) characteristic concentration which we iden-

tify with $c^\star$. A piecewise fit of $D(c_p, \Phi_F)$ as a function of c_p,

$$D(c_p, \Phi_F) = D(0, \Phi_F), \qquad\qquad\qquad c_p \leqslant c^\star,$$

$$D(c_p, \Phi_F) = D^\star(\Phi_F) \exp(-c_p/c_2), \qquad\qquad c_p > c^\star, \qquad (4.1)$$

with exponential dependence above $c^\star$ and a plateau value below, provides a good fit to all the results. From this, we extract the dilute-limit diffusion coefficient $D(0, \Phi_F)$ as well as $c^\star$ and a second characteristic concentration c_2 for each Ficoll70 volume fraction Φ_F. $D^\star(\Phi_F) = D(0, \Phi_F) \exp(c^\star/c_2)$ is not fit, but evaluated from continuity at $c^\star$.

For $\Phi_F = 0$, referring to Figure 4.1, we expect $D(c_p, \Phi_F = 0) \sim c_p^0$ in the dilute (blue hashed) regime and $D \sim c_p^{-7/4}$ in the des Cloizeaux (also referred to as the semi-dilute entangled) regime [26]. As a higher-order correction, the friction coefficient is expected to show a linear dependence on polymer concentration due to the occasional interactions of polymer chains in the dilute regime, but this dependence has been seen to be very weak for short chain polymers [28]. The log-log representation in Figure 4.2(b) shows, first, that the plateau regime is well-defined in all cases, and second, that a power law cannot fit. While the presence of a plateau for all Φ_F is experimentally clear, the reason for it is not obvious: it signifies that a dilute polymer limit continues to exist in the limit of crowding!

Figure 4.2(c) shows that $c^\star$ is a decreasing function of Φ_F, not only for $M_w = 20,000$ ($\lambda = R_g/R_c = 1.09$), but also for two other longer polymers ($M_w = 42,800$ and $132,000$, see Supplemental Material, Figure 4.7), corresponding to $\lambda = 1.78$ and 2.85. For all polymer molecular weights and crowder volume fractions, there is a characteristic polymer concentration $c^\star$ below which the dynamics is `independent` of polymer concentration: the "polymer-dilute" regime. In addition, in all cases, $c^\star$

110

changes little beyond $\Phi_F \sim 0.1$, perhaps indicative of the onset of crowding.

From the exponential decay in Figure 4.2, we also obtain a second characteristic concentration c_2; e.g. for $\lambda = 1.09$, c_2 decreases from 0.035 to 0.005 g/cm^3 as Φ_F approaches the crowding limit (Figure 4.2(d)), which implies a 7-fold increase in "effective" PEG concentration for $\Phi_F = 0.3$. Physically, the value of c_2 appears consistent with the end of the crossover regime. The decrease in c_2 with Φ_F is consistent, too, with the decrease in the observed phase separation concentration as Φ_F increases (dashed blue line in Figure 4.2(a)).
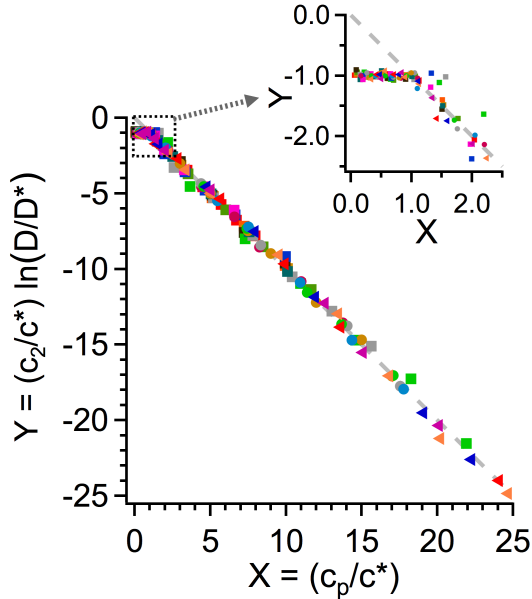
Figure 4.3: Universal behavior in the dynamics: Using the values $D^\star$, $c^\star$ and c_2 (all functions of only Φ_F) from each fit, `all` the diffusion results (as a function of c_p and Φ_F) are replotted in dimensionless form, $Y = (c_2/c^\star) \ln(D(c_p, \Phi_F)/D^\star)$ as a function of a scaled polymer concentration $X = c_p/c^\star$. For all 3 polymers, there is good collapse onto one master plot that shows a sharp transition at $X = 1$ (see inset) from a polymer-dilute plateau to an exponential concentration dependence of the diffusion coefficient.

Using the fitted $c^\star$ and c_2, as well as $D^\star(\Phi_F)$, we plot a scaled and dimensionless version of the self-diffusion coefficients $Y = (c_2/c^\star) \ln(D/D^\star)$ as a function of a scaled polymer concentration $X = c_p/c^\star$. From the model equation 5.3, $Y = -1$ for $X \leqslant 1$

111

and $Y = -X$ for $X > 1$. Figure 4.3 shows a master plot of all data for all three polymers: clearly, both the plateau below $c^\star$ and the exponential dependence above $c^\star$ are universally valid in the crossover regime at all λ and Φ_F.

Why is there no power-law scaling, even for pure polymer? Indeed, there is clear **experimental** indication (Callaghan and Pinder [28]) that power-law scaling fails for short-chain polymers. It is also possible (see Figure 2(b) and Supplemental Material, Figure 4.7) that there could be power-law scaling at large concentrations (the red-hashed regime in Figure 4.1) if this was accessible in the presence of crowding. Why the exponential dependence? Rosenfeld [29] and Dzugutov [30] have proposed an exponential relationship between atomic diffusion and the excess entropy S_2/k_B (in the 2-particle approximation); moreover, recent 2D simulations and colloids experiments [31] show that S_2/k_B is proportional to the colloid packing fraction for packing fractions less than 0.4. Due to the PEG's conformational degrees of freedom, it is inadvisable to invoke the 2-particle excess entropy; nevertheless it is reasonable to believe that the exponential dependence of the long-time self-diffusion coefficient at all Φ_F is purely structural in origin. To our knowledge, this is the first evidence of this in 3D.

4.4 Polymer Size

Next, we describe our SANS measurements for d-PEG-Ficoll70 solutions (carried out at HFIR at Oak Ridge National Laboratories on the GP-SANS instrument [32]) for PEG concentrations between 0.005 and 0.03 g/cm^3 and Ficoll70 volume fractions between 0 and 0.3. In contrast with PFG NMR, measurements at lower polymer concentrations were impractical due to long acquisition times. Polymer radius of gyration R_g was obtained in two ways: by a fit of the q-dependent scattering intensity to the
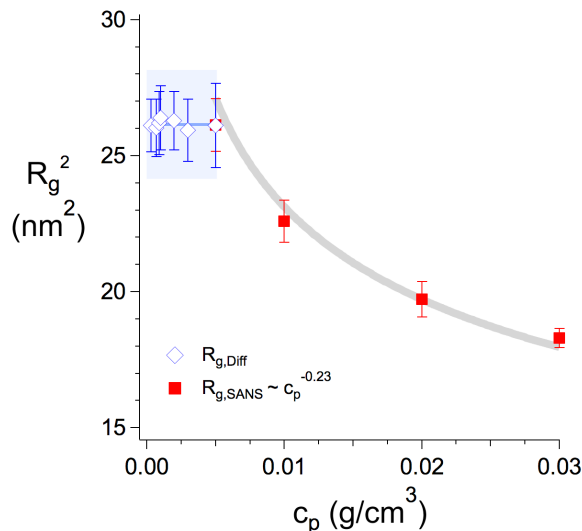
Figure 4.4: Diffusion *vs.* SANS: A comparison of R_g^2 from diffusion (blue, $c_p <$ 0.005g/cm^3) and SANS ($c_p > 0.005$g/cm^3) for PEG/water solution ($\Phi_F = 0$) confirms that the overlap concentration deduced from diffusion ($c_{Diff}^\star = 0.005$g/cm^3) is also meaningful as the thermodynamic overlap concentration $c^\star$.

Debye model as well as by fitting the low-q scattering intensity using the Guinier approximation. Both gave consistent R_g; an example is shown in the Supplemental Material, (Figure 4.6). Consistent with the previously reported SANS study of Le Coeur et al. [24], Figure 4.5(a)) shows that for pure PEG/water, there is a decrease in R_g with increasing PEG concentration, while at $\Phi_F = 0.1$, 0.15, 0.2 and 0.3, there is an `increase`. When each data set is fit to a straight line, a linear extrapolation at each Ficoll70 concentration suggests a convergence at non-zero c_p: around $c_p \sim 0.003$ g/cm^3. Quantitatively, the linear-extrapolated $R_g^\star$ in our work (denoted by a star symbol in Figure 4.5(a)) and those of Le Coeur et al. are in rough agreement for low Φ_F but deviate at $\Phi_F \geqslant 0.2$ (a comparison is shown in Supplemental Material, Figure 4.8). In both cases, linear extrapolation would imply a decrease in size of isolated polymer chains due to increasing Φ_F. The self-diffusion measurements, however, have demonstrated clearly that such an extrapolation from the crossover regime ($c_p > c^\star$) to the dilute (plateau) regime ($c_p < c^\star$) is not valid. We identify
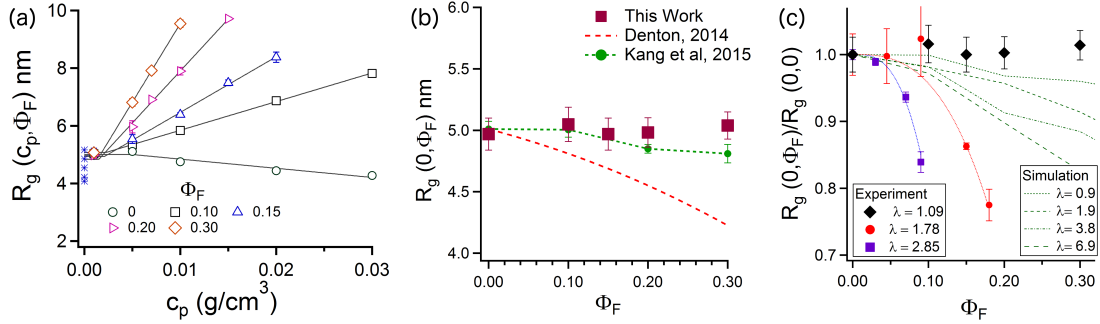
Figure 4.5: SANS: (a) $R_g(c_p, \Phi_F)$ vs. polymer concentration c_p for $\lambda = 1.09$. R_g is fit to Equation 4.2 assuming that the $c^\star$ is the same as for the diffusion experiment. The blue asterisks reflect the value that would be obtained by a naive extrapolation of R_g from the crossover regime. (b) The fit shows that $R_g(0, \Phi_F)$ in the "polymer-dilute" limit exhibits at most a weak dependence on Ficoll70 volume fraction Φ_F. (c) R_g dependence on packing fraction Φ_F for three polymer molecular weights, corresponding to $\lambda = 1.09$, 1.78 and 2.85 respectively. Results are compared with simulations from Kang et al. [12].

the $c^\star$ obtained from diffusion measurements with the thermodynamic overlap concentration. The validity of this identification is shown in Figure 4.4, which shows (for $\Phi_F = 0$) that R_g^2 from diffusion at lower polymer concentrations c_p and SANS mostly at higher c_p converge at a common $c^\star$; this is further discussed in Supplemental Material. Since the self-diffusion coefficient is unchanging in the polymer-dilute regime, R_g must therefore also be constant. Simulations [33] have also observed that the polymer $R_g(0,0)$ (no crowder) is essentially constant in the dilute limit.

In Figure 4.5(a), we plot R_g as a function of c_p for the different Φ_F, and employ a piecewise linear fit,

$$R_g(c_p, \Phi_F) = R_g(0, \Phi_F), \qquad\qquad\qquad c_p \leqslant c^\star,$$

$$R_g(c_p, \Phi_F) = R_g(0, \Phi_F) + m(\Phi_F)(c_p - c^\star), \qquad c_p > c^\star, \qquad (4.2)$$

with slope $m(\Phi_F)$, and a plateau value $R_g(0, \Phi_F)$ at and below $c_p = c^\star$, i.e., in the polymer-dilute limit. $c^\star$ itself is not a fit parameter, since we have it from the

diffusion measurements carried out to much lower c_p. In the absence of crowder, we can calculate the ratio $R_g(0,0)/R_H$. $R_g(0,0)$ is obtained from SANS and R_H from $D(0,0)$ and the Stokes-Einstein relation: we obtain a value $R_g(0,0)/R_H = 1.18 \pm 0.04$ consistent with renomalization group calculations [34].

The resulting $R_g(0, \Phi_F)$, for $\lambda = 1.09$, is shown in Figure 4.5(b). This R_g value is remarkably insensitive to the Ficoll70 volume fraction, and is quantitatively consistent with the simulations of Kang et al. [12], but not with the simulation and free volume theory of Denton and coworkers [11]. This quantitative agreement signals that Ficoll70 is an inert crowder in this experiment. Identifying macromolecule-crowder interactions is a key challenge in the study of macromolecular crowding, and this is therefore significant.

Interestingly, R_g in the dilute polymer limit is insensitive to Φ_F (Figure 4.5(b)) but the value of the overlap concentration $c^\star$ is not (Figure 4.2(c)). At first glance this might seem strange because $c^\star \sim N/R_g^3$ where N is the number of monomers. Note, however, that this relation comes from equating the "internal concentration" of the polymer (N/R_g^3) to the overall concentration of pure polymer solutions; at $c^\star$ different molecules being to touch each other on average. The presence of crowders decreases the volume available to polymers and therefore as Φ_F increases one expects $c^\star$ to decrease: the internal concentration is still N/R_g^3 but the relevant overall concentration is not the polymer concentration. Using an effective medium or mean-field model one would expect $c^\star$ to decrease linearly with Φ_F at low values of Φ_F. We do not have a good structural explanation for why $c^\star$ is insensitive to Φ_F for large values of Φ_F but note that at high Φ_F the system is closer to phase separation, and the crowder structure might be heterogeneous.

4.5 Varying the Macromolecule-Crowder Size Ratio

Next, we use the $c^\star$ obtained from our diffusion studies for the 2 polymers with larger molecular weights ($\lambda = 1.78$ and 2.85) in order to reanalyze pre-existing SANS results [35]. The overlap concentration obtained from diffusion measurements decreases substantially with increasing λ (Figure 4.2(b)). Figure 4.5(c) shows that the radius of gyration exhibits significant compression as a function of Φ_F. While the data at $\lambda \sim 1$ is close to those from simulation at a similar λ (Figure 4.5(c)), those for higher λ show much stronger compression than predicted by simulation.

4.6 Conclusion

We have obtained polymer size as well as diffusion coefficients of a polymer-crowder solution using SANS and PFG NMR in tandem, as a function of the crowder packing fraction Φ_F. The spectral selectivity of PFG NMR provides us with the sensitivity to measure diffusion coefficients at low polymer concentrations. These diffusion measurements unambiguously establish that there exists a "polymer-dilute" regime, $c^\star(\Phi_F)$, for each crowder packing fraction. One upshot of this study is that the polymer (polyethylene glycol), in the dilute limit, appears to be unchanged in hydrodynamic size even at relatively large crowder (Ficoll70) volume fractions for polymer-crowder size ratio $\lambda \sim 1$, as predicted in the simulation of Kang et al. [12].

In contrast with $\lambda = 1.09$, we find significant chain compression for isolated polymers when λ is 1.78 and 2.85 respectively. This is much more pronounced than the predictions from simulation; however, the 10 - 15% reduction in R_g at $\Phi_F = 0.1$ for $\lambda = 2.85$ are close in magnitude to experimental observations in IDPs [21].

4.7 Supplemental Material

4.7.1 Materials

For PFG NMR studies, we used three different molecular weights of polyethylene glycol (PEG, M_w= 22,000 with M_w/M_n = 1.10, M_w= 42,800 with M_w/M_n = 1.18, and M_w= 132,000 with M_w/M_n = 1.20), purchased from Polymer Source Inc. In SANS experiments, for contrast reasons, we used deuterated PEG ($M_w = 20,000$ with M_w/M_n = 1.15). Deuterated PEG was also obtained from Polymer Source Inc. Ficoll®PM 70 (referred to as Ficoll70 in the text) with average molecular weight of 70,000 (R_c = 4.6 nm) was purchased from Sigma Aldrich. Deuterium Oxide (D_2O, 99.9%) was purchased from Cambridge Isotope Laboratories, Inc.

4.7.2 Method: PFG NMR

For sample preparation, the desired volume fraction of Ficoll70 was dissolved in deionized H_2O. The solution was stirred for 10 hours. For each polymer concentration the appropriate mass of (undeuterated) polyethylene glycol (M_w= 22,000 with M_w/M_n = 1.10, M_w= 42,800 with M_w/M_n = 1.18, and M_w= 132,000 with M_w/M_n = 1.20) was added to 1 cm^3 of this solution. Each time, the solution was stirred five hours before experiment. Samples were then transferred to 5 mm outer diameter NMR tubes.

PFG NMR measurements were carried out on a Bruker Avance II 600 spectrometer equipped with a Bruker 14.08 T magnet and a Bruker diffusion Diff30 probe with a maximum Z gradient strength of 1800 G/cm (18 T/m). A stimulated echo pulse sequence was used to measure the diffusion coefficient. The gradient steps were varied and the signal for H_2O, PEG and Ficoll70 were collected as a function of gradient. The procedure for analysis of the results is described elsewhere in detail [27]. To avoid probe heating and to control sample temperature, the probe was cooled by flowing water and the temperature was maintained at 25°C.

4.7.3   Method: SANS
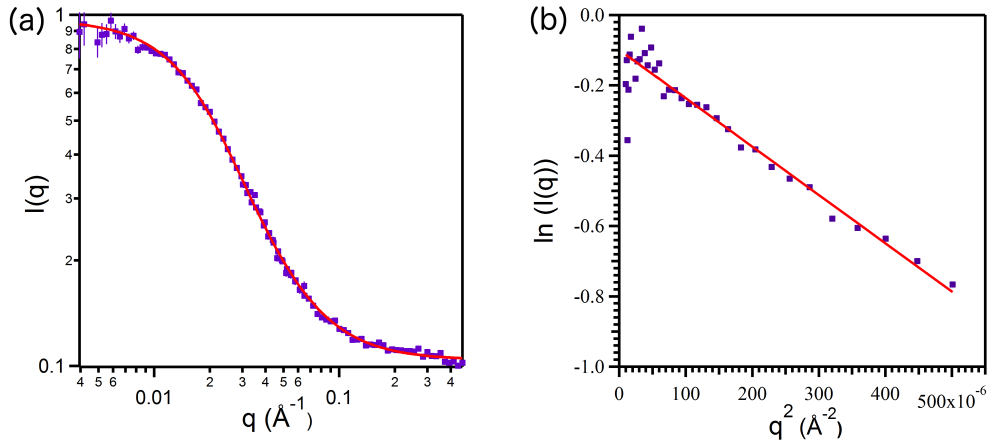
Figure 4.6: SANS scattering intensity $I(q)$ vs q for a PEG/Ficoll70 mixture with a c_p=0.05g/cm^3 and $\Phi_F = 0.3$. (a) Radius of gyration, R_g, of PEG, obtained from a fit to the Debye model is 6.9 ± 0.96 nm. (b) Guinier plot shows linearity of $\ln(I(q)$ as a function of q^2 for $qR \leqslant 0.89$, yielding R_g equals to 6.8 ± 1.9 nm.

Solution preparation was identical to that for PFG NMR, with the only difference that we used deuterated PEG (M_w= 20,000 with $M_w/M_n = 1.15$, from Polymer Source Inc.), and the solutions were made in 60%:40% H_2O:D_2O. In order to check for consistency between NMR and SANS, one set of PFG NMR measurements were carried out in 60% H_2O/40% D_2O solutions.

118

For sample preparation, the desired volume fraction of Ficoll70 was dissolved in a solution of H_2O and D_2O with 40% in D_2O. The solution was stirred for 10 hours. An appropriate mass of deuterated polyethylene glycol was added to 1 cm^3 of this solution. Each time, the solution was stirred five hours before experiment.

SANS measurements were conducted at Oak Ridge National Laboratory (ORNL) on the GP-SANS instrument [32]. Two sample to detector distances were used (1.7 m and 18.5 m) for a range of scattering vectors from 0.001 Å^{-1} to 0.5 Å^{-1}. The H_2O/D_2O composition points of minimum scattering intensity for Ficoll70 were determined using contrast variation Ficoll70 samples in solutions containing various H_2O/D_2O ratios. The ratio at which the scattering length densities of Ficoll70 and H_2O/D_2O were matched and therefore Ficoll70 did not contribute to the scattering signal was determined as $60 \pm 1\%$ H_2O and $40 \pm 1\%$ D_2O. Samples were loaded into quartz banjo cells mounted in temperature-controlled brass sample holders and a constant temperature of 25°C were maintained for all experiments. Scattering intensity profiles were analyzed using Igor Pro macros developed at NIST [36].

SANS data are presented as plots of the intensity of the scattered neutron beam, $I(q)$ as a function of scattering vector $q = (4\pi \sin\theta/\lambda)$, where θ is one half of the scattering angle and λ is the neutron wavelength. The intensity can be written as $I(q) = I_0 P(q)$, where $P(q)$ is the form factor which provides information on the size and shape of the scatterers. For a Gaussian polymer radius of gyration R_g, the shape factor is determined by the Debye formula, $P(q) = \frac{2}{x^2}\left(e^{-x} - 1 + x\right)$, where $x = q^2 R_g^2$ and the radius of gyration of the scattering object, R_g, can be extracted from fitting the plot of $I(q)$ vs q to the Debye model: this is shown in Figure 5.9(a) for a PEG/Ficoll70 mixture with a c_p=0.05g/cm^3 and $\Phi_F = 0.3$.

In the limit of very low angle or small q (the Guinier approximation) one can further write $P(q) = \exp\left(\frac{-q^2 R_g^2}{3}\right)$, where the radius of gyration of the scattering

object, R_g, can be extracted from the slope of a plot of $\ln(I(q))$ vs q^2. Such a fit is shown for a PEG/Ficoll70 mixture with a $c_p=0.05\text{g/cm}^3$ and $\Phi_F = 0.3$ in Figure 5.9(b).

4.7.4   Scaling Form for the Osmotic Pressure

We present a short discussion of polymer scaling following Cohen et al [25], which shows that the osmotic pressure of neutral flexible polymer in solution may be written down as a phenomenological sum of scalings as a function of the polymer concentration, enabling perfect collapse of two very dense datasets of rather dissimilar polymers (PEG in water and poly-α-methylstyrene in toluene). The concentration is scaled with respect to a crossover concentration $c^\# = \alpha^{-4/5}c^\star = \alpha^{-4/5}N^{-4/5}/\bar{V}$, where $c^\star$ is the overlap concentration, and for PEG, $\alpha = 0.49 \pm 0.01$, and the partial specific volume $\bar{V} = 0.825$ cm^3/g. For the polymer in the Le Coeur et al. SANS study [24] ($M_w = 18,000$), the degree of polymerization for PEG is $N = (M_w - M_{\text{end}})/M_m$; with end-group and monomer molecular weight $M_{\text{end}} = 18.02$ and $M_m = 44.05$ for PEG, $N = 408$. In terms of the normalized osmotic pressure $\tilde{\Pi} = \Pi/(RT/M_m\bar{V})$, the scaling form is

$$\Pi^{\text{scale}} = \tilde{\Pi}N^{9/5}\alpha^{4/5} = \left(\frac{c_p}{c^\#}\right) + \left(\frac{c_p}{c^\#}\right)^{9/4}. \tag{4.3}$$

In this form, crossover occurs at $c^{\text{scale}} \equiv c_p/c^\# = 1$. For PEG with molecular weight 18,000, the scaled concentration $c^\# = \alpha^{-4/5}N^{-4/5}/\bar{V} \sim 0.02$ g/cm^3, which is related by a constant factor of 1.77 to the overlap concentration $c^\star = 0.01$ g/cm^3. It can be seen that the expected dilute limit (look in the main manuscript for Figure 1, dotted blue line) occurs for $c^{\text{scale}} < 0.2$ (actual polymer concentrations $c_p < 0.002$ g/cm^3) and the semi-dilute regime (look in the main manuscript for Figure 1, dashed red line) for $c^{\text{scale}} > 6$ ($c_p > 0.1$ g/cm^3). The SANS experiments in this
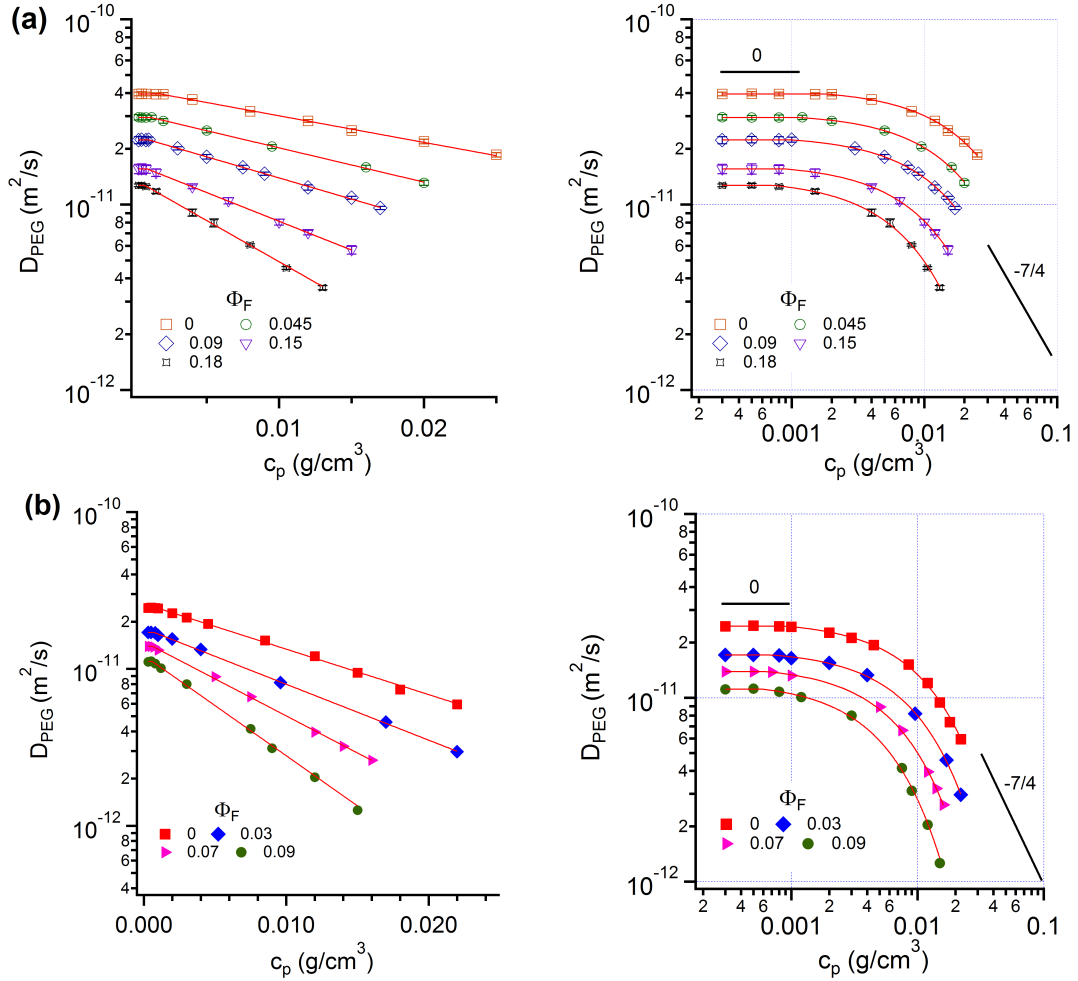
Figure 4.7: Diffusion coefficient shown (left) on log-linear and (right) on log-log scale for (a) PEG ($M_w = 42,800$) and (b) PEG ($M_w = 132,000$) in water as a function of polymer concentration c_p. Results are shown in the absence of the crowder, Ficoll70, as well as for several Ficoll70 volume fractions Φ_F. Similar to shorter-chain PEG ($M_w = 22,000$), a good fit to pure exponential behaviour is possible, `in all cases`, above a characteristic PEG concentration $c^\star$, with an extrapolated value $D^\star$. Below $c^\star$, a plateau is observed at $D(0, \Phi_F)$. A power-law fit (e.g., of $-7/4$) is not possible, but is a plausible asymptote.

work are carried out in the range 0.001 g/cm^3 < c_p < 0.03 g/cm^3, corresponding to $0.05 < c^{\text{scale}} < 1.5$. All except the $c_p = 0.001$ g/cm^3 experiment are thus completely in the cross-over regime. The PFG NMR results are carried out over a wider range, 0.0003 g/cm^3 < c_p < 0.04 g/cm^3, corresponding to $0.015 < c^{\text{scale}} < 2$.

4.7.5 Diffusion Measurements for Higher-Molecular-Weight Polymers

For completeness, we plot D_{PEG} vs. c_p for the two longer-chain (higher molecular-weight) polymers here. Figure 4.7 shows that the two higher-molecular-weight polyethylene glycol, $M_w = 42,800$ and $M_w = 132,000$, both exhibit a trend that is similar to that of the short PEG chain ($M_w = 22,000$). For low c_p, there is a plateau value for each crowder packing fraction, that indicates $D_{PEG} \sim c^0$. There is also a characteristic polymer concentration $c^\star$, above which the dynamics depends exponentially on polymer concentration. Callaghan et al. [28] had found power law scaling, $D_{PEG} \sim c^{-7/4}$, for longer polymers (but not for short-chain polymers). While our results are clearly not consistant with a power law, such a power law at higher concentrations (not physically accessible due to phase separation) cannot be ruled out.

The log-log plot shows that there is no power law scaling in the crossover regime, even for longer-chain polymers. While we do not observe the $(-7/4)$ power law reported by Callaghan et al. [28] for longer-chain polymers, it is likely because our measurements are **not** carried out in the semi-dilute (entangled) regime, but instead in the crossover regime. Indeed, even the experimental results shown by Callaghan et al.for shorter-chain polymers are consistent with an exponential concentration dependence.

4.7.6 Comparison of SANS Radius of Gyration Results

We compare the SANS results from this work with those from previous SANS experiments [24], for the PEG-Ficoll70 system with $\lambda \sim 1$. In plotting the data from Le Coeur et al., we have converted their mass fractions into volume fractions using the partial specific volume of Ficoll70, which is 0.67 cm^3/g [37]. The true $R_g(0, \Phi_F)$ is
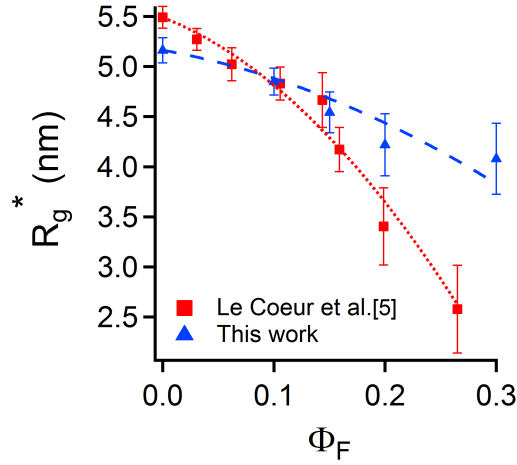
Figure 4.8: Comparison of $R_g^\star$, the radius of gyration, obtained by linear extrapolation to zero c_p from the crossover regime, as a function of Ficoll70 volume fraction Φ_F.

obtained by linear extrapolation to $c^\star$, as reported in the main manuscript. However, in order to aid comparison with the previously reported SANS results, we carry out a linear extrapolation to zero c_p of our results of $R_g(c_p, \Phi_F)$ vs c_p at each Φ_F, Our results show a weaker dependence on Φ_F as compared to the ones in the work of Ref. [24].

4.7.7 The Validity of Using Diffusion Measurements to Estimate the Overlap Concentration

It is not clear, a priori, if the concentration above which one observed the onset of hydrodynamic coupling has anything to do with the thermodynamic overlap concentration. For pure polymer, in the absence of crowder, one can obtain the hydrodynamic radius R_H from diffusion measurements and the Stokes-Einstein relation in the dilute regime for diffusion: $c_p \leqslant c_{Diff}^\star = 0.005 \text{g/cm}^3$. From R_H, we can obtain a radius of gyration $R_{g,Diff} = kR_H$ in the dilute limit ($k = 1.24$ from renormalization group calculations and 1.16 from past experiments; given the experimental uncertain-

ties we use $k = 1.2 \pm 0.04$ [34]). Using this, $R^2_{g,\text{Diff}}$ is plotted (Figure 4 in the main manuscript) for $c_p \leqslant c^\star_{\text{Diff}}$ (random errors indicated by the error bars and systematic uncertainties indicated by blue shading).

From the SANS measurements carried out above $c^\star$, at concentrations $0.005 \leqslant c_p \leqslant 0.03 \text{g/cm}^3$, we get the radius of gyration: $R_{g,\text{SANS}}$. Observing the decrease, we test the scaling expected for semi-dilute polymer solutions above $c^\star$: $R^2_g \sim c_p^{-0.23}$ [38]. While there are not many data points, it is to be noted (see Figure 4 in the main manuscript) that the fit is a one-parameter fit to the pre-factor of the -0.23 power law. It is thus a better fit than the piecewise linear fit employed in Figure 5 of the manuscript, but the resulting radius of gyration is not significantly different, given the uncertainties.

In Figure 4 (main manuscript), the self-diffusion and SANS measurements appear to converge at $c^\star_{\text{Diff}}$, suggesting that this concentration is also not far from the thermodynamic overlap concentration $c^\star$, within the uncertainties.

Bibliography

[1] S. B. Zimmerman and A. P. Minton, "Macromolecular crowding: biochemical, biophysical, and physiological consequences," Annual Review of Biophysics and Biomolecular Structure, vol. 22, no. 1, pp. 27–65, 1993.

[2] A. P. Minton, "The influence of macromolecular crowding and macromolecular confinement on biochemical reactions in physiological media," Journal of Biological Chemistry, vol. 276, p. 10577, 2001.

[3] A. P. Gast, C. K. Hall, and W. Russel Journal of Colloid and Interface Science, vol. 96, no. 1, pp. 251–267, 1983.

[4] R. Dickman and A. Yethiraj The Journal of Chemical Physics, vol. 100, no. 6, pp. 4683–4690, 1994.

[5] A. Yethiraj, C. K. Hall, and R. Dickman Journal of Colloid and Interface Science, vol. 151, no. 1, pp. 102–117, 1992.

[6] D. Banerjee and K. S. Schweizer, "Multi-scale entropic depletion phenomena in polymer liquids," The Journal of Chemical Physics, vol. 142, p. 214903, June 2015.

[7] H. X. Zhou, G. Rivas, and A. P. Minton, "Macromolecular crowding and confinement: biochemical, biophysical, and potential physiological consequences," Annual Review of Biophysics, vol. 37, pp. 375–397, 2008.

[8] M. Sarkar, A. E. Smith, and G. J. Pielak, "Impact of reconstituted cytosol on protein stability," Proceedings of the National Academy of Sciences of the United States of America, vol. 110, no. 48, pp. 19342–19347, 2013.

[9] S. Asakura and F. Oosawa, "On interaction between two bodies immersed in a solution of macromolecules.," Journal of Chemical Physics, vol. 22, p. 1255, 1954.

[10] K. J. Mutch, J. S. van Duijneveldt, and J. Eastoe, "Colloid–polymer mixtures in the protein limit," Soft Matter, vol. 3, no. 2, pp. 155–167, 2007.

[11] A. R. Denton, "Crowding in polymer–nanoparticle mixtures," International Review of Cell and Molecular Biology, vol. 307, p. 27, 2014.

[12] H. Kang, P. A. Pincus, C. Hyeon, and D. Thirumalai, "Effects of Macromolecular Crowding on the Collapse of Biopolymers," Physical Review Letters, vol. 114, p. 068303, Feb. 2015.

[13] K. A. Sharp, "Analysis of the size dependence of macromolecular crowding shows that smaller is better," Proceedings of the National Academy of Sciences, vol. 112, pp. 7990–7995, June 2015.

[14] R. W. Chang and A. Yethiraj Physical Review Letters, vol. 96, no. 10, p. 107802, 2006.

[15] B. J. Sung, R. Chang, and A. Yethiraj The Journal of Chemical Physics, vol. 130, no. 12, p. 124908, 2009.

[16] A. P. Minton, "Models for excluded volume interaction between an unfolded protein and rigid macromolecular cosolutes: macromolecular crowding and protein stability revisited," Biophysical Journal, vol. 88, p. 971, 2005.

[17] D. Tsao and N. V. Dokholyan, "Macromolecular crowding induces polypeptide compaction and decreases folding cooperativity," Physical Chemistry Chemical Physics, vol. 12, p. 3491, 2010.

[18] N. A. Denesyuk and D. Thirumalai, "Crowding promotes the switch from hairpin to pseudoknot conformation in human telomerase rna," Journal of the American Chemical Society, vol. 133, no. 31, p. 11858, 2011.

[19] S. Qin and H.-X. Zhou, "Effects of macromolecular crowding on the conformational ensembles of disordered proteins," Journal of Physical Chemistry Letters, vol. 4, p. 3429, 2013.

[20] N. A. Denesyuk and D. Thirumalai, "Entropic stabilization of the folded states of rna due to macromolecular crowding," Biophysical Reviews, vol. 5, no. 2, p. 225, 2013.

[21] D. Johansen, C. M. Jeffries, B. Hammouda, J. Trewhella, and D. P. Goldenberg, "Effects of macromolecular crowding on an intrinsically disordered protein characterized by small-angle neutron scattering with contrast matching," Biophysical Journal, vol. 100, p. 1120, 2011.

[22] D. P. Goldenberg and B. Argyle, "Minimal effects of macromolecular crowding on an intrinsically disordered protein: a small-angle neutron scattering study," Biophysical Journal, vol. 106, no. 4, pp. 905–914, 2014.

[23] A. Soranno, I. Koenig, M. B. Borgia, H. Hofmann, F. Zosel, D. Nettels, and B. Schuler, "Single-molecule spectroscopy reveals polymer effects of disordered proteins in crowded environments," Proceedings of the National Academy of Science, vol. 111, p. 4874, Apr. 2014.

[24] C. Le Coeur, B. Demé, and S. Longeville, "Compression of random coils due to macromolecular crowding," Physical Review E, vol. 79, p. 031910, Mar. 2009.

[25] J. A. Cohen, R. Podgornik, P. L. Hansen, and V. A. Parsegian, "A phenomenological one-parameter equation of state for osmotic pressures of peg and other neutral flexible polymers in good solvents," The Journal of Physical Chemistry B, vol. 113, no. 12, p. 3709, 2009.

[26] U. Zettl, S. T. Hoffmann, F. Koberling, G. Krausch, J. Enderlein, L. Harnau, and M. Ballauff, "Self-diffusion and cooperative diffusion in semidilute polymer solutions as measured by fluorescence correlation spectroscopy," Macromolecules, vol. 42, no. 24, pp. 9537–9547, 2009.

[27] S. Barhoum, S. Palit, and A. Yethiraj, "Diffusion NMR studies of macromolecular complex formation, crowding and confinement in soft materials," Progress in Nuclear Magnetic Resonance Spectroscopy, vol. 94-95, pp. 1–10, 2016.

[28] P. T. Callaghan and D. N. Pinder, "Self-diffusion of random-coil polystyrene determined by pulsed field gradient nuclear magnetic resonance: dependence on concentration and molar mass," Macromolecules, vol. 14, pp. 1334–1340, Sept. 1981.

[29] Y. Rosenfeld, "Relation between the transport coefficients and the internal entropy of simple systems," Physical Review A, vol. 15, pp. 2545–2549, June 1977.

[30] M. Dzugutov, "A universal scaling law for atomic diffusion in condensed matter," Nature, vol. 381, pp. 137–139, May 1996.

[31] A. L. Thorneywork, R. E. Rozas, R. P. Dullens, and J. Horbach, "Effect of hydrodynamic interactions on self-diffusion of quasi-two-dimensional colloidal hard spheres," Physical Review Letters, vol. 115, no. 26, p. 268301, 2015.

[32] G. D. Wignall, K. C. Littrell, W. T. Heller, Y. B. Melnichenko, K. M. Bailey, G. W. Lynn, D. A. Myles, V. S. Urban, M. V. Buchanan, D. L. Selby, and P. D. Butler, "The 40m general purpose small-angle neutron scattering instrument at Oak Ridge National Laboratory," Journal of Applied Crystallography, vol. 45, pp. 990–998, Oct 2012.

[33] W. Jiang, J. Huang, Y. Wang, and M. Laradji, "Hydrodynamic interaction in polymer solutions simulated with dissipative particle dynamics," The Journal of Chemical Physics, vol. 126, no. 4, p. 044901, 2007.

[34] Y. Oono, "Renormalization group theory of transport properties of polymer solutions. I. Dilute solutions," The Journal of Chemical Physics, vol. 78, no. 1, p. 520, 1983.

[35] C. Le Coeur, Influence de l'encombrement cytoplasmique sur la stabilité et la diffusion des protéines. Ph.D. thesis, L'université Pierre et Marie Curie, 2010.

[36] S. R. Kline, "Reduction and analysis of sans and usans data using igor pro," Journal of Applied Crystallography, vol. 39, pp. 895–900, 2006.

[37] P. N. Lavrenko, O. I. Mikriukova, and O. V. Okatova, "On the separation ability of various ficoll gradient solutions in zonal centrifugation," Analytical Biochemistry, vol. 166, pp. 287–297, Nov. 1987.

[38] M. Daoud, J. Cotton, B. Farnoux, G. Jannink, G. Sarma, H. Benoit, C. Duplessix, C. Picot, and P. De Gennes, "Solutions of flexible polymers. neutron experiments and interpretation," Macromolecules, vol. 8, no. 6, pp. 804–818, 1975.

Chapter 5 Synopsis

The tandem use of pulsed-gradient NMR (PFG NMR), SANS and rheology on near-identical systems is not very common. In this chapter, using these methods, we measure macromolecular size and self-diffusivity of an uncharged polymer in the "crowding regime" that corresponds to physiological concentrations. This work is published in The Journal of Chemical Physics, vol. 147, no. 11, p. 114902, 2017. SP carried out all the NMR experiments. Neutron scattering experiments at Oak Ridge National Lab were carried out by SP and AY with the assistance of instrument scientists Lilin He and William A. Hamilton. SP and AY co-wrote the paper with input from all other authors.

Erratum: In the published article, the cell lysate concentration is reported incorrectly as "13.7 g/cm^3". The corrected sentence is "The bacterial cell lysate solution is prepared at a mass fraction of 13.7%".

Chapter 5

The Effect of Crowder Charge in a Model Polymer–Colloid System for Macromolecular Crowding: Polymer Structure and Dynamics

5.1   Abstract

We have examined the effect of crowder particle charge on macromolecular structure, studied *via* small-angle neutron scattering (SANS), and translational dynamics, studied *via* pulsed-field gradient (PFG) NMR, in addition to bulk viscosity measurements, in a polymer macromolecule (polyethylene glycol, PEG)–nanoparticle crowder (polysucrose, Ficoll70) model system, in the case where polymer size and crowder size are comparable. While there are modest effects of crowder charge on polymer dynamics at relatively low packing fractions, there is only a tiny effect at the high packing fractions that represent the limit of molecular crowding. We find, *via* different measures of macromolecular mobility, that mobility of the flexible polymer in the

crowding limit is 10-100 times larger than that of the compact, spherical crowder in spite of their similar size, implying that the flexible polymer chain is able to squeeze through crowder interstices.

5.2 Introduction

The cell cytoplasm is crowded [1, 2] and macromolecular crowding affects molecular transport inside living cells profoundly, with a nanoparticle soup of crowders of different sizes, shapes, hydrophobicities, and charge occupying much of the intracellular space. While much study of macromolecular crowding has focused on the (entropic) volume exclusion effect [3–5], other (enthalpic or chemical) interactions are likely equally important: examples are charge, hydrophobicity, and hydrogen bonding [6–9]. In addition to these, solution micro-viscosity has also been identified to play a big role in macromolecular crowding [10–13]. As a result, depending on the environment, macromolecules can either compact into smaller localized regions (as happens with DNA in the presence of added polymer and salt solutions [14]) or adopt more complex conformations. Thus, a careful unraveling of the effect of intermolecular interactions on macromolecular conformations and dynamics in crowded environments have been recognized to be important [6].

The local environment plays an important role in macromolecular transport, and molecular shape has been suggested to be important: in particular Wang et al. [15] have shown that a disordered protein that diffuses slower than a globular protein in dilute conditions in fact exhibits 5-to-50-fold faster diffusion in a crowded environment, indicating shape-dependence of the macromolecular dynamics. Such a dramatic speed up could be important in phenomena from protein diffusion to cell signalling *in vivo* [16–18]. Addressing the question of macromolecular transport in a simple

colloid-polymer system would thus enable a deeper understanding of this enhanced dynamics.

A colloidal sphere in dilute solution obeys the Stokes-Einstein (S-E) relation, which relates the molecular self-diffusion coefficient to its hydrodynamic radius and the bulk solvent viscosity. A modified S-E relation, where the self-diffusivity of the macromolecule varies inversely as the bulk suspension viscosity, remains valid even in environments where it might be expected to break down: a recent example in soft colloids finds that it is valid, surprisingly, even close to the glass transition [19]. In crowded cellular environments, however, breakdown of the modified S-E relation has been inferred via the observation of multiple microscopic viscosities, distinct from the bulk suspension viscosity, in a single multi-component medium [10]. While the validity of an S-E like relationship between self-diffusivity, hydrodynamic size and viscosity is not obvious in a heterogeneous environment, the microscopic viscosities, or alternatively, diffusion timescales $\tau = R_H^2/D$, provide a useful way to report simultaneously the change in macromolecular size and the change in macromolecular dynamics.

Experimentally disentangling the effects of changes to macromolecular size, hydrodynamic coupling between macromolecules, and direct obstructed diffusion, which all occur simultaneously, is very challenging in nanoscale systems. In this study, we employ multiple experimental techniques to examine the effect of crowder particle charge on macromolecular structure and dynamics. Via pulsed-field-gradient (PFG) NMR, we can obtain self-diffusivities of each chemical species in a simple model system consisting of non-ionic polymer (polyethylene glycol, PEG) and a compact, spherical polysucrose crowder (Ficoll70), both of roughly the same size, with the ratio of polymer radius of gyration R_g and crowder radius R, i.e $\lambda = R_g/R \sim 1$.

The Ficoll70 diffusivity exhibits complex behaviour that we examine in a related work, see companion paper [20]. We obtain polymer size (R_g) in very similar samples,

apart from using deuterated PEG and contrast-matched Ficoll70 solutions, by small-angle neutron scattering (SANS). The independent access to diffusivity and size allows us to examine other contributions to macromolecular dynamics: e.g., in this system the polymer and crowder have very similar hydrodynamic sizes, but the polymer is a Gaussian chain while the crowder is compact spherical object.

In a recent study [21], we have shown that the uncharged Ficoll70 crowder induces little compression in the polymer, consistent with a simulation that assumes hard-sphere crowders [22]; this suggests that Ficoll70 does not associate, and is thus an inert crowder, at least with respect to PEG. However, it is unclear whether an uncharged, hard-sphere crowder is relevant to real biophysical situations, such as macromolecular crowding in living cells where the macromolecules are charged entities, such as proteins and nucleic acids.

This work examines the biophysical relevance of the polysucrose crowder. We introduce charge on the crowder as a way of softening the crowder-crowder interactions *via* electrostatic repulsions, and compare polymer diffusion in charged crowders with those in bacterial cell lysates.

5.3   Background

The spectral sensitivity of PFG NMR allows one to obtain dynamics of multiple species in complex systems simultaneously [23–26]. Using this spectral selectivity, we measure the self-diffusion coefficient (of both polymer and crowder) as a function of polymer concentration (c_p) and crowder packing fraction (Φ_F). For a polymer diffusing in a colloidal suspension, one may write a modified Stokes-Einstein equation,

$$D(c_p, \Phi_F) = \frac{k_B T}{6\pi\eta_\mu(c_p, \Phi_F)R_H(c_p, \Phi_F)} \tag{5.1}$$

where $R_H(c_p, \Phi_F)$ is the hydrodynamic radius and $\eta_\mu(c_p, \Phi_F)$ is an effective microscopic viscosity that is not necessarily the same as the suspension viscosity $\eta(\Phi_F)$ (due to the low polymer concentrations, the suspension viscosity depends only on the crowder packing fraction). $\eta_\mu(c_p, \Phi_F)$ is sensitive to hydrodynamic coupling and is thus a function of c_p and Φ_F: in dilute aqueous solution ($c_p \to 0$ and $\Phi_F \to 0$), $\eta_\mu(c_p, \Phi_F)/\eta_0 \to 1$, where η_0 is the viscosity of water.

While writing D in a S-E like form is valid in the Zimm regime where $D \sim 1/R_H$, deviation of $\eta_\mu(c_p, \Phi_F)$ from the bulk suspension viscosity $\eta_{Bulk}(\Phi_F)$ signals breakdown of the S-E relation. One can, regardless, always define a characteristic timescale for a macromolecule to diffuse its own size

$$\tau = R_H{}^2/D \tag{5.2}$$

which also accounts for both size and diffusivity changes.

Using SANS, we measure the radius of gyration, R_g, of the deuterated polymer as a function of c_p and Φ_F in an environment where the crowder contrast has been minimized (see Materials and Methods for details). The ratio $\alpha = R_g/R_H$, is known to be constant in the dilute regime, and its value varies from 1.2 to 1.5 as one goes from a Gaussian to a self-avoiding polymer chain. The c_p and Φ_F dependence of α is thus relatively weak, and we can replace $R_H \approx R_g/\alpha$ in Equation 5.1 and obtain the microscopic viscosity $\eta_\mu(c_p, \Phi_F)$ of the polymer chain: generically a decreasing function of both c_p and Φ_F. Measuring all the above quantities would allow a complete comparison to any theoretical model for the hydrodynamics of macromolecular crowding.

In previous work on polymer dynamics in the presence of uncharged crowders [21], we discovered that the polymer self-diffusion coefficient exhibits a sharp change from

a polymer-concentration independent dilute regime (with a plateau value $D(0, \Phi_F)$) to a crossover regime above a concentration $c^\star$ where $D(c_p, \Phi_F)$ could be fitted with an exponential dependence on c_p. This is expressed in the piecewise function

$$D(c_p, \Phi_F) = D(0, \Phi_F), \qquad\qquad\qquad c_p \leqslant c^\star,$$
$$D(c_p, \Phi_F) = D^\star(\Phi_F) \exp(-c_p/c_2), \qquad\qquad c_p > c^\star. \qquad (5.3)$$

For each Ficoll70 packing fraction Φ_F, we obtain, in addition to $D(0, \Phi_F)$ and $c^\star$, a second characteristic concentration c_2 that describes the exponential dependence above $c^\star$. The polymer radius of gyration R_g, measured *via* SANS, was constant below a characteristic concentration $c^\star$–we refer to this value as $R_g(0, \Phi_F)$–and showing a linear dependence on polymer concentration above $c^\star$. The existence of a common polymer overlap concentration $c^\star$ to the diffusivity and size is unsurprising in pure polymer solution, but the surprise was that this persists even for finite crowder packing fraction Φ_F, and even into the crowding limit.

5.4   Materials and Methods

For PFG NMR studies, we used PEG (M_w= 22000 with $M_w/M_n = 1.10$), purchased from Polymer Source Inc. In SANS experiments, for contrast reasons, we used deuterated PEG ($M_w = 20000$ with $M_w/M_n = 1.15$). Deuterated PEG was also obtained from Polymer Source Inc. Ficoll®PM 70 with average molecular weight of 70000 ($R_c = 4.5 - 5.5$ nm) was purchased from Sigma Aldrich. Deuterium oxide (D_2O, 99.9%) was purchased from Cambridge Isotope Laboratories, Inc. Charged Ficoll (Ficoll CM 70) was a carboxymethylated derivative of Ficoll PM70, made as described in reference [27]. It was a gift from Dr. William H. Fissell, and was used as received after having been neutralized and dialyzed against distilled water for 4 days.
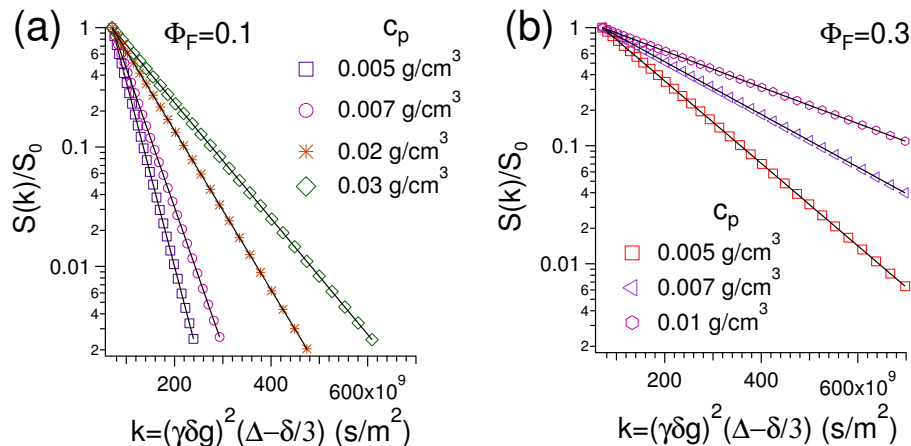
Figure 5.1: The attenuation of the signal $S(k)/S(0)$ on a log scale versus the gradient strength parameter $k = (\gamma \delta g)^2 (\Delta - \delta/3)$ for PEG/charged Ficoll70 mixture of different PEG concentration and (a) $\Phi_F = 0.1$ and (b) $\Phi_F = 0.3$. All signal attenuation curves exhibits simple mono-exponential behaviour.

5.4.1 PFG NMR

For all samples the desired packing fraction of Ficoll70 was dissolved in deionized H_2O. For charged Ficoll70 solutions, the conductivity was controlled, using KCl, to a value of ≈ 1 mS/cm in order to ensure a consistent Debye-Hückel screening length for all samples. The solution was stirred for 10 hours. Appropriate concentration of (undeuterated) polyethylene glycol ($M_w = 22000$ with $M_w/M_n = 1.10$) was added to $1 \, cm^3$ of this solution. Each time, the solution was stirred five hours before experiment.

Samples were then transferred to 5 mm outer diameter NMR tubes. To avoid probe heating and to control sample temperature, the probe was cooled by flowing water and the temperature was maintained at 25°C.

PFG NMR measurements were carried out on a Bruker Avance II 600 spectrometer equipped with a Bruker 14.08 T magnet and a Bruker diffusion Diff30 probe with a maximum Z gradient strength of 1800 G/cm (18 T/m). A stimulated echo pulse sequence was used to measure the diffusion coefficient. The gradient steps were varied and the signal for H_2O, PEG and Ficoll70 were collected as a function of gradient.

137
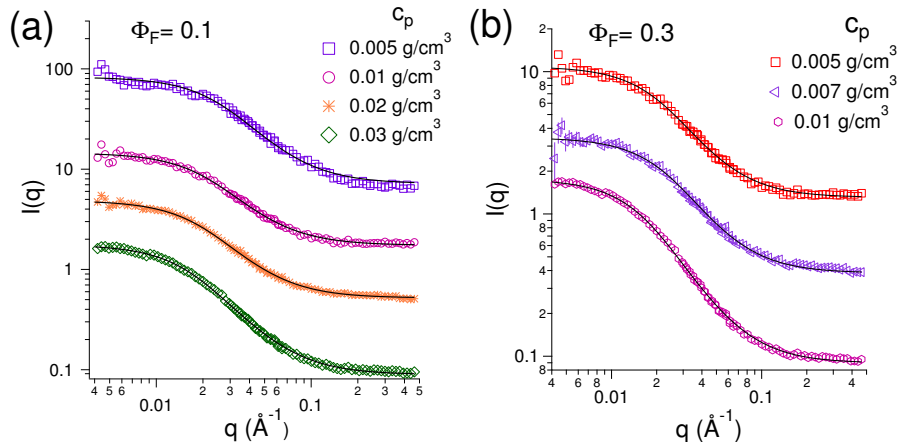
Figure 5.2: SANS scattering intensity I(q) vs q for PEG/charged Ficoll70 mixture of different PEG concentration: (a) $\Phi_F = 0.1$ and (b)$\Phi_F = 0.3$. In all cases radius of gyration, R_g, of PEG, obtained from a fit to the Debye model.

The procedure for analysis of the results is described elsewhere in detail [26]. In Figure 5.1 the attenuation in PEG signal intensities were observed as a function of k. All plots were linear for all Φ_F used in this study, which indicates that PEGs have a single diffusion component.

5.4.2 SANS

The solution preparation was identical to that for PFG NMR, with the only difference that the PEG (M_w= 20000 with $M_w/M_n = 1.15$, from Polymer Source Inc.) was deuterated and the solutions were made in 60%:40% H_2O:D_2O. In order to check for consistency between NMR and SANS, one set of PFG NMR measurements were carried out in 60% H_2O/40% D_2O solutions.

For sample preparation, the desired packing fraction of Ficoll70 was dissolved in a solution of H_2O and D_2O with 40% in D_2O. The solution was stirred for 10 hours. Appropriate concentration of deuterated polyethylene glycol was added to 1 cm^3 of this solution. Each time, the solution was stirred five hours before experiment.

SANS measurements were performed at General Purpose (GP-SANS) CG-2 instru-

ment at Oak Ridge National Laboratory [28]. The scattered neutrons from samples were detected using a 1 m^2 area detector at two sample to detector distances of 1.7 and 18.5 m with a detector offset of 40 cm and a neutron wavelength of $\lambda = 6$Å. This resulted in the overall q ($q = 4\pi \sin\Theta/\lambda$, where Θ is one half of the scattering angle) range of from 0.004Å^{-1} to 0.5Å^{-1}. Due to the coherent-scattering length differences [29] between hydrogen (-3.741×10^{-15} m) and deuterium (6.671×10^{-15} m), the neutron-scattering length density difference between fully hydrogenated Ficoll70 and the deuterated PEG is very significant. The H_2O/D_2O composition points of minimum scattering intensity for Ficoll70 were determined using contrast variation Ficoll70 samples in solutions containing various H_2O/D_2O ratios. The ratio at which the scattering length densities of Ficoll70 and H_2O/D_2O were matched and therefore Ficoll70 did not contribute to the scattering signal was determined as $(60 \pm 1)\%$ H_2O and $(40 \pm 1)\%$ D_2O. Therefore only the PEG contribution appears as a q dependent intensity in the spectra regardless of Ficoll70 packing fractions.

Samples were loaded into quartz banjo cells with a thickness of 2.0 mm mounted in temperature-controlled brass sample holders and a constant temperature of 25°C were maintained for all experiments. Data were corrected for background and empty cell contributions, and normalized to an absolute intensity using standard procedure. Scattering intensity profiles were analyzed using Igor Pro macros developed at NIST [30]. The measured neutron scattering intensity in dilute solutions per unit volume is expressed as [31]

$$I(q) = \frac{c_p \, (\Delta\rho)^2 \, \nu_p^2}{N_a} \, M_w \, P(q) \left(1 - 2A_2 \, c_p \, M_w \right), \tag{5.4}$$

where c_p is the concentration in g/cm^3, M_w is the weight average molecular weight, $\Delta\rho$ is the scattering length density difference between the polymer and solvent, ν_p is the volume of one polymer, and N_a is the Avogadro number. A_2 is the second

virial coefficient that characterizes the average interactions between two polymers in infinitely dilute solutions, $P(q)$ is the form factor, and $P(q = 0) = 1$.

The intensity as shown in Equation 5.4 can be written as $I(q) = I_0 P(q)$, where $P(q)$ is the form factor which provides information on the size and shape of the scatterers. As shown in Figure 5.2, SANS data are presented as plots of the intensity of the scattered neutron beam, $I(q)$ as a function of scattering vector, q. For a Gaussian polymer radius of gyration R_g, the shape factor is determined by the Debye formula [32], $P(q) = \frac{2}{x^2} \left(e^{-x} - 1 + x \right)$, where $x = q^2 R_g^2$ and the radius of gyration of the scattering object, R_g, can be extracted from fitting the plot of $I(q)$ vs q to the Debye model.

5.4.3 Zeta Potential

The Zeta potential (ζ) and electrophoretic mobility of Ficoll70 solutions were measured by a Zetasizer Nano Z system (Malvern Instruments Ltd, Malvern, United Kingdom). The dimensionless Zeta potential $\Psi = \zeta e / k_B T = 1.1 \pm 0.2$ and 0.21 ± 0.02 for charged and uncharged Ficoll70 respectively. The solutions of charged Ficoll70 were all prepared with added salt in order to keep the conductivity at 1 mS/cm, resulting in a Debye-Hückel screening length $\kappa^{-1} = 3.2 \pm 0.5$ nm. This corresponds to a $\kappa R_c \sim 1.4$. Given the value of the dimensionless Zeta potential Ψ and κR_c, i.e., both of order unity, electrostatics should clearly be important, but not overwhelmingly so.

5.4.4 Bulk Viscosity Measurement

Experiments were performed on an Anton Paar Physica MCR 301 rheometer, where the cone-plate measuring system was used to extract the flow curves. The cone-plate geometry has a diameter of 50 mm and cone angle of 0.5^0. The flow curves experiments were carried out with shear rate varying from 0.001 to 150 s^{-1}.
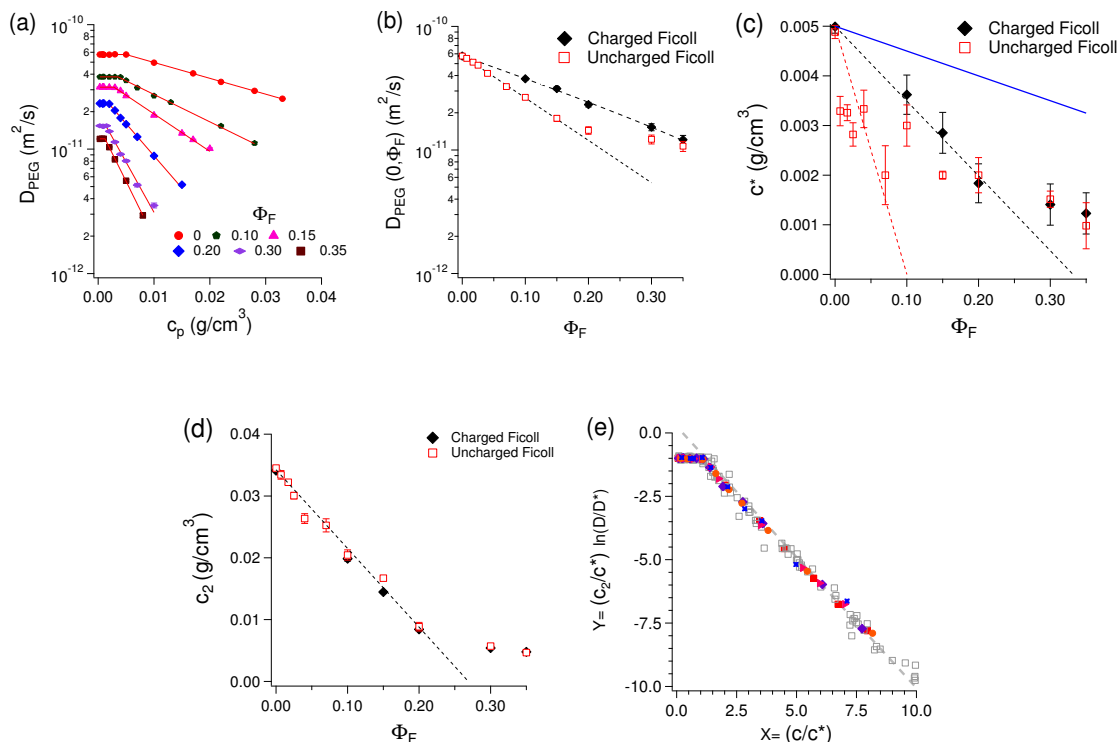
Figure 5.3: Polymer dynamics in charged crowder: (a) Self-diffusion coefficient of PEG ($M_w = 20,000$) polymer in water as a function of polymer concentration c_p, and for several packing fractions Φ_F of charged (color, filled symbols) Ficoll70. Each dependency is fit to Equation 5.3 to obtain $D(0, \Phi_F)$, and the characteristic concentrations $c^\star$ and c_2. (b) For each Ficoll70 packing fraction, a plateau in the self-diffusion coefficient, $D(0, \Phi_F)$, obtained *via* fits to the concentration dependence, is observed below a characteristic PEG concentration $c^\star$, indicating the existence of a "polymer-dilute" regime at all Φ_F. (c) For `every` crowder packing fraction, there is a characteristic PEG concentration $c^\star$, below which the diffusion coefficient is unchanging. The value of $c^\star$ shows a very different dependence on packing fraction Φ_F for uncharged and charged Ficoll70; however, it converges near $\Phi_F = 0.3$. (d) Above $c^\star$, the diffusion coefficient shows an exponential decrease; yield a `second` characteristic PEG concentration c_2 as a function of uncharged and charged Ficoll70 packing fractions Φ_F. (e) Using the values $D^\star$, $c^\star$ and c_2, from each fit, `all` the diffusion results (as a function of c_p and Φ_F) are replotted in dimensionless form, $Y = (c_2/c^\star) \ln(D(c_p, \Phi_F)/D^\star)$ as a function of a scaled polymer concentration $X = c_p/c^\star$. There is good collapse onto one master plot that shows a sharp transition at $X = 1$ from a polymer-dilute plateau to an exponential concentration dependence of the diffusion coefficient. The results for uncharged Ficoll70 are shown in gray.

5.5 Polymer Self-Diffusivity in Charged Crowder

Figure 5.3(a) shows plots of the diffusion coefficient of PEG in aqueous suspension of charged polysucrose (charged Ficoll70, colored symbols represents diffusivities for different Ficoll70 packing fraction Φ_F). In all cases, below a critical concentration $c^\star$ which is a function of Φ_F, there is a plateau in the diffusion coefficient. This plateau is indication of the approach (with decreasing concentration) to a "polymer-dilute" regime.

Qualitatively, the existence of a polymer-dilute regime for all Φ_F for PEG self-diffusion suggests that charged Ficoll70 crowders behave similarly to uncharged crowder (which were studied previously [21]). Figure 5.3(b) shows $D_{PEG}(0, \Phi_F)$ as a function of Φ_F, obtained from fits of the results in Figure 5.3(a) to Equation 5.3. $D_{PEG}(0, \Phi_F)$ in both curves is of course identical for $\Phi_F = 0$ because there is no crowder. For $\Phi_F > 0$, $D(0, \Phi_F)$ decreases for both charged and uncharged crowder; however, the difference in $D(0, \Phi_F)$ between charged and uncharged crowder increases to a maximum near $\Phi_F = 0.15$, and then the two curves converge. The mechanisms responsible for the difference in polymer dynamics between charged and uncharged Ficoll70 is uncertain. This cannot be explained by a simple volume exclusion model of crowding. It is feasible that the structure of the cluster and void space of charged and uncharged Ficoll70 are different. A more detailed understanding of Ficoll70 structure and inter-particle interactions will be necessary in order to understand this difference; computer simulations with charged and uncharged crowders as a function of the packing fraction would be useful in this regard.

We see in Figure 5.3(c) that the critical concentration $c^\star$ is very sensitive to electrostatics: as Φ_F is increased, $c^\star$ is initially 0.005 g/cm^3 at $\Phi_F = 0$, but decreases much less rapidly for charged Ficoll70 than for uncharged Ficoll70.

However, the two decreases converge for larger Φ_F, with $c^\star \sim 0.015 \mathrm{g/cm^3}$ for $\Phi_F = 0.3$. For polymer solutions, one normally expects $c^\star(0) \sim N/R_g^3$ (where N is the number of monomers). Therefore, in the presence of crowder, if one expects the "internal concentration" $c^\star(0)$ to be constant, then we would expect $c^\star(\Phi_F) = c^\star(0)(1 - \Phi_F)$ (solid blue line in Figure 5.3(c)). Instead one sees roughly linear behavior at low Φ_F with $c^\star(\Phi_F) = c^\star(0)(1 - \beta_1 \Phi_F)$, where $\beta_1 = 10 \pm 3$ for uncharged Ficoll70 and 3.0 ± 0.2 for anionic Ficoll70. This suggests that even if the picture above is correct, the effective free volume is reduced much more than expected but this reduction is much smaller for anionic Ficoll70, where one would expect less self-clustering.

Above $c^\star$, the story is different. The exponential dependence of $D(c_p, \Phi_F)$ on polymer concentration c_p yields a `second` characteristic concentration, c_2, shown in Figure 5.3(d), which decreases from $c_2 = 0.0345 \mathrm{g/cm^3}$ to $c_2 = 0.005 \mathrm{g/cm^3}$: note that this behavior is identical for charged and uncharged crowder, suggesting that while the diffusivity at infinite polymer dilution depends on crowder charge, its dependence on polymer concentration is independent of crowder charge. We can use the fitted results to recast all the measurements of polymer self-diffusion in charged Ficoll70 (colored symbols), as well as the previous results with uncharged Ficoll70 [21] (gray symbols), plotting a dimensionless quantity $Y = (c_2/c^\star) \ln(D(c_p, \Phi_F)/D^\star)$ as a function of a scaled polymer concentration $X = c_p/c^\star$. Agreement with Equation 5.3 would require $Y = -1$ when $X \leqslant 1$, and $Y = -X$ otherwise. Clearly, all the results (for polymer dynamics in both charged and uncharged crowder) obey this behaviour. Moreover, the sharp transition in the dynamics that separates the dilute and the crossover regime is valid, regardless of the degrees of crowding, or the crowder charge.

As discussed in the Background, and in previous work in the presence of uncharged crowder [21], such an exponential relationship could be consistent with theory for atomic liquids where an exponential relationship between atomic diffusion and the

excess entropy is predicted [33,34]. Such a remarkably universal exponential dependence at all Φ_F, and independent of crowder charge, suggests that above $c^\star$, only structure is important, and colloidal hydrodynamics is unimportant. One should also be able to examine the Φ_F dependence of c_2 further. Up to $\Phi_F = 0.2$, one can fit the dependence to $c_2(\Phi_F) = c_2(0)(1 - \beta_2\Phi_F)$, with $\beta_2 = 3.8 \pm 0.2$ for both uncharged and anionic Ficoll70. This suggests, interestingly, that the effective free volume above the polymer overlap concentration is insensitive to crowder structure, and decreases proportionally with increasing Φ_F. The reason for the observed value of β_1 and β_2 is not known. However, it is noted that there is a relationship between c_2 and the polymer concentration, c_{ps}, where phase separation is first observed in the PEG-Ficoll system (see Supplementary Materials). Indeed the ratio c_2/c_{ps}, at a given Φ_F, depends neither on polymer molecular weight M_w nor on crowder charge, suggesting that it is related in some way to polymer-polymer association.
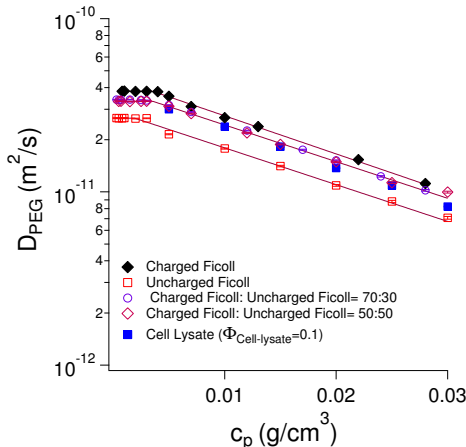
Figure 5.4: Comparison of polymer diffusion in bacterial cell lysate and Ficoll70: The self-diffusion coefficient of PEG in bacterial cell lysate lies in between the corresponding values in charged and uncharged crowder(at comparable packing fractions, $\Phi = 0.1$): a good match is found to a 50:50 mixture of charged and uncharged crowder.

Whether high concentrations of inert synthetic crowders can faithfully mimic cytosolic conditions is an important question. One could ask "What is the relevance

to cellular environments of the dynamics of a polymer chain in charged and uncharged colloidal crowder?" The cellular environment is composed of macromolecules of different shape and size (entropy), with, additionally, electrostastic and chemical interactions of all macromolecules (enthalpy). Bacterial cell lysates are physiologically more relevant and more closely mimic the soft interactions of the cytosol, but it was unclear a priori if macromolecular dynamics is even qualitatively similar to model crowders. What the above shows is that macromolecular dynamics in cell lysates is indeed, qualitatively and at least semi-quantitatively, comparable to model crowders.

In Figure 5.4, we make a first attempt at addressing this question by comparing polymer self-diffusion coefficients at $\Phi_F = 0.1$, for PEG (as a function of polymer concentration c_p) for charged Ficoll70, uncharged Ficoll70, and a bacterial cell lysate solution. The bacterial cell lysate solution is prepared at a mass fraction of 13.7% which corresponds to a packing fraction of 0.1, chosen because there is much more quantitative difference in diffusivities between uncharged and charged crowders at $\Phi_F = 0.1$ than in the crowding limit. The polymer self-diffusivity in the bacterial cell lysate shows the same exponential dependence as a function of polymer concentration. In addition, the polymer self-diffusivity in bacterial cell lysate lies in between the charged and uncharged crowder. Indeed, shown in Figure 5.4, PEG diffusion in bacterial cell lysate is quantitatively close to PEG diffusion in 70:30 and 50:50 mixtures of charged and uncharged Ficoll70. This suggests that once one controls for crowder charge, macromolecular diffusion in an artificial crowder might be meaningful in biologically relevant systems.
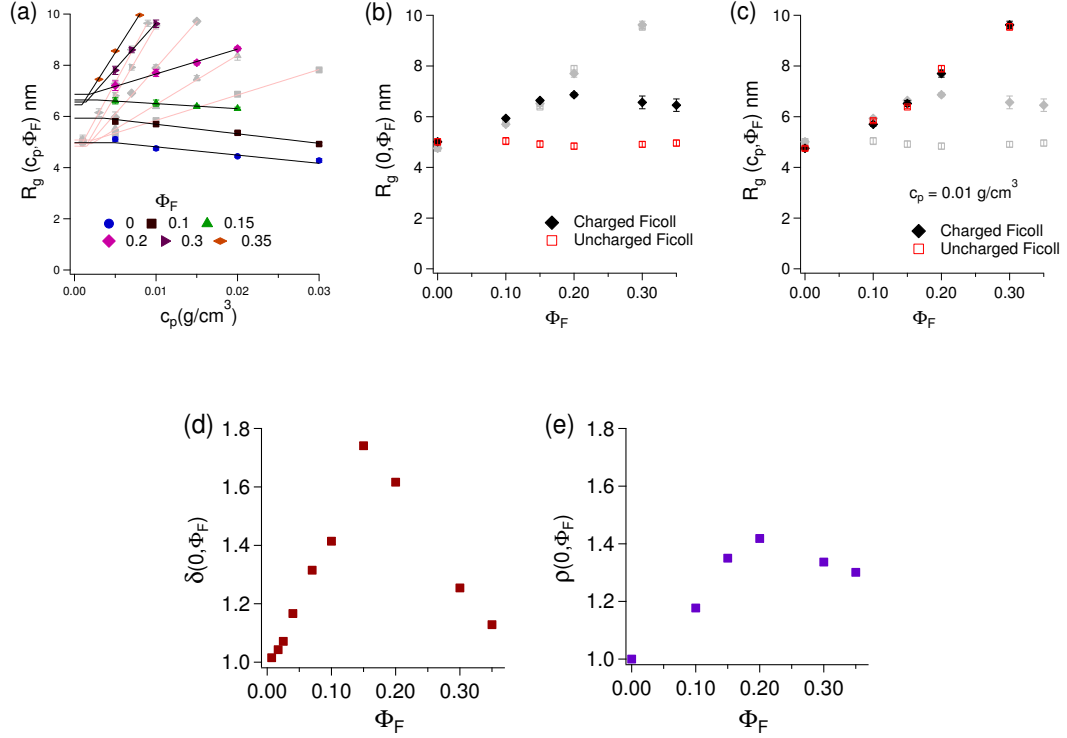
Figure 5.5: The effect of crowder charge: (a) Radius of gyration $R_g(c_p, \Phi_F)$ in the crossover regime shows a linear dependence with c_p at each Φ_F. In gray symbols, $R_g(c_p, \Phi_F)$ for uncharged crowders (data from Palit et al. [21]) is shown for comparison. A linear extrapolation of the radius of gyration $R_g(c_p, \Phi_F)$ to $c^\star$ yields the polymer size in the polymer-dilute regime: $R_g(0, \Phi_F)$. (b) A linear extrapolation of the radius of gyration $R_g(c_p, \Phi_F)$ to $c^\star$ yields the polymer size in the polymer-dilute regime: $R_g(0, \Phi_F)$. (c) Above $c^\star$, the radius of gyration $R_g(c_p, \Phi_F)$ for uncharged crowder is plotted as a function of Φ_F. In (b) and (c), the c_p=0.01 g/cm³ and $c_p = 0$ results are shown in gray to aid comparison. (d) Ratio of self-diffusion coefficients $\delta(0, \Phi_F) = D^{charged}(0, \Phi_F)/D^{uncharged}(0, \Phi_F)$ has a maximum value of 1.75 at $\Phi_F = 0.15$ and then decreases to ~ 1.1 at $\Phi_F = 0.35$ (e) The ratio of $R_g(0, \Phi_F)$ of PEG in charged and uncharged Ficoll70, $\rho(0, \Phi_F) = R_g^{charged}(0, \Phi_F)/R_g^{uncharged}(0, \Phi_F)$ increases to a maximum value of 1.4, and then decreases to 1.3 in the crowding limit, i.e. at $\Phi_F = 0.35$.

5.6 Quantifying the Effect of Crowder Charge

In Figure 5.5(a), the polymer radius of gyration R_g, obtained from SANS, is plotted as a function of c_p, for different charged Ficoll70 packing fractions Φ_F. For each Φ_F, the polymer-concentration dependence is linear, and actually shows an `increase`

above $\Phi_F = 0.15$. The expansion in polymer size is most likely due to the formation of clusters of polymer, a phenomenon that is known for aqueous solution of PEG without crowder [35].

One can linearly extrapolate the radius of gyration $R_g(c_p, \Phi_F)$ (in Figure 5.5(a)) to $c^\star$. This yields (Figure 5.5(b)) the polymer size in the polymer-dilute regime: $R_g(0, \Phi_F)$. For uncharged crowder results from previous work [21] show a weak dependence on Φ_F. For charged crowders, there is a $\approx 30 - 40\%$ increase in R_g in both cases, which is significant. Above the overlap concentration, $c^\star$, the radius of gyration $R_g(c_p, \Phi_F)$, for $c_p = 0.01$ g/cm^3, is plotted as a function of Φ_F (Figure 5.5(c)). Here there is a steady and significant increase of R_g, attributed to polymer-polymer clustering. This increase is insensitive to the crowder charge.

5.7   Enhanced Micro-Scale Mobilities

Figure 5.5(d) shows the Φ_F dependence of the `ratio` $\rho(0, \Phi_F) = \frac{R_g^{charged}(0, \Phi_F)}{R_g^{uncharged}(0, \Phi_F)}$, which compares polymer size in charged versus uncharged Ficoll70. PEG `in the dilute limit` is relatively unchanged when the crowder is uncharged. There is evidence from previous work [21] that the size of isolated PEG chains in PEG-Ficoll70 suspensions agrees quantitatively with simulation, indicating that Ficoll70 is an inert crowder for PEG. For charged crowder, however, PEG expands by a factor of 1.35 at $\Phi_F = 0.15$ and 1.3 at $\Phi_F = 0.35$.

From Figure 5.3, we can also calculate the ratio $\delta = D^{charged}/D^{uncharged}$ (in the polymer-dilute limit) as a function of Φ_F, shown in Figure 5.5(e), which increases from unity at $\Phi_F = 0$ to 1.75 at $\Phi_F = 0.15$, but decreases back to 1.1 at $\Phi_F = 0.35$. Hence, in the crowding limit, the polymer dynamics is nearly unaffected by crowder charge in spite of the size (shown in Figure 5.5(d)) increasing modestly by 30% of its value in

dilute solution. Above the polymer concentration `c⋆`, how polymer chains `interact with other polymer chains` is also not sensitive to the charge of the crowder, and exhibits universal exponential behaviour. This is seen both in the structure (Figure 5.5(c), colored symbols) and in the dynamics (Figure 5.3(e)). A precise understanding of the behavior in this regime would require unraveling polymer-polymer clustering and the structure of the free volume, and will be the focus of future work where we can examine the structure of the crowder via SANS.

We do not know the reason either for the expansion of R_g in the presence of charged crowder or the enhancement of self-diffusion in the presence of charged crowder. Polymer-crowder interaction is unlikely since PEG is uncharged, so it must be indirectly be the result of Ficoll-Ficoll interactions. While examining Ficoll70 structure via SANS requires extensive experiments with deuterated Ficoll, crowder dynamics is accessible directly from PFG NMR experiments, and is discussed in a companion paper [20].

We are finally ready to examine the macromolecular environments for polymer and crowder, by looking at the relative polymer self-diffusivities, timescales and microviscosities.

Using Equation 5.1, and the diffusion coefficient $D(0,0)$ (from PFG NMR) and $R_g(0,0)$ (from SANS) of an isolated polymer in the presence of crowder, and setting $\eta_\mu(0,0) \equiv \eta_0$, we obtain $R_g/R_H = 1.18$. This may be compared with the theoretical and experimental values of 1.24 and 1.16 respectively (for a θ solvent) [36], as tabulated by Oono & Kohmoto [36].

In a companion work [20], we find that Ficoll70 solutions form clusters above a characteristic Φ_F (0.05 for uncharged and 0.1 for charged Ficoll70). In addition, we obtain the the fraction of cluster $f_{cluster}$ and the fraction of monomer $1 - f_{cluster}$, for a range of Φ_F, and the diffusivities $D_{cluster}$ and $D_{monomer}$ of both cluster and

monomer species.
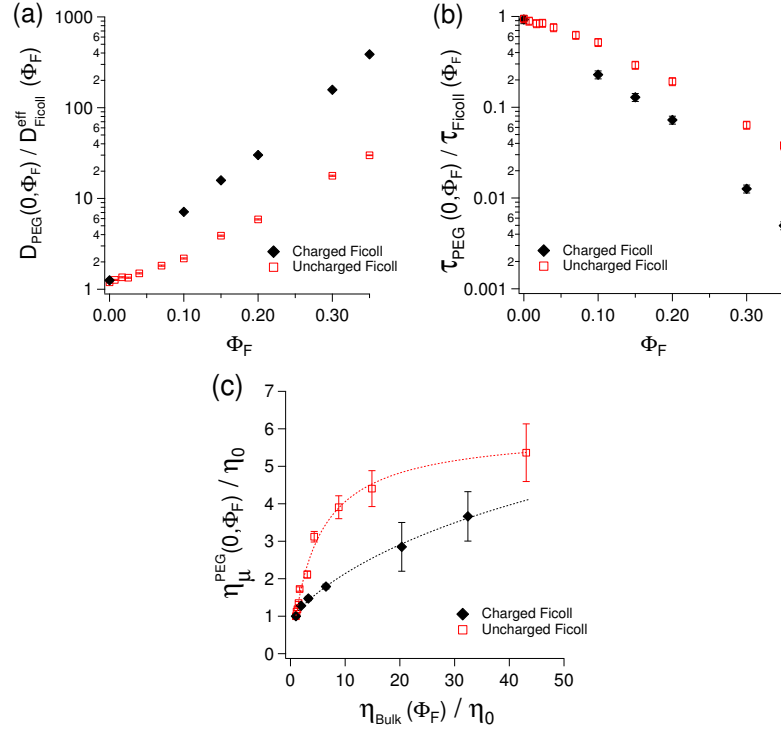
Figure 5.6: Enhanced micro-scale mobilities: (a) Comparison of the diffusivity ratio $D_{PEG}(0, \Phi_F)/D_{Ficoll}^{eff}$ for charged and uncharged Ficoll70 as a function of Φ_F shows a significant (10 - 100 fold) enhancement of the polymer (PEG) dynamics, relative to the compact (Ficoll70) crowder. (b) The ratio of characteristic time scale τ_{PEG}/τ_{Ficoll} concomitantly `decreases` by 1 - 2 orders of magnitude as a function of Φ_F. (c) Relative micro-scale viscosity of PEG, $\eta_\mu^{PEG}(0, \Phi_F)/\eta_0$, obtained from $D(0, \Phi_F)$ and $R_g(0, \Phi_F)$ as a function of uncharged and charged relative Ficoll70 viscosity η_{Bulk}/η_0. The broken curves may be treated as a guide to the eye.

Figure 5.6(a) shows the ratio of polymer to crowder self-diffusivity, D_{PEG}/D_{Ficoll}^{eff}, as a function of Φ_F. Since the Ficoll70 forms clusters, D_{Ficoll}^{eff} is obtained by a weighted average $D_{Ficoll}^{eff} = f_{cluster}D_{cluster} + (1 - f_{cluster})D_{monomer}$. All the quantities in this weighted average are measured (Figure 6.3 (a) and (b) and Figure 6.4 in the companion article [20]). PEG dynamics is enhanced sharply (by a factor of 10 - 100 with respect to Ficoll70 dynamics, in uncharged and charged crowder) as Φ_F approached the crowding limit. Denoting τ as the timescale for a macromolecule to

diffuse its own radius (Equation 5.2), the ratio τ_{PEG}/τ_{Ficoll} (Figure 5.6(b)) shows a concomitant decrease by 1 - 2 orders of magnitude with increasing Φ_F.

Finally, we plot the `relative` polymer microscale viscosity $\eta_\mu(0, \Phi)/\eta_0$ against its bulk equivalent $\eta(\Phi)/\eta_0$ (Figure 5.6(d)), using the Ficoll70 suspension viscosity measured using a cone-plate rheometer to obtain both the viscosity of water η_0, and the viscosity of the suspension as a function of Φ, $\eta(\Phi)$ (see Materials and Methods). At $\Phi_F = 0$, $\eta_\mu^{PEG}(0, \Phi_F)/\eta_0 = 1$. As Φ_F increases to $\Phi_F = 0.3$, $\eta_\mu^{PEG}(0, \Phi_F)/\eta_0$ increases only by a factor of ≈ 4, while $\eta_{Bulk}(\Phi_F)/\eta_0$ increases by a factor of 30-40; the micro-viscosity is thus approximately 10 times smaller than the bulk viscosity in the limit of crowding.

Fluorescence correlation spectroscopy (FCS) has been used to obtain the micro-viscosity `via` diffusion of a probe molecule (protein) in in the presence of a macro-molecular crowder (Ficoll70). According to these studies, depending on the size of the protein, the micro-viscosity of Ficoll70 is found 4-7 times larger than the viscosity of pure water [11, 37]. Other studies have also reported diffusion coefficients of proteins that suggest a difference between micro-viscosity and bulk viscosity [38, 39]. Rashid et al. [13] have reported that the micro-viscosity experienced by a fluorescent probe molecule in Ficoll70 is up to 8 times smaller than the bulk viscosity in the limit of crowding, roughly consistent with our findings.

By all measures, two macromolecules of `similar nanometric size` have very different mobilities. The flexible linear polymer, which has access to chainlike dynamical modes (such as reptation) is 10 to 100 times more mobile than the more compact crowder.

5.8   Discussion and Conclusion

In this work, we examine the role of crowder charge on macromolecular dynamics, with no other parameters changing.

Charge has a weak effect on crowding: At $\Phi_F = 0.35$, crowder charge only barely affects dynamics. The ratio $\delta(0, \Phi_F)$ of polymer diffusivity (for charged versus uncharged crowder), while large at $\Phi_F = 0.15$, is only ~ 1.1 in the crowding limit.

Ficoll70 has biophysical relevance in crowding: While Ficoll70 is thus non-ideal, its use as a crowder might nevertheless have biophysical relevance. The concentration dependence of polymer self-diffusivity in charged and uncharged Ficoll70 appear to be upper and lower bounds for the self-diffusivity in a more biologically relevant cell lysate solution at the same concentration! We find that we can construct an artificial crowder that mimics polymer dynamics in cell lysate by making an appropriate mixture of charged and uncharged crowder.

Flexibility aids macromolecular transport: A comparison between the polymer self-diffusivity and diffusion timescales with that of the compact crowder (and a polymer micro-viscosity with the bulk suspension viscosity) suggests that the microscopic dynamics of the polymer is significantly enhanced in the crowding limit relative to the expectations for a homogenous solution of the same bulk viscosity. In particular, the polymer (PEG) has a mobility that is 10 - 100 times larger than the compact, Ficoll70 crowder. Wang et al. [15] have indicated that macromolecular shape might be a key parameter in protein diffusion in the presence of macromolecular crowding. The current work implies, in a simple model system for crowding, that `flexibility` (i.e., the changing transient shape) makes a diffusing chainlike macromolecule very different from a diffusing colloid and affects its mobility profoundly.

It is, of course, possible that it is not the polymer dynamics that is enhanced,

but that the crowder hydrodynamic size is enhanced due to factors such as hydrogen bonding. Having measured Ficoll70 cluster size (Figure 6.3 (c) in the companion article [20], $R_{cluster}/R_{monomer} < 3$), this would account for only a small enhancement, not the 10 -100 fold enhancement seen.

The long time goal of tandem PFG NMR and SANS studies of crowding is to study charged polymers or proteins in charged crowder. In addition, examining the role of flexibility (e.g. comparing disordered proteins with globular proteins) is of interest. The current work represents an important step towards that goal.

5.9   Supplementary Material

The Supplementary Material contains physical interpretation of second characteristic concentration (c_2), a plot of the optimum contrast matching to wipe out the contribution of Ficoll70 in scattering intensity, and comparison of R_g obtained from Debye and Guinier fits.
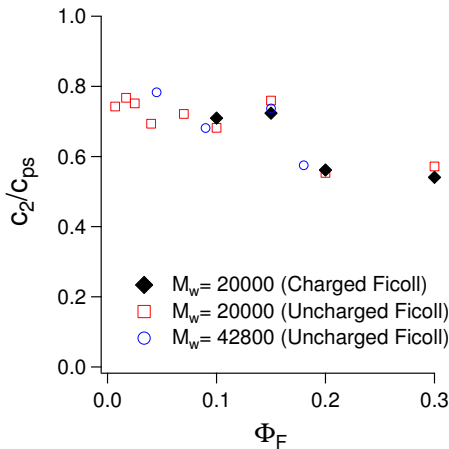
Figure 5.7: Ratio of c_2 and c_{ps}: The ratio of second characteristic concentration to phase separtion concention (c_2/c_{ps}) as a function of Φ_F. This ratio at a given Φ_F is the same for all samples.

5.10 Acknowledgments

5.11 Supplemental Material

5.11.1 Physical Interpretation of c_2

In this work, diffusion measurements were carried out for PEG-Ficoll70 from a low polymer concentration, c_p, in the dilute limit, to a value close to the limit of phase separation (c_{ps}). In all cases, the second characteristic concentration, c_2, shows a linear decrease with increasing Φ_F for three independent samples of PEG (Mw= 20000 (in charged and uncharged Ficoll70, and Mw= 42800 (in uncharged Ficoll70)). The qualitative behavior of c_{ps} correlates strongly with c_2 that decreases rapidly with Ficoll70 packing fraction. Figure 5.7 suggests the ratio, c_2/c_{ps}, at a given Φ_F is independent of polymer molecular weight and crowder charge–suggesting that c_2 is indeed an indicator of the threshold of polymer stability in the PEG-Ficoll70 solution.

5.11.2 Contrast Variation Study

In this paper small-angle neutron scattering (SANS) with D_2O based contrast matching was used to examine the effects of a crowder (Ficoll70) on the structure of a chain like molecule (PEG). In these experiments, in order to obtain the scattering signal, deuterium labeled PEG was used. The scattering contrast between the solvent and unlabeled Ficoll70 was eliminated by adjusting the D_2O fraction (Φ_{D_2O}) of the solvent.
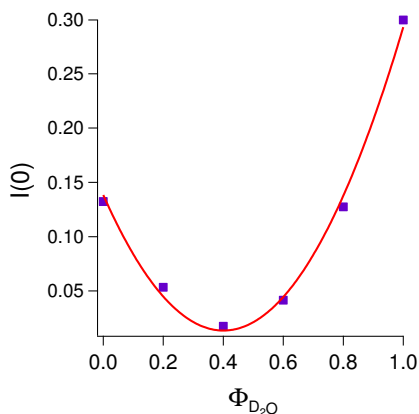
Figure 5.8: Contast matching: The H_2O/D_2O composition points of minimum scattering intensity for Ficoll70 were determined using contrast variation Ficoll70 samples in solutions containing various H_2O/D_2O ratios. The ratio at which the scattering length densities of Ficoll70 and H_2O/D_2O were matched and therefore Ficoll70 did not contribute to the scattering signal was determined as $(60\pm1)\%$ H_2O and $(40\pm1)\%$ D_2O.

The Φ_{D_2O} for optimum contrast matching was determined by recording scattering profiles for Ficoll70 ($\Phi_F = 0.3$) dissolved in solutions containing 0, 20, 40, 60, 80, and 100% D_2O. The scattering intensity was plotted as a function of Φ_{D_2O} (Figure 5.8) from which the minimum scattering was determined using a quadratic funtion. In this work we used $(60 \pm 1)\%$ H_2O and $(40 \pm 1)\%$ D_2O to wipe out the contribution Ficoll70 selectively in scattering intensity.
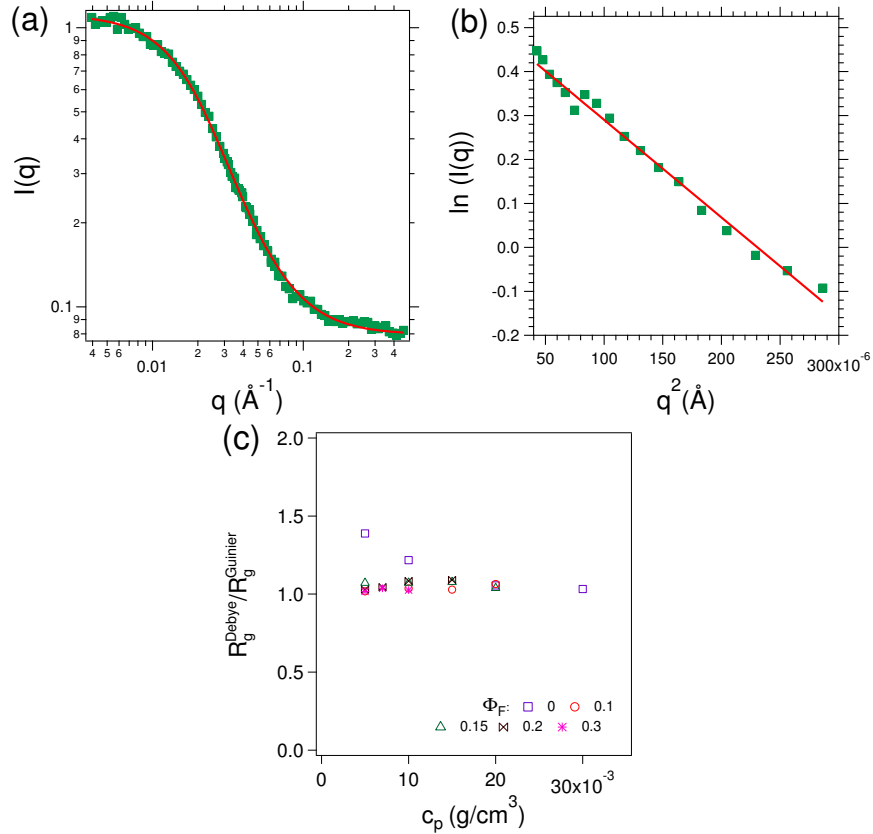
Figure 5.9: Debye and Guinier fits: SANS scattering intensity I(q) vs q for a PEG/charged Ficoll70 mixture with a c_p=0.015g/cm^3 and $\Phi_F = 0.2$. (a) Radius of gyration, R_g, of PEG, obtained from a fit to the Debye model is 8.1 ± 0.08 nm. (b) Guinier plot shows linearity of $\ln(I(q))$ as a function of q^2 for $qR_g \leqslant 0.92$, yielding R_g equals to 8.2 ± 1.9 nm. (c) Comparison of R_g obtained from Debye and Guinier fits.

5.11.3 Debye and Guinier Plot

The radius of gyration of the scattering object, R_g, can be extracted from fitting the plot of I(q) vs q to the Debye model: this is shown in Figure 5.9(a) for a PEG/charged Ficoll70 mixture with a c_p= 0.05 g/cm^3 and $\Phi_F = 0.3$.

In the limit of very low angle or small q, the scattering pattern of an isolated polymer can approximated by a Gaussian, the width of which is proportional to the square of the radius of gyration of the particle: this is known as the Guinier relation. This is valid when $qR_g < 1$. Using the Guinier approximation one can

155

further write [40]:

$$I(q) = \exp \left(\frac{-q^2 R_g{}^2}{3} \right) \tag{5.5}$$

In this work, a linearized representation was used, by plotting $\ln(I(q))$ vs q^2–known as Guinier plot–where a simple linear regression yields the radius of gyration from the slope. Such a fit is shown for a PEG/Ficoll70 mixture with a $c_p = 0.05$ g/cm^3 and $\Phi_F = 0.3$ in Figure 5.9(b).

As shown in Figure 5.9(c), while for pure PEG at low c_p the Debye fit (Figure 5.9(a)) and a Guinier fit (Figure 5.9(b)) at small q give slightly different R_g (suggesting it is not a Gaussian polymer chain), for all samples with any crowder in it, the Debye and Guinier fits give the same R_g.

Bibliography

[1] A. B. Fulton, "How crowded is the cytoplasm?," <u>Cell</u>, vol. 30, no. 2, pp. 345–347, 1982.

[2] R. J. Ellis, "Macromolecular crowding: Obvious but underappreciated," <u>Trends in Biochemical Sciences</u>, vol. 26, no. 10, pp. 597–604, 2001.

[3] A. P. Minton, "Excluded volume as a determinant of macromolecular structure and reactivity," <u>Biopolymers</u>, vol. 20, no. 10, pp. 2093–2120, 1981.

[4] S. B. Zimmerman and A. P. Minton, "Macromolecular crowding: biochemical, biophysical, and physiological consequences," <u>Annual Review of Biophysics and Biomolecular Structure</u>, vol. 22, no. 1, pp. 27–65, 1993.

[5] A. P. Minton, "Influence of excluded volume upon macromolecular structure and associations in 'crowded' media," <u>Current Opinion in Biotechnology</u>, vol. 8, no. 1, pp. 65–69, 1997.

[6] H. X. Zhou, G. Rivas, and A. P. Minton, "Macromolecular crowding and confinement: biochemical, biophysical, and potential physiological consequences," Annual Review of Biophysics, vol. 37, pp. 375–397, 2008.

[7] Y. Wang, M. Sarkar, A. E. Smith, A. S. Krois, and G. J. Pielak, "Macromolecular crowding and protein stability," Journal of American Chemical Society, vol. 134, p. 16614, 2012.

[8] A. C. Miklos, M. Sarkar, Y. Wang, and G. J. Pielak, "Protein crowding tunes protein stability," Journal of the American Chemical Society, vol. 133, no. 18, pp. 7116–7120, 2011.

[9] M. Sarkar, A. E. Smith, and G. J. Pielak, "Impact of reconstituted cytosol on protein stability," Proceedings of the National Academy of Sciences of the United States of America, vol. 110, no. 48, pp. 19342–19347, 2013.

[10] A. B. Goins, H. Sanabria, and M. N. Waxham, "Macromolecular crowding and size effects on probe microviscosity," Biophysical Journal, vol. 95, no. 11, pp. 5362–5373, 2008.

[11] S. Mukherjee, M. M. Waegele, P. Chowdhury, L. Guo, and F. Gai, "Effect of macromolecular crowding on protein folding dynamics at the secondary structure level," Journal of molecular biology, vol. 393, no. 1, pp. 227–236, 2009.

[12] I. M. Kuznetsova, B. Y. Zaslavsky, L. Breydo, K. K. Turoverov, and V. N. Uversky, "Beyond the excluded volume effects: mechanistic complexity of the crowded milieu," Molecules, vol. 20, no. 1, pp. 1377–1409, 2015.

[13] R. Rashid, S. M. L. Chee, M. Raghunath, and T. Wohland, "Macromolecular crowding gives rise to microviscosity, anomalous diffusion and accelerated actin polymerization," Physical biology, vol. 12, no. 3, p. 034001, 2015.

[14] L. S. Lerman, "A transition to a compact form of dna in polymer solutions," Proceedings of the National Academy of Sciences, vol. 68, no. 7, p. 1886, 1971.

[15] Y. Wang, L. A. Benton, V. Singh, and G. J. Pielak, "Disordered protein diffusion under crowded conditions," The Journal of Physical Chemistry Letters, vol. 3, no. 18, pp. 2703–2706, 2012.

[16] M. C. Konopka, I. A. Shkel, S. Cayley, M. T. Record, and J. C. Weisshaar, "Crowding and confinement effects on protein diffusion $invivo$," Journal of Bacteriology, vol. 188, no. 17, pp. 6115–6123, 2006.

[17] Y. Phillip and G. Schreiber, "Formation of protein complexes in crowded environments - From in vitro to in vivo," FEBS Letters, vol. 587, no. 8, pp. 1046–1052, 2013.

[18] L. M. Iakoucheva, C. J. Brown, J. D. Lawson, Z. Obradović, and A. K. Dunker, "Intrinsic disorder in cell-signaling and cancer-associated proteins," Journal of Molecular Biology, vol. 323, no. 3, pp. 573–584, 2002.

[19] S. Gupta, J. Stellbrink, E. Zaccarelli, C. N. Likos, M. Camargo, P. Holmqvist, J. Allgaier, L. Willner, and D. Richter, "Validity of the Stokes-Einstein relation in soft colloids up to the glass transition," Physical Review Letters, vol. 115, no. 12, p. 128302, 2015.

[20] S. Palit and A. Yethiraj, "The effect of crowder charge in a model polymer–colloid system for macromolecular crowding: Part II. crowder dynamics," Journal of Chemical Physics, p. submitted, 2017.

[21] S. Palit, L. He, W. A. Hamilton, A. Yethiraj, and A. Yethiraj, "Combining diffusion NMR and SANS enables precise measurements of polymer chain compression in a crowded environment," Physical Review Letters, vol. 118, p. 097801, 2017.

158

[22] H. Kang, P. A. Pincus, C. Hyeon, and D. Thirumalai, "Effects of macromolecular crowding on the collapse of biopolymers," <u>Physical Review Letters</u>, vol. 114, no. 6, p. 068303, 2015.

[23] O. Söderman and P. Stilbs, "NMR studies of complex surfactant systems," <u>Progress in Nuclear Magnetic Resonance Spectroscopy</u>, vol. 26, pp. 445–482, 1994.

[24] K. I. Momot and P. W. Kuchel, "PFG NMR diffusion experiments for complex systems," <u>Concepts in Magnetic Resonance Part A</u>, vol. 28A, p. 249, 2006.

[25] T. Stait-Gardner, S. A. Willis, N. N. Yadav, G. Zheng, and W. S. Price, "NMR diffusion measurements of complex systems," <u>diffusion-fundamentals.org</u>, vol. 11, p. 15, 2009.

[26] S. Barhoum, S. Palit, and A. Yethiraj, "Diffusion NMR studies of macromolecular complex formation, crowding and confinement in soft materials," <u>Progress in Nuclear Magnetic Resonance Spectroscopy</u>, vol. 94-95, pp. 1–10, 2016.

[27] J. Groszek, L. Li, N. Ferrell, R. Smith, C. A. Zorman, C. L. Hofmann, S. Roy, and W. H. Fissell, "Molecular conformation and filtration properties of anionic ficoll," <u>American Journal of Physiology - Renal Physiology</u>, vol. 299, no. 4, pp. F752–F757, 2010.

[28] G. D. Wignall, K. C. Littrell, W. T. Heller, Y. B. Melnichenko, K. M. Bailey, G. W. Lynn, D. A. Myles, V. S. Urban, M. V. Buchanan, D. L. Selby, and P. D. Butler, "The 40 m general purpose small-angle neutron scattering instrument at oak ridge national laboratory," <u>Journal of Applied Crystallography</u>, vol. 45, pp. 990–998, 2012.

[29] Y. B. Melnichenko and G. D. Wignall, "Small-angle neutron scattering in materials science: recent practical applications," Journal of applied physics, vol. 102, no. 2, p. 3, 2007.

[30] S. R. Kline, "Reduction and analysis of SANS and USANS data using Igor Pro," Journal of Applied Crystallography, vol. 39, pp. 895–900, 2006.

[31] G. D. Wignall and Y. B. Melnichenko, "Recent applications of small-angle neutron scattering in strongly interacting soft condensed matter," Reports on Progress in Physics, vol. 68, pp. 1761–1810, Aug. 2005.

[32] P. Debye, "Light scattering in solutions," Journal of Applied Physics, vol. 15, pp. 338–342, Apr. 1944.

[33] Y. Rosenfeld, "Relation between the transport coefficients and the internal entropy of simple systems," Physical Review A, vol. 15, no. 6, pp. 2545–2549, 1977.

[34] M. Dzugutov, "A universal scaling law for atomic diffusion in condensed matter," Nature, vol. 381, no. 6578, pp. 137–139, 1996.

[35] B. Hammouda, D. Ho, and S. Kline, "SANS from Poly(ethylene oxide)/Water Systems," Macromolecules, vol. 35, no. 22, pp. 8578–8585, 2002.

[36] Y. Oono, "Renormalization group theory of transport properties of polymer solutions. I. Dilute solutions," The Journal of Chemical Physics, vol. 78, no. 1, p. 520, 1983.

[37] S. Patra, N. Erwin, and R. Winter, "Translational dynamics of lipidated ras proteins in the presence of crowding agents and compatible osmolytes," ChemPhysChem, vol. 17, no. 14, pp. 2164–2169, 2016.

[38] D. Lavalette, C. Tétreau, M. Tourbez, and Y. Blouquit, "Microscopic viscosity and rotational diffusion of proteins in a macromolecular environment," Biophysical journal, vol. 76, no. 5, pp. 2744–2751, 1999.

[39] N. A. Busch, T. Kim, and V. A. Bloomfield, "Tracer diffusion of proteins in dna solutions. 2. green fluorescent protein in crowded dna solutions," Macromolecules, vol. 33, no. 16, pp. 5932–5937, 2000.

[40] A. Guinier and G. Fournet, "Small angle scattering of X-rays," J. Wiley & Sons, New York, 1955.

Chapter 6 Synopsis

A commonly available polysaccharide, Ficoll70, has been used as a macromolecular crowding agent to produce a resemblance of the high total concentrations that are encountered in the cytoplasm. In this chapter, using pulsed-field gradient (PFG) NMR and rheology, we assess the most prominent characteristics of charged and uncharged Ficoll70 in water. This work is published in the Journal of Chemical Physics, vol. 147, no. 7, p. 074901, 2017. SP carried out all experiments. SP and AY co-wrote the paper.

Chapter 6

Dynamics and Cluster Formation in Charged and Uncharged Ficoll70 Solutions

6.1 Abstract

We apply pulsed-field-gradient NMR (PFG NMR) technique to measure the translational diffusion for both uncharged and charged polysaccharide (Ficoll70) in water. Analysis of the data indicate that NMR signal attenuation above a certain packing fraction can be adequately fitted with a bi-exponential function. The self-diffusion measurements show also that the Ficoll70, an often-used compact, spherical poly-sucrose molecule, is itself non-ideal, exhibiting signs of both softness and attractive interactions in the form of a stable suspension consisting of monomers and clusters. Further, we can quantify the fraction of monomer and cluster. This work strengthens the picture of the existence of a bound water layer within and around a porous Ficoll70 particle.

6.2   Introduction

A highly branched copolymer of two short building blocks, sucrose and epichlorohy-drin, Ficoll70 has been widely used in studies of macromolecular crowding, and for applications in blood preservation and renal filtration due to its high hydrophobicity as well as its charge neutral globular form [1–12]. This synthetic carbohydrate poly-mer has been used by many investigators to produce a resemblance of the high total concentrations that are encountered in the cytoplasm [13].

While some experiments found that the diffusion of Ficoll70 fits the accepted model for diffusion of hard sphere through cylindrical pores [14,15], other experiments found either that Ficoll70 was more spherical and protein-like than dextran [16], or that it is more deformable than globular proteins [17]. Based on experiments *in vivo*, Asgeirsson et al. conjectured that Ficoll70 is sufficiently crosslinked that it cannot reptate, but is not a rigid sphere [18]. Fissell and collaborators measured transport of Ficoll70 through silicon slit nanopore membranes. They observed that Ficoll70 molecules could penetrate the pore even when the Stokes-Einstein radius was greater than the slit width, implying deformability. They surmised Ficoll70 molecule either is not spherical, is not rigid, or exhibits a different conformation in ionic solutions [5].

The most advanced analysis of Ficoll70 solution properties has been done in the renal filtration literature [4–6, 19–22]. Fissell et al. used standard multidetector size-exclusion chromatography (SEC) on Ficoll to show that the Mark-Houwink exponents for the molecular mass dependence of the intrinsic viscosity were 0.34 (Ficoll70) and 0.36 (Ficoll400), between the value of 0 for a solid sphere and 0.5 - 0.8 for a random coil [23]. Their result agree closely with those of Lavrenko et al. [24]. Groszek et al. used similar experiments to demonstrate that charged Ficoll70 was significantly retarded compared with uncharged Ficoll70 across the rat glomerular filtration bar-

rier [4]. Georgalis et al. found two different sizes of particles in Ficoll70 by means of light scattering experiments [25].
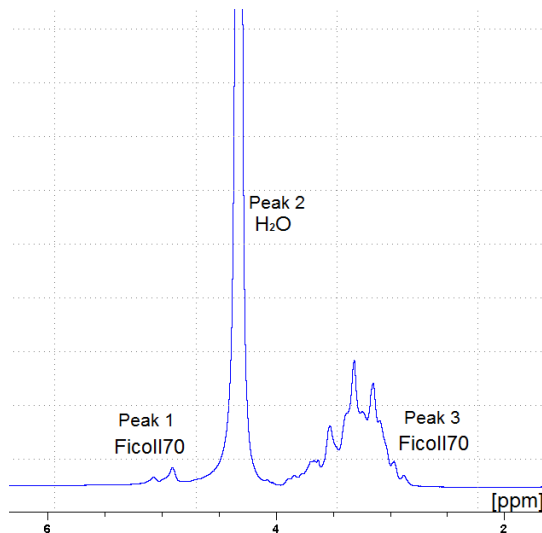
Figure 6.1: 1D ^{1}H-NMR spectrum for Ficoll70 /H_2O sample at a sample temperature 298 K.

In this study, we employ pulsed-field-gradient (PFG) NMR to monitor the self-diffusivities of uncharged and charged Ficoll70 in deionized water. Because of the spectral selectivity of NMR, we can simultaneously (see Figure 6.1) obtain signal from both the Ficoll70 and water species. In a companion work, we focus on polymer structure and dynamics [26] in the presence of Ficoll70 crowder. Ficoll is an often-used crowder. In the understanding of macromolecular crowding, it is important to understand well the properties of the crowder. In this work, we examine the properties of both charged and uncharged Ficoll70 for evidence of cluster formation in equilibrium, a phenomenon, distinct from bulk phase separation, that has been identified in colloids and proteins where short-ranged attractions coexist with longer-ranged (typically electrostatic) repulsive interactions [27–32].

6.3 Materials and Methods

Ficoll®PM 70 (referred to as Ficoll70 in the text) with average molecular weight of 70000 (mean radius (R_c) 4.5-5.5 nm [8, 25, 33–35]) was purchased from Sigma Aldrich and used without further purification. In this work, we use the value of R_c=4.6 nm [34]. Charged Ficoll70 (Ficoll CM 70) was a carboxymethylated derivative of Ficoll PM70, made as described in reference [4]. It was a gift from Dr. William H. Fissell, and was used as received after having been neutralized and dialyzed against distilled water for 4 days. Experimental packing fractions (Φ_F) of Ficoll70 were calculated using the partial specific volume of Ficoll70, $\bar{v} = 0.67$ cm^3/g [10] and are defined as:

$$\Phi_F = \left(\frac{M_{Ficoll} \times 0.67}{M_{Ficoll} \times 0.67 + V_{H_2O}} \right) \tag{6.1}$$

Here M_{Ficoll}, and V_{H_2O} are the mass of Ficoll70 in units of gram and volume of water in units of cm^3 respectively.

For sample preparation, the desired packing fraction of Ficoll70 was dissolved in deionized H_2O. For charged Ficoll70 solutions, the conductivity was controlled, using KCl, to a value of ≈ 1 mS/cm (see Table 1) in order to ensure a consistent Debye-Hückel screening length ($\kappa R_c \sim 1.4$) for all samples. The solution was stirred for 10 hours. Samples were then transferred to 5 mm outer diameter NMR tubes.

6.3.1 PFG NMR

The one-dimensional 1D proton NMR spectrum has been observed for different species in all samples at a resonance frequency of 600 MHz on a Bruker Avance II spectrometer. Figure 6.1 shows well-separated peak regions related to this system. Peak 1 and Peak 3 are the Ficoll70 peaks whereas Peak 2 is for H_2O molecules in solution.

Table 6.1: Comparison of the zeta potential for charged and uncharged Ficoll70

Species	Zeta Potential (mV)	Mobility (μm cm V/s)	Conductivity (mS/cm)
Charged Ficoll70 (without salt)	-27 ± 4	- 1.4 ± 0.2	0.1 ± 0.02
Charged Ficoll70 (salt added)	-29 ± 2	-1.3 ± 0.4	1.1 ± 0.01
Uncharged Ficoll70	-5.2 ± 0.2	- 0.4 ± 0.02	0.04 ± 0.01

All NMR experiments were performed at T =298K. The self-diffusion measurements were carried out in a diffusion probe Diff 30 and with maximum field gradient 1800 G/cm (18 T/m). Diffusion was measured with a pulsed-field-gradient stimulated echo sequence with trapezoidal gradient pulses [36]. The diffusion coefficient of a molecule in aqueous solution is obtained from the attenuation of the signal according to the equation

$$S(k) = S(0) \exp(-Dk), \tag{6.2}$$

where $S(k)$ is the intensity of the signal in the presence of field gradient pulse, $S(0)$ is the intensity of the signal in the absence of field gradient pulse, $k = (\gamma \delta g)^2 (\Delta - \delta/3)$, $\gamma = \gamma^H = 2.657 \times 10^8 \ T^{-1}.s^{-1}$ is the proton gyromagnetic ratio, δ= 2 ms is the duration of field gradient pulse, Δ= 100 ms is the time period between two field gradient pulses, and g is the amplitude of field gradient pulse.

6.3.2   Zeta Potential

The Zeta potential (ζ) and electrophoretic mobility of Ficoll70 solutions, shown in Table 1, were measured by a Zetasizer Nano Z system (Malvern Instruments Ltd,

Malvern, United Kingdom). The dimensionless Zeta potential $\Psi = \zeta e / k_B T = 1.1 \pm 0.2$ and 0.21 ± 0.02 for charged and uncharged Ficoll70 respectively. The solutions of charged Ficoll70 were all prepared with added salt in order to keep the conductivity at 1 mS/cm, resulting in a Debye-Hückel screening length $\kappa^{-1} = 3.2 \pm 0.5$ nm. This corresponds to a $\kappa R_c \sim 1.4$. Given the value of the dimensionless Zeta potential Ψ and κR_c, i.e., both of order unity, electrostatics should clearly be important, but not overwhelmingly so.

6.3.3 Bulk Viscosity Measurement

Experiments were performed on an Anton Paar Physica MCR 301 rheometer, where the cone-plate measuring system was used to extract the flow curves. The cone-plate geometry has a diameter of 50 mm and cone angle of 0.5^0. All samples were pre-sheared for 1 minute before collecting data. The flow curves experiments were carried out with shear rate varying from 0.001 to 100 s^{-1}. For all samples reported in this work, viscosity remains constant as the shear rate is varied.

6.4 Diffusion Model

The PFG NMR signal attenuation of Ficoll70 shows a monoexponential decay with the gradient strength parameter at low packing fraction ($\Phi_F < 0.05$ (uncharged) and $\Phi_F < 0.1$ (charged)). This implies either that it is a single component system or that there are multiple components (e.g. a monomer and cluster) that exchanges very rapidly between monomer and aggregate on the timescale of the NMR experiment [37]. Given the larger size of Ficoll70, the diffusion time of the monomer $\sim 1\mu$s; thus residence times of the Ficoll70 molecule within clusters will be a few micro-seconds or longer. Hence the fact that the signal attenuation associated with the Ficoll70 peak
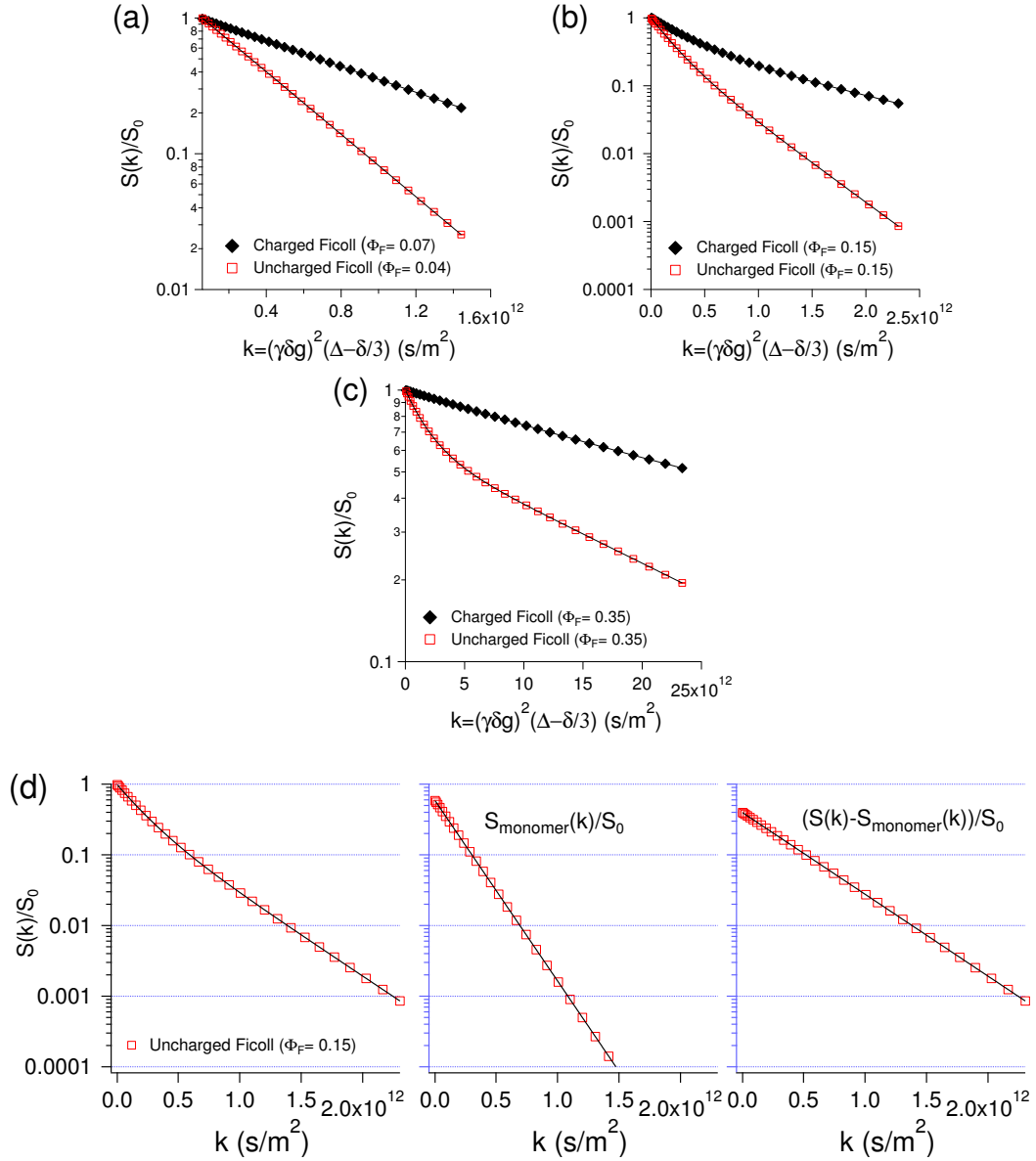
Figure 6.2: (a) The attenuation of the signal $S(k)/S(0)$ on a log scale versus the gradient strength parameter $k = (\gamma \delta g)^2 (\Delta - \delta/3)$ for an aqueous solution Ficoll70 is mono-exponential at low Φ_F for both uncharged and charged Ficoll70 solutions. Signal attenuation for Ficoll70 solution at $\Phi_F = 0.02$ exhibits simple mono-exponential behaviour. (b) For $\Phi_F > 0.05$ (0.10) for uncharged (charged) Ficoll70, the signal attenuation is not mono-exponential. As an example, signal attenuation for Ficoll70 solution at $\Phi_F = 0.15$ and (c) at $\Phi_F = 0.35$, is well-fit to a bi-exponential form. (d) Signal attenuation for uncharged Ficoll70 solution at $\Phi_F = 0.15$ is shown alongside decoupled monomer and cluster signal attenuations obtained after the bi-exponential fit.

exhibits monoexponential behaviour (Figure 6.2(a)) at low packing fractions suggests that the exchange between Ficoll70 clusters and monomers must be very rapid on the NMR time scale.
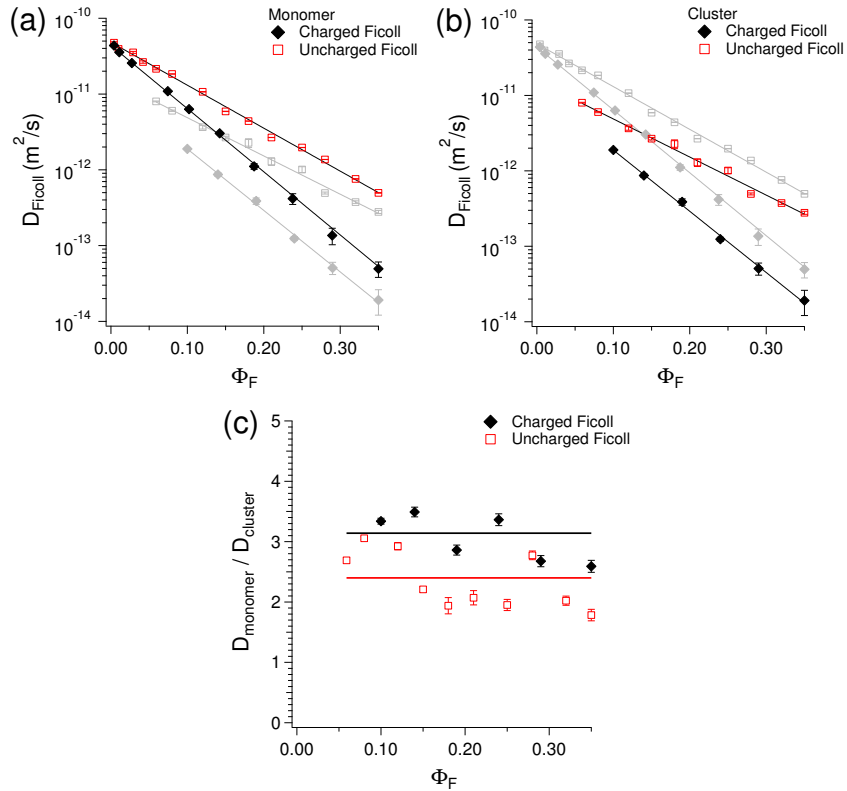
Figure 6.3: Ficoll70 forms clusters: Biexponential signal attenuation indicates emergence of a cluster state above $\Phi_F = 0.05$ (uncharged) and $\Phi_F = 0.1$ (charged). (a) Ficoll70 monomer diffusion coefficient as a function of Φ_F and (b) Ficoll70 cluster diffusion coefficient as a function of Φ_F. (c) The monomer-to-cluster self-diffusivity ratio shows no clear dependence on Φ_F, but appears somewhat larger for charged Ficoll70 than for uncharged Ficoll70. In (a) and (b) cluster and monomer diffusion results are shown in gray to aid comparison.

On the other hand, if the molecular exchange between monomer and cluster is

very slow, one expects the total Ficoll70 signal to be given by

$$
\begin{aligned}
S(k) \ &= \ S_{monomer}(k) + S_{cluster}(k) \\
&= \ S_{monomer}(0) \exp(-D_{monomer}k) \\
&+ \ S_{cluster}(0) \exp(-D_{cluster}k) \tag{6.3}
\end{aligned}
$$

which is bi-exponential in nature (Figure 6.2(b) and (c)). A generalization to multi-exponential behaviour may be made for macromolecules existing in more than two species: $S(k) = \sum_i S_i(k)$, where i= momomer or cluster. For two species, Equation 6.3 may be written in the form $S(k)/S(0) = f \exp(-D_{monomer}k) + (1 - f) \exp(-D_{cluster}k)$, where $f = S_{monomer}(0)/(S_{monomer}(0) + S_{cluster}(0))$.

6.5   Results

6.5.1   Ficoll70 Forms Clusters

The self-diffusion coefficient is obtained in pure Ficoll70 aqueous solutions. The key observation is that the PFG NMR signal attenuation is not mono-exponential when Φ_F is greater than a threshold value: 0.05 (0.10) for uncharged (charged) Ficoll70. When there are two species with the same chemical signatures, and when there is slow exchange (or no exchange) between the species, one obtains bi-exponential signal attenuations in a PFG NMR experiment (Figure 6.2(b) and (c)). Shown in Supplemental Material is a plot of the coefficient of determination R^2 in a linear fit of $\log(S(k)$ vs. k. For $\Phi_F = 0.05$ and greater, there is marked decrease in R^2 below a plateau value of 0.99. This signals the onset of cluster formation. Our observations thus indicate the co-existence of (fast diffusing) monomers and (slow diffusing) clusters of Ficoll70.

We plot the diffusion coefficients for charged and uncharged crowder, and for

monomer (Figure 6.3(a)) and for cluster (Figure 6.3(b)), as a function of Φ_F. Every D dependence on Φ_F is exponential! In dilute polymer solutions one sees a linear decrease in diffusivity. The corresponding diffusion interaction parameter k_D is ~ -2.3 for polystyrene solutions when the second virial coefficient A_2 is zero [38]; A_2 is negative for lower (more negative) k_D. For hard-sphere colloids, the linear Φ_F term would have a prefactor of ~ -2.5. A linearization of the exponential dependence that we observe yields $k_D \sim -9.5$ (-10.4) for uncharged (charged) Ficoll70, much larger than those for typical polymer solutions or hard-sphere colloids, possibly indicative of the propensity for Ficoll to self-associate.

As discussed in earlier [1] and companion [26] works, the work of Rosenfeld [39] and Dzugutov [40] connected structural properties of atomic liquids to their diffusion coefficients. Both studies have proposed an exponential relationship between atomic diffusion and the excess entropy S_2/k_B (in the 2-particle approximation); moreover, recent 2D simulations and colloids experiments [41] show that S_2/k_B is proportional to the colloid packing fraction for packing fractions less than 0.4. The same connection would hold in colloidal suspensions if hydrodynamics is not important in the long-time limit.

The spectral selectivity of PFG NMR allows us to simultaneously obtain diffusion coefficients of water and Ficoll70. We can thus obtain, not only Ficoll70 dynamics, but also the information about the interaction of water with the crowder.

The monomer-to-cluster self-diffusivity ratio (Figure 6.3(c)) shows no clear dependence on Φ_F, but appears somewhat larger for charged Ficoll70 than for uncharged Ficoll70. When the Stokes-Einstein relation remains valid (i.e., at low enough Φ_F), this ratio should report on the ratio of cluster to monomer sizes. This ratio is approximately 2.5 and 3, respectively, for uncharged and charged Ficoll70. For uncharged Ficoll70, Georgalis et al. have measured the value of $D_{monomer}/D_{cluster} = 2.37$ [25],
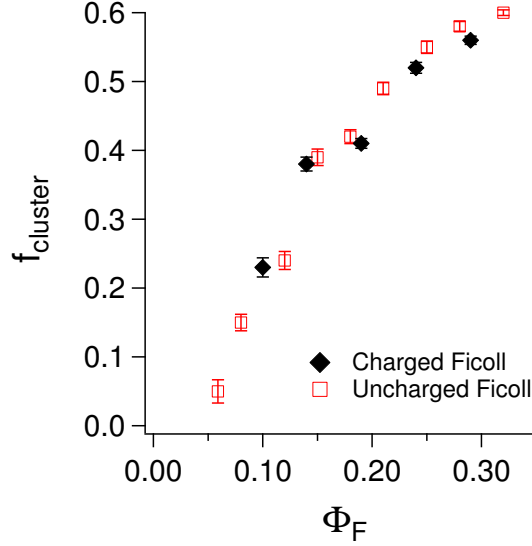
Figure 6.4: Structure of Ficoll70 *via* diffusion: Fraction of Ficoll70 cluster ($f_{cluster}$) as a function of Φ_F for both charged and uncharged Ficoll70.

which is consistent with this work. The fraction of clusters (shown in Figure 6.4) increases from 5% at onset of clustering to $\sim 60\%$ in the crowding regime: in fact, this fraction is very similar for charged and uncharged crowder.

The clusters reported here are unlike micellar aggregates in that the cluster sizes are tiny (2-3 as opposed to an aggregation number of 50-80 in micelles), and are more similar to the equilibrium clusters seen in protein solutions and in colloids with competing attractive and repulsive interactions [28, 29]. As an additonal note, one would expect there to be a distribution of cluster sizes. However, we cannot obtain fit to a distribution without adding an additional fit parameter. The cluster size should thus be treated as a mean cluster size.

One can use the measured monomer and cluster self-diffusivities to calculate an effective diffusion coefficient D_{eff}

$$D_{Ficoll}^{eff} = f_{cluster}D_{cluster} + (1 - f_{cluster})D_{monomer}. \tag{6.4}$$

173

This diffusivity may be compared to its bulk analog from the measured bulk Ficoll70 viscosity η_{Bulk} and the hydrodynamic radius of Ficoll70 monomer $R_H = 4.6$ nm using a Stokes-Einstein form $k_B T/(6\pi\eta_{Bulk}R_H)$. A slope of 1 in the plot of $k_B T/(6\pi\eta_{Bulk}R_H)$ versus D_{eff} would imply agreement with Stokes-Einstein behaviour (dashed line). As can be seen in Figure 6.5, there is agreement for uncharged Ficoll70 solutions so long as cluster formation is not significant, while for charged Ficoll70 there is significant deviation for much smaller Φ_F than the cluster-forming threshold. Even for uncharged Ficoll70 solutions, there is significant deviation for $\Phi_F > 0.15$.

6.5.2 Ficoll Hydration is Quantifiable *via* Water Dynamics

Another interesting aspect is the water diffusion coefficient. The similarity of the water diffusion for charged and uncharged Ficoll70 in Figure 6.6 is reassuring, as it indicates that the physical structure of the polysucrose is unchanged by the charge.

Why does the water diffusion coefficient change with Φ_F? Water dynamics, measured on PFG NMR timescales, is well modeled by assuming rapid exchange of the water molecule between bulk and surface-associated environments [42]. In the present case the self-diffusion of the surface-associated water would be similar to that of the Ficoll70 particle, i.e., between 20 and 1000 times slower than the bulk water self-diffusion coefficient. In the rapid exchange limit, the observed diffusion coefficient $D_{H_2O}(\Phi_F) = f\,D_0 + (1-f)D_{surface}$, where f is the fraction of free (bulk) water, while $(1-f)$ is the fraction of surface-associated water. Since $D_{surface} << D_0$, this yields the approximate form for the fraction of free (bulk) water $f \approx D_{H_2O}(\Phi_F)/D_0$; this fraction is shown in Figure 6.6.

For solid, spherical colloids, the fraction f of bulk water would be expected to decrease with Φ_F. One water layer is approximately 0.3 nm thick and the Ficoll radius is 4.6 nm. The dependence of $f \equiv D_{H_2O}(\Phi_F)/D_0$ for $n = 1, 3$ and 5 water
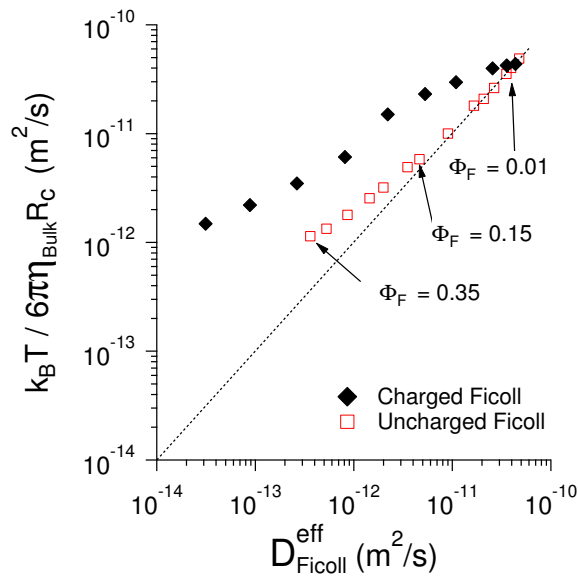
Figure 6.5: Effective diffusion coefficient of Ficoll70: Comparison of a self-diffusivity $k_B T/6\pi\eta_{Bulk}R_c$, calculated from the bulk Ficoll70 viscosity η_{Bulk} and the mean radius of Ficoll70 monomer $R_c = 4.6$ nm, as a function of the measured effective diffusion coefficient D^{eff}, shows agreement with Stokes-Einstein behaviour (dashed line) upto $\Phi_F = 0.15$ for uncharged Ficoll70, while for charged Ficoll70 there is significant deviation for much smaller Φ_F.

layers is shown. In contrast, the measured dependence of f on Φ_F (Figure 6.6) shows a high degree of linearity, with a fit to $D_{H_2O}/D_0 = 1 - \beta_1 \Phi_F$, with $\beta_1 = 2.10 \pm 0.03$. As shown in Supplemental Material (Section IV), $\beta \sim 2$ implies that a water volume per gram of Ficoll70 that corresponds roughly to $2\bar{v}$ (i.e., twice the partial specific volume of Ficoll70) is surface-associated.

At $\Phi_F = 0.3$, as much as 60% of the water is surface associated, suggesting that Ficoll70 is very porous and hydrated; this is not surprising, in hindsight, but we believe that it has not been adequately recognized in the crowding literature, apart from clear indications that Ficoll70 is not a rigid sphere [5,6], as well as the practical knowledge about the lack of overall stability of Ficoll70 solutions above $\Phi_F = 0.35$. It should be noted that this bound water is likely not available to the polymer, and should be accounted for in any free-volume calculations.

6.6 Discussion and Conclusion

In this work, we examine the dynamics of Ficoll70 in water, for both uncharged and charged system. Ficoll70, an often-used artificial crowder, is not hard-sphere-like. This has been indicated elsewhere [5,6], but our water diffusion measurements suggest that 60% of the water is surface-associated in the crowding limit, indicating that the polysucrose particle is highly porous. Even more surprisingly, Ficoll70 diffusivity is bi-modal, indicating that it self-clusters at modest concentrations, with cluster sizes approaching 2 to 3 times the size of the single Ficoll70 particle size ("monomer"). This is reminiscent of indications, from maximum entropy analyses of fluorescence correlation spectroscopy experiments, of multiple modes of probe mobility in crowded solutions [43].

Coexistence of monomers and clusters in equilibrium has been seen experimen-
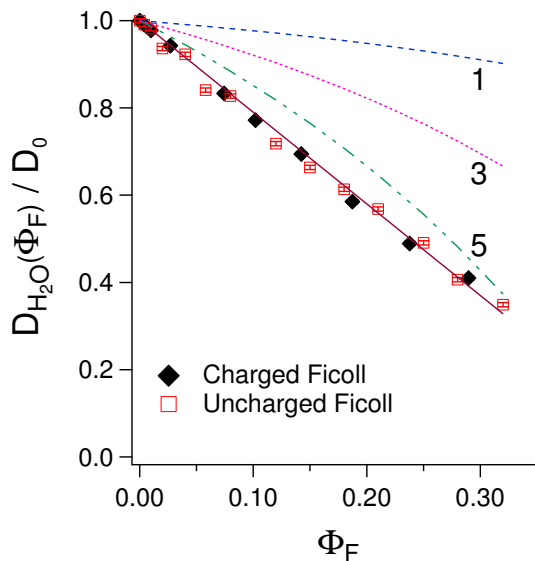
Figure 6.6: Ficoll70 hydration: Linear decrease in water diffusion coefficient with increasing Φ_F indicates a linear increase in the fraction of surface-associated water. The slope is a useful quantifier of Ficoll70 hydration. The dashed curves show that the expectation for n water layers ($n = 1, 3, 5$) on the surface of a solid is non-linear.

tally [28–30], and is expected in systems which have short-ranged attractions and longer-ranged repulsions [27, 32]. Considering both the 5 nm particle scale and that polysaccharide surfaces in water have a Hamaker constant of $\sim 2k_BT$ [44]), attractive forces should be relevant in the presence of even small long-ranged (e.g. electrostatic) repulsions, and is consistent with the observed weak clustering.

The generic behavior–formation of small clusters with the fraction of clusters increasing with packing fraction Φ_F, and the exponential dependence of all the self-diffusivities as a function of Φ_F–is the same for uncharged and charged Ficoll70 solutions. The striking difference is in the actual values of the self-diffusivities, with the charged Ficoll70 being as much as an order of magnitude slower in the crowding limit. A more detailed understanding of Ficoll70 structure and inter-particle interactions will be necessary in order to understand this difference.

6.7 Supplemental Material

6.7.1 Bulk Viscosity Measurement

The rheological measurements were carried out on an Anton Paar Physica MCR 301 rheometer, where the cone-plate measuring system was used to extract the flow curves. The cone-plate geometry used in this study was of R = 50 mm diameter and 0.5° cone angle. The main advantage of using cone-plate geometry is that the shear rate is homogeneous and it remains constant throughout the sample. All samples were pre-sheared for 1 minute before collecting data. The flow curves experiments were carried out with shear rate varying from 0.001 to 100 s^{-1}.
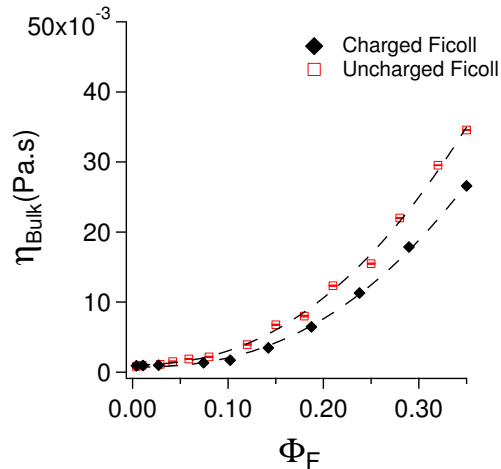
Figure 6.7: Viscosity of Ficoll70: Comparison of the bulk viscosity η_{Bulk} for charged and uncharged Ficoll70 as a function of packing fraction Φ_F. The dashed lines may be treated as a guide to the eye.

A plot of the viscosity values $\eta_{Bulk}(\Phi_F)$ versus the packing fractions Φ_F of the aqueous dispersions of Ficoll70 is shown in Figure 6.7.

6.7.2 The Self-Diffusion Measurement

One of the key observations of this study is that Ficoll70 diffusivity is bi-modal, indicating that it self-clusters at modest concentrations. The PFG NMR signal attenuation exhibit bi-exponential when Φ_F is greater than a threshold value: 0.05 (0.10) for uncharged (charged) Ficoll70.

Shown in a plot (Figure 6.8) of the coefficient of determination R^2 from a linear fit of $\ln(S(k)/S(0))$ vs. $k = (\gamma\delta g)^2(\Delta - \delta/3)$ for aqueous solutions of uncharged Ficoll70. It is seen that there is relatively sharp decrease in R^2 at Φ_F. This is how we determine the onset of the biexponential fit.
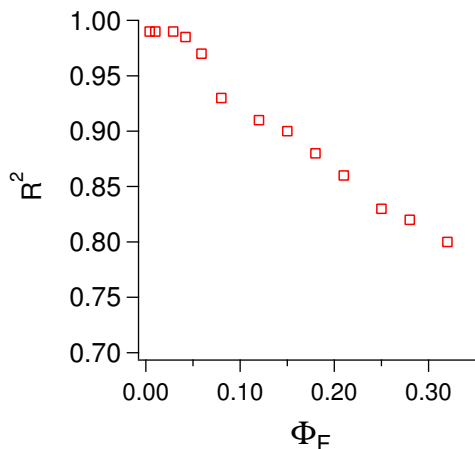
Figure 6.8: Onset of the biexponential: Coefficient of determination R^2 from a linear fit demonstrates a significant change above Φ_F: 0.05 for uncharged Ficoll70.

6.7.3 Effective Diffusion Coefficient

The fact that the signal attenuation associated with the Ficoll70 peak exhibits bi-exponential behaviour over $\Phi_F > 0.05$ (0.1) for uncharged (charged) suggests that the observed self-diffusion coefficient of Ficoll70 is a linear combination of the self-diffusion coefficient $D_{monomer}$ of the free molecules in bulk and that of the bound molecules in
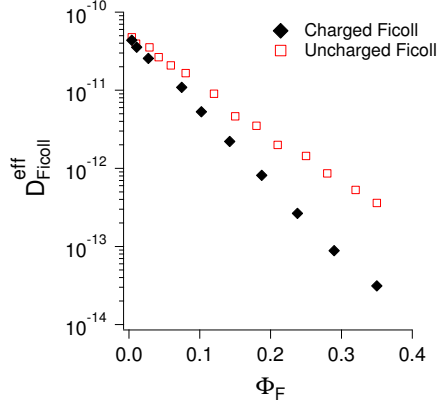
Figure 6.9: Effective diffusion coefficient: Effective diffusion coefficient for charged and uncharged Ficoll70 as a function of packing fraction Φ_F.

the cluster $D_{cluster}$ in the solution. The validity of this "two-species model" has long been known [45–48]. Using the two-species model, the effective diffusion coefficient (D_{eff}) is written as:

$$D^{eff}_{Ficoll} = f_{cluster}D_{cluster} + (1 - f_{cluster})D_{monomer}. \tag{6.5}$$

Hence we obtain D^{eff}_{Ficoll} (Figure 6.9) from the fraction of cluster $f_{cluster}$ and the fraction of monomer $(1 - f_{cluster})$, for a range of Φ_F, and the diffusivities $D_{cluster}$ and $D_{monomer}$ of both cluster and monomer species.

6.7.4 Linear Dependence of the D_{H_2O} on Φ_F

Given a partial specific volume $\bar{v}$ for Ficoll70, we can write $\Phi_F = \bar{v}M_{Ficoll}/V$, where V is the total solution volume. Let f be the fraction of bulk water. The fraction of water that is associated with the Ficoll70 surface must, if we treat Ficoll70 as a branched polymer, be proportional to the Ficoll70 concentration, i.e.,

$$1 - f = \alpha M_{Ficoll}/V, \tag{6.6}$$

180

which means that the fraction of surface-associated water

$$1 - f = \frac{\alpha}{v}\Phi_F \equiv \beta\Phi_F, \qquad (6.7)$$

would increase linearly with the volume fraction Φ_F (or the concentration M_{Ficoll}/V in g/cm^3).

In contrast, if we were considering water layers on a solid sphere, we would expect

$$(1 - f)V_{H_2O} = N\left[(4\pi/3)(R_c + x)^3 - (4\pi/3)R_c^3\right], \qquad (6.8)$$

where R_c is Ficoll radius, and $x = n(0.3)$ nm is the thickness of n water monolayers. Using $\Phi_F = V_{Ficoll}/V = N(4\pi/3)R_c^3/V$ and $1 - \Phi_F = V_{H_2O}/V$, we get the expectation that the fraction of surface-associated water depends nonlinearly on Φ_F:

$$1 - f = g(n)\frac{\Phi_F}{1 - \Phi_F}, \qquad (6.9)$$

where $g(n) = (1 + x/R_c)^3 - 1$.

6.8 Acknowledgements

Bibliography

[1] S. Palit, L. He, W. A. Hamilton, A. Yethiraj, and A. Yethiraj, "Combining diffusion NMR and SANS enables precise measurements of polymer chain compression

in a crowded environment," Physical Review Letters, vol. 118, p. 097801, 2017.

[2] Y. Wang, M. Sarkar, A. E. Smith, A. S. Krois, and G. J. Pielak, "Macromolecular crowding and protein stability," Journal of American Chemical Society, vol. 134, p. 16614, 2012.

[3] K. H. Wong, R. D. Sandlin, T. R. Carey, K. L. Miller, A. T. Shank, R. Oklu, S. Maheswaran, D. A. Haber, D. Irimia, S. L. Stott, et al., "The role of physical stabilization in whole blood preservation," Scientific reports, vol. 6, 2016.

[4] J. Groszek, L. Li, N. Ferrell, R. Smith, C. A. Zorman, C. L. Hofmann, S. Roy, and W. H. Fissell, "Molecular conformation and filtration properties of anionic ficoll," American Journal of Physiology - Renal Physiology, vol. 299, no. 4, pp. F752–F757, 2010.

[5] W. H. Fissell, S. Manley, A. Dubnisheva, J. Glass, J. Magistrelli, A. N. Eldridge, A. J. Fleischman, A. L. Zydney, and S. Roy, "Ficoll is not a rigid sphere," American Journal of Physiology - Renal Physiology, vol. 293, no. 4, pp. F1209–F1213, 2007.

[6] D. Venturoli and B. Rippe, "Ficoll and dextran vs. globular proteins as probes for testing glomerular permselectivity: effects of molecular size, shape, charge, and deformability," American Journal of Physiology - Renal Physiology, vol. 288, no. 4, pp. F605–F613, 2005.

[7] A. Dhar, A. Samiotakis, S. Ebbinghaus, L. Nienhaus, D. Homouz, M. Gruebele, and M. S. Cheung, "Structure, function, and folding of phosphoglycerate kinase are strongly perturbed by macromolecular crowding," Proceedings of the National Academy of Sciences, vol. 107, no. 41, pp. 17586–17591, 2010.

[8] J. R. Wenner and V. A. Bloomfield, "Crowding effects on ecorv kinetics and binding," Biophysical Journal, vol. 77, no. 6, p. 3234–3241, 1999.

[9] A. Galan, B. Sot, O. Llorca, J. L. Carrascosa, J. Valpuesta, and A. Muga, "Excluded volume effects on the refolding and assembly of an oligomeric protein," Journal of Biological Chemistry, vol. 276, no. 2, pp. 957–964, 2001.

[10] P. N. Lavrenko, O. I. Mikriukova, and O. V. Okatova, "On the separation ability of various ficoll gradient solutions in zonal centrifugation," Analytical Biochemistry, vol. 166, no. 2, pp. 287–297, 1987.

[11] N. Tokuriki, M. Kinjo, S. Negi, M. Hoshino, Y. Goto, I. Urabe, and T. Yomo, "Protein folding by the effects of macromolecular crowding," Protein Science, vol. 13, p. 125, 2004.

[12] Y. Wang, L. A. Benton, V. Singh, and G. J. Pielak, "Disordered Protein Diffusion under Crowded Conditions," The Journal of Physical Chemistry Letters, vol. 3, no. 18, pp. 2703–2706, 2012.

[13] S. B. Zimmerman and A. P. Minton, "Macromolecular crowding: biochemical, biophysical, and physiological consequences," Annual Review of Biophysics and Biomolecular Structure, vol. 22, no. 1, pp. 27–65, 1993.

[14] M. Bohrer, G. D. Patterson, and P. Carroll, "Hindered diffusion of dextran and ficoll in microporous membranes," Macromolecules, vol. 17, no. 6, pp. 1170–1173, 1984.

[15] W. Deen, M. Bohrer, and N. Epstein, "Effects of molecular size and configuration on diffusion in microporous membranes," AIChE Journal, vol. 27, no. 6, pp. 952–959, 1981.

[16] J. D. Oliver, S. Anderson, J. L. Troy, B. M. Brenner, and W. Deen, "Determination of glomerular size-selectivity in the normal rat with Ficoll.," Journal of the American Society of Nephrology, vol. 3, no. 2, pp. 214–228, 1992.

[17] J. Axelsson, K. Sverrisson, A. Rippe, W. Fissell, and B. Rippe, "Reduced diffusion of charge-modified, conformationally intact anionic ficoll relative to neutral ficoll across the rat glomerular filtration barrier in vivo," American Journal of Physiology-Renal Physiology, vol. 301, no. 4, pp. F708–F712, 2011.

[18] D. Asgeirsson, D. Venturoli, E. Fries, B. Rippe, and C. Rippe, "Glomerular sieving of three neutral polysaccharides, polyethylene oxide and bikunin in rat. Effects of molecular size and conformation," Acta Physiologica, vol. 191, no. 3, pp. 237–246, 2007.

[19] C. Rippe, D. Asgeirsson, D. Venturoli, A. Rippe, and B. Rippe, "Effects of glomerular filtration rate on ficoll sieving coefficients (θ) in rats," Kidney international, vol. 69, no. 8, pp. 1326–1332, 2006.

[20] M. Ohlson, J. Sörensson, and B. Haraldsson, "Glomerular size and charge selectivity in the rat as revealed by FITC-Ficoll and albumin," American Journal of Physiology - Renal Physiology, vol. 279, no. 1, pp. F84–F91, 2000.

[21] D. Asgeirsson, D. Venturoli, B. Rippe, and C. Rippe, "Increased glomerular permeability to negatively charged Ficoll relative to neutral ficoll in rats," American Journal of Physiology-Renal Physiology, vol. 291, no. 5, pp. F1083–F1089, 2006.

[22] C. M. Öberg and B. Rippe, "A distributed two-pore model: theoretical implications and practical application to the glomerular sieving of ficoll," American Journal of Physiology-Renal Physiology, vol. 306, no. 8, pp. F844–F854, 2014.

[23] W. H. Fissell, C. L. Hofmann, R. Smith, and M. H. Chen, "Size and conformation of ficoll as determined by size-exclusion chromatography followed by multiangle light scattering," American Journal of Physiology-Renal Physiology, vol. 298, no. 1, pp. F205–F208, 2010.

[24] P. Lavrenko, O. Mikryukova, and S. Didenko, "Hydrodynamic properties and the shape of the molecules of the polysaccharide ficoll-400 in solution," Polymer Science USSR, vol. 28, no. 3, pp. 576–584, 1986.

[25] Y. Georgalis, M. Philipp, R. Aleksandrova, and J. Krüger, "Light scattering studies on ficoll pm70 solutions reveal two distinct diffusive modes," Journal of Colloid and Interface Science, vol. 386, no. 1, pp. 141–147, 2012.

[26] S. Palit, L. He, W. A. Hamilton, A. Yethiraj, and A. Yethiraj, "The effect of crowder charge in a model polymer–colloid system for macromolecular crowding: Part I. polymer structure and dynamics," Journal of Chemical Physics, p. submitted, 2017.

[27] J. Groenewold and W. K. Kegel, "Anomalously large equilibrium clusters of colloids," The Journal of Physical Chemistry B, vol. 105, pp. 11702–11709, 2001.

[28] A. Stradner, H. Sedgwick, F. Cardinaux, W. Poon, S. Egelhaaf, and P. Schurtenberger, "Equilibrium cluster formation in concentrated protein solutions and colloids," Nature, vol. 432, no. 7016, pp. 492–495, 2004.

[29] S. Barhoum and A. Yethiraj, "NMR detection of an equilibrium phase consisting of monomers and clusters in concentrated lysozyme solutions," The Journal of Physical Chemistry B, vol. 114, pp. 17062–17067, 2010.

[30] L. Porcar, P. Falus, W.-R. Chen, A. Faraone, E. Fratini, K. Hong, P. Baglioni, and Y. Liu, "Formation of the Dynamic Clusters in Concentrated Lysozyme Protein Solutions," The Journal of Physical Chemistry Letters, vol. 1, pp. 126–129, 2010.

[31] S. Barhoum, A. Agarwal, and A. Yethiraj, Cluster phases in colloids and proteins. Pan Stanford, 2013.

[32] M. B. Sweatman, R. Fartaria, and L. Lue, "Cluster formation in fluids with competing short-range and long-range interactions," The Journal of Chemical Physics, vol. 140, no. 12, p. 124508, 2014.

[33] J. Sörensson, M. Ohlson, K. Lindström, and B. Haraldsson, "Glomerular charge selectivity for horseradish peroxidase and albumin at low and normal ionic strengths," Acta physiologica Scandinavica, vol. 163, no. 1, pp. 83–91, 1998.

[34] C. Le Coeur, Influence de l'encombrement cytoplasmique sur la stabilité et la diffusion des protéines. Ph.D. thesis, L'université Pierre et Marie Curie, 2010.

[35] K. Luby-Phelps, P. E. Castle, D. L. Taylor, and F. Lanni, "Hindered diffusion of inert tracer particles in the cytoplasm of mouse 3t3 cells," Proceedings of the National Academy of Sciences, vol. 84, no. 14, pp. 4910–4913, 1987.

[36] W. S. Price, "Pulsed-field gradient nuclear magnetic resonance as a tool for studying translational diffusion: Part I. basic theory," Concepts in Magnetic Resonance, vol. 9, pp. 299–336, 1997.

[37] S. Barhoum, S. Palit, and A. Yethiraj, "Diffusion NMR studies of macromolecular complex formation, crowding and confinement in soft materials," Progress in Nuclear Magnetic Resonance Spectroscopy, vol. 94-95, pp. 1–10, 2016.

[38] C. C. Han and Z. A. Akcasu, Scattering and dynamics of polymers. Singapore: Wiley, 2011.

[39] Y. Rosenfeld, "Relation between the transport coefficients and the internal entropy of simple systems," Physical Review A, vol. 15, no. 6, pp. 2545–2549, 1977.

[40] M. Dzugutov, "A universal scaling law for atomic diffusion in condensed matter," Nature, vol. 381, no. 6578, pp. 137–139, 1996.

[41] A. L. Thorneywork, R. E. Rozas, R. P. Dullens, and J. Horbach, "Effect of Hydrodynamic Interactions on Self-Diffusion of Quasi-Two-Dimensional Colloidal Hard Spheres," Physical Review Letters, vol. 115, no. 26, p. 268301, 2015.

[42] A. Yethiraj, D. Capitani, N. E. Burlinson, and E. E. Burnell, "An NMR study of translational diffusion and structural anisotropy in magnetically alignable nonionic surfactant mesophases," Langmuir, vol. 21, pp. 3311–3321, Apr. 2005.

[43] A. B. Goins, H. Sanabria, and M. N. Waxham, "Macromolecular crowding and size effects on probe microviscosity," Biophysical Journal, vol. 95, no. 11, pp. 5362–5373, 2008.

[44] M. Holmberg, J. Berg, S. Stemme, L. Ödberg, J. Rasmusson, and P. Claesson, "Surface force studies of Langmuir-Blodgett cellulose films," Journal of Colloid and Interface Science, vol. 186, no. 2, pp. 369–381, 1997.

[45] S. Barhoum and A. Yethiraj, "An NMR study of macromolecular aggregation in a model polymer-surfactant solution," The Journal of Chemical Physics, vol. 132, p. 024909, 2010.

187

[46] O. Soderman and P. Stilbs, "NMR studies of complex surfactant systems," Progress in Nuclear Magnetic Resonance Spectroscopy, vol. 26, pp. 445–482, 1994.

[47] P. Stilbs, "Fourier transform NMR pulsed-gradient spin-echo (FT-PFGSE) self diffusion measurements of solubilization equilibria in sds solutions," Journal of Colloid and Interface Science, vol. 87, pp. 385–394, 1982.

[48] P. Stilbs, "A comparative study of micellar solubilization for combinations of surfactants and solubilizates using the fourier transform pulsed-gradient spin-echo NMR multicomponent self-diffusion technique," Journal of Colloid and Interface Science, vol. 94, pp. 463–469, 1983.

Chapter 7 Synopsis

In this chapter we report the dynamics of macromolecules in the presence of hierarchical confinement: in a nanometer-scale porous gel matrix and within stable and monodisperse micrometer-scale water- in-oil drops. This work is published in Soft Matter, vol. 14, no. 3, p. 448, 2018. SP carried out all experiments. SKT performed the calculations to obtain the droplet size distribution reported in Figure 7.2. SP and AY co-wrote the paper.

Chapter 7

Realization of a Stable, Monodisperse Water-in-Oil Droplet System with Micro-Scale and Nano-Scale Confinement for Tandem Microscopy and Diffusion NMR Studies

7.1 Abstract

In this work we generate stable and monodisperse water-in-oil emulsions using a co-flowing geometery that produced droplet sizes between 13 μm and 250 μm. The drops survived transfer to NMR tubes and were stable for at least 26 hours, enabling the performance of pulsed-field-gradient NMR experiments in addition to microscopy. The drops sizes achieved as a function of flow rate agree well with a simple model for droplet generation: this yields a precise measure of the interfacial tension. The design of a cell mimetic environment with nano-scale confinement has also been demon-

strated with diffusion measurements on macromolecules (PEG and Ficoll70) within droplets that are further structured internally using agarose gel networks. Containing the agarose gel in droplets appears to provide very reproducible and homogeneous network environments, enabling quantitative agreement of Ficoll70 dynamics with a theoretical model, with no fit parameters, and, with PEG, yielding a systematic polymer-size dependent slowing down in the network. This is in contrast with bulk agarose, where identical macromolecular diffusion measurements indicate the presence of heterogeneities with water pockets.

7.2   Introduction

Diffusion in inhomogeneous media such as biological cells is complex because molecules encounter obstructing structures at both nano- and micro-scales [1]. In living cells the presence of the cytoplasm provides compartmentalization, crowding and above all a heterogeneous distribution of macromolecules [2,3]. In vitro compartmentalisation, using water-in-oil emulsions, is one system that can begin to mimic this complexity [4]. Encapsulation of macromolecules in microscopic water droplets is also powerful in that it enables the performance of laboratory operations using a fraction of the volume of reagents and significantly less time [5,6].

Microfluidics offer opportunities for fundamental studies in cell biology [7,8]. In particular, it has been used for the generation of well-defined cellular microenvironments by encapsulating cells in droplets or microgels, followed by studies of cell growth and viability [9,10], gene expression [11], and enzymatic activity [12]. Hydrogels are an attractive starting point for re-creating the hierarchical structure of biological cells [13,14]. Agarose is a neutral polysaccharide that forms hydrogels at reduced temperatures [15]. It is extensively used in biomedical research because it is gener-

ally bio-inert, non-adsorptive to proteins and non-adhesive to cells, and its mechanical properties can be tuned by varying the agarose concentration in the gel [16,17]. While hydrogels can mimic nano-scale confinement, it is more challenging to generate robust and controlled multi-scale confinement spanning the nanometer and the micrometer scales.

The microfluidic encapsulation strategy has several important advantages: the ability to create 3D cellular microenvironments with precisely controlled dimensions, the capability to vary the properties of these environments at high throughputs of about 100 to 1000 highly monodisperse aqueous droplets per second [18–20] However, it is not always obvious that these high-throughput strategies produce droplets that are stable when produced in the large quantities and for the long durations that are needed for small-angle scattering or nuclear magnetic resonance (NMR) spectroscopy. Thus, the challenge is to achieve long-time stability for droplets that can be loaded with macromolecules of choice and confining environments on the micro- and nano-scale.

One of the primary objectives of the current study is the generation of stable and monodisperse water-in-oil emulsions where we can incorporate micro-scale confinement *via* control of the water drop size, and nano-scale confinement by loading the drops with agarose gel, which forms a filamentous network that may be considered a physical, non-active analog of the cytoskeletal network.

In this study, the diffusion behaviors of two kinds of macromolecules–a flexible non-ionic polymer, polyethylene glycol (PEG) and a compact uncharged polysaccharide (Ficoll70)–are determined in three kinds of environments using pulsed-field-gradient NMR (PFG NMR), while employing, in tandem, the more rapid technique (optical microscopy) to ensure that the drops remain unchanged from production to NMR. The first environment is a simple water-in-oil emulsion which generates micro-scale

confinement. The second environment is bulk agarose gel. The third is a water-in-oil emulsion where the aqueous phase is loaded with agarose gel: we refer to these as agarose gel microbeads. Using these three environments, we can examine the role of macromolecular diffusion in the presence of micro-scale confinement, nano-scale confinement, and a hierarchical micro- and nano-scale confinement. The significance of this work is that the results will enable a deep understanding of the diffusion behavior of these solutes in a biomimetic system, which is needed for further progress in research of molecular diffusion in vivo.

7.3 Background

7.3.1 Stable and Monodisperse Micron-Scale Droplets

Using microfluidic technology, one can produce a uniform stream of droplets having diameters ranging from a few micrometres to hundreds of micrometres (corresponding to volumes between 0.5 pl and 4 nl) in a uniform, evenly spaced, continuous stream. Popular geometries for microfluidic droplet generation geometries are the T-junction, flow-focusing and the co-flow geometry. In the T-junction geometry, droplet formation occurs due to the combined effect of pressure changes in the continuous phase and the squeezing of the dispersed phase. This geometry is popular due to the ease with which droplets can be formed and the uniformity of the resulting droplets [21,22]. In flow-focusing microfluidics, the dispersed and continuous phases are forced through a narrow region in the microfluidic device. The design employs symmetric shearing by the continuous phase on the dispersed phase which enables more controlled and stable generation of droplets [23,24]. In a co-flowing geometry there are two concentric channels: the dispersed phase liquid is driven into the inner channel into parallel flowing stream of the continuous phase liquid. Co-flowing configurations result in

highly monodisperse droplets with polydispersity values ranging from 1% to 2%. The droplet sizes produced range from as small as 80 μm up to a few hundred micrometres in diameter [25, 26].

Making stable water-in-oil emulsions is challenging. Emulsions can be stabilized by amphiphilic surfactants and surface-active polymers [27], colloidal particles [28], or a combination of particles and surfactants [29]. In surfactant-stabilized emulsions, the HLB value, which is a measure for the ratio of hydrophilic to hydrophobic parts of the surfactant, is often considered to classify low-molecular-weight amphiphiles, while the main factor influencing the ability of colloidal particles to form so-called Pickering emulsions is the particle-surface wettability [28].

7.3.2   Agarose Gel and Nano-Scale Confinement

For a macromolecule in dilute solution, the Stokes-Einstein relation,

$$D_0 = \frac{k_B T}{6\pi\eta R_H},$$

(7.1)

relates the self-diffusion coefficient D_0 with the hydrodynamic radius, R_H, and the solvent viscosity, η.

Agarose gel is an irregular 3D matrix of fibers filled with water [30]. A solute can diffuse freely in the water, but in agarose it will be impeded by the fibers. The arrangement of the fibers in the matrix also has an effect on the magnitude of steric interaction. An ordered arrangement of fibers impedes diffusion less than a disordered or random arrangement, as is found in agarose [31].

The relationship between the hydrodynamic radius of a solute and the pore size of a fibrous medium plays a large role in how the solute is able to diffuse in such a medium. The pore size describes the amount of space between the fibers that make

up the medium. It is well known that the mesh sizes in polymer hydrogels depend on the volume fraction, Φ, or mass fraction μ (in agarose $\mu = 1.025\Phi$), of polymeric material in solution: this is also referred to as the fiber density. There is wide variance in pore size, from 1 nm to 900 nm [32–40]. A smaller pore size results from a higher fiber density (higher μ or Φ) and results in a greater hindrance to diffusion. Typical mass fractions for agarose gel range from 0.5% to 7.5%.

In general, the relative diffusivity (the diffusivity in the gel divided by the corresponding aqueous value in unconfined water) is found to decrease as molecular size and/or gel polymer concentration are increased. One way to describe the effects of molecular size is to use hindered transport theories developed for membranes with long, regularly shaped (such as cylindrical) pores [41]. Thus, a given gel might be viewed as having a certain effective pore size and pore number density. However, there is no clear way to predict those pore parameters from actual compositional variables, such as the volume fraction of crosslinked polymer. Closer to reality are models that envision a gel as a network of polymeric fibers with fluid-filled interstices. In such models, it is usually assumed that a single type of rigid, cylindrical fiber is arranged in either a random or spatially periodic array. Thus, a given gel might be viewed as having a certain effective pore size and pore number density. Ogston et al. proposed a stochastic model for the hindered diffusion coefficient of a solute molecule in a random fiber matrix [42]. They assumed that a single type of rigid, cylindrical fiber is arranged in either a random or spatially periodic array, and that the hindered mobility is due to steric obstructions of the fibers. In their picture, the reduced diffusion coefficient, D_g/D_0, is equal to the probability of a random-walk step of the test particle without collision. The derived expression for the reduced diffusion coefficient is

$$\frac{D_g}{D_0} = \exp\left(-\frac{(R_H + R_f)}{R_f}\,\Phi^{0.5}\right), \tag{7.2}$$

where Φ represents the volume fraction of the polymer, R_H the hydrodynamic radius of the diffusing molecule and R_f defines the effective cylindrical radius of the fiber. A recent experimental work on dextran molecules diffusing as probe through a poly-acrylamide hydrogel shows excellent agreement with Ogston model [43]. However, the Ogston model is sometimes unsatisfactory for agarose gels, overestimating the influence of polymer concentration on the diffusion coefficients in cases where the proteins and polymeric macromolecules are flexible in structure. [44, 45]

NMR relaxation measurements can also be used to get information about pore size. D'Agostino et al [46] measured the change in relaxation rate with gel concentration. The relaxation rate is expected to depend linearly on the surface-volume ratio, so they used the relation

$$\Delta\left(\frac{1}{T_1}\right) \equiv \frac{1}{T_1(\Phi_A)} - \frac{1}{T_1(\Phi_A = 0)} = \frac{2}{R_{Pore}}\rho, \tag{7.3}$$

where $\frac{2}{R_{Pore}}$ is the surface-to-volume ratio assuming that the pores are cylindrical in shape with a pore radius R_{Pore}; ρ is a material property known as the surface relaxivity.

7.4 Method

7.4.1 Droplet Generation

The liquids we employ were deionized water as the aqueous phase, and mineral oil (Fisher Scientific, CAS 0122B-4) with a density of 870 kg/m^3 and dynamic viscosity of 32×10^{-3} Pa s as the oil phase. A non-ionic surfactant span-80 (Sigma-Aldrich)
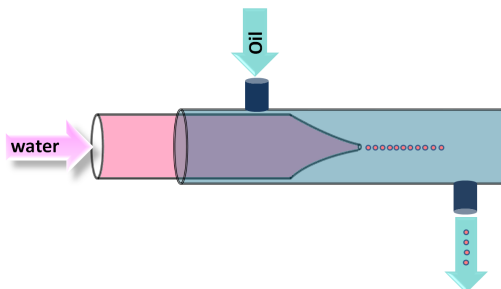
Figure 7.1: Droplet formation: Schematic of production of water-in-oil emulsion droplets in microfluidic device with coflowing geometry.

was added into the 100 ml oil phase at 4.5% (v/v) as a surfactant. The resulting oil-surfactant mixture was stirred on a magnetic stir plate for an hour.

As shown in Figure 7.1, the experimental device used in this work is made of two coaxially aligned cylindrical capillary tubes. The inner capillary tube with a tip tapered to an inner diameter, D_{tip}, that is varied between (26 ± 0.5) μm and (15 ± 0.2) μm and an outer diameter $D_{out} = 1.2 \pm 0.2$ mm. The coaxial alignment of the tubes is achieved by matching the outer diameter of the untapered portion of the inner capillary to the inner dimension of the outer capillary.

In all the experiments reported here, the generation of droplets of variable size is achieved by changing both the inner capillary diameter (D_{tip}) as well as the oil flow rate (Q_{oil}). The inner fluid is deionized water and the outer fluid is mineral oil (with Span80), which leads to water drops that form in a continuous phase of oil. Both liquids are injected through syringe pumps. In this study, the experiments are performed at constant dispersed phase flow rate ($Q_{water} = 0.001$ cm^3/min), where Q_{oil} is always much greater than Q_{water}.

The measured size distribution of droplets remained unchanged for the maximum measured duration of 26 hours. However, the water-in-oil droplets were breaking into smaller droplets while transferring from the production container to the NMR tube. Several methods had been used to prevent droplet break up. The idea of adding 1%

(w/v) hydrophobic fumed silica nanoparticles (Aerosil @ R972, Evonik, with a mean particle diameter of 16 nm [47]) with mineral oil proved to be the most effective. The silica nano-particles form a thin layer around the water droplets and provide better stability against break up. Measurements for simple micro-scale confinement reported in this article are therefore for the silica particle stabilized water-in-mineral oil emulsion. As also stated in the next sub-section, introducing nanoscale confinement in the form of agarose gel was itself adequate to drop stability, and in that case, nano-particle stabilization was not necessary.

7.4.2 The NMR Self-Diffusion Measurement

Pulsed field gradient nuclear magnetic resonance (PFG-NMR) is a common non-invasive technique to study the size distribution and dynamics of single emulsion systems with advantages that it can be used on concentrated opaque emulsions and is a non-destructive technique [48, 49]. PFG NMR measurements were carried out on a Bruker Avance II 600 spectrometer equipped with a Bruker 14.08 T magnet, and a Bruker diffusion Diff30 probe (with a ^{1}H radiofrequency coil insert with an inner diameter of 5 mm) with a maximum Z gradient strength of 30 Gauss/cm/Amp. The spectrometer was also equipped with a (60A maximum current) gradient amplifier and thus a maximum gradient of 1800 Gauss/cm (18 T/m). To avoid probe heating and to control sample temperature, the probe was cooled by flowing water and the temperature maintained at 25°C. We use a pulsed-field-gradient stimulated echo pulse program to measure diffusion [50]. The gradient steps were varied and the signal for H$_2$O, PEG of different molecular weight and Ficoll70 were collected as a function of gradient. Signal attenuation due to diffusion in the stimulated echo sequence is given by

$$S(g) = S_0 \exp\left(-\gamma^2 g^2 \delta^2 (\Delta - \delta/3) D\right), \tag{7.4}$$

where $S(g)$ is the intensity of the signal in the presence of field gradient pulse, $S(0)$ is the intensity of the signal in the absence of field gradient pulse, $\gamma = \gamma^H = 2.657 \times 10^8$ $T^{-1}.s^{-1}$ is the proton gyromagnetic ratio, $\delta = 2$ ms is the duration of field gradient pulse, $\Delta = 500$ ms is the time period between two field gradient pulses, and g is the amplitude of field gradient pulse.

Also, for agarose gel, we measured longitudinal relaxation time (T_1) values from a series of spectra collected using a standard inversion-recovery pulse sequence.

7.4.3 Restricted Diffusion and the Droplet Size Distribution

Diffusion of molecules inside a cavity is known as "restricted diffusion". As the molecules inside the cavity are not diffusing freely, the behavior of signal attenuation is different from that of unrestricted diffusion. Callaghan et al. used pulsed-field gradient spin echo experiment to measure the diffusion coefficients of water and fat in Cheddar and Swiss cheeses [48]. They considered a cheese matrix as a collection of droplets with a Gaussian distribution of sphere volume. The resulting echo attenuation was

$$S(g) = S_0 \exp\left(-\alpha^2 a_0^2 \left[1 + \sigma^2 \alpha^2\right]^{-1} - \frac{1}{2} \ln\left[1 + \sigma^2 \alpha^2\right]\right), \tag{7.5}$$

where a_0 is the mean radius and $\sigma/\sqrt{2}$ is the standard deviation. The variable α^2 depends on the gradient strength and gradient pulse duration, $\gamma^2 g^2 \delta^2$. The above expression is valid for the condition $\exp\left(-a_0^2/\sigma^2\right) << 1$.
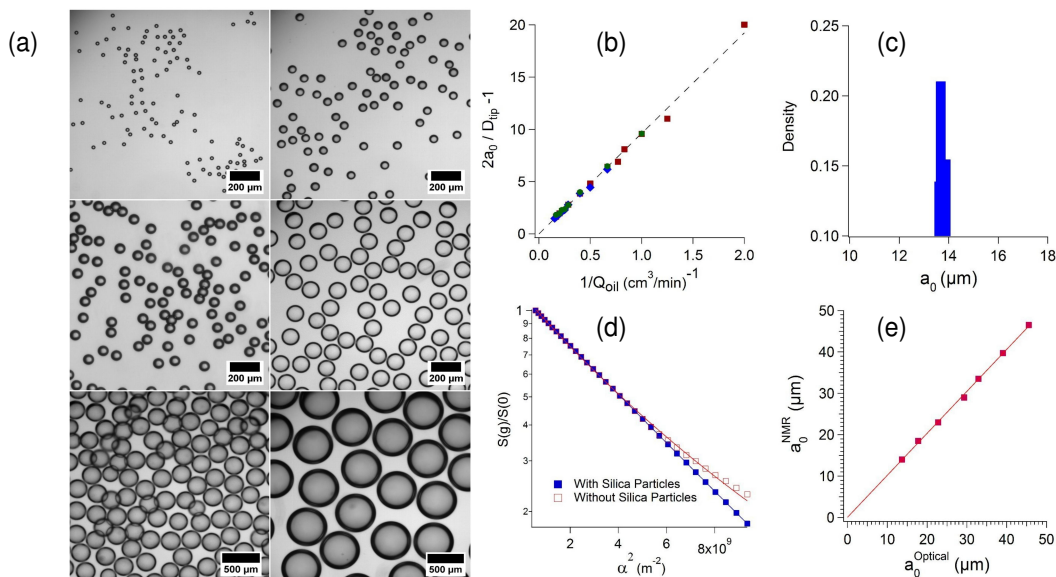
Figure 7.2: **Stable and monodisperse droplets:** Monodisperse water-in-oil emulsion of different droplet sizes are generated in microfluidic device. These droplets were verified to be stable for at least 26 hours. (a) Droplet radius are: (13.7 ± 0.2) —m; (23.2 ± 0.4) —m using $D_{tip} = (15 \pm 0.2)$ µm **(top)**, (38.2 ± 0.4) —m; (59 ± 1) —m using $D_{tip} = (19 \pm 0.4)$ µm **(middle)**, (126 ± 3) —m; (265 ± 4) —m using $D_{tip} = (26 \pm 0.5)$ µm **(bottom)**. (b) Flow curve for droplet diameter, normalized by the tip diameter (D_{tip}) of the inner capillary, as a function of the external oil flow rate. Here the dashed line has a functional form of $2a_0/D_{tip} - 1 = b/Q_{oil}$ that is consistent with the form suggested by Umbanhowar et al. [25]. The agreement is excellent, with the one fit parameter b= (9.7 ± 0.1) cm^3/min. (c) Using optical microscopy and image-processing methods (see text), the mean radius of the water droplets in silica nanoparticle stabilized mineral oil was measured. For example, the droplets in Figure (a) (top left) had a size distribution yielding (13.7 ± 0.2) µm. (d) PFG NMR signal attenuation of water. From the fit (blue line) the droplet radius was measured (14 ± 0.5) µm. In case of water in oil emulsion without silica nanoparticles, from the fit (red line), droplet radius was measured (14 ± 6) µm (e) Comparison of mean droplet diameter (using silica nanoparticle stabilization) obtained by PFG NMR and microscopy. In all cases shown, the drops were stabilized with silica nanoparticles, as described in the text.

7.4.4 Optical Microscopy and Characterization

In this work, a Nikon Eclipse 80i upright optical microscope was used. A high speed camera (model PCO.Edge) was mounted on the microscope rear port. Bright field microscopy was used to measure the emulsion size and stability. The size distribution

of droplets was analyzed using a computer program that was coded in Interactive Data Language (IDL).

7.5 Results: Achieving Stable Confinement

In this work we generated stable, monodisperse water-in-oil emulsion with micro-scale and nano-scale confinement.

7.5.1 Preparation of Micro-Scale Confinement

As shown in Figure 7.2 (see also Appendix Figure 7.9), our microfluidic system demonstrates a high degree of versatility in the size of droplets produced. By varying Q_{oil}, a wide range of droplet sizes (14 µm to 265 µm) was produced with excellent size selectivity: a summary of results is shown here for silica-nanoparticle stabilized suspensions (with details in the Appendix). We find that a decrease in the rate of flow of the continuous phase increases the size of the droplets–a phenomenon consistent with previous studies [23,51]. We observe that the channel dimension governs the size of the water droplet. With a smaller inner capillary dimension, smaller droplets are generated. This is because the higher flow rate in the smaller channels increases the shear rate in the system, resulting smaller droplets.

For small inner fluid flow rates, following Umbanhowar et al. [25], we may write an equation relating the droplet size ($2a_0$) (scaled by the inner diameter, D_{tip}, of the capillary tube) to the velocity v of the continuous phase:

$$\frac{2a_0}{D_{tip}} = 1 + \frac{v_s}{v}.$$

In this equation $v_s = \gamma/3\eta_c$, where γ is the interfacial tension and η_c is the viscosity

of the continuous phase. By introducing the cross-sectional area of the outer channel $(\pi(D_{out}/2)^2)$ one can write the above equation as

$$\frac{2a_0}{D_{tip}} - 1 = \frac{\pi(D_{out}/2)^2 \frac{\gamma}{3\eta_c}}{Q_{oil}} \tag{7.6}$$
$$= \frac{b}{Q_{oil}},$$

where $b = \pi(D_{out}/2)^2 \frac{\gamma}{3\eta_c}$.

Experiments were performed using three different tip diameters (D_{tip}): $(15 \pm 0.2)\mu m$, $(19 \pm 0.4)\mu m$, and $(26 \pm 0.5)\mu m$. The resulting drops, imaged with a microscope, are shown in Figure 7.2(a) (the top, middle and bottom panels refer to $(D_{tip}= (15 \pm 0.2)\mu m$, $(19 \pm 0.4)\mu m$, and $(26 \pm 0.5)\mu m$ respectively). A complete set of drop sizes generated is shown in the Appendix (Figure 7.9). The resulting drop radii a_0 are shown as a function of Q_{oil} in Figure 7.10 (Appendix). In Figure 7.2(b), the plot of $2a_0/D_{tip} - 1$ against $1/Q_{oil}$ collapses all the results of drop sizes onto one master curve that is remarkably linear and thus in agreement with Equation 7.6, with a fitted b= (9.7 ± 0.1) cm^3/min. Knowing $D_{out} = 12$ mm and the measured value of viscosity $\eta_c = 0.05$ Pa.s, we calculate the interfacial tension between water and nanoparticle-mineral oil suspension: $\gamma = (21 \pm 0.3)$ mN/m. The reported value of water-mineral oil interfacial tension is about 50 mN/m [52, 53]. So, the addition of nanoparticles reduces the interfacial tension which is consistent with expectations [54]; in addition, due to the good agreement with the model function [25], we obtain a rather precise determination of the interfacial tension in this system.

Next, we transferred these water-in-oil suspensions into NMR tubes for PFG NMR studies. Without silica nanoparticles, water drops that are monodisperse upon production are observed to not only break into smaller droplets, but also coalesce into larger ones during the transfer to the NMR tube. In Figure 7.2(d), the signal at-

202

tenuation of water-in-oil droplets, whose mean radius was determined by microscopy (Figure 7.2(c)) to be (13.7 ± 0.2) μm, was plotted as a function of α^2, the gradient variable in Equation 7.5.

We used Equation 7.5 in order to determine the droplet size distribution for both cases: with and without silica particles dispersed in oil phase. From the fit, the mean droplet radius $a_0 = (14 \pm 6)$ μm for the system without silica particles. On the other hand, the addition of silica particles (Figure 7.2(d), solid blue line) as Pickering stabilizers dramatically reduced the width of the droplet size distribution: here, $a_0 = (14 \pm 0.5)$ μm. This difference was seen systematically in two trials. Hence, water drops that are monodisperse upon production (and thus during sizing by microscopy) not only break into smaller droplets, but also coalesce into larger ones during the transfer to the NMR tube, but this broadening of the size distribution is mitigated by Pickering stabilization.

We show, in Figure 7.2(e) that droplet radii, as determined by NMR in a single ensemble measurement, correlate very well with those determined painstakingly by microscopy. This reassures us that the droplet systems that we generate, and characterize using microscopy are not changed upon loading into NMR tubes for long-time experiments.

7.5.2   Preparation of Nano-Scale Confinement

We used eight different molecular weights of PEG (8000 to 5000000), purchased from Alfa Aesar. Ultra-low gelling agarose and Ficoll®PM 70 (referred to as Ficoll70 in the text) with average molecular weight of 70000 (mean radius, $R_H = 5.5$ nm [55]) were purchased from Sigma Aldrich.

Agarose gels with different agarose concentrations were prepared in a series of steps. The desired weight of ultra-low gelling temperature agarose purchased from
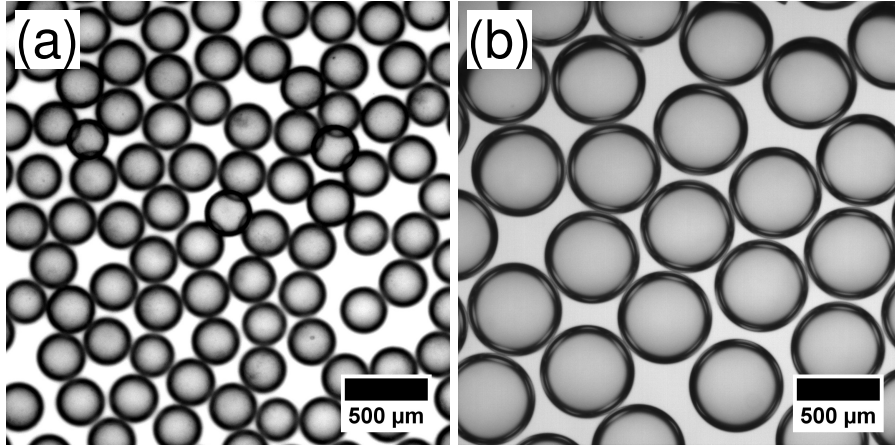
Figure 7.3: Introducing nano-scale confinement: Agarose microbeads with diameter (a) $2a_0 = (283 \pm 6)$ μm and (b) $2a_0 = (561 \pm 8)$ μm generated by the microfluidic device.

Sigma Aldrich was added to distilled water, and then the mixture was heated to the boiling temperature of the solution for complete dissolution of the agarose. Ficoll70 and PEGs were mixed into the agarose solution before gelation. The volume fraction of agarose in the gel was calculated with a density of dry agarose powder (1.64 g/cm^3) and a mass fraction of agarose in the agarose gel fiber (0.625) according to Pluen's method [38].

Uniform-sized agarose microbeads were prepared by the microfluidic technique in this study. A mixture of agarose gel with Ficoll70/PEG was used as the aqueous phase. Agarose-loaded drops did not need the additional silica nanoparticle stabilization. Both the liquids were driven through the capillaries by syringe pumps. We choose ultra-low gelling agarose, which has a gelling point of around 16°C. Once melted, this agarose will remain in the liquid phase until the temperature drops below 16°C, which ensures easy generation of agarose droplet under room temperature. Uniform agarose microbeads in oil were cooled to 4°C for 23 hours. When the temperature dropped to 4°C, agarose emulsion droplets solidified.

We generated agarose microbeads (Figure 7.3) of two different diameters $2a_0$, using

the microfluidic device, for our studies of nanoscale confinement: $2a_0 = (283 \pm 6)$ μm and $2a_0 = (561 \pm 8)$ μm. For the results reported, we used (561 ± 8) μm microbeads.

7.6 Results: Self-diffusion

7.6.1 Microscale Confinement: Diffusion of PEG Polymer

Polyethyleneglycols (PEG) have been selected as model solutes to study the effects of confinement. This offers a series of key advantages: a broad range of molecular weights can be covered, within the same family of unbranched, highly flexible macromolecules. A polydispersity factor close to unity is achievable within this family of macromolecules which prevents complications arising from molecular weight distribution effects. Moreover, the fact that water is a good solvent of PEG at room temperature ensures a behaviour in solution that is relatively easy to predict. Figure 7.4 presents the self-diffusion coefficient of PEG ($M_w = 20000$, $R_H = 4.8$ nm) as a function of polymer concentration c_p in bulk water (red squares) as well as in water droplet (blue diamonds). In recent work, we found that the polymer self-diffusion coefficient exhibits a plateau below a characteristic polymer concentration and in a crossover region between the dilute and semidilute regime, there is an exponential decrease in the long-time self-diffusion coefficient with polymer concentration [56]. This behaviour is seen here as well, but what Figure 7.4 shows is that the diffusion of PEG in a bulk water is indistinguishable both qualitatively and quantitatively from that of PEG in the water droplet. This is not surprising: the diffusion time Δ is much less than $(a_0)^2/2D_0^{PEG}$, where a_0 is the radius of the droplet and D_0^{PEG} is the diffusion coefficient of the PEG molecules at infinite dilution. Thus, the PEG chains spend a very small fraction of their time near the droplet surface. This reassures us that the PEG is uniformly distributed within the drop and not associating strongly at the
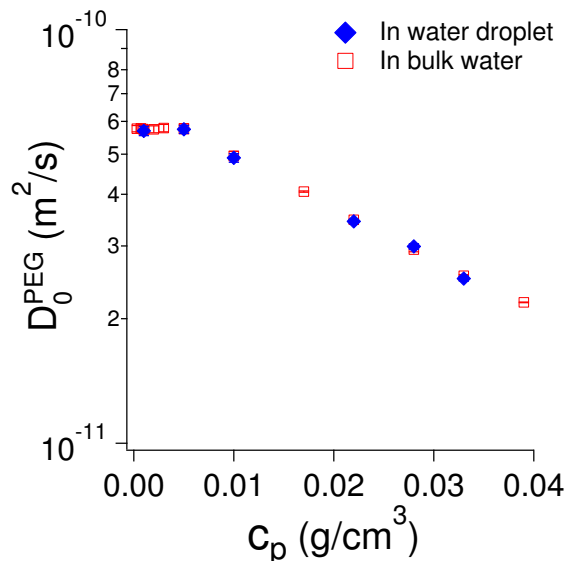
Figure 7.4: Micro-scale confinement is essentially bulk for PEG: Self-diffusion coefficient of PEG ($M_w = 20000$) as a function of polymer concentration c_p in bulk water (red squares) as well as in water droplets of radius $a_0 = (14 \pm 0.5)\mu m$ (blue diamonds): there is no discernible difference. The diffusion time, $\Delta < a_0{}^2/2D_0^{PEG}$, and therefore, PEG chains do not experience the confinement.

drop surface.

7.6.2 Nanoscale Confinement: Diffusion of Ficoll70 Spheres

Polymers have the ability to deform in order to go through nanopores. Diffusion models for macromolecules in gel network use the radius of the solute (R_H) in their predictive computations. This hard sphere analogy can be worthwhile for the diffusion of a spherical polysaccharide (e.g. Ficoll70) but is unlikely to hold for chain molecules. Thus, we begin by quantitatively examining the experimental self-diffusion of Ficoll70 (which have a compact spherical shape) in agarose gels, which provide the nanoscale confinement, both without ("bulk") and with ("bead") the micro-scale confinement.

Diffusion coefficients of Ficoll70 in H_2O and inside the agarose gel were extracted from the NMR measurements using Equation 7.4 to fit the echo amplitudes. Figure 7.5
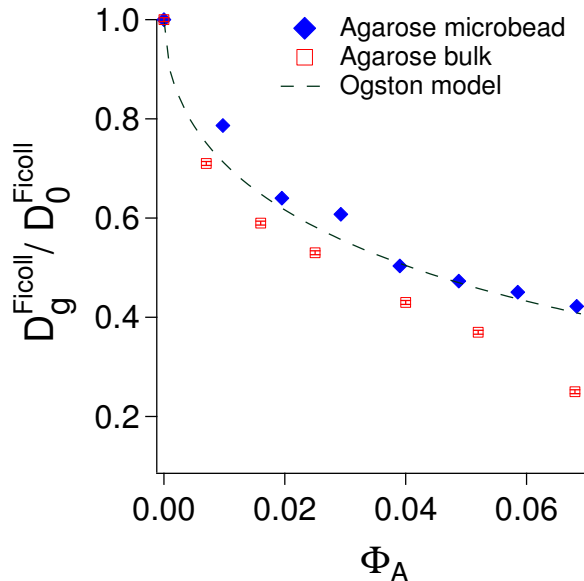
Figure 7.5: Dynamics of spherical macromolecule in gel: Diffusion coefficients of Ficoll70 ($\Phi_F = 0.02$) for several volume fractions Φ_A of agarose gel both in bulk and microbead. Diffusion coefficients of Ficoll70 in agarose gel microbeads agrees reasonably well with Ogston model (green dashed line).

presents the dependence of the diffusion coefficients of Ficoll70 on the volume fraction (Φ_A) of agarose gel. A systematic decrease in diffusion coefficients is observed as a function of increasing agarose volume fraction in the gels. A decrease is, of course, expected and can be attributed to the fact that the increase in the volume fraction of agarose in the gels reduces the space for the diffusion of Ficoll70. It is also consistent with previous measurements [57–60].

Here, however, we make quantitative connection with a theoretical model.

The dashed lines in Figure 7.5 represent the curve calculated with the Ogston model (Equation 7.2) using a particle hydrodynamic radius $R_H = 5.5$ nm and the previously determined agarose gel fibre cylinder radius $R_f = 1.9$ nm [61,62]. This is especially notable because the model is overlaid atop the data, with `no free parameters`.

What is also notable is that, while the agreement of the Ogston model is excellent for the system with `hierarchical` nanoscale and micro-scale confinement (agarose
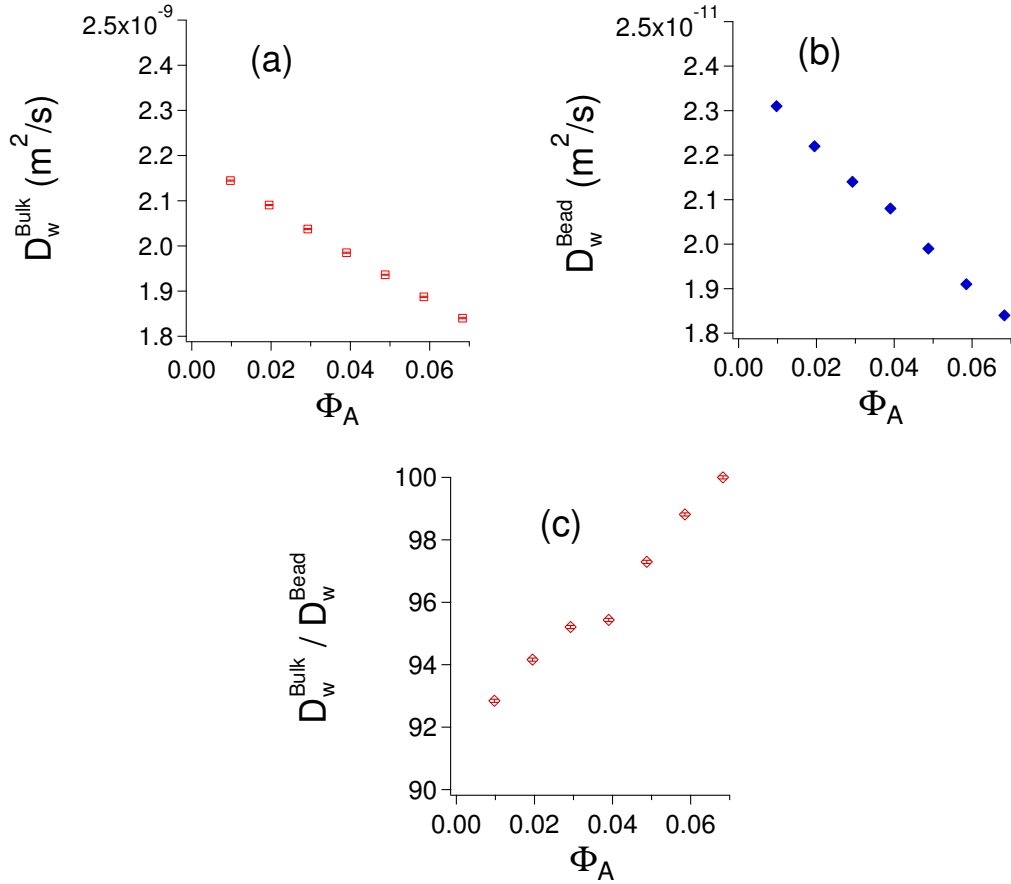
Figure 7.6: Dynamics of water in gel: Diffusion coefficients of water as a function of volume fractions for agarose gel (Φ_A) in (a) bulk and (b) microbead. (c) Ratio of self-diffusion coefficients of water in bulk and microbeads as a function of Φ_A. This ratio increases linearly with Φ_A.

in microbeads), it is less predictive for diffusion in bulk agarose. This suggests that producing gel-loaded microbeads might provide a more homogeneous gel environment, and is an issue we examine next.

7.6.3 Water Dynamics: Bulk versus Microbead Agarose

The reductions in Ficoll70 diffusivities in agarose microbeads as a function of Φ_A are well described by Ogston model. But why is the dynamics of Ficoll70 different for bulk agarose? Water dynamics allows us to explore this further.
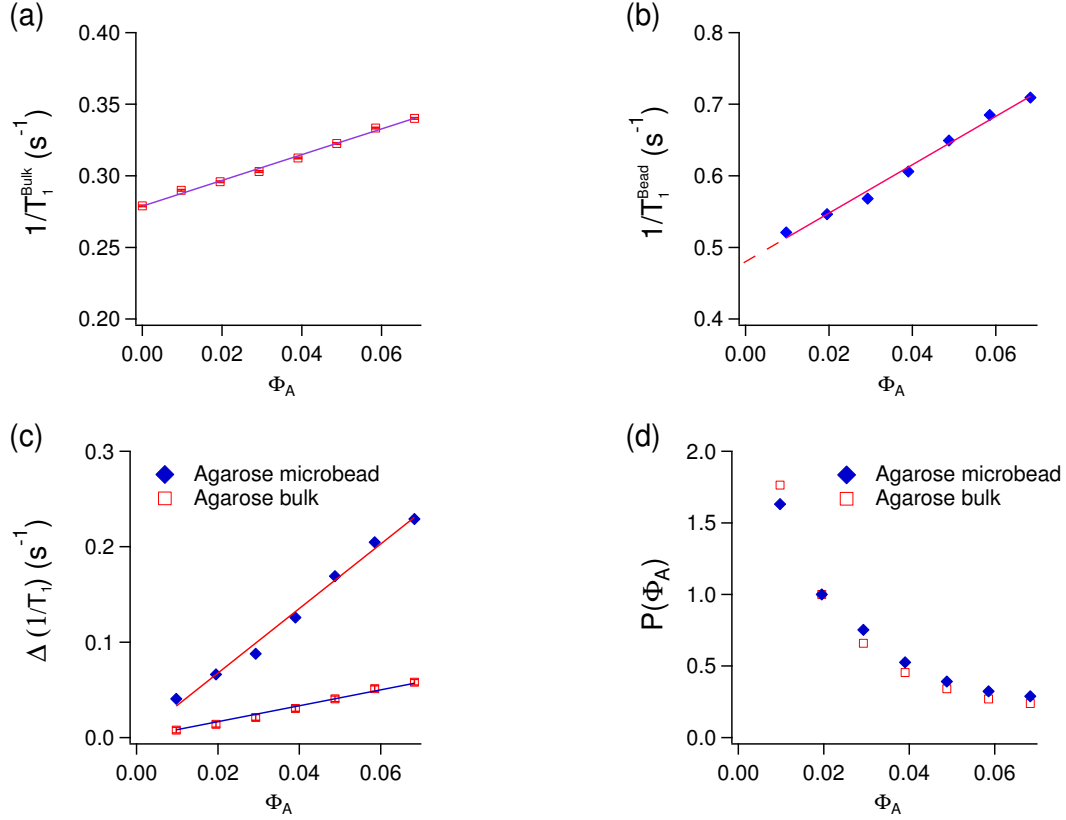
Figure 7.7: Relaxation rate and pore radius: Relaxation rates of water as a function of volume fractions for agarose gel (Φ_A) in (a) bulk and (b) agarose microbead, (c) Difference in longitudinal relaxation rate, $\Delta\left(\frac{1}{T_1}\right)$ for both bulk and agarose microbead, (d) pore radius as a function of agarose gel volume fractions, Φ_A.

Figure 7.6 shows the self-diffusion of water in agarose gel, both in bulk (Figure 7.6(a)) and in microscale beads (Figure 7.6(b)), as a function of agarose volume fraction Φ_A. A linear decrease of D_w with Φ_A was found in both bulk and microbead environments. This likely can be ascribed to previous findings [63] that the number of water molecules interacting with hydroxyl groups of agarose gel, through mechanisms including hydrogen bonding and chemical exchange of protons, depends on the volume fraction of the agarose.

However, what is the most remarkable finding is highlighted in Figure 7.6(c): the self-diffusivity in bulk agarose is nearly a factor of 100 larger than that for microbead
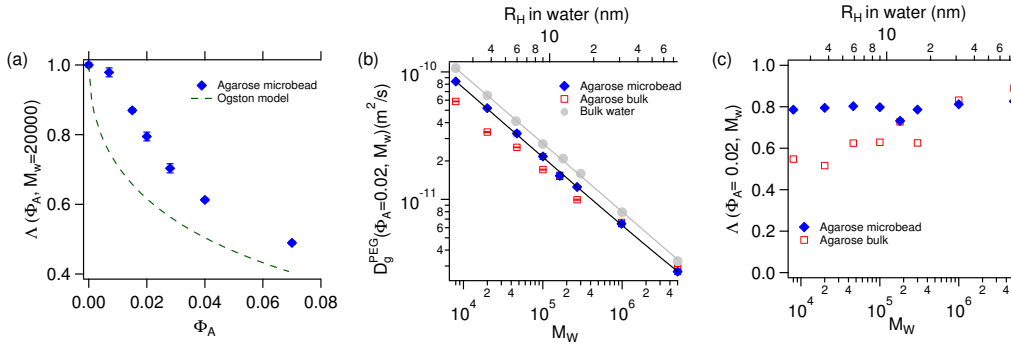
Figure 7.8: Dynamics of chain macromolecule in gel: (a) Relative diffusivity of PEG ($\Lambda(\Phi_A, M_w = 20000)$) of $c_p = 0.005 \mathrm{g/cm^3}$ in agarose microbeads do not agree with Ogston model (green dashed line). (b) Diffusion coefficients of PEG in agarose gel ($D_g^{PEG}(\Phi_A, M_w)$) as a function of molecular weight (M_w) both for bulk and microbead form. Here the diffusion coefficients of PEG in bulk water ($D_0^{PEG}(0, M_w)$) are shown in grey. From the power law fit ($D_0^{PEG}(0, M_w) = k M_w^{-\nu}$), ν is obtained to be 0.54 ± 0.01 for PEG in dilute aqueous solution and 0.53 ± 0.01 for PEG in agarose microbeads. (c) The relative value of PEG diffusion coefficients in agarose gel (D_g^{PEG}) compared to those in solution (D_0^{PEG}) are plotted as a function of molecular weight (M_w). This ratio is independent of M_w for the microbead environment but increases with M_w for bulk agarose. The corresponding hydrodynamic radius (R_H) for equivalent spheres as estimated by the Stokes Einstein equation is shown for reference. In (b) and (c) the volume fraction of gel, $\Phi_A = 0.02$ and $c_p = 0.005$ g/cm^3.

210

agarose, when in principle, the two should be identical!

Another way to probe water dynamics is via relaxation rate measurements [46]. We observe in Figure 7.7 (a) and (b) that the longitudinal relaxation rate $(1/T_1)$ of hydrogen atoms of water increased with agarose gel volume fraction. The increase with Φ_A is linear in both bulk and microbead agarose environments (with intercepts of (0.27 ± 0.001) s^{-1} and (0.48 ± 0.006) s^{-1} for bulk and microbead agarose, respectively) and is consistent with the model represented by Equation 7.3. The intercept for bulk agarose corresponds to the relaxation rates of pure water $(1/T_1(\Phi_A = 0))$ at 25°C.

In Figure 7.7 (c) we plot the difference $\Delta(1/T_1) \equiv \frac{1}{T_1(\Phi_A)} - \frac{1}{T_1(\Phi_A=0)}$ for both bulk and agarose microbead against Φ_A: one sees a proportional relationship with respect to Φ_A, but with very different (a factor of 4) slopes. Equation 7.3 predicts a proportional relationship of $\Delta(1/T_1)$ with the surface-to-volume ratio, so this implies that the surface-to-volume ratio is proportional to Φ_A.

Regardless of pore geometry, $\Delta(1/T_1)$ will always be inversely related to pore radius, and we can thus extract `relative` pore radii as a function of Φ_A. In Figure 7.7 (d), we plot a `relative` pore radius $P(\Phi_A) \equiv R_{Pore}/R_{Pore}(\Phi_A = 0.02)$, and this relative radius shows a very similar dependence for bulk and microbead agarose.

Finally, we can obtain numerical estimates of R_{Pore} as a function of Φ_A using the $P(\Phi_A)$ shown in Figure 7.7(d) and tabulated in Table 7.1 (Appendix), along with the literature values of pore radius for isolated samples. The pore radius reported for bulk agarose, for a sample at $\Phi_A = 0.02$, is (103 ± 13) nm [38], while for a microbead sample reported in the literature at $\Phi_A = 0.04$, it is (120 ± 2) nm [64]. For bulk agarose, we obtain $R_{Pore}^{Bulk}(\Phi_A)$ using $R_{Pore}^{Bulk}(\Phi_A) = P^{Bulk}(\Phi_A) \times 103$ nm while for microbead agarose, we can obtain $R_{Pore}^{Bead}(\Phi_A)$ using $R_{Pore}^{Bead}(\Phi_A) = \frac{P^{Bead}(\Phi_A)}{P^{Bead}(\Phi_A=0.04)} \times 120$ nm. At $\Phi_A = 0.02$, for example, this yields $R_{Pore}^{Bead} = 230$ nm.

We hypothesize at this point that one reason for discrepancy in water dynamics could be that the pore sizes are more regular in the microbeads, and more heterogeneous in the bulk agarose with large water pockets that behave essentially like bulk water. In order, to examine this hypothesis we measured, next, the diffusivities of different molecular weights of PEG in agarose gel. If the pore size is regular, one should see a clear decrease in the diffusivity of PEG, relative to its bulk water value, as its hydrodynamic size approaches the agarose network pore size.

7.6.4 Diffusion of PEG in Agarose Gel: Bulk vs. Microbeads

As shown in Figure 7.4, dynamics of PEG is insensitive to micro-scale confinement. Here, we examine the introduction nano-scale confinement, *via* the agarose gel network. Once again, we compare self-diffusion in bulk agarose with that in microbeads.

The diffusion coefficients for PEGs in water $(D_0^{PEG}(0, M_w))$ and in agarose gel $(D_g^{PEG}(\Phi_A, M_w))$ are measured by the PFG NMR method, at a polymer concentration $c_p = 0.005 g/cm^3$ that is in the dilute limit. We define the ratio of the PEG diffusivity in agarose gel to that in water at dilute solute concentrations as:

$$\Lambda(\Phi_A, M_w) = D_g^{PEG}(\Phi_A, M_w)/D_0^{PEG}(0, M_w). \tag{7.7}$$

In Figure 7.8(a), $\Lambda(\Phi_A, M_w = 20000)$ is not at all in agreement with the Ogston model, but in fact is more mobile than the predicted value, consistent with the fact that PEG is a flexible chainlike molecule.

Next, in Figure 7.8(b), we show the diffusion coefficient of PEGs in agarose gel $(D_g^{PEG}(\Phi_A = 0.02, M_w))$ in both microbeads (blue diamonds) and in bulk agarose (red squares). Shown for comparison is the corresponding diffusion coefficient $D_0^{PEG}(0, M_w)$ in pure water, with no confinement (grey circles). The polymer hydrodynamic radius

R_H is calculated with Equation 7.1 from $D_0^{PEG}(0, M_w)$: for M_w ranging from 8,000 to 5000,000, R_H ranged from 2.2 to 73 nm. The diffusion coefficients of PEG in the gel decrease with an increase in the molecular weight of PEG both for bulk agarose and agarose in microbeads. However, there is a clear scaling behaviour for unconfined PEG (in water) and for PEG in microbeads. If the diffusion follows Zimm dynamics, that is, the interior volume of the polymer behaves like a solid diffusing object, then, the relationship between M_w and the diffusion coefficient in a dilute solution, $D_0^{PEG}(0, M_w)$, can be expressed as [65]

$$D_0^{PEG}(0, M_w) = k M_w^{-\nu}, \tag{7.8}$$

where k is a pre-factor related to the segment size of the polymer chain and ν is a scaling exponent that depends on the polymer-solvent system. From a linear fitting of the plot of $D_0^{PEG}(0, M_w)$ and $D_g^{PEG}(\Phi_A, M_w)$ in agarose microbead with respect to M_w, ν is obtained to be 0.54 ± 0.01 for PEG in dilute aqueous solution and 0.53 ± 0.01 for PEG in agarose microbeads.

Figure 7.8(c) highlights the difference between agarose bulk *vs.* microbead by showing $\Lambda(\Phi_A = 0.02, M_w)$ for both environments. We find both ratios converging for the largest molecular weights, but the key observation is that while $\Lambda(\Phi_A = 0.02, M_w)$ is independent of M_w for the microbead environment, it increases with M_w for bulk agarose.

As shown by Monte Carlo simulation of molecular diffusion in gels, this ratio would be expected to depend on the ratio of the radius of the macromolecule and agarose gel pore radius (R_H/R_{pore}) for $R_H/R_{Pore} > 0.2$ [66]. For $\Phi_A = 0.02$, the calculated value of pore radius is 230 nm for agarose microbead. While we do probe polymer sizes from R_H= 2 nm to 70 nm, we observe no dependence of R_H in this range for

microbead. Experiments are planned for larger R_H.

7.7 Discussion and Conclusions

In this work, we have successfully generated a system with hierarchical micro-scale and nano-scale confinement. We are able to generate water-in-oil systems (without and with nano-scale confinement) that are stable with respect to transfer and over a period of days.

While micro-scale confinement is not expected to directly induce confinement for large macromolecules, because of the large diffusion times, there is, however, a more subtle effect. The regular procedure for making micro-scale agarose gel microbeads appears to be an excellent way to manufacture systematic homogeneous gel environments.

There are three results for dynamics in the nanoscale gel environment. First, for the case of spherical polysaccharide (Ficoll70) nanoparticles, the diffusivity is in agreement with the Ogston model with no free parameter. Second, the ratio of bulk-to-microbead diffusivity of water is approximately a factor of 100, suggesting the presence of large water pockets in the bulk agarose. Finally, the relative diffusivity in agarose (with respect to its value in water), as a function of the molecular weight of a flexible (PEG) polymer, is constant in the case of the encapsulated (microbead) agarose, but the corresponding ratio in bulk agarose shows an increase with increasing molecular weight.

How can these results be consistent? While we are simply reporting the experimental observations here, we offer a conjecture that is consistent with these results. If the bulk gel is more heterogeneous, then it contains regions with larger pores (i.e., water pockets). This results in the larger values for the measured water self-diffusivity.

At the same time, it is feasible that the macromolecules, Ficoll70 and PEG, preferentially partition into the bulk gel's agarose-rich regions when the hydrodynamic radius is smaller than the pore size, but preferentially reside in the water pockets when R_H exceeds the pore size. At a given Φ_A, the agarose-rich regions have a smaller pore size, and hence result in lower self-diffusivity due to the increased confinement.

Regardless of whether the above picture is correct, one issue is clear. The agarose in the hierachical nanoscale/microbead environment shows clean agreement with a simple model (for the spherical Ficolls), shows a low diffusivity for water consistent with fully confined water, and shows consistent molecular-weight-dependent scaling behaviour for flexible chainlike polymer in pure water and in the presence of confinement. Examination of larger and/or more complex macromolecules that have more direct biophysical relevance is our next target.

Acknowledgments

Appendix

7.7.1 Micro-Scale Drop Generation

We used the co-flowing method to generate stable and monodisperse water-in-oil emulsions in a glass microcapillary device. As shown in Figure 7.9, we produce uniform droplets with wide range of size using 3 tip diameters: (a-d) $D_{\tt tip} = (15 \pm 0.2)\mu m$; (e-h) $D_{\tt tip} = (19 \pm 0.4)\mu m$; (i-l) $D_{\tt tip} = (26 \pm 0.5)\mu m$. The key size-controlling factor is the flow of the continuous (oil) phase that has been altered in a controlled manner.
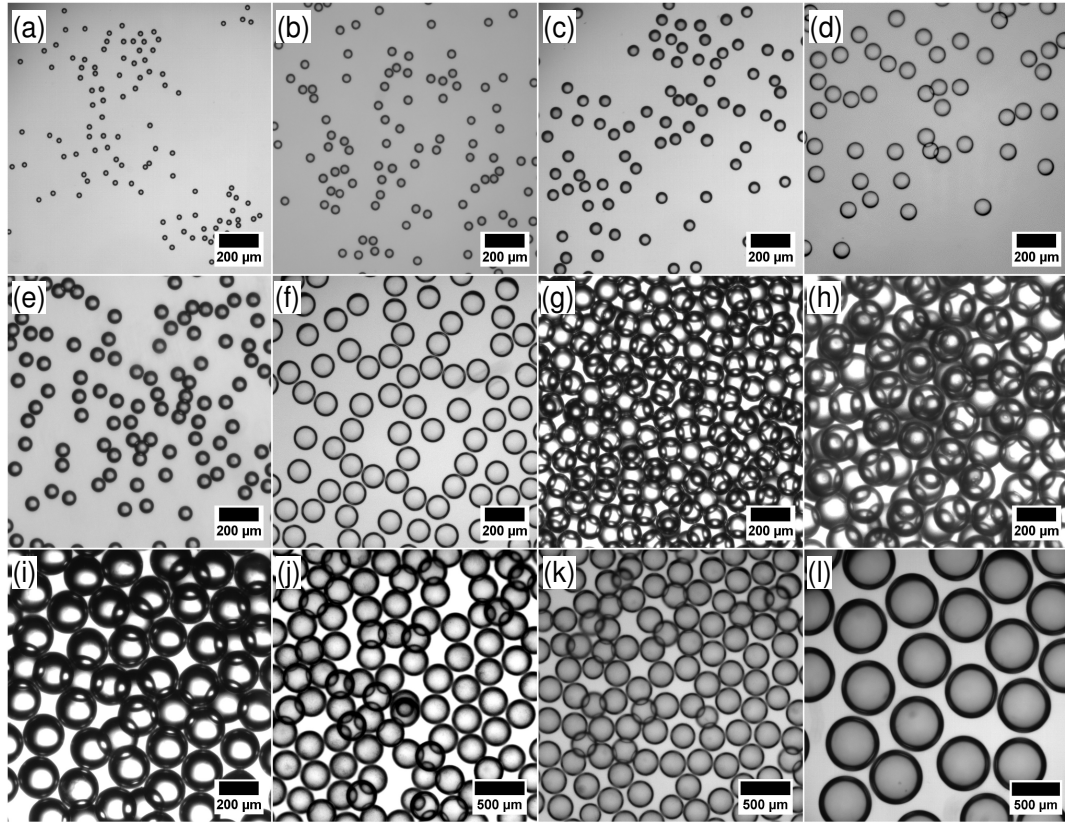
Figure 7.9: Stable and monodisperse droplets: Monodisperse water-in-oil emulsion of different droplet sizes are generated in microfluidic device. These droplets were verified to be stable for at least 26 hours. Droplet diameters are: (a) 27.4 ± 0.4 µm; (b) 46.5 ± 0.9 µm; (c) 60 ± 1.2 µm; (d) 85.2 ± 0.8 µm; (e) 76.4 ± 0.9 µm; (f) 116 ± 2 µm; (g) 125 ± 3 µm; (h) 183 ± 5 µm; (i) 214 ± 4 µm; (j) 292 ± 6 µm; (k) 253 ± 6 µm; (l) 530 ± 7 µm. In all cases shown, the drops were stabilized with silica nanoparticles, as described in the text.

This results in monodisperse droplets whose size can be tuned.

The effect of flow rates on droplet size has been measured using bright field microscopy. In Figure 7.10, droplet radius is plotted as a function of increasing oil flow rate. Here we note the fact that at higher flow rates, droplet size decreases up to a point where the droplet radius approaches to the tip diameter of the inner capillary.
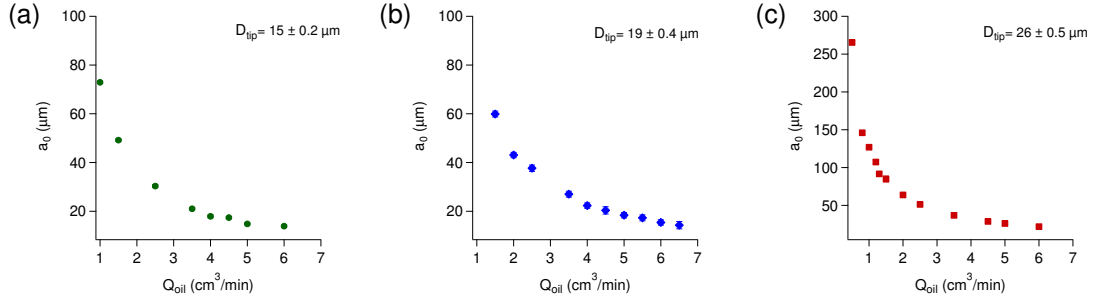
Figure 7.10: Control of drop size: Dependence of the mean radius, a_0, measured *via* image processing of optical micrographs, as a function of oil flow rate Q_{oil} for various tip diameters D_{tip}. (a) $D_{tip} = (15 \pm 0.2)\mu m$, (b) $D_{tip} = (19 \pm 0.4)\mu m$, (c) $D_{tip} = (26 \pm 0.5)\mu m$. The examples shown are for silica-nanoparticle stabilized suspensions.

.

$P(\Phi_A)$		
Volume fraction (Φ_A)	Agarose bulk	Agarose microbead
0.01	1.76	1.63
0.02	1	1
0.03	0.66	0.75
0.04	0.45	0.53
0.05	0.34	0.39
0.06	0.27	0.32
0.07	0.24	0.29

Table 7.1: $P(\Phi_A) \equiv R_{Pore}/R_{Pore}(\Phi_A = 0.02)$ for different volume fractions of bulk and agarose microbeads

.

7.7.2 Relative Pore Sizes in Agarose Gel

The relative pore sizes $P(\Phi_A) = R_{Pore}/R_{Pore}(\Phi_A = 0.02)$ in agarose microbeads were determined precisely. These values are tabulated in Table 7.1 in order to serve as a

look-up table.

Bibliography

[1] D. Boal, <u>Mechanics of the Cell</u>. Cambridge University Press, 2012.

[2] A. B. Fulton, "How crowded is the cytoplasm?," <u>Cell</u>, vol. 30, no. 2, pp. 345–347, 1982.

[3] R. J. Ellis, "Macromolecular crowding: obvious but underappreciated," <u>Trends in Biochemical Sciences</u>, vol. 26, no. 10, pp. 597–604, 2001.

[4] D. S. Tawfik and A. D. Griffiths, "Man-made cell-like compartments for molecular evolution," <u>Nature Biotechnology</u>, vol. 16, no. 7, pp. 652–656, 1998.

[5] X.-Y. Wang, Y. Pei, M. Xie, Z.-H. Jin, Y.-S. Xiao, Y. Wang, L.-N. Zhang, Y. Li, and W.-H. Huang, "An artificial blood vessel implanted three-dimensional microsystem for modeling transvascular migration of tumor cells," <u>Lab on a Chip</u>, vol. 15, no. 4, pp. 1178–1187, 2015.

[6] I. K. Zervantonakis, S. K. Hughes-Alford, J. L. Charest, J. S. Condeelis, F. B. Gertler, and R. D. Kamm, "Three-dimensional microfluidic model for tumor cell intravasation and endothelial barrier function," <u>Proceedings of the National Academy of Sciences</u>, vol. 109, no. 34, pp. 13515–13520, 2012.

[7] L. Shang, Y. Cheng, and Y. Zhao, "Emerging droplet microfluidics," <u>Chemical Reviews</u>, vol. 117, no. 12, pp. 7964–8040, 2017. PMID: 28537383.

[8] L. Rosenfeld, T. Lin, R. Derda, and S. K. Tang, "Review and analysis of performance metrics of droplet microfluidics systems," <u>Microfluidics and Nanofluidics</u>, vol. 16, no. 5, pp. 921–939, 2014.

[9] J. Clausell-Tormos, D. Lieber, J.-C. Baret, A. El-Harrak, O. J. Miller, L. Frenz, J. Blouwolff, K. J. Humphry, S. Köster, H. Duan, et al., "Droplet-based microfluidic platforms for the encapsulation and screening of mammalian cells and multicellular organisms," Chemistry & Biology, vol. 15, no. 5, pp. 427–437, 2008.

[10] E. Brouzes, M. Medkova, N. Savenelli, D. Marran, M. Twardowski, J. B. Hutchison, J. M. Rothberg, D. R. Link, N. Perrimon, and M. L. Samuels, "Droplet microfluidic technology for single-cell high-throughput screening," Proceedings of the National Academy of Sciences, vol. 106, no. 34, pp. 14195–14200, 2009.

[11] J.-u. Shim, L. F. Olguin, G. Whyte, D. Scott, A. Babtie, C. Abell, W. T. Huck, and F. Hollfelder, "Simultaneous determination of gene expression and enzymatic activity in individual bacterial cells in microdroplet compartments," Journal of the American Chemical Society, vol. 131, no. 42, pp. 15251–15256, 2009.

[12] J.-C. Baret, O. J. Miller, V. Taly, M. Ryckelynck, A. El-Harrak, L. Frenz, C. Rick, M. L. Samuels, J. B. Hutchison, J. J. Agresti, et al., "Fluorescence-activated droplet sorting (fads): efficient microfluidic cell sorting based on enzymatic activity," Lab on a Chip, vol. 9, no. 13, pp. 1850–1858, 2009.

[13] L. Kisley, K. A. Serrano, D. Guin, X. Kong, M. Gruebele, and D. E. Leckband, "Direct imaging of protein stability and folding kinetics in hydrogels," ACS Applied Materials & Interfaces, vol. 9, no. 26, pp. 21606–21617, 2017. PMID: 28553706.

[14] G. Karoubi, M. L. Ormiston, D. J. Stewart, and D. W. Courtman, "Single-cell hydrogel encapsulation for enhanced survival of human marrow stromal cells," Biomaterials, vol. 30, no. 29, pp. 5445–5455, 2009.

[15] A. Hayashi and T. Kanzaki, "Swelling of agarose gel and its related changes," Food Hydrocolloids, vol. 1, no. 4, pp. 317–325, 1987.

[16] A. G. Carlos, Y. Teramura, and H. Iwata, "Cryopreserved agarose-encapsulated islets as bioartificial pancreas: a feasibility study," Transplantation, vol. 87, no. 1, pp. 29–34, 2009.

[17] D. Pelaez, C.-Y. Charles Huang, and H. S. Cheung, "Cyclic compression maintains viability and induces chondrogenesis of human mesenchymal stem cells in fibrin gel scaffolds," Stem Cells and Development, vol. 18, no. 1, pp. 93–102, 2009.

[18] O. Bonhomme, J. Leng, and A. Colin, "Microfluidic wet-spinning of alginate microfibers: a theoretical analysis of fiber formation," Soft Matter, vol. 8, no. 41, pp. 10641–10649, 2012.

[19] L. Yobas, S. Martens, W.-L. Ong, and N. Ranganathan, "High-performance flow-focusing geometry for spontaneous generation of monodispersed droplets," Lab on a Chip, vol. 6, no. 8, pp. 1073–1079, 2006.

[20] T. Nisisako and T. Torii, "Microfluidic large-scale integration on a chip for mass production of monodisperse droplets and particles," Lab on a Chip, vol. 8, no. 2, pp. 287–293, 2008.

[21] T. Thorsen, R. W. Roberts, F. H. Arnold, and S. R. Quake, "Dynamic pattern formation in a vesicle-generating microfluidic device," Physical Review Letters, vol. 86, no. 18, p. 4163, 2001.

[22] D. Link, S. L. Anna, D. Weitz, and H. Stone, "Geometrically mediated breakup of drops in microfluidic devices," Physical Review Letters, vol. 92, no. 5, p. 054503, 2004.

[23] S. L. Anna, N. Bontoux, and H. A. Stone, "Formation of dispersions using "flow focusing" in microchannels," <u>Applied Physics Letters</u>, vol. 82, no. 3, pp. 364–366, 2003.

[24] A. Woodward, T. Cosgrove, J. Espidel, P. Jenkins, and N. Shaw, "Monodisperse emulsions from a microfluidic device, characterised by diffusion nmr," <u>Soft Matter</u>, vol. 3, no. 5, pp. 627–633, 2007.

[25] P. Umbanhowar, V. Prasad, and D. Weitz, "Monodisperse emulsion generation *via* drop break off in a coflowing stream," <u>Langmuir</u>, vol. 16, no. 2, pp. 347–351, 2000.

[26] A. S. Utada, A. Fernandez-Nieves, J. M. Gordillo, and D. A. Weitz, "Absolute instability of a liquid jet in a coflowing stream," <u>Physical Review Letters</u>, vol. 100, no. 1, p. 014502, 2008.

[27] J.-C. Baret, "Surfactants in droplet-based microfluidics," <u>Lab on a Chip</u>, vol. 12, no. 3, pp. 422–433, 2012.

[28] B. Binks and S. Lumsdon, "Pickering emulsions stabilized by monodisperse latex particles: effects of particle size," <u>Langmuir</u>, vol. 17, no. 15, pp. 4540–4547, 2001.

[29] R. Miller, V. Fainerman, V. Kovalchuk, D. Grigoriev, M. Leser, and M. Michel, "Composite interfacial layers containing micro-size and nano-size particles," <u>Advances in Colloid and Interface Science</u>, vol. 128, pp. 17–26, 2006.

[30] S. Arnott, A. Fulmer, W. Scott, I. Dea, R. Moorhouse, and D. Rees, "The agarose double helix and its function in agarose gel structure," <u>Journal of Molecular Biology</u>, vol. 90, no. 2, pp. 269IN11273–272284, 1974.

[31] E. M. Johnson, D. A. Berk, R. K. Jain, and W. M. Deen, "Hindered diffusion in agarose gels: test of effective medium model," Biophysical Journal, vol. 70, no. 2, pp. 1017–1023, 1996.

[32] S. Waki, J. Harvey, and A. Bellamy, "Study of agarose gels by electron microscopy of freeze-fractured surfaces," Biopolymers, vol. 21, no. 9, pp. 1909–1926, 1982.

[33] G. A. Griess, E. T. Moreno, R. A. Easom, and P. Serwer, "The sieving of spheres during agarose gel electrophoresis: quantitation and modeling," Biopolymers, vol. 28, no. 8, pp. 1475–1484, 1989.

[34] G. A. Griess, K. B. Guiseley, and P. Serwer, "The relationship of agarose gel structure to the sieving of spheres during agarose gel electrophoresis," Biophysical Journal, vol. 65, no. 1, pp. 138–148, 1993.

[35] E. M. Johnson, D. A. Berk, R. K. Jain, and W. M. Deen, "Diffusion and partitioning of proteins in charged agarose gels," Biophysical Journal, vol. 68, no. 4, pp. 1561–1568, 1995.

[36] N. Pernodet, M. Maaloum, and B. Tinland, "Pore size of agarose gels by atomic force microscopy," Electrophoresis, vol. 18, no. 1, pp. 55–58, 1997.

[37] M. Maaloum, N. Pernodet, and B. Tinland, "Agarose gel structure using atomic force microscopy: gel concentration and ionic strength effects," Electrophoresis, vol. 19, no. 10, pp. 1606–1610, 1998.

[38] A. Pluen, P. A. Netti, R. K. Jain, and D. A. Berk, "Diffusion of macromolecules in agarose gels: comparison of linear and globular configurations," Biophysical Journal, vol. 77, no. 1, pp. 542–552, 1999.

[39] J. P. Gong, N. Hirota, A. Kakugo, T. Narita, and Y. Osada, "Effect of aspect ratio on protein diffusion in hydrogels," The Journal of Physical Chemistry B, vol. 104, no. 42, pp. 9904–9908, 2000.

[40] N. Fatin-Rouge, K. Starchev, and J. Buffle, "Size effects on diffusion processes within agarose gels," Biophysical Journal, vol. 86, no. 5, pp. 2710–2719, 2004.

[41] W. Deen, "Hindered transport of large molecules in liquid-filled pores," AIChE Journal, vol. 33, no. 9, pp. 1409–1425, 1987.

[42] A. Ogston, B. Preston, and J. Wells, "On the transport of compact particles through solutions of chain-polymers," in Proceedings of the Royal Society of London A: Mathematical, Physical and Engineering Sciences, vol. 333, pp. 297–316, The Royal Society, 1973.

[43] D. Sandrin, D. Wagner, C. Sitta, R. Thoma, S. Felekyan, H. Hermes, C. Janiak, N. de Sousa Amadeu, R. Kühnemuth, H. Löwen, et al., "Diffusion of macromolecules in a polymer hydrogel: from microscopic to macroscopic scales," Physical Chemistry Chemical Physics, vol. 18, no. 18, pp. 12860–12876, 2016.

[44] M. Moussaoui, M. Benlyas, and P. Wahl, "Diffusion of proteins in sepharose cl-b gels," Journal of Chromatography A, vol. 591, p. 115, 1992.

[45] J. Tong and J. L. Anderson, "Partitioning and diffusion of proteins and linear polymers in polyacrylamide gels," Biophysical Journal, vol. 70, no. 3, pp. 1505–1513, 1996.

[46] C. D'Agostino, R. Liuzzi, L. F. Gladden, and S. Guido, "Swelling-induced structural changes and microparticle uptake of gelatin gels probed by nmr and clsm," Soft Matter, vol. 13, no. 16, pp. 2952–2961, 2017.

[47] J. Meyer and M. Scholz, "Fumed silanized silica," July 3 2012. US Patent 8,211,971.

[48] P. Callaghan, K. Jolley, and R. Humphrey, "Diffusion of fat and water in cheese as studied by pulsed field gradient nuclear magnetic resonance," Journal of Colloid and Interface Science, vol. 93, no. 2, pp. 521–529, 1983.

[49] S. Barhoum, S. Palit, and A. Yethiraj, "Diffusion nmr studies of macromolecular complex formation, crowding and confinement in soft materials," Progress in Nuclear Magnetic Resonance Spectroscopy, vol. 94, pp. 1–10, 2016.

[50] J. E. Tanner, "Use of the stimulated echo in nmr diffusion studies," The Journal of Chemical Physics, vol. 52, no. 5, pp. 2523–2526, 1970.

[51] A. M. Gañán-Calvo and J. M. Gordillo, "Perfectly monodisperse microbubbling by capillary flow focusing," Physical Review Letters, vol. 87, no. 27, p. 274501, 2001.

[52] M. Sun, S. S. Bithi, and S. A. Vanapalli, "Microfluidic static droplet arrays with tuneable gradients in material composition," Lab on a Chip, vol. 11, no. 23, pp. 3949–3952, 2011.

[53] C. A. Stan, S. K. Tang, and G. M. Whitesides, "Independent control of drop size and velocity in microfluidic flow-focusing generators using variable temperature and flow rate," Analytical Chemistry, vol. 81, no. 6, pp. 2399–2402, 2009.

[54] H. Fan and A. Striolo, "Nanoparticle effects on the water-oil interfacial tension," Physical Review E, vol. 86, no. 5, p. 051610, 2012.

[55] J. R. Wenner and V. A. Bloomfield, "Crowding effects on ecorv kinetics and binding," Biophysical Journal, vol. 77, no. 6, pp. 3234–3241, 1999.

[56] S. Palit, L. He, W. A. Hamilton, A. Yethiraj, and A. Yethiraj, "Combining diffusion nmr and small-angle neutron scattering enables precise measurements of polymer chain compression in a crowded environment," <u>Physical Review Letters</u>, vol. 118, no. 9, p. 097801, 2017.

[57] J. J. Sahlin and N. A. Peppas, "An investigation of polymer diffusion in hydrogel laminates using near-field ftir microscopy," <u>Macromolecules</u>, vol. 29, no. 22, pp. 7124–7129, 1996.

[58] C. I. Bica, R. Borsali, E. Geissler, and C. Rochas, "Dynamics of cellulose whiskers in agarose gels. 1. polarized dynamic light scattering," <u>Macromolecules</u>, vol. 34, no. 15, pp. 5275–5279, 2001.

[59] S. Kwak and M. Lafleur, "Self-diffusion of macromolecules and macroassemblies in curdlan gels as examined by pfg-se nmr technique," <u>Colloids and Surfaces A: Physicochemical and Engineering Aspects</u>, vol. 221, no. 1, pp. 231–242, 2003.

[60] I. Sebti, D. Blanc, A. Carnet-Ripoche, R. Saurel, and V. Coma, "Experimental study and modeling of nisin diffusion in agarose gels," <u>Journal of Food Engineering</u>, vol. 63, no. 2, pp. 185–190, 2004.

[61] B. Amsden, "Solute diffusion within hydrogels. mechanisms and models," <u>Macromolecules</u>, vol. 31, no. 23, pp. 8382–8395, 1998.

[62] M. Djabourov, A. Clark, D. Rowlands, and S. Ross-Murphy, "Small-angle x-ray scattering characterization of agarose sols and gels," <u>Macromolecules</u>, vol. 22, no. 1, pp. 180–188, 1989.

[63] J. Narayanan, J.-Y. Xiong, and X.-Y. Liu, "Determination of agarose gel pore size: Absorbance measurements vis a vis other techniques," in <u>Journal of Physics: Conference Series</u>, vol. 28, p. 83, IOP Publishing, 2006.

[64] J. Chou, A. Lennart, J. Wong, M. F. Ali, P. N. Floriano, N. Christodoulides, J. Camp, and J. T. McDevitt, "Modeling analyte transport and capture in porous bead sensors," Analytical Chemistry, vol. 84, no. 5, pp. 2569–2575, 2012.

[65] M. Doi and S. F. Edwards, The Theory of Polymer Dynamics, vol. 73. Oxford University Press, 1988.

[66] P. A. Netz and T. Dorfmüller, "Computer simulation studies of anomalous diffusion in gels: structural properties and probe-size dependence," The Journal of Chemical Physics, vol. 103, no. 20, pp. 9074–9082, 1995.

Chapter 8

Conclusion

The effects of macromolecular crowding can have implications for intracellular transport. The presence of large amounts of macromolecules in solution results in an entropic effect: the excluded volume effect as a result of which proteins in the cell have a significantly smaller portion of volume conformationally accessible to them than proteins in dilute solution. Entropy can lead to effective attractions: the depletion force can cause compression of polymer chains. On the other hand, electrostatic interactions can lead to repulsions, and hence can lead to expansion of macromolecules. In living cells macromolecular size is likely affected by entropy as well as specific and non-specific interactions. In addition, cytoskeletal elements can provide confining spaces.

Macromolecular dynamics at low concentrations is directed by macromolecular size *via* the Stokes-Einstein relation. In a crowded system, however, hydrodynamic interactions can be said to lead to an effective microscale viscosity or mobility that is different from the solvent viscosity. Measuring both size and mobility directly provides access to this micro-viscosity.

In this thesis, we consider a toy model of a biological system in order to understand

the effects of crowding in a relatively simple environment. Our model system has two components: (1) polymer that mimics protein, and (2) a polysaccharide that mimics the macromolecular crowder. We approach crowding systematically by varying the key parameters: the concentration of polymers, packing fraction of polysaccharide, and the charge of the crowding agent.

Do synthetic polymers provide an accurate model for the crowded environment in cells? Are there important factors that cannot be captured by pure volume exclusion models? The studies that we have performed should help inform these questions, and lead us to a better understanding of polymer-nanoparticle system.

8.1 Structure and Dynamics in a Polymer-Crowder System

In Chapter 4, we reported on pulsed-gradient stimulated echo (PFG-NMR) diffusion and small-angle neutron scattering (SANS) experiments on a system of uncharged polymer, polyethylene glycol (PEG) and uncharged crowders (Ficoll 70) at a range of polymer concentrations and crowder packing fractions. We find that, as a function of polymer concentration, there are two clear behaviors: for all crowder packing fractions (Φ_F) there is a characteristic concentration c^* below which the diffusion coefficient is independent of polymer concentration. In pure PEG, c^* is identified as the overlap concentration. In the presence of crowder c^* is a characteristic concentration that identifies a "polymer-dilute" regime. What is remarkable is that there is a polymer-dilute regime even in the crowding limit!

Above c^*, there is an exponential decrease in the long-time self-diffusion coefficient with polymer concentration. This exponential behavior is valid for 3 polymer molecular weights and several crowder packing fractions ($0 < \Phi_F < 0.35$), and in that

sense is universal. It should be noted that these experimental observations provide impetus for theory and simulation studies on this model system.

Above c^*, we established that the system is in a crossover regime between polymer-dilute and semi-dilute, and results from there cannot be naively extrapolated into the polymer-dilute regime. We also used SANS to examine the system of PEG and Ficoll70 at a range of polymer concentrations and crowder volume fractions. In these experiments, the scattering length density of the solvent, a mixture of H_2O and D_2O, was matched [x H_2O + (1-x) H_2O] to the scattering-length density of the Ficoll70 crowder (for x = 0.41), while providing a significant contrast with respect to the deuterated PEG. The primary observable was the radius of gyration R_g of the PEG (monomer or aggregate). It was found that R_g decreases only weakly with increasing crowder volume fraction fraction, for a macromolecule-to-crowder size ratio $\lambda = 1.1$; however, there appears to be significant compression for $\lambda = 1.8$ and 2.9.

8.2 The Effect of Crowder Charge on Polymer Dynamics and Structure

The tandem use of pulsed-gradient NMR (PFG NMR), SANS, and rheology on near-identical systems is not very common. In Chapter 6, we used these methods in order to examine the role of crowder charge on transport in a model polymer-colloid system for macromolecular crowding. We have examined the effect of crowder particle charge on macromolecular structure, studied *via* small-angle neutron scattering (SANS), and translational dynamics, studied *via* pulsed-field gradient (PFG) NMR, in addition to bulk viscosity measurements, in a polymer macromolecule (polyethylene glycol, PEG) – nanoparticle crowder (polysucrose, Ficoll70) model system, in the case where polymer size and crowder size are comparable.

There are modest effects of crowder charge on polymer dynamics at relatively low volume fractions: there is a factor of 2 speed up relative to uncharged crowder. Polymer size R_g, also shows a modest increase, relative to uncharged crowder at large crowder packing fractions Φ_F. The reason for an increase is not known to us. However, there is only a tiny effect ($\approx 10\%$) at the high volume fractions that represent the limit of molecular crowding.

By tracking polymer and crowder dynamics *via* different measures of macromolecular mobility, we find that mobility of the flexible polymer in the crowding limit is 10-100 times faster than that of the compact, spherical crowder in spite of their similar size. How we picture this result is that the flexible polymer chain is able to squeeze through crowder interstices while the compact sphere is not. Hence, a key result of this work is that macromolecular flexibility can be employed to accelerate transport in cells.

Finally, we examined the role of enthalpic contributions and compared the model crowder with bacterial cell lysates. Interestingly, the behavior of PEG in cell lysate is not different from PEG in the Ficolls: one still sees the exponential decay as a function of polymer concentration. In addition, the quantitative value of the diffusivity of the cell lysate lies in between the uncharged and charged Ficoll70, indicating that once one controls for crowder charge, macromolecular diffusion in an artificial crowder might be meaningful in biologically relevant systems.

8.3   Charged and Uncharged Colloid

Chapter 5 and 6 dealt with polymer structure and dynamics in the presence of Ficoll70, a polysaccharide that is often used as a model crowder. However, in the course of our studies, we found that Ficoll70 had interesting non-ideal behaviors. Chapter 7

reported on these behaviors.

Ficoll70 has been extensively used for application to cryopreservation for different living cells and renal filtration due to its high hydrophobicity as well as its charge neutral globular form. This synthetic carbohydrate polymer has also been used as a macromolecular crowding agent to produce a resemblance of the high total concentrations that are encountered in the cytoplasm. The characteristics of Ficoll70 have not been adequately recognized in the literature. One unsolved question among researchers is whether Ficoll70 in solution is an ensemble of hard spheroids, or whether it is soft. In Chapter 7 we have applied pulsed-field gradient (PFG) NMR and rheology in order to assess the most prominent characteristics of charged and uncharged Ficoll70 in water.

Analysis of the data indicate that NMR signal attenuation above a certain packing fraction can be adequately fitted with a bi-exponential function. The self-diffusion measurements show also that the Ficoll70, an often-used compact, spherical poly-sucrose molecule, is itself non-ideal, exhibiting signs of both softness and attractive interactions in the form of a stable suspension consisting of monomers and clusters. Further, we can quantify the fraction of monomer and cluster. This work strengthens the picture of the existence of a bound water layer within and around a porous Ficoll70 particle.

This work suggests that in order to properly model the polymer-crowder system, simulations must begin by successfully modeling the crowder qualitatively. The question arises whether one should use an even simpler crowder. This is possible, however, we must keep in mind that the crowder should reproduce behaviors seen in more biophysically relevant crowders such as cell lysates, and thus some degree of complexity might be necessary.

8.4 Micro- and Nano-Scale Confinement

Cytoplasm provides compartmentalization, macromolecular crowding, and small volume to the cell; features that affect transport inside living cells profoundly. Biological materials have structures across many length scales. These hierarchical structures restricts the ability of a solute to diffuse, and such effects often vary depending on the size of the solute.

In Chapter 7, we study the macromolecular dynamics in of hierarchical length scale with a heterogeneous distribution of macromolecules. We employed the pulsed-field-gradient (PFG) NMR technique to monitor the dynamics of macromolecules in the "hard" (impenetrable) spherical confinement of water droplets as well as in "soft" gel matrices where molecules can move from one pore to others.

We generated (i) highly monodisperse micro-confinement of water droplets in a bulk liquid and (ii) homogeneous nano-confinement (iii) hierarchical microscale and nanoscale confinement in the form of agarose microbeads–both amenable to NMR studies.

We find, not surprisingly, that micro-scale confinement has no effect on macromolecular dynamics. By measuring macromolecular self-diffusivity in the presence of nano-scale confinement, we find excellent agreement (`with zero fit parameters`) to a simple obstruction model for the compact and spherical macromolecule (Ficoll70). A flexible polymer chain (PEG), not surprisingly, diffuses faster than Ficoll70 in the presence of nanoscale confinement. We also report the dynamics of water that presents a difference in gel structure between agarose bulk and microbeads. Our main finding is that the introduction of microscale confinement also has the side effect of making the nanoscale confining environment less heterogeneous.

In this thesis, we have thus examined in detail many aspects of crowding: flexible polymer vs. compact crowder, role of charge, and non-ideality of crowder. We have also constructed a model system that incorporates hierarchical micro- and nano-scale confinement that are stable enough that they can be accessed by slow experiments like NMR (and in principle SANS or other experimental techniques).

8.5   Future Directions

In this report we have emphasized the fact that the free and random motion of a macromolecular system undergoes rapid dynamical and conformational modification with the change of its environment. Future directions could include the diffusion of macromolecules in the presence of other macromolecules in an environment that can be altered chemically and by geometric confinement. The flexibility of the polymers can be changed. For example, the diffusion of rigid, semi-flexible and flexible polymers (actually changing the entropy) in a crowding environment is of interest.

Another possible future direction is to complement existing and ongoing studies of structure (SANS) and long-time dynamics (PFG-NMR) with a study of short-time dynamics using the Fluorescence correlation spectroscopy (FCS) technique. The inherent global averaging in FCS is significantly lower than NMR which provides a unique opportunity for using single-molecule probes in crowded environments in the µs to ms temporal range. The short-time diffusion coefficient should be more sensitive to hydrodynamic interactions. Direct comparison between NMR and FCS studies on crowding effects on diffusion would elucidate the role of hydrodynamics in macromolecular crowding. To our knowledge, no previous work has examined the question of macromolecular crowding *via* a combination of SANS, NMR and FCS studies.

One can also compare these experiments with simulations in 3D, with the simulations carried both with and without hydrodynamic interactions.

❧⁊❦